Structural Evaluation of Hybrid Double-Lap Shear Bolted Connections Incorporating Additively Manufactured 316L Stainless Steel Inner Plates

by

Hasan Almuhanna

A thesis submitted in partial fulfilment of the requirements for the degree of Doctor of Philosophy

School of Mechanical, Aerospace and Civil Engineering
The University of Sheffield

May 2026

Declaration

I, Hasan Almuhanna, confirm that the thesis titled "Structural Evaluation of Hybrid Double-Lap Shear Bolted Connections Incorporating Additively Manufactured 316L Stainless Steel Inner Plates" is my own work. Any work from other sources included in this thesis is properly cited and referenced. I am aware of the University's Guidance on Academic Integrity. This work has not previously been presented for an award at this, or any other, university.

Publications arising from this thesis are acknowledged below. The contribution of all co-authors is explained in the introductory chapter and in the forward commentary for each journal article chapter.

Published articles

- Almuhanna, H., Torelli, G., Kindermann, R., and Susmel, L. "Failure investigation of hybrid double-lap shear bolted connections with additively manufactured 316L stainless steel inner plates." *Engineering Failure Analysis*, vol. 179, 2025, 109756. https://doi.org/10.1016/j.engfailanal.2025.109756
- Almuhanna, H., Torelli, G., and Susmel, L. "Machine Learning Models to Predict the Static Failure of Double-Lap Shear Bolted Connections." *Fatigue and Fracture of Engineering Materials and Structures*, first published 28 June 2025. https://doi.org/10.1111/ffe.70019
- Almuhanna, H., Torelli, G., and Susmel, L. "Static Assessment of Hybrid Double Lap Bolted Joints With Additively Manufactured 316L Plates." *Fatigue and Fracture of Engineering Materials and Structures*, first published 15 February 2026. https://doi.org/10.1111/ffe.70218
- Almuhanna, H., Torelli, G., and Susmel, L. "The Theory of Critical Distances for Predicting the Static Failure of Double-Lap Bolted Joints With Conventional and Additively Manufactured 316L Stainless Steel Inner Plates." *Fatigue and Fracture of Engineering Materials and Structures*, first published 01 July 2026. http://doi.org/10.1111/ffe.70349

Signed: Hasan Almuhanna

Date: May 2026

Abstract

This study investigates hybrid double-lap shear bolted connections incorporating additively manufactured 316L stainless steel inner plates, alongside conventionally produced reference plates, in single- and double-bolted configurations with different geometric design variables. The additive manufacturing technologies considered are wire arc additive manufacturing and selective laser melting. The tests were designed to invoke failure at the inner plates, while additive manufacturing-related material properties, surface undulations and thickness variation can further influence the failure mechanism. The study integrates experimental testing with analytical, numerical, and machine learning assessments to build a comprehensive evaluation framework. First, coupon tests were used to characterise the mechanical response of all manufacturing methods, while double-lap shear tests were used to identify failure modes observed in the inner plates. The additively manufactured specimens were examined under different extraction angles relative to the printing direction, including 0°, 45°, 60° and 90°, and under both machined and as-built conditions. The measured response is then compared against design code-based strength estimations to evaluate the extent to which conventional design equations remain applicable when the inner plates are additively manufactured. These estimations are also compared with literature-based equations to identify which method provides better agreement with the test results. A stress-based prediction technique is subsequently examined by applying the Theory of Critical Distances using linear elastic finite element stress fields to estimate static failure in the tested joints. Finally, machine learning models are evaluated to predict failure load and failure mode using a dataset collected from the literature, which is later expanded using results from the present tests and additional literature data on additively manufactured inner plates. Ultimately, this study evaluates whether additively manufactured plates can be used safely and beneficially in structural bolted connections, and it provides experimentally supported and validated prediction methods as practical alternatives for structural integrity assessment.

Acknowledgments

I am very grateful for the support I received from my supervisors throughout my PhD and in completing this thesis. I sincerely thank Professor Luca Susmel for his supervision and for consistently pushing the work to a higher standard, particularly in ensuring the rigour of the research. I genuinely valued our weekly meetings, which kept me motivated and focused. I also thank Dr Giacomo Torelli for his support, especially his guidance on the machine learning part of this study, and for his thorough reviews during the preparation of the journal articles. I am grateful to Professor Iman Hajirasouliha for his support as my internal supervisor.

I thank Dr Renan Kindermann for his contribution to producing the specimens. I also thank the technicians Paul Blackbourn, Kieren O. Howarth, Samuel J. Gibson, and Joseph S. Marples for their support with the experimental work. I thank my colleagues for the constructive scientific discussions and for fostering a positive environment throughout my PhD.

I would like to acknowledge the Kuwait Institute for Scientific Research (KISR) for sponsoring my PhD. This work was also supported by the Henry Royce Institute for Advanced Materials, funded through EPSRC grants EP/R00661X/1, EP/P025021/1, and EP/S019367/1.

Finally, I thank my family for their constant support. I thank my wife for her patience and for carrying the pressure of the PhD period with me. I also thank my child for putting up with the time I spent away from him. To my parents and siblings, thank you for always being there for me.

Table of Contents

List of Figures

List of Tables

Part I. Thesis Overview and Research Context

Chapter 1. Introduction

1.1 Research scope, aim, and objectives

In steel structures, connections are the components of the structural system where steel sections are joined to perform as one entity to withstand different types of loads. Steel and stainless steel connections are typically designed to be bolted or welded, and their design guidelines, rules, and design resistance checks are well established in design standards [1–4] . In this study, the primary focus is on the structural static response of bolted connections, as their widespread use in steel construction is supported by the efficiency they offer in prefabrication and rapid site installation [5]. Their structural response under static loading is therefore of practical importance, particularly when different manufacturing methods are introduced into connection components. Accordingly, additive manufacturing (AM) is increasingly being considered in structural engineering due to its potential for manufacturing flexibility, automation, bespoke geometries, and improved design efficiency of structural components [6,7]. However, its application in structural load-bearing components remains limited and is still developing [7,8]. To support the development of hybrid steel connections incorporating additively manufactured components, the aim is to investigate the structural integrity of hybrid double-lap shear bolted connections incorporating AM 316L stainless steel inner plates produced via wire arc additive manufacturing (WAAM) and selective laser melting (SLM). Although SLM is currently less suitable than WAAM for large-scale structural applications because of its limited build volume and lower productivity, it remains relevant for smaller and geometrically complex structural components. Its high geometric precision and distinct powder-bed manufacturing process also provide a useful basis for examining how different AM methods influence connection behaviour. Thus, this study was conducted through experimental characterisation of the mechanical behaviour of the hybrid connections and the application of distinct prediction methods to assess their static failure. The objectives are as follows:

a) Experimentally characterise the material properties of the parent material, and failure modes and crack behaviour of double-lap shear bolted connections using conventional (CON), WAAM, and SLM 316L stainless steel inner plates, including different configurations, geometric design variables, print or extraction direction, and surface conditions.
b) Analyse the load-displacement response of the connections and evaluate the codified design resistance estimations and literature-based equations against the experimental results,

quantifying accuracy and conservatism for the studied configurations and manufacturing methods.

c) Apply the Theory of Critical Distances (TCD) to linear elastic finite element (FE) models to assess static failure in CON inner plates using local stress fields and evaluate transferability across manufacturing methods.
d) Explore the potential of machine learning models to predict static failure loads and failure modes using the experimental and literature-based dataset.

1.2 Thesis structure and contributions

This thesis is presented as a thesis by publication and is organised into three parts. It consists of four published journal articles. Part I provides the thesis overview and research context. In Part I, Chapter 1 introduces the research scope, aim, objectives, and the overall thesis structure. Chapter 2 presents the background and broad literature review. It covers additive manufacturing and structural engineering, WAAM and SLM manufacturing methods, additively manufactured bolted connections, an overview of codified and literature-based strength estimations, and the alternative prediction methods adopted in this study, namely TCD and machine learning. Part II contains the four journal articles that form the main body of the thesis. Chapter 3 investigates the failure behaviour of hybrid double-lap shear bolted connections with conventional and additively manufactured 316L stainless steel inner plates. Chapter 4 evaluates their static response and the codified and literature-based resistance estimations. Chapter 5 examines the applicability of TCD for static failure prediction and assesses its transferability from conventional to additively manufactured inner plates. Chapter 6 presents the potential of machine learning models for predicting static failure loads and failure modes of double-lap shear bolted connections. Part III summarises the overall conclusions of the thesis, where Chapter 7 presents the main conclusions drawn from the combined findings of the journal articles and outlines recommendations for future work. Supplementary appendices are provided to present additional design plots, experimental data, further TCD analysis plots, and machine learning datasets and scripts.

The journal articles presented in Part II are co-authored publications. Hasan Almuhanna was the lead author of all four articles and was responsible for the primary investigation, analysis, and original drafting of the manuscripts. Professor Luca Susmel contributed across the articles through supervision, conceptualisation, methodology, and critical review and editing. Dr Giacomo Torelli contributed through supervision, technical support, and manuscript review and editing. Dr Renan Kindermann also contributed to the review and editing of the failure investigation article. Full authorship contribution details are provided in the forward commentary of each chapter.

Chapter 2. Background and Literature Review

This chapter provides a broad overview of additive manufacturing in structural engineering. It explores sources of uncertainty and undesired conditions associated with wire arc additive manufacturing and selective laser melting, followed by a review of materials investigated in the literature. The discussion focuses on additively manufactured bolted joints, which form the core of this study, and outlines relevant design resistance estimations and alternative prediction methods. On this basis, the main research gaps addressed in this thesis are identified. As this is a thesis by publication, each journal article included in Part II contains its own detailed literature review relevant to its specific scope, together with the procedures, equations, and theoretical formulations.

2.1 Additive manufacturing in structural engineering

As generally known in structural engineering, structural metal components are typically produced using conventional processes such as rolling and casting. Nevertheless, additive manufacturing (AM), as an emerging technology, is being considered as an alternative manufacturing method for structural applications [9]. Wu et al. [10] noted that the AM process starts from a 3D digital model, then the model is sliced into layers and sent to the printing machine for layer-by-layer fabrication. Lange et al. [11] discussed additive manufacturing in steel construction and highlighted the potential of wire arc additive manufacturing (WAAM), as one of the metal additive manufacturing methods for producing connection and other structural components. Furthermore, Lange et al. [11] showed that WAAM can support topology optimised steel details, enabling more efficient geometries with reduced material use in connection applications. However, AM includes several process categories and sub-methods, and the discussion of its integration into structural engineering should not be limited to WAAM alone. Therefore, this study conducted tests on two distinct AM methods including WAAM and selective laser melting (SLM). To understand the AM terminologies used in this thesis and to position WAAM and SLM within the wider process categories, the standard classification of additive manufacturing methods based on BS EN ISO/ASTM 52900 [12] is given in Table 2.1. Based on this classification, WAAM belongs to the directed energy deposition (DED) category, whereas SLM belongs to the powder bed fusion (PBF) category.

Table 2.1: AM process categories and their descriptions according to BS EN ISO/ASTM 52900 [12]

process category	Abbreviation	Brief description	Relevance to this thesis
Binder jetting	BJT	Powder bed bonding through selective liquid binder deposition	metal capable but not considered in this study
Directed energy deposition	DED	Deposition of feedstock material with localised melting using a heat source	WAAM is classified under this category and is one of the two AM methods studied in this thesis
Material extrusion	MEX	Material dispensed through a nozzle following a controlled deposition path	metal capable but not considered in this study
Material jetting	MJT	Jetting material droplets in a controlled pattern	Predominately polymer based and not relevant to this study
Powder bed fusion	PBF	Selective fusing of powder bed regions using localised heat input	SLM is treated as a PBF process using laser melting of metal powder.
Sheet lamination	SHL	Bonding sheets of a material through heat or pressure	metal capable but not considered in this study
Vat photopolymerization	VPP	Selectively hardening a liquid photopolymer with light	Predominately polymer based and not relevant to this study

2.2 Sources of uncertainty and undesirable conditions in WAAM

It is important to address uncertainties and undesirable features when assessing the feasibility of utilising WAAM for hybrid connections involving steel and other metals. Kyvelou et al. [13] investigated the mechanical behaviour of WAAM stainless steel coupons by examining the degree of anisotropy and the influence of the as-built geometry. Their results showed that material anisotropy significantly affected the stress-strain response and strength, with the mechanical properties varying according to the specimen extraction orientation of 0°, 45°, and 90°. In addition, comparison between as-built and machined specimens showed that the surface undulations inherent to the as-built condition were detrimental, leading to lower Young's modulus and strength. Kühne et al. [14] also highlighted important process related challenges in WAAM, showing that distortion, shape deviations, and residual stresses must be considered even under identical WAAM process parameters. Zhang et al. [15] reported that heat input and interpass temperature control influence the macro morphology and surface quality of WAAM deposited material, with higher heat input leading to poorer surface finish and a greater tendency for heat accumulation related defects. Tankova et al. [16] likewise reported rough surface finish, local bulging, and thickness variation along the height of a WAAM wall and showed that machined specimens exhibited higher strength and ductility than their as-built counterparts.

2.3 Sources of uncertainty and undesirable conditions in SLM

According to Sing et al. [17], one of the major drawbacks of using SLM is the undesirable formation of pores within the material. The authors noted that this issue can be reduced through careful selection of process parameters such as laser power, scan speed, and hatch spacing. Ahmed et al. [18] further showed that residual stress induced distortion is more severe in thin SLM fabricated specimens, which are more prone to shrinkage, bending, and geometric distortion. Their results also demonstrated that distortion decreased markedly with increasing specimen thickness, with the thinnest specimens exhibiting the greatest distortion.

2.4 WAAM materials reported in the literature

Recent studies have investigated a range of WAAM steels and alloys. Huang et al. [19] compiled an extensive database of WAAM carbon steel studies and noted that ER70S-6, classified according to AWS A5.18/A5.18M [20], is the most widely used feedstock wire for normal-strength steels, whereas ER110S, classified according to AWS A5.28/A5.28M [21], is commonly used for high-strength steels. In a separate experimental study, Huang et al. [22] examined the mechanical and microstructural behaviour of WAAM normal-strength and high-strength steels using as-built and machined coupons extracted from plates of different thicknesses and orientations. Their results showed that WAAM normal-strength steels generally exhibit a well-defined yield region and strain hardening, similar to hot-rolled steels, whereas WAAM high-strength steels display a more rounded stress-strain response without a distinct yield point. The authors also reported weak crystallographic texture and generally consistent, almost isotropic mechanical behaviour for the WAAM carbon steels.

For WAAM stainless steels, Kyvelou et al. [13] tested coupons produced from Grade 308LSi austenitic stainless steel wire and reported pronounced anisotropy, with the mechanical response strongly affected by the extraction direction relative to the print orientation and by the as-built surface condition. The 45° coupons exhibited the highest Young's modulus and strength, while the 90° coupons showed the lowest values. Similar findings were reported by Laghi et al. [8] for WAAM ER308LSi stainless steel, where diagonal specimens exhibited the highest elastic and plastic properties, confirming the anisotropic nature of the printed material.

WAAM has also been explored for aluminium alloys. Gu et al. [23] investigated a customised Al-Cu4.3-Mg1.5 alloy and compared the behaviour of as-deposited and heat-treated WAAM material. The results showed that heat treatment significantly improved the mechanical properties, while anisotropic tensile behaviour was also observed, with superior properties reported in the horizontal direction.

2.5 SLM materials reported in the literature

Taha et al. [24] investigated the effect of scan speed and post heat treatment on ultra-high carbon steel produced by SLM. Their results showed that increasing scan speed led to higher porosity and crack content, lower relative density, and a marked reduction in hardness. Sanjari et al. [25] studied the influence of build orientation on the microstructure and tensile behaviour of SLM fabricated CX maraging stainless steel. The results showed that changing the build orientation significantly affected the mechanical response, with the horizontally printed specimens exhibiting a better combination of strength and ductility than the vertically printed ones. Bartolomeu et al. [26] compared SLM, hot pressing, and conventional casting for 316L stainless steel and reported that the SLM specimens achieved the highest mechanical performance. The authors attributed this improvement mainly to the finer microstructure produced by the SLM process.

2.6 AM bolted connections

Previous studies on AM bolted connections have focused mainly on WAAM carbon steel connections, with fewer studies on WAAM stainless steel and on SLM stainless steel connections under fire exposure [27–34]. The main studies relevant to the present work are summarised in Table 2.2. The earliest AM bolted connections study was reported by Guo et al. [27], who examined WAAM carbon steel single-lap shear connections in single-bolt configuration and showed that, although the extraction direction had only a limited effect on ultimate resistance in most cases, it influenced the observed failure mode. The same study also reported failure modes not accounted for in current design provisions, such as end-splitting, curl-bearing and localised tearing. This was then extended to WAAM carbon steel double-lap shear connections, as Guo et al. [28] investigated a single-bolt configuration over a range of geometries and also reported that the extraction direction had a relatively small influence on load capacity, although the governing failure mode remained sensitive to both plate configuration and extraction direction, with end-splitting also reported among the observed failure modes. Liu et al. [29] studied WAAM steel double-lap shear bolted connections in a single-bolt configuration and found a clearer influence of extraction direction at the material level, with the 0° direction showing better tensile properties than the 90° direction, while the connection tests again showed that direction could alter the governing failure mode even when its effect on resistance was less pronounced. Similar to Guo et al. [27] and Guo et al. [28], Liu et al. [29] also reported end-splitting failure mode. Liu et al. [30] further extended this work to thick WAAM steel plates in a single-bolt double-lap shear configuration and found that thicker plates exhibited more stable structural behaviour and better agreement with existing design provisions than thin WAAM plates.

In addition to carbon steel WAAM joints, more recent work has started to consider stainless steel additively manufactured bolted connections. Zuo et al. [31] investigated WAAM 316L austenitic stainless steel single-lap shear bolted connections in a single-bolt configuration, providing one of the first direct structural studies on WAAM stainless steel bolted joints. The aforementioned study showed that extraction orientation and surface condition had little effect on connection resistance, but could influence the failure pattern of the connections, while the existing design methods generally provided conservative resistance predictions. Zuo et al. [32] later examined WAAM 316L austenitic stainless steel double-lap shear bolted connections in a single-bolt configuration, again considering different surface conditions and test orientations. Zuo et al. [32] reported that the connection behaviour and governing failure mode were influenced primarily by the bolt hole position, whereas the effect of extraction orientation was less pronounced. The study also showed that, for the specimens considered, literature-based equations provided more accurate resistance predictions than the design provisions. Zuo et al. [33] also studied WAAM duplex stainless steel single-lap shear bolted connections in a single-bolt configuration under different extraction orientations and surface conditions. Their results likewise showed that the connection behaviour was governed mainly by the bolt hole position, while extraction orientation and surface condition had a smaller influence. They also found that the literature-based equations generally provided the most accurate resistance predictions. While some WAAM stainless steel studies reported non-standard failure patterns, including localised tearing, curl-bearing, and end-curling related behaviour [31,33], Zuo et al. [32] mainly observed conventional bolted connection failure modes in double-lap shear specimens, possibly owing to differences in both the test arrangement and the material behaviour.

More recently, Kong et al. [34] examined the post-fire shear behaviour of SLM 316L stainless steel bolted connections in both single-bolt and double-bolt configurations. Their results showed that the post-fire ultimate strength of the AM stainless steel plates initially increased with increasing exposure temperature before decreasing at higher temperatures, while exposure to high temperatures also appeared to enhance ductility.

Collectively, these studies show that the structural response of AM bolted connections is influenced by the manufacturing method, material properties, extraction or print direction, and surface condition, even though the effect of these parameters on ultimate resistance is not always pronounced [27–34]. They further indicate that current design rules do not always capture the governing failure mechanism reliably. However, although recent studies have expanded the evidence base for stainless steel AM bolted connections, comparatively less evidence is available on 316L stainless steel hybrid double-lap shear connections, particularly where WAAM and SLM inner plates are assessed alongside conventional counterparts under comparable geometrical conditions and different bolt configurations.

Table 2.2: Summary of previous studies on additively manufactured bolted connections

AM method	Feedstock wire/powder	Test arrangement	Connection configuration	Tested plates surface finish	Extraction/printing orientation	Reference study
WAAM	ER70S-6 carbon steel	single-lap shear	single-bolted	as-built	0° and 90°	[27]
WAAM	ER70S-6 carbon steel	double-lap shear	single-bolted	as-built	0° and 90°	[28]
WAAM	ER50-6 carbon steel	double-lap shear	single-bolted	as-built	0° and 90°	[29]
WAAM	ER50-6 carbon steel	double-lap shear	single-bolted	as-built	0° and 90°	[30]
WAAM	ER316L austenitic stainless steel	single-lap shear	single-bolted	as-built and machined	0°, 30°, 45°, 60° and 90°	[31]
WAAM	ER316L austenitic stainless steel	double-lap shear	single-bolted	as-built and machined	0°, 30°, 45°, 60° and 90°	[32]
WAAM	ER2209 duplex stainless steel	single-lap shear	single-bolted	as-built and machined	0°, 30°, 45°, 60° and 90°	[33]
SLM	316L stainless steel powder	single-lap shear	single-bolted and double-bolted	as-built	not specified	[34]

2.7 Design code and literature-based analytical strength estimations

The static design resistance of structural steel parts including bolted connections is typically estimated using design rules that check a number of possible failure modes and adopt the lowest calculated resistance as the governing resistance. In steel and stainless steel structures, this approach is reflected in the widely used design provisions, including BS EN 1993-1-8 [1], BS EN 1993-1-4 [2], ANSI/AISC 360 [3], and ANSI/AISC 370 [4], which provide equations for the principal failure modes of bolted connections as functions of joint geometry, bolt configuration, and material strength properties. These methods are widely used because they are simple, practical, and suitable for routine design checks.

Despite their practical use, the design equations provided by the provisions mentioned above are based on simplified idealisations of bolted connection behaviour. Their use becomes more uncertain when the response of the connection plate is affected by features that are not represented directly in the codified equations, such as directional material behaviour and surface irregularities. This issue is particularly relevant for AM bolted plates, where the manufacturing method and resulting material morphology may influence both the load-carrying response and the governing failure mode. As discussed in Section 2.6, previous studies on AM bolted connections have shown that these effects can lead to failure modes and resistance capacities that are not always predicted accurately by standard design equations [27–34], and that literature-based equations can provide more accurate predictions of the resistance capacity [27,29–34]. Such approaches offer a useful intermediate solution between standard codified equations and more advanced predictive methods. However, they still remain simplified strength estimation tools, since they continue to assess failure through prescribed analytical checks rather than through a direct analysis of local stress development or a broader data-driven prediction of the structural response.

2.8 Alternative prediction methods

Since conventional analytical methods rely on simplified resistance equations, other approaches have been explored to provide more advanced predictions of bolted connection failure. In the present study, these prediction methods are grouped into two distinct approaches. The first consists of a stress-based method, in which failure is interpreted through the local stress state near a stress raiser. The second consists of data-driven methods, in which the relationship between connection parameters and structural response is inferred from available datasets. These two approaches are represented by the Theory of Critical Distances and machine learning, respectively.

2.8.1 Application of the Theory of Critical Distances

The Theory of Critical Distances is a local method formalised to assess failure in components containing notches, cracks, and other geometric features that act as stress raisers [35]. Its fundamental principle is that failure is governed not simply by the peak stress at the stress raiser, but rather by the effective stress determined over a material characteristic distance

[35,36]. One of the main advantages of this method is that the stress field required for static strength assessment of structural components can be obtained from a linear elastic finite element (FE) analysis, making it considerably simpler than full non-linear modelling [37]. This concept is potentially relevant to bolted connections since the bolt hole acts as a pronounced stress raiser within the plate. It is therefore attractive in the present study, where conventional analytical solutions or non-linear FE analysis may be inadequate for AM components or computationally inefficient.

2.8.2 Machine learning

Interest in applying machine learning to structural engineering problems, including bolted connections, has increased in recent years, with published studies exploring a range of algorithms [38–40]. Among these, one study [38] focused only on double shear bolted connections in structural steel, while two studies [39] and [40] considered high-strength steel and stainless steel bolted connections, respectively, with different arrangements and several bolt configurations. These studies have shown that machine learning can provide strong predictive capability for failure loads [38–40] and, in one study, failure modes [39]. At the same time, the reported best performing algorithm has not been consistent across studies, suggesting that predictive performance depends on the characteristics of the collected dataset [38–40]. Machine learning can therefore be viewed as a potential alternative to codified estimation when dealing with the complex behaviour of bolted connections incorporating AM plates.

2.9 Summary of research gaps and thesis novelty

Overall, it is evident from the literature reviewed in this chapter that research on AM bolted connections in structural applications remains limited, particularly for 316L stainless steel hybrid double-lap shear connections assessed under comparable geometrical conditions using CON, WAAM, and SLM inner plates. The following research gaps are therefore identified:

a) The manufacturing method, extraction or print direction, surface condition, and bolt configuration may all play a role in connection behaviour and observed failure patterns.
b) Existing codified design estimations and literature-based predictions still require further investigation.
c) Although TCD is widely used for notched components and other stress raisers, its application to bolted joints has not been established.
d) Although machine learning has shown promise for bolted connection prediction, its application to AM hybrid bolted connections remains worth exploring.

Accordingly, the novelty of this thesis lies in using a controlled hybrid double-lap shear bolted-joint in which the CON outer plates confine the critical deformation and failure to the 316L inner plates produced by CON, WAAM and SLM methods. In practice, hybrid connections allow AM components to be used only where needed within otherwise conventionally fabricated structures, rather than requiring the entire connection or structural system to be additively manufactured. The novelty does not arise solely from the use of a hybrid double-lap arrangement, since similar test arrangements have been adopted in earlier WAAM studies [29,32]. Rather, it lies in using this arrangement as a controlled comparative test setup to isolate and directly compare the influence of CON, WAAM and SLM manufacturing methods on the behaviour of 316L inner plates under comparable joint conditions. The thesis combines experimental investigation with distinct predictive approaches, including codified and literature-based analytical estimations, stress-based local analysis, and data-driven machine learning methods, to assess the static failure behaviour of hybrid double-lap shear bolted connections with 316L stainless-steel inner plates produced by CON, WAAM and SLM routes. Gap (a) is addressed in Chapter 3, gap (b) in Chapter 4, gap (c) in Chapter 5, and gap (d) in Chapter 6.

Part II. Journal Articles

Chapter 3. Failure Investigation of Hybrid Double-Lap Shear Bolted Connections with Additively Manufactured 316L Stainless Steel Inner Plates

Forward Commentary

This article, titled "Failure investigation of hybrid double-lap shear bolted connections with additively manufactured 316L stainless steel inner plates", was published in *Engineering Failure Analysis* on 25 May 2025 [41]. The article presents the design and experimental procedure adopted in the study and reports the parent material properties, failure modes, and cracking behaviour of the inner plates of double-lap shear bolted connections made from conventional and additively manufactured 316L stainless steel. The initial concept for the experimental work was developed jointly by Hasan Almuhanna and Professor Luca Susmel to understand the behaviour of additively manufactured components integrated into structural parts. Hasan Almuhanna carried out the overall work, including designing the experimental programme, conducting the tests, and writing the manuscript. Professor Luca Susmel, Dr Giacomo Torelli, and Dr Renan Kindermann contributed through critical review, editing, and technical suggestions throughout the drafting process.

Abstract

The growing body of research on additive-manufactured components in structural engineering highlights the importance of assessing their potential, particularly in understanding how key manufacturing and design parameters influence performance. In this context, alongside conventional inner plates, this study investigates the failure behaviour of additive-manufactured inner plates of 316L stainless steel as a hybrid component in double-lap shear bolted configurations. Two distinct printing methods were considered: wire arc additive manufacturing and selective laser melting. The study considered different surface conditions (as-built and machined) and extraction/print direction (θ = 0° ,45° ,60° and 90°). By evaluating the actual failure mode and cracking behaviour, this study explores the influence of the manufacturing process and variations in geometrical design parameters, treated as key

variables affecting the failure mechanism of the inner plates. The findings indicate that while the test coupons exhibited significant variations in stiffness and ductility, the failure behaviour of conventional and additively manufactured inner plates remained largely similar when accounting for surface condition and printing direction. Differences in load capacity across manufacturing methods were found to be limited when thickness was controlled. However, distinctly different crack propagation paths were observed in as-built wire arc additive-manufactured inner plates extracted at θ = 45° and 60°, attributed to the effect of diagonal printing layers. These insights contribute to understanding overall connection integrity and highlight both the challenges and opportunities of integrating additive manufacturing into bolted connections.

3.1 Introduction

Additive manufacturing (AM) is increasingly being adopted in the construction industry as an alternative to traditionally produced materials, offering advantages in design optimisation and performance [42,43]. The integration of AM into construction practices aligns with advancements in industries such as aerospace and automotive manufacturing, ensuring that construction does not lag in innovation and productivity. AM offers several key potential benefits to the construction industry, including enhanced production efficiency, reduced material waste, improved precision in both off-site and on-site fabrication, and its utilisation as a solution for repairing structural defects [44]. Furthermore, AM materials have the potential to expand design possibilities for hybrid applications and various structural configurations. However, challenges remain in the adoption of AM components, including the limited availability of standards and guidelines to guide engineering design.

In response to increasing demand, the BS EN ISO/ASTM 52900 standard was published to define general terms, seven processing categories, and processing data relevant to additive manufacturing [12]. The standard classifies wire arc additive manufacturing (WAAM) under the direct energy deposition (DED) category, which involves material fusion through melting during deposition. A limitation of this standard is that it does not specifically address selective laser melting (SLM) but instead covers the broader powder bed fusion (PBF) category, under which SLM is classified as a sub-method. Additionally, ASTM F3187-16, last updated in February 2024, serves as a guideline for DED sub-methods [45]. It defines deposition methods for DED sub-methods, which utilise either Metal Inert Gas (MIG) welding or an electron beam. In the case of WAAM, deposition is typically carried out using an inert gas arc system.

Recent studies [19,46–53] have primarily focused on the two prominent AM approaches: WAAM and SLM. Metals produced using these techniques have been extensively tested and evaluated for use in structural buildings and other applications. These studies have examined print parameters, mechanical behaviour, and microstructural characteristics.

In terms of printing capabilities, WAAM is the most suitable AM technique for producing structural components, as it enables the fabrication of large-scale structural elements and allows for the production of standard steel structural geometries [7]. Additionally, unlike PBF sub-methods such as electron-beam melting (EBM) and selective laser melting (SLM), WAAM does not require a vacuum or an inert gas atmosphere. A study conducted by Ron et al. [54], highlighted notable disadvantages of using EBM and SLM, including the high cost of raw powder materials and significant energy consumption compared to WAAM. Moreover, WAAM provides substantially higher deposition rate, ranging from 4-9 kg/h, whereas PBF methods typically achieve only 50 g/h [44]. Nevertheless, PBF sub-methods like SLM offer superior dimensional accuracy and improved surface finish compared to other AM methods including WAAM making SLM more suitable for complex geometries requiring precise fabrication [55]. However, the performance of SLM-produced metals in structural components such as bolted connections remains largely unexplored. Therefore, examining their performance in hybrid joints and comparing their mechanical behaviour with conventional (CON) and WAAM counterparts is necessary for a comprehensive assessment of their potential.

Despite the growing body of research on WAAM components, studies on their integration with bolted connections remain limited. To date, as far as the authors are aware, four systematic investigations have examined double-lap configurations [28–30,32], while three studies have investigated single-lap configurations [27,31,33]. Notably, only one study has specifically investigated the inner plates of 316L stainless steel double-lap configurations, and it was limited to single-bolt plates [32]. This highlights the need for further research into the structural integrity and anisotropic nature of such plates.

The aforementioned studies have examined various bolt configurations, as-built and machined surfaces, interchangeable geometrical variables, and different extraction angles relative to the printing direction, θ, ranging from 0°, 30°, 45° ,60° and 90°. These studies have thoroughly demonstrated failure mechanisms in WAAM bolted connections. For instance, it was observed in [32] that the inner plates of 316L double-lap shear bolted connections with single-bolt configuration exhibited failure modes such as bolt shear (BS) edge bearing (EB), net-section tensions (NST), Shear-out (SO), or a combination of two failure modes. Furthermore, the study revealed that print direction, θ had a minor influence, as machined and as-built plates exhibited the same failure modes despite a 10% reduction in load-carrying capacity for the as-built plates. For clarity, Figure 3.1 illustrates all possible failure modes for such connections, as defined by BS EN 1993-1-8 [1] and ANSI/AISC 370 [4] standards including bolt shear failure (BS) and block tearing (BT).

Building on the existing literature, this study aims to enhance the understanding of WAAM and SLM 316L stainless steel bolted connections by examining the failure and cracking behaviour of the inner plates in double-lap shear connections. It considers the effects of different surface conditions, print orientations, and both single- and double-bolt configurations. Additionally, the study investigates the influence of key geometrical parameters on failure mechanisms.

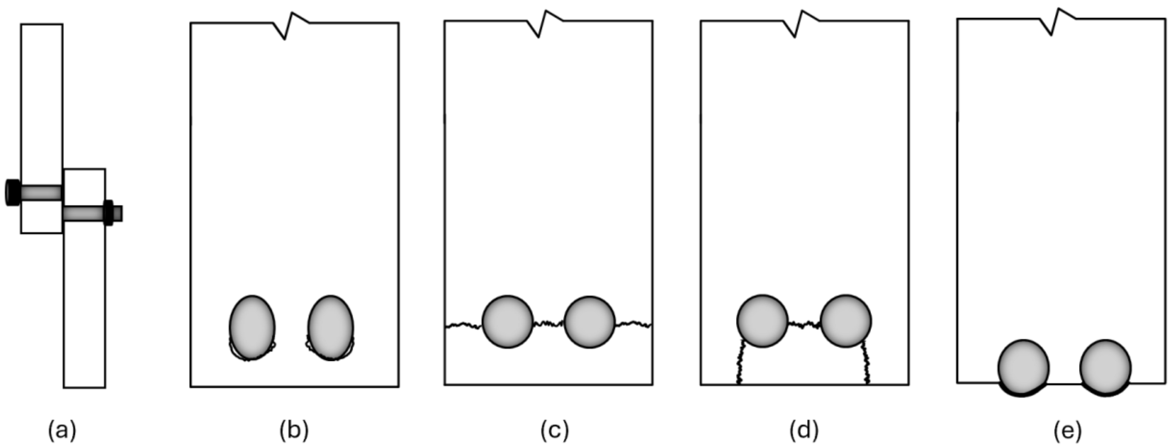

Figure 3.1: Failure modes in bolted connections: (a) BS, (b) EB, (c) NST, (d) BT, and (e) SO.

3.2 Experimental work

3.2.1 Materials

The tested 316L stainless steel inner plates for the double-lap shear bolted connections were fabricated using three distinct methods: CON, WAAM, and SLM, while the outer, thicker plates were conventionally manufactured for all tests. Both the inner and outer CON plates were sourced from cold-rolled 316L stainless steel wrought sheets to ensure a smooth surface finish and serve as a reference.

For the WAAM process, the materials used consisted of a 1.2 mm diameter 3Dprint AM 316L wire from Voestalpine Boehler [56] and a carbon steel substrate plate measuring 295×295×29 mm. For the SLM process, the 316L powder was supplied by Nikon SLM Solutions [57] and had a particle size of 10-45 μm, with a typical apparent density of 4.5 g/cm^3. It was produced via gas atomisation with nitrogen. The 316L stainless steel substrate plate measured 278×278×25 mm. Table 3.1 and Table 3.2 summarise the chemical composition and mechanical properties of the raw materials employed in the CON, SLM, and WAAM processes.

Table 3.1: Typical chemical composition of 316L stainless steel raw material obtained from different production methods [56–58].

Material condition	Chemical composition, (wt%)						
	C	Si	Mn	Cr	Ni	Mo	N
Wrought	0.02	0.45	0.91	17.20	10.00	2.04	0.05
Wire	0.015	0.45	1.60	18.50	12.00	2.60	0.04
Powder	0.02	0.71	0.75	17.87	12.70	2.36	0.10

Table 3.2: Mechanical properties of 316L stainless steel raw material obtained from different production methods according to supplier datasheets [56,58,59].

Material condition	Offset yield stress, $\sigma_{0.2}$ (MPa)	Ultimate stress, σ_u (MPa)	Elongation (%)
Wrought	340	656	53
Wire	430	580	38
Powder	540	615	39

3.2.2 Manufacturing procedure

The fabrication of WAAM specimens involved four steps (see Figure 3.2): first, designing a parent tubular section; second, planning the extraction based on the number of coupons and plates required; third, producing the tubular sections using a robotic welding cell; and finally, extracting the coupons and plates from the tubes from different directions, θ relative to the deposition direction, including 0° ,45° ,60° and 90°. A tubular parent specimen was selected because preliminary trials indicated that this type of build approach ensures more uniform cooling, thereby reducing residual stresses and distortions compared to the more commonly used single-bead linear walls. Two 250×250 mm tubular parent specimens were found adequate for extracting the desired number of inner plates.

The deposition of the samples was carried out by a KUKA KR 70 industrial robot arm equipped with a Fronius TransPuls Synergic 4000 CMT Power Source and a Robacta push-pull welding torch. The welding torch was oriented orthogonally to the travel direction, with a layer height set to 2 mm. The wire was deposited using a local argon shielding gas with a gas flow rate of 15 L/min, following specific printing parameters from Table 3.3. Initially, in the first two layers, due to the direct contact with the substrate plate, it was necessary to reduce the travel speed and increase the wire feed speed to increase the bead width and to ensure a consistent layer width throughout the sample. Furthermore, to allow the heat from the tube to dissipate, the deposition process was stopped every 25-50 layers to allow cleaning and cool-down of the welding torch, during which the tube was also allowed to cool down to room temperature naturally.

After production, the as-built plates were extracted using wire electrical discharge machining from the tubes with a final thickness, t varying around the nominal target of 5 mm (see Figure 3.3 for plate length, l and breadth, b views), while the machined plates were milled down to 2 mm. This integrated approach to printing and extraction allowed us to minimise material waste.

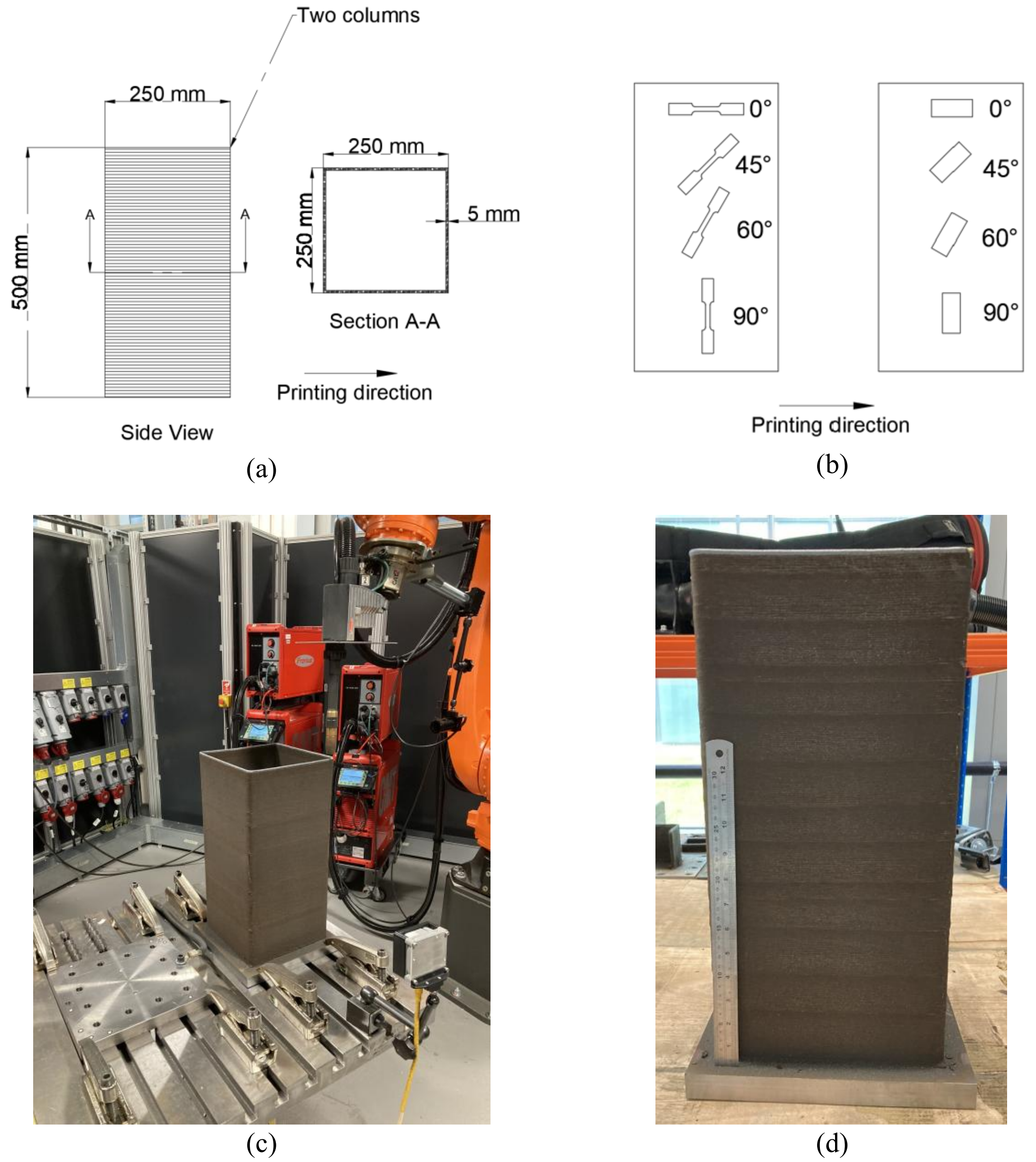

Figure 3.2: The process of producing WAAM specimens: (a) parent material design, (b) extraction plan, (c) additive manufacturing via robotic cell, and (d) final parent material product.

Table 3.3: Printing parameters used during fabrication of tubular section specimens with WAAM.

Layers	Travel speed, (m/min)	Wire feed speed, (m/min)	Average Current, (A)	Average Voltage (V)
1	0.45	8	225	13.5
2	0.60	6	188	12.5
3 – 250	0.78	6	188	12.5

(a)

(b)

Figure 3.3: Thickness, t variation in WAAM plates with extraction θ = 90° due to surface undulations: (a) view perpendicular to the breadth, b, and (b) view perpendicular to the length, l.

The SLM specimens were produced using an SLM 280 2.0® system (Figure 3.4a), which has a build volume of 280×280×365 mm. The material was deposited under a controlled atmosphere of Argon with a gas flow speed of 24 m/s, with a maximum oxygen level of 500 ppm and process pressure of 12 mbar. The build plate was kept at 100 ℃ during printing. The printing parameters used (Table 3.4) were those recommended by the original equipment manufacturer for a layer height of 50 µm. Additionally, the printing (scanning) direction after every layer was kept the same during the printing to understand the impact of the printing direction on sample orientation and the resulting effect on the mechanical anisotropy.

The SLM system offers a distinct advantage over WAAM because it fabricates specimens directly from CAD files with final dimensions similar to the original design file, including the desired printing direction, θ, requiring only extraction from the base plate and supports (Figure 3.4b) depending on the application. To minimise edge distortions, solid supports were used to allow the sample to be printed on the desired printing orientations relative to the build plate. Solid supports proved more effective than meshed ones during trials to prevent part distortion and consequent damage between the interface of the support with the actual samples. The build preparation software Netfabb from Autodesk [60] was used for orienting and positioning the samples and assigning the required printing parameters and supports.

After manufacturing, it was observed that the as-built SLM specimens exhibited a uniform noticeable surface roughness, R_a with an average value of 8 μm according to the equipment specifications. Therefore, some plates were machined to remove the roughness and observe any possible variation of failure mechanism. Unlike the samples produced by WAAM, both the as-built and machined SLM plates were designed to maintain a consistent thickness, t of 2 mm.

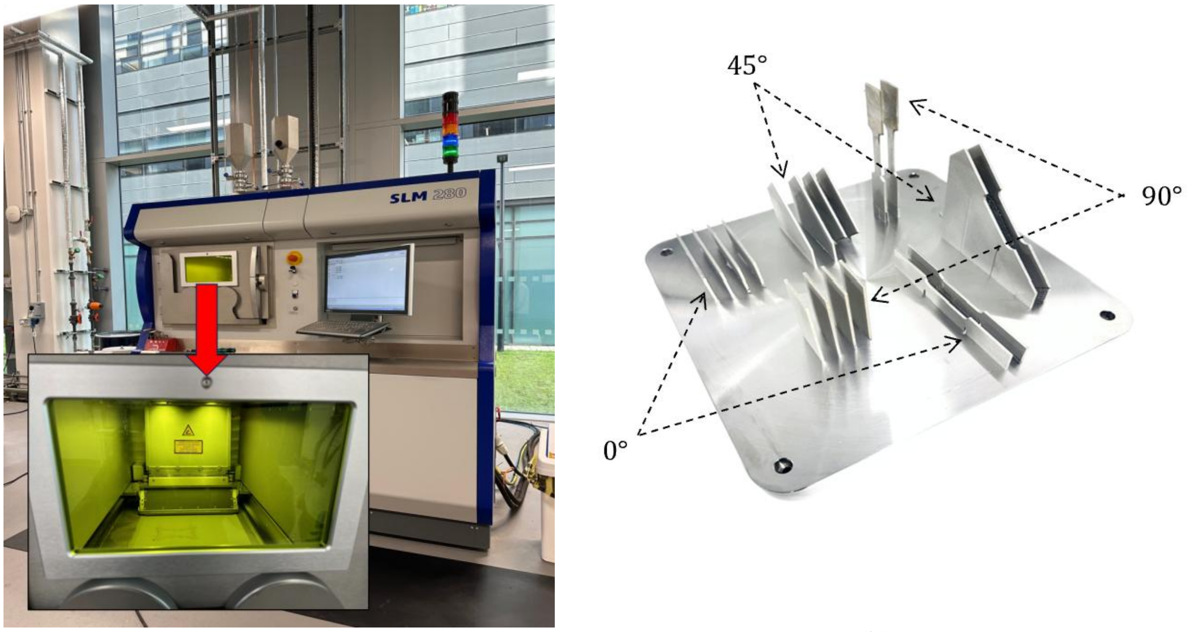

(a) (b)

Figure 3.4: SLM production process: (a) SLM 280 2.0® system with an arrow showing a zoom in to the powder bed, and (b) the final product, indicating the printing direction, θ, before extraction.

Table 3.4: Printing parameters of SLM specimens.

Scanning region	Scanning strategy	Laser Power (W)	Scanning Speed (mm/s)	Stripe size (mm)	Hatch distance (mm)	Scan Rotation (°)
Volume (Hatching)	Stripe	250	950	7	0.1	0
Border	Single lines	150	450	-	-	-

3.2.3 Mechanical properties in standard test conditions

Prior to the bolted connections investigation, coupon uniaxial tensile tests were conducted on CON and AM metals at a displacement rate of 1 mm/min. The coupon design followed ASTM E8/E8M [61], adhering to the acceptable design thresholds for sub-size coupons. This allowed for the evaluation of the mechanical properties of AM metals in different extraction directions against the printing direction, θ, under plain conditions. WAAM coupons were tested in four different extraction directions (θ = 0° ,45° ,60° and 90°) under both machined (WAAM-M) and as-built (WAAM-AB) conditions. As-built SLM coupons were tested in various orientations (θ = 0° ,45° and 90°); the θ = 60° orientation was omitted due to production constraints. For SLM coupons the machined condition was excluded, as machining was shown not to impact the thickness, t of the specimen. Each coupon had a gauge breadth, b and length, l of 8 mm and 38 mm, respectively. All specimens had t = 2 mm, except for the WAAM-AB coupons, which had a mean t = 5.3 mm.

As shown in the stress-strain curves (Figure 3.5a-d) and summarised results in Table 3.5, the manufacturing process has a noticeable effect on the mechanical properties of the plain material. The CON coupons exhibited the highest ultimate tensile stress (σ_u = 667 MPa), highest fracture strain (ε_f = 0.51 mm/mm), and a relatively high strain hardening exponent (n = 0.32), indicating its superior ability to sustain plastic deformation before fracture. Among the WAAM coupons, orientation and surface condition played a critical role in mechanical response. WAAM-AB coupons exhibited lower modulus of elasticity, E values (ranging from 91 GPa to 139 GPa) compared to CON, WAAM-M, and SLM coupons. This reduction in stiffness can be attributed to possible inherited imperfections in the as-built condition, including micro voids, surface irregularities, and localised residual stresses. WAAM-M and WAAM-AB coupons extracted at θ = 45° and 60° exhibited slightly higher σ_u and ε_f, a behaviour linked to the diagonal orientation of the slip planes during uniaxial tensile testing, which hinders slip activity and results in higher tensile stress [62]. However, for the WAAM-AB coupon at θ = 60°, strain was lower due to variations in thickness, t, and uneven surface condition along the gauge area. Additionally, both WAAM-M and WAAM-AB coupons at θ = 90° exhibited a significantly lower ε_f than all other coupons. This can be attributed to the load being applied perpendicular to the interlayer boundaries, making the coupon more susceptible to early crack initiation and lower overall ductility. The SLM coupons displayed the highest offset yield strength, $\sigma_{0.2}$ among all tested materials, with SLM-AB of θ = 0° reaching 520 MPa and maintaining a high yield ratio, $\sigma_{0.2}/\sigma_u$ with a value of 0.83, reflecting strong resistance to plastic deformation. However, with the exception of WAAM-M and WAAM-AB printed at θ =90°, the ε_f values for SLM coupons are lower than CON, and WAAM coupons, suggesting lower ductility despite their high strength. Furthermore, it is evident that the print direction, θ of SLM has less impact compared to WAAM coupons. These findings illustrate the influence of manufacturing method, surface condition, and material orientation on the structural integrity and mechanical performance of AM material.

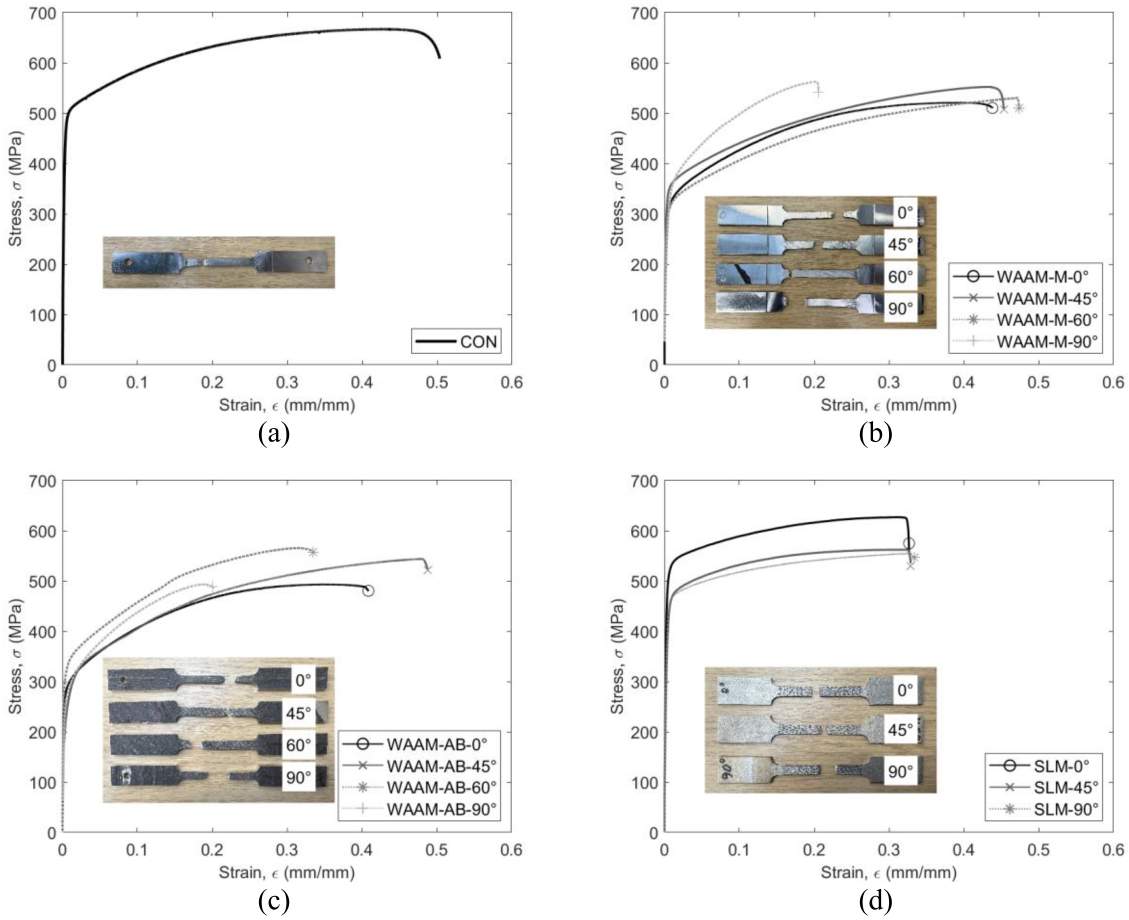

Figure 3.5: 316L stainless steel test coupons stress-strain curves: (a) conventional, (b) WAAM-M, (c) WAAM-AB, and (d) SLM.

Table 3.5: Summary of 316L stainless steel test coupons results.

Designation	Modulus of elasticity, E (GPa)	Offset yield stress, $\sigma_{0.2}$ (MPa)	Ultimate stress, σ_u (MPa)	Strain at maximum stress, ε_u (mm/mm)	Fracture strain, ε_f (mm/mm)	Strain hardening exponent, n	Strength coefficient, K (MPa)	Yield ratio, $\sigma_{0.2}/\sigma_u$
CON	184	488	667	0.46	0.51	0.32	1211	0.73
WAAM-M-0°	143	288	521	0.39	0.44	0.34	1055	0.55
WAAM-M-45°	185	324	552	0.43	0.45	0.39	1166	0.59
WAAM-M-60°	160	297	530	0.47	0.47	0.41	1135	0.56
WAAM-M-90°	103	281	562	0.20	0.21	0.27	1025	0.50
WAAM-AB-0°	124	278	493	0.35	0.40	0.35	1012	0.56
WAAM-AB-45°	119	282	544	0.48	0.48	0.42	1181	0.52
WAAM-AB-60°	139	323	566	0.32	0.34	0.37	1193	0.57
WAAM-AB-90°	91	273	493	0.19	0.20	0.31	1002	0.55
SLM-AB-0°	160	520	627	0.31	0.32	0.25	1133	0.83
SLM-AB-45°	126	422	562	0.32	0.33	0.25	1014	0.75
SLM-AB-90°	120	419	554	0.33	0.33	0.26	1006	0.76

3.2.4 Double-lap shear test design and setup

The test setup (Figure 3.6) consisted of double-lap shear connections designed to test the inner plates and minimise potential secondary bending during testing. Instead of using a typical auxiliary (spacer) plate at one end, both inner plates were directly connected to simulate a more realistic scenario. In all tests, both plates reached the ultimate load, with one plate failing completely. This behaviour was expected due to minor differences in material properties, fabrication tolerances, or bolt preload, which caused slight stress imbalances. Consequently, the failure mode presented in this study involves the complete failure of one inner plate. To ensure failure was confined to the inner plates, all outer plates were CON manufactured with increased thickness, t to provide additional stiffness and prevent unintended failures and minimise deformations. The plates were connected by high-strength 10.9, fully threaded M6 bolts to eliminate the possibility of shear failure, with a tightening torque of 10 N·m applied. For proper assembly, a medium fit 0.6 mm hole clearance was chosen based on ISO 273 [63]. The tested plates featured two main configurations: single-bolted and double-bolted. Supplementary design drawings of the tested plates are provided in Appendix A. As with the coupon design, the plates were intentionally kept relatively small to maximise the number of specimens produced while adhering to the printing limitations of WAAM and SLM. In both single- and double-bolt configurations, critical design geometrical parameters serve as the key variables affecting the plates' failure loads and modes [1]. These geometrical variables included end distance, e_1, edge distance, e_2, breadth, b, and pitch distance, p. Variations in these variables, along with changes in surface condition and print orientation, were introduced to promote the occurrence of specific failure modes, thereby enhancing our understanding of the behaviour of the AM printed plates. For the single-bolt plates, the end distance, e_1, was progressively reduced to promote increasingly pronounced EB/SO behaviour, while the reduced breadth, b, and edge distance, e_2, of the IP1-5 configuration were selected to promote NST failure. For the double-bolt plates, e1, e_2, and p were varied to investigate transitions between failure modes. The relatively small differences between some specimen configurations were intentional, as they allowed transitions between neighbouring failure modes to be examined while changing one geometrical parameter at a time and maintaining the remaining dimensions as consistently as possible. Moreover, the bolt size and the range over which the geometrical parameters could be varied were constrained by the limited dimensions of the plates. It should be noted that the inner plate thickness, t was maintained at 2 mm for CON, WAAM-M, SLM-AB, and SLM-M specimens, while it varied for WAAM-AB specimens with a mean t = 5.3 mm (similar to WAAM-AB coupons), which closely matches the nominal target of t = 5 mm (Figure 3.7). Similar to the coupon tests, the double-lap shear tests were performed at a displacement rate of 1 mm/min.

Due to the increased thickness, t of WAAM-AB plates and the corresponding enlargement of the outer plates, standard design estimations and experimental trials confirmed that the bolt specifications should be upgraded to a grade 12.9 bolt with a non-threaded M8 configuration. A close fit hole clearance of 0.4 mm was selected to account for the absence of bolt threads. This adjustment was implemented to prevent the bolt shear (BS) failure, which was observed during preliminary trials (see Figure 3.8). Although increasing the bolt size required enlarging the hole diameter, d_o, all other variables such as end distance, e_1, edge distance, e_2, and pitch distance, p were kept unchanged to assess whether the failure mode remained consistent. As a result, these variables in most WAAM-AB plates were slightly below the minimum requirements specified in BS EN 1993-1-8 [1], where $e_1, e_2 = 1.2d_o$ and p = $2.4d_o$. However, they remained within 20% of these recommended values, except one specimen where it reached 30%. For instance, with a hole diameter of 8.4 mm, a minimum end distance, e_1 would be approximately 10 mm, whereas the actual distance used was 8 mm, representing a small deviation from the standards. Experimental tests confirmed that these minor deviations had a negligible impact on the failure mode of the inner plates.

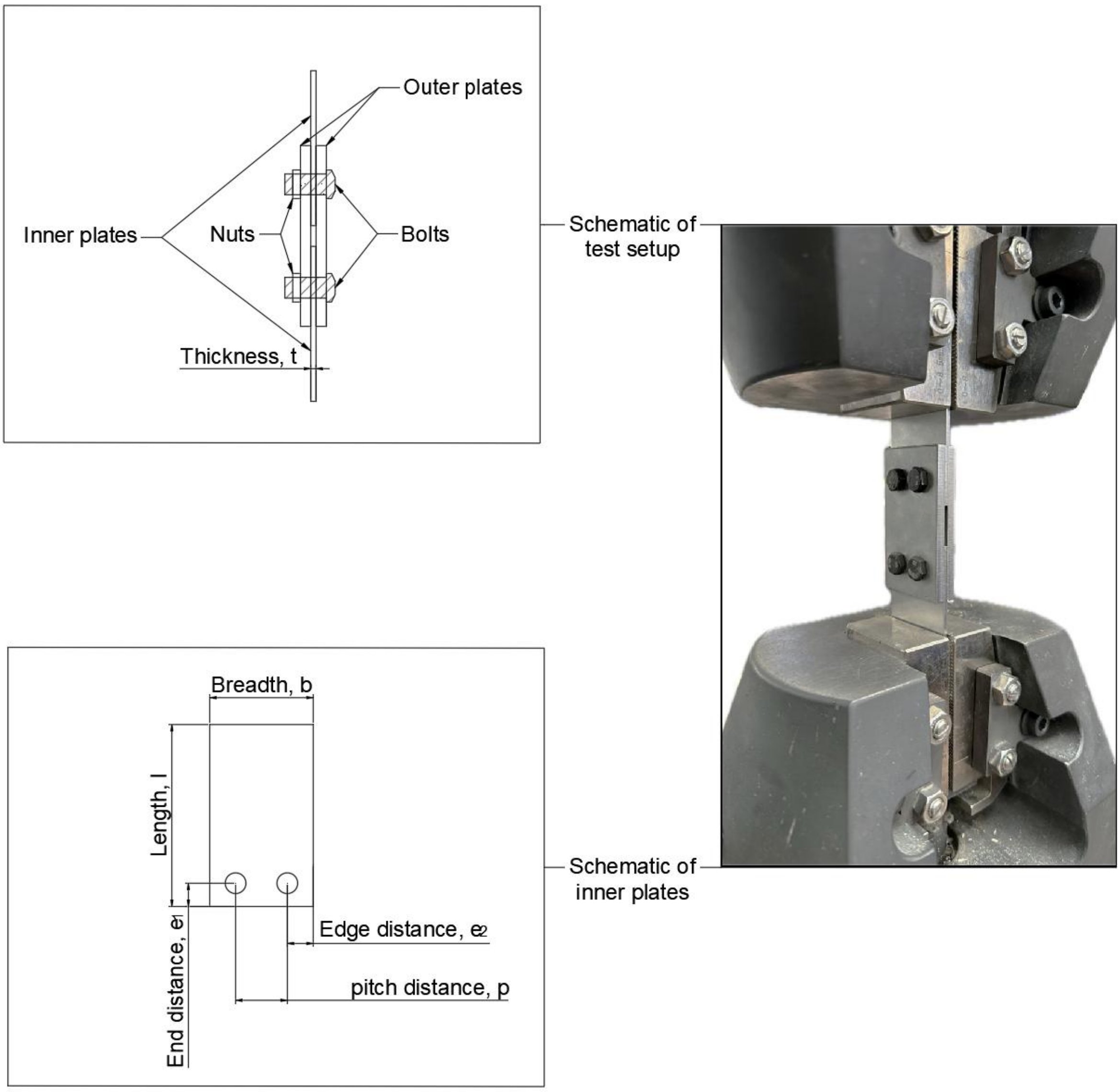

Figure 3.6: Test setup for double-lap shear bolted connections, including schematics illustrating the test components and geometrical design variables of the inner plate, specifically for the double-bolted configuration.

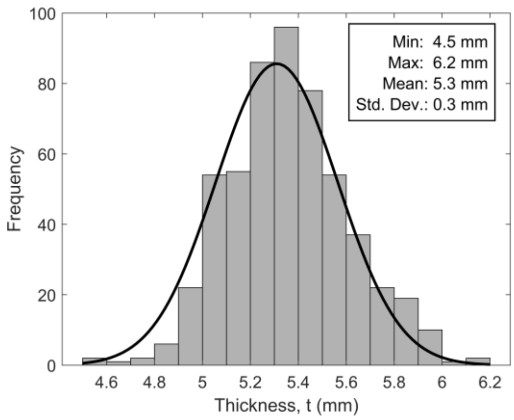

Figure 3.7: Histogram of the measured thicknesses, *t* of all WAAM-AB inner plates along their breadth, *b* and length, *l*.

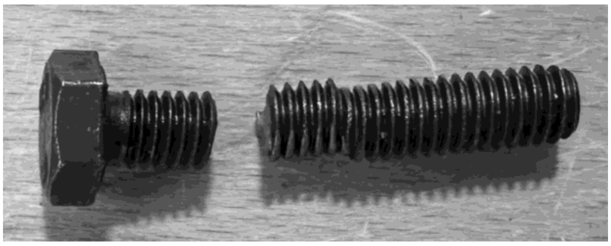

Figure 3.8: BS failure of a grade 10.9 type M6 bolt as a result of increasing the thickness, *t* of the WAAM-AB inner plates.

Table 3.6 and Table 3.7 present the design variables of the produced inner plates for the one-bolt and two-bolt configurations, respectively. Each inner plate is uniquely designated to indicate its configuration and manufacturing process. The notation (IP) refers to an inner plate, with plates featuring a one-bolt configuration labelled (IP1) and those with a two-bolt configuration labelled (IP2). The number following IP1 or IP2 (e.g., in IP1-1) represents the specimen number, which corresponds to a unique set of geometrical variables such as end distance, e_1, edge distance, e_2, and breadth, b. For specimens produced via AM, the designation also includes the surface condition and the extraction or printing angle. In this context, (M) indicates that the surface was machined either to achieve the specified thickness, t for WAAM or to remove the surface roughness in SLM, while (AB) denotes an as-built condition. Finally, the last number specifies the angle of printing/extraction, θ . For example, the designation IP1-1-WAAM-M-0° identifies an inner plate produced using WAAM with a one-bolt configuration, specimen number 1, where M signifies that the surface was machined to achieve t = 2 mm, with the angle of printing/extraction of θ = 0°. Although one inner plate in the WAAM-AB specimen experienced total failure, the mean thickness, t reported is based on both plates, as each contributed to the load-bearing capacity prior to rupture.

Table 3.6: Design variables of produced inner plates for one-bolt configuration.

Designation	Bolt type	Bolt grade	Hole diameter, d_o	Thickness, t (mm)	End distance, e_1 (mm)	Edge distance, e_2 (mm)	Breadth, b (mm)
IP1-1-CON	M6	10.9	6.6	2	14	15	30
IP1-2-CON	M6	10.9	6.6	2	13	15	30
IP1-3-CON	M6	10.9	6.6	2	11	15	30
IP1-4-CON	M6	10.9	6.6	2	8	15	30
IP1-5-CON	M6	10.9	6.6	2	15	8	16
IP1-1-WAAM-M-0°	M6	10.9	6.6	2	14	15	30
IP1-1-WAAM-M-45°	M6	10.9	6.6	2	14	15	30
IP1-1-WAAM-M-60°	M6	10.9	6.6	2	14	15	30
IP1-1-WAAM-M-90°	M6	10.9	6.6	2	14	15	30
IP1-2-WAAM-M-0°	M6	10.9	6.6	2	13	15	30
IP1-2-WAAM-M-45°	M6	10.9	6.6	2	13	15	30
IP1-2-WAAM-M-60°	M6	10.9	6.6	2	13	15	30
IP1-2-WAAM-M-90°	M6	10.9	6.6	2	13	15	30
IP1-3-WAAM-M-0°	M6	10.9	6.6	2	11	15	30
IP1-4-WAAM-M-0°	M6	10.9	6.6	2	8	15	30
IP1-1-WAAM-AB-0°	M8	12.9	8.4	5.4	14	15	30
IP1-2-WAAM-AB-0°	M8	12.9	8.4	5.4	13	15	30
IP1-2-WAAM-AB-45°	M8	12.9	8.4	5.3	13	15	30
IP1-2-WAAM-AB-60°	M8	12.9	8.4	5.2	13	15	30
IP1-2-WAAM-AB-90°	M8	12.9	8.4	5.2	13	15	30
IP1-3-WAAM-AB-0°	M8	12.9	8.4	5.3	11	15	30
IP1-4-WAAM-AB-0°	M8	12.9	8.4	5.4	8	15	30
IP1-5-WAAM-AB-0°	M8	12.9	8.4	5.2	15	8	16
IP1-5-WAAM-AB-45°	M8	12.9	8.4	5.4	15	8	16
IP1-5-WAAM-AB-60°	M8	12.9	8.4	5.3	15	8	16
IP1-5-WAAM-AB-90°	M8	12.9	8.4	5.3	15	8	16
IP1-1-SLM-M-0°	M6	10.9	6.6	2	14	15	30
IP1-1-SLM-AB-0°	M6	10.9	6.6	2	14	15	30
IP1-2-SLM-AB-0°	M6	10.9	6.6	2	13	15	30
IP1-2-SLM-AB-45°	M6	10.9	6.6	2	13	15	30
IP1-2-SLM-AB-90°	M6	10.9	6.6	2	13	15	30
IP1-5-SLM-AB-0°	M6	10.9	6.6	2	15	8	16
IP1-5-SLM-AB-45°	M6	10.9	6.6	2	15	8	16
IP1-5-SLM-AB-90°	M6	10.9	6.6	2	15	8	16

Table 3.7: Design variables of produced inner plates for two-bolt configuration.

Designation	Bolt type	Bolt grade	Hole diam-eter, d_o	Thick-ness, t (mm)	End distance, e_1 (mm)	Edge distance, e_2 (mm)	Pitch distance, p (mm)	Breadth, b (mm)
IP2-1-CON	M6	10.9	6.6	2	12	12	16	40
IP2-2-CON	M6	10.9	6.6	2	11	12	16	40
IP2-3-CON	M6	10.9	6.6	2	8.2	12	16	40
IP2-4-CON	M6	10.9	6.6	2	8	12	16	40
IP2-5-CON	M6	10.9	6.6	2	7	12	16	40
IP2-6-CON	M6	10.9	6.6	2	16	8	24	40
IP2-7-CON	M6	10.9	6.6	2	15	11	18	40
IP2-1-WAAM-M-0°	M6	10.9	6.6	2	12	12	16	40
IP2-1-WAAM-M-45°	M6	10.9	6.6	2	12	12	16	40
IP2-1-WAAM-M-60°	M6	10.9	6.6	2	12	12	16	40
IP2-1-WAAM-M-90°	M6	10.9	6.6	2	12	12	16	40
IP2-2-WAAM-M-0°	M6	10.9	6.6	2	11	12	16	40
IP2-3-WAAM-M-0°	M6	10.9	6.6	2	8.2	12	16	40
IP2-3-WAAM-M-45°	M6	10.9	6.6	2	8.2	12	16	40
IP2-3-WAAM-M-60°	M6	10.9	6.6	2	8.2	12	16	40
IP2-3-WAAM-M-90°	M6	10.9	6.6	2	8.2	12	16	40
IP2-4-WAAM-M-0°	M6	10.9	6.6	2	8	12	16	40
IP2-5-WAAM-M-0°	M6	10.9	6.6	2	7	12	16	40
IP2-7-WAAM-M-0°	M6	10.9	6.6	2	15	11	18	40
IP2-2-WAAM-AB-0°	M8	12.9	8.4	5.5	11	12	16	40
IP2-3-WAAM-AB-0°	M8	12.9	8.4	5.6	8.2	12	16	40
IP2-3-WAAM-AB-45°	M8	12.9	8.4	5.2	8.2	12	16	40
IP2-3-WAAM-AB-60°	M8	12.9	8.4	5.5	8.2	12	16	40
IP2-3-WAAM-AB-90°	M8	12.9	8.4	5.3	8.2	12	16	40
IP2-4-WAAM-AB-0°	M8	12.9	8.4	5.0	8	12	16	40
IP2-5-WAAM-AB-0°	M8	12.9	8.4	5.3	7	12	16	40
IP2-6-WAAM-AB-0°	M8	12.9	8.4	5.4	16	8	24	40
IP2-6-WAAM-AB-45°	M8	12.9	8.4	5.0	16	8	24	40
IP2-6-WAAM-AB-60°	M8	12.9	8.4	5.3	16	8	24	40
IP2-6-WAAM-AB-90°	M8	12.9	8.4	5.0	16	8	24	40
IP2-7-WAAM-AB-0°	M8	12.9	8.4	5.4	15	11	18	40
IP2-7-SLM-M-0°	M6	10.9	6.6	2	15	11	18	40
IP2-6-SLM-AB-0°	M6	10.9	6.6	2	16	8	24	40
IP2-6-SLM-AB-45°	M6	10.9	6.6	2	16	8	24	40
IP2-6-SLM-AB-90°	M6	10.9	6.6	2	16	8	24	40
IP2-7-SLM-AB-0°	M6	10.9	6.6	2	15	11	18	40

3.3 Effect of the manufacturing method on load capacity

For single-bolt configurations, the experimental loads of WAAM and SLM tests were compared to their respective CON counterparts for each test geometry. WAAM-M tests generally exhibited comparable performance with variations ranging from a reduction of 10.5% in IP1-2-WAAM-M-90° to a modest increase of 5.0% in IP1-2-WAAM-M-45°. SLM tests, both machined and as-built, exhibited variations generally within ±5%, with a few cases showing reductions of up to 10.8% compared to their CON counterparts. Although the WAAM-AB tests appeared to yield significantly higher failure loads, in some cases more than double the CON values, such as a 136% increase in IP1-1-WAAM-AB-0°, these increases are attributed to their greater thickness and are therefore not directly comparable to the 2 mm thick tests in terms of load capacity.

For double-bolt configurations, WAAM-M tests showed small variations, with the largest reduction being 7.3% in IP2-1-WAAM-M-90° and a minor increase of 5.6% in IP2-3-WAAM-M-45°. SLM tests also exhibited variations within $\pm$5% of the corresponding CON values. The WAAM-AB tests displayed noticeable increases in failure load, with IP2-6-WAAM-AB-0° showing the highest increase at 133%, relative to its CON counterpart. Nonetheless, when the comparison is restricted to tests with consistent thickness, the differences in load capacity across all manufacturing methods are not significant.

3.4 Failure mode and crack behaviour of the plates

3.4.1 Single-bolt configuration

The investigation on failure modes and crack behaviour across both conventional and AM approaches was conducted through visual observation of the completely failed test plates. Starting with the single-bolt configurations, Figure 3.9 that represents IP1-1 shows that all plates failed due to a combined EB and SO, primarily induced by a relatively small end distance, e_1 in the bolted connection. The deformation around the hole indicates that localised bearing stresses led to a significant plasticity before final failure. This is evident from the compressed and plastically deformed region at the bottom edge of the hole, where the bolt exerted high contact pressure. Additionally, a distinct crack at the hole edge was observed in IP1-1-CON and IP1-1-WAAM-M-90°, suggesting that the shear-induced hole elongation led to a tensile stress concentration in this region, in turn resulting in early micro-cracking and crack initiation. In most cases, SO crack extended from the hole along e_1, following a straight tearing path. Notably, the curved nature of the crack in IP1-1-WAAM-M-45° and IP1-1-WAAM-M-60° suggests secondary tensile effects, possibly influenced by the layered structure of WAAM, which may have altered crack propagation behaviour to be diagonal. Similarly, Figure 3.10, representing the IP1-2 configuration, exhibited a combined failure mode of EB and SO. However, in the IP1-2-CON plate, crack propagation along the breadth was more pronounced, suggesting that manufacturing-induced anisotropy in the CON material may have contributed to guiding the crack path. This contrasts with the WAAM specimens, where the layered structure and its orientation were the governing factors affecting crack propagation. Despite the increased thickness, t and hole diameter, d_o, WAAM-AB plates exhibited the same failure mode and crack behaviour as the other CON and AM plates. Alongside the observed load bearing capacity results of experimental tests, this outcome suggests that unlike other geometric parameters (e.g., e_1, e_2, and b), the thickness, t has larger effects on the final failure capacity than on the failure mode. As e_1 decreases, the failure modes observed in Figure 3.11 and Figure 3.12 remained similar to those shown in the earlier figures, though SO failure was more pronounced. In Figure 3.13 , the significantly smaller plate breadth, b resulted in an NST failure mode. Cracks initiated at one edge of the bolt hole and propagated directly to the plate boundary, a behaviour observed consistently across all IP1-5 plates, except for the CON plates, where crack propagation remained incomplete. However, no notable differences were observed in crack initiation or propagation paths, highlighting the dominant influence of the reduced breadth, b on the NST failure mechanism.

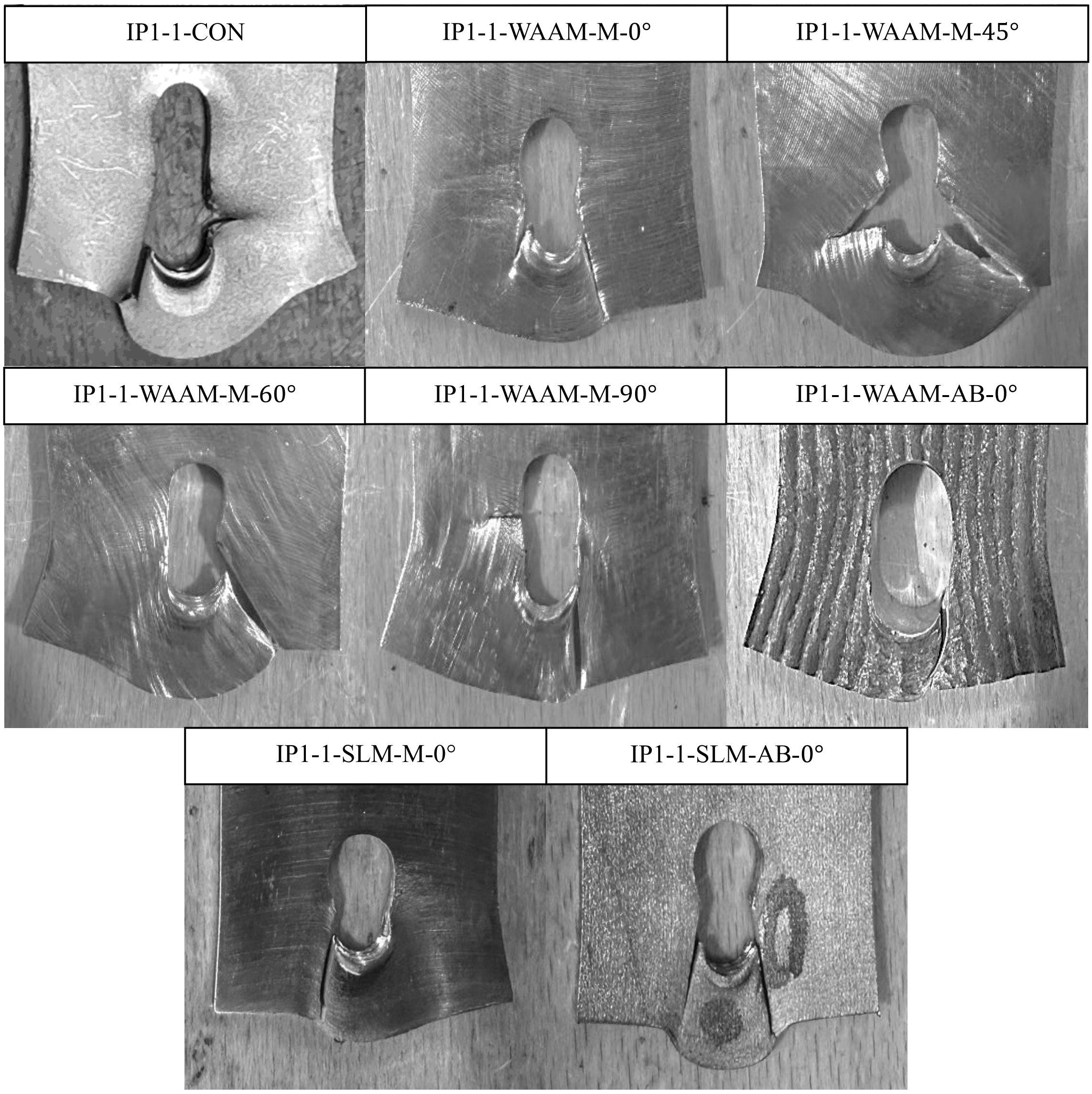

Figure 3.9: Failure modes for IP1-1 configuration of CON and AM plates.

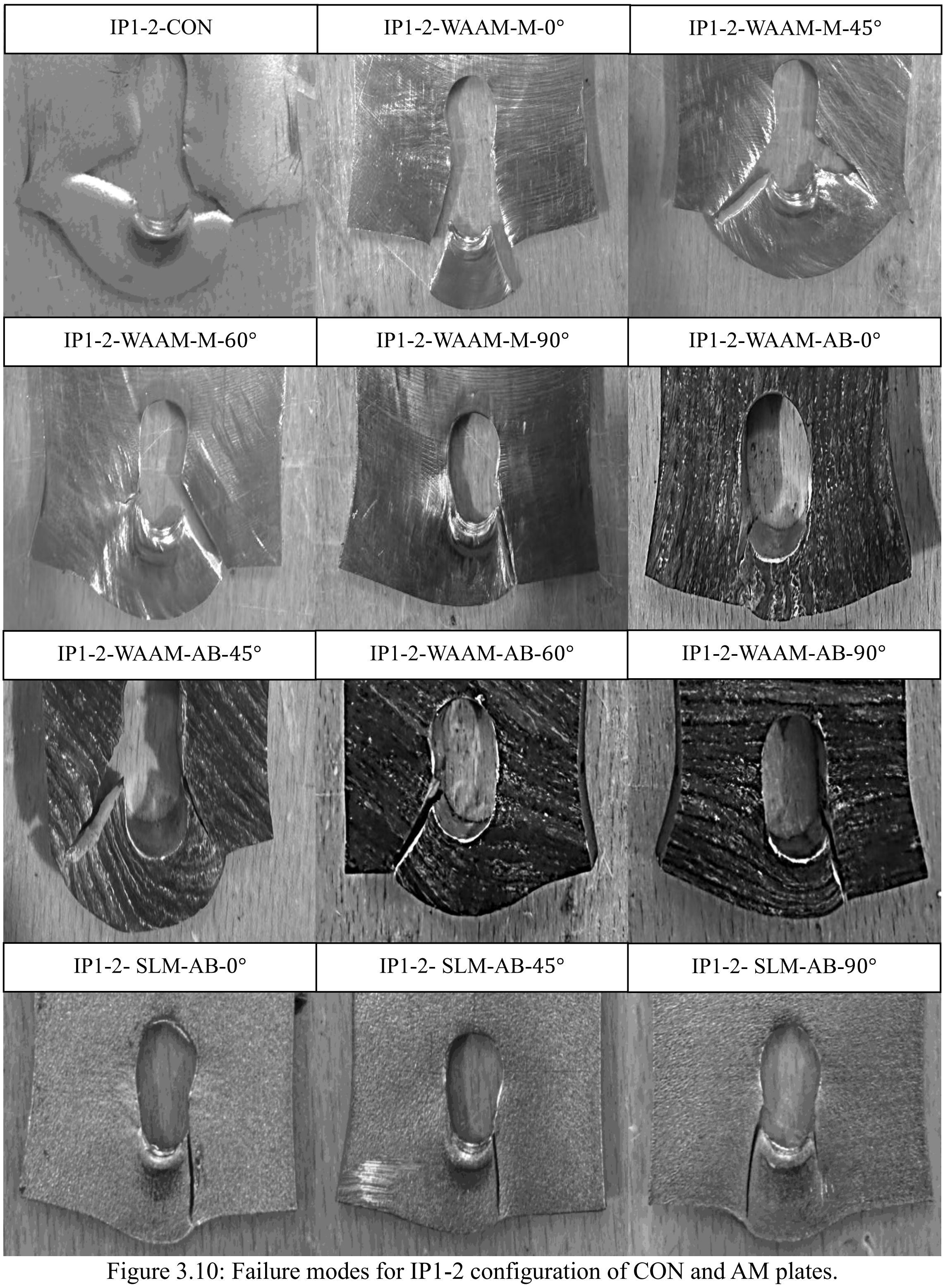

Figure 3.10: Failure modes for IP1-2 configuration of CON and AM plates.

IP1-3-CON	IP1-3-WAAM-M-0°	IP1-3-WAAM-AB-0°

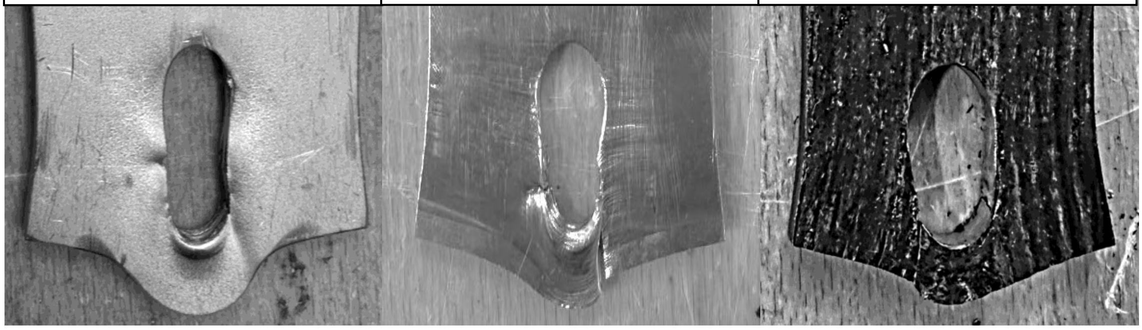

Figure 3.11: Failure modes for IP1-3 configuration of CON and AM plates.

IP1-4-CON	IP1-4-WAAM-M-0°	IP1-4-WAAM-AB-0°

Figure 3.12: Failure modes for IP1-4 configuration of CON and AM plates.

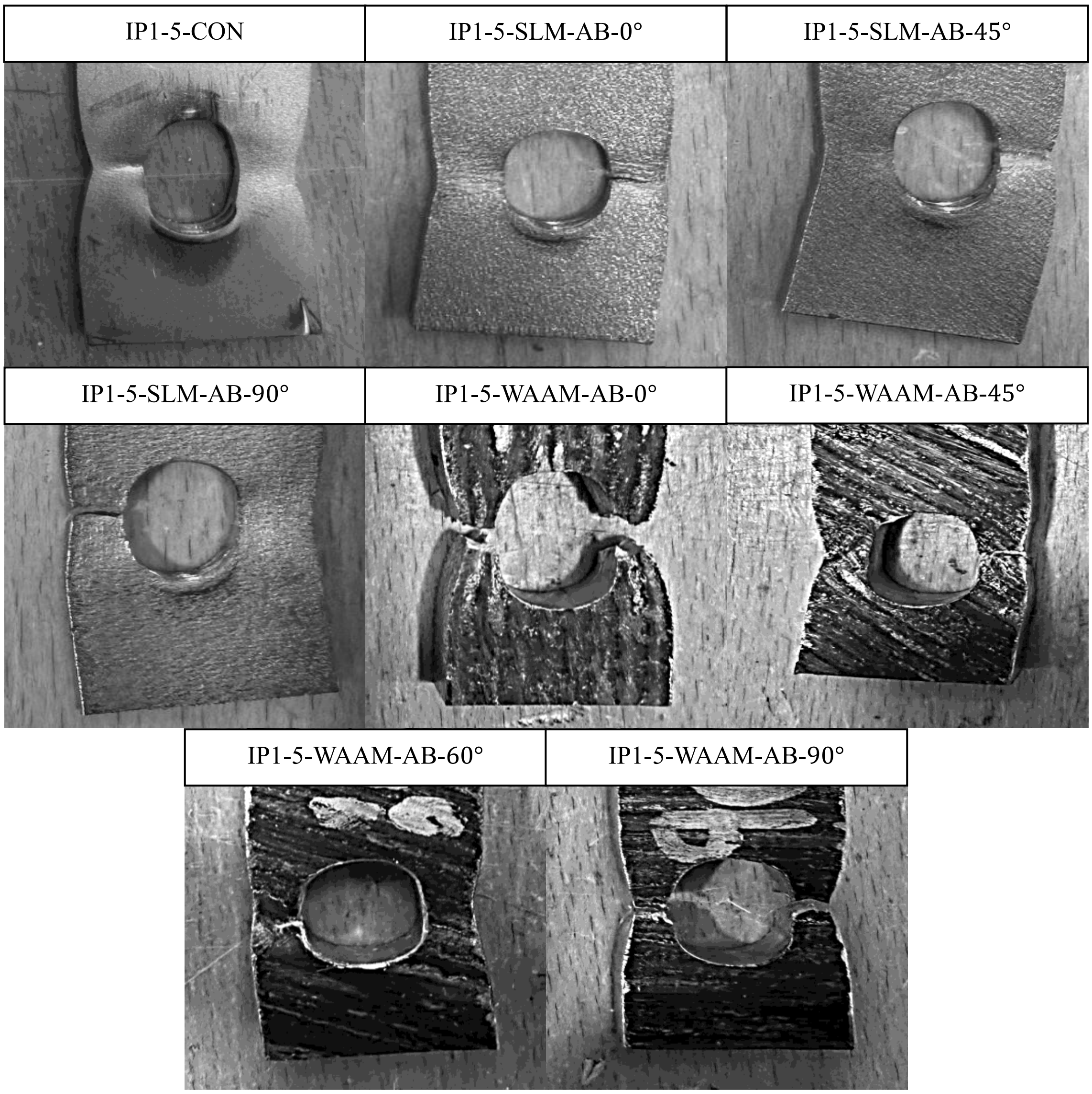

Figure 3.13: Failure modes for IP1-5 configuration of CON and AM plates.

3.4.2 Double-bolt configuration

For the double-bolt configurations, failure in both CON and AM plates was investigated under varying geometrical conditions, including varying pitch distance, p between the centres of the bolt holes. As shown in Figure 3.14, the small value of p promoted crack initiation between the holes, resulted in a combination of EB and the onset of partial BT failure modes for the IP2-1-CON and IP2-1-WAAM-M-0° plates, while in all other plates the partial BT crack propagated further. Similar to the single-bolt configuration, crack propagation in the WAAM-M plates was influenced by the printing layered structure, with diagonal crack paths observed in the IP2-1-WAAM-M-45° and IP2-1-WAAM-M-60° specimens. Figure 3.15 shows that a slight decrease in e_1 relative to IP1-1 plates did not alter the failure mode of IP2-2-CON and IP2-2-WAAM-AB-0°. However, a complete BT failure was observed in IP2-2-WAAM-M-0°. This can be attributed to the combined effect of tension cracking across the net section between the holes and shear cracking along the hole edges. As shown in Figure 3.16 and Figure 3.17 for the IP2-3 and IP2-4 plates, further reductions in e_1, resulted in failure modes consisting of either EB combined with complete BT or EB combined with SO. Next, Figure 3.18 illustrates that the IP2-5 plates, which had the smallest e_1, underwent exclusively EB and SO failures. Hence, for double-bolt configuration, as e_1 decreases, the failure mode transitions from partial BT to either EB combined with complete BT or EB combined with SO, emphasising the critical role of this variable in driving the progression toward shear-dominated failures. Subsequently, Figure 3.19 examines the influence of increasing p, which in turn reduces e_2, causing the failure to shift toward EB and partial NST along the edges. This behaviour was consistently observed across both CON and AM plates, indicating that p can significantly influence crack initiation and propagation. Finally, Figure 3.20 shows that providing sufficient e_1 and p led to EB and initiation of partial BT in all plates, except for IP2-7-WAAM-AB-0°, where EB was accompanied by complete NST failure occurred. This exceptional failure could be attributed to manufacturing defects inherent to the WAAM process highlighting the significant influence of manufacturing procedures on overall failure modes.

CON and AM plates exhibited broadly similar failure modes and crack patterns. However, a detailed analysis of the WAAM machined and as-built plates extracted at θ = 45° and 60° revealed distinct crack paths. This highlights the complex interplay of geometric and manufacturing factors in determining the failure process. Although these subtle differences in crack propagation are noteworthy, they do not result in a fundamentally different overall failure mode between the CON and AM plates.

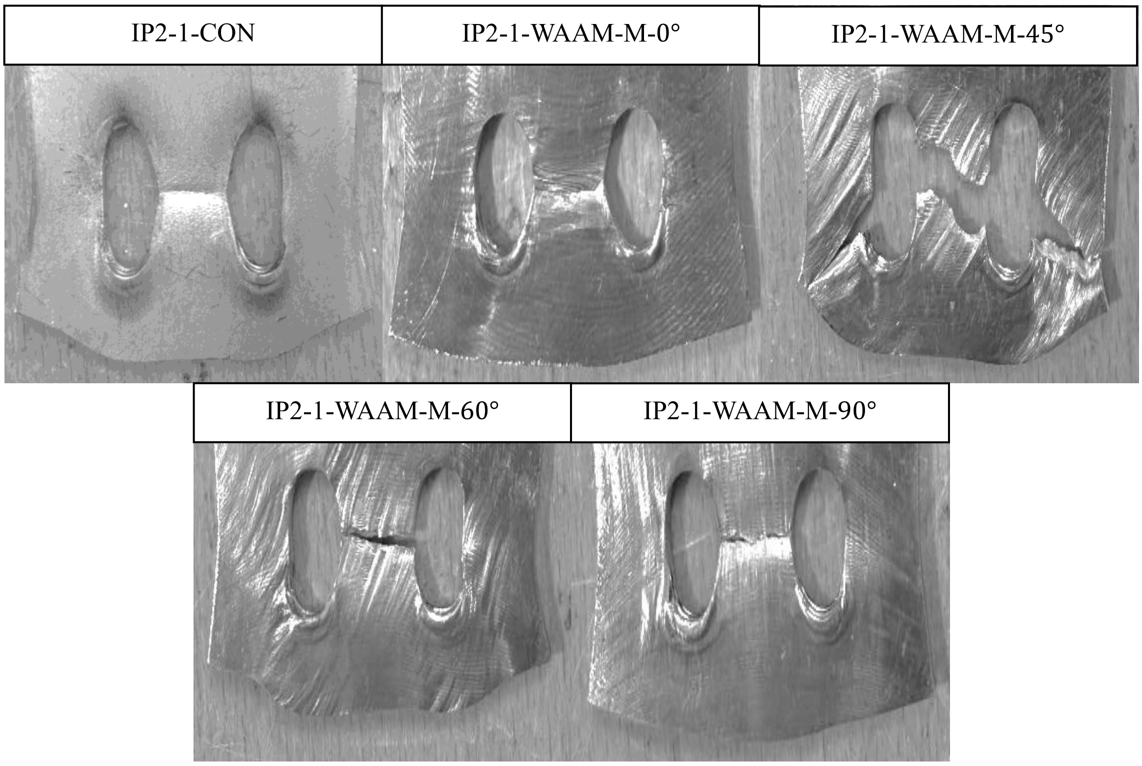

Figure 3.14: Failure modes for IP2-1 configuration of CON and AM plates.

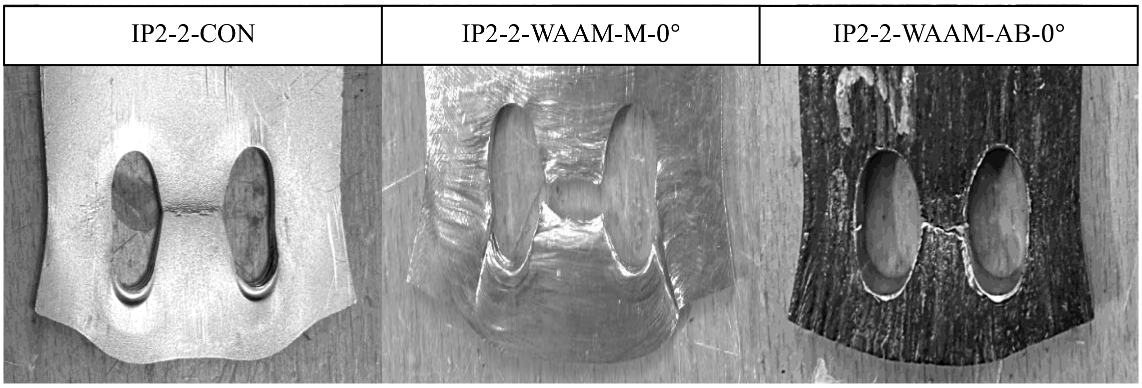

Figure 3.15: Failure modes for IP2-2 configuration of CON and AM plates.

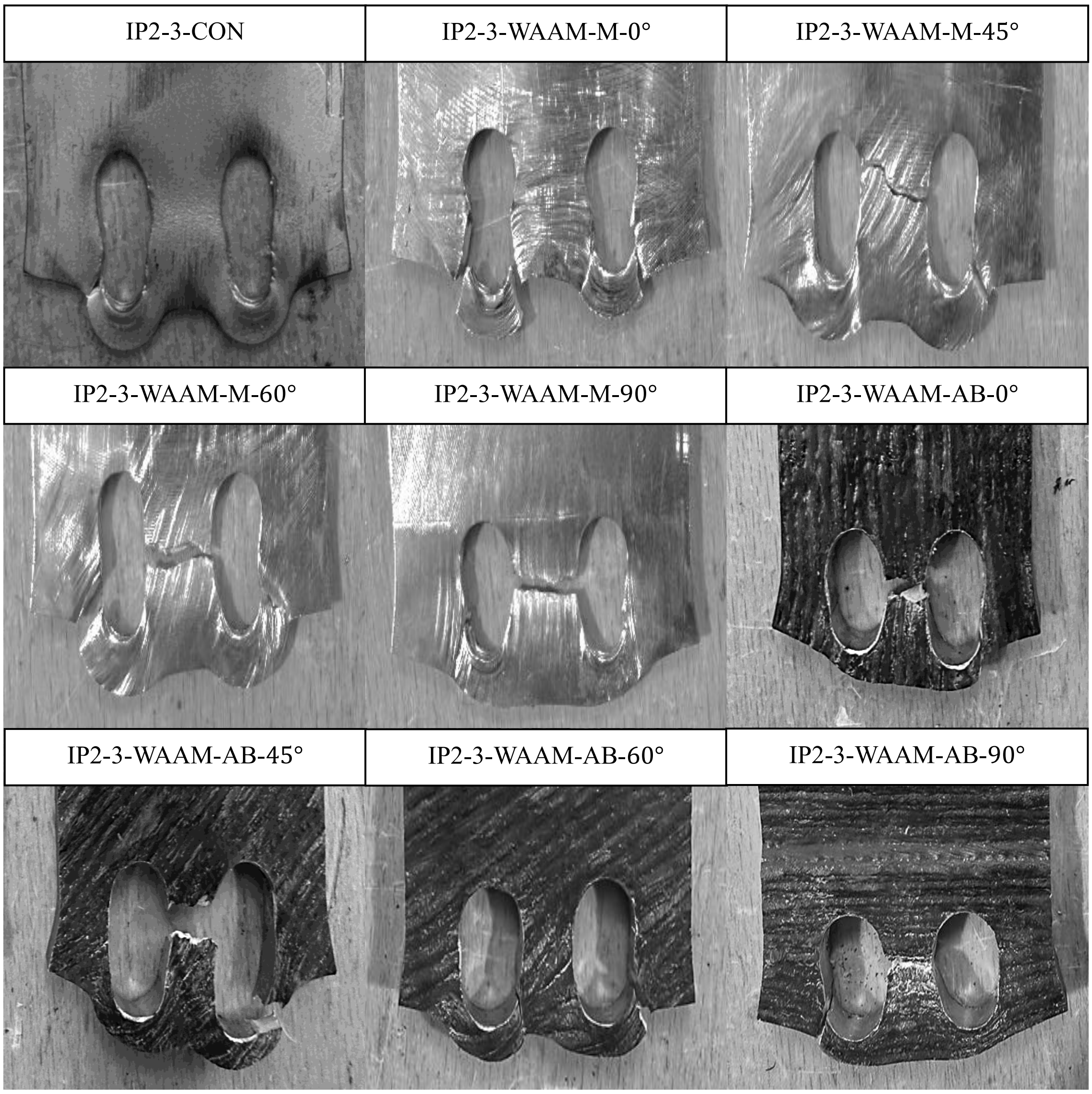

Figure 3.16: Failure modes for IP2-3 configuration of CON and AM plates.

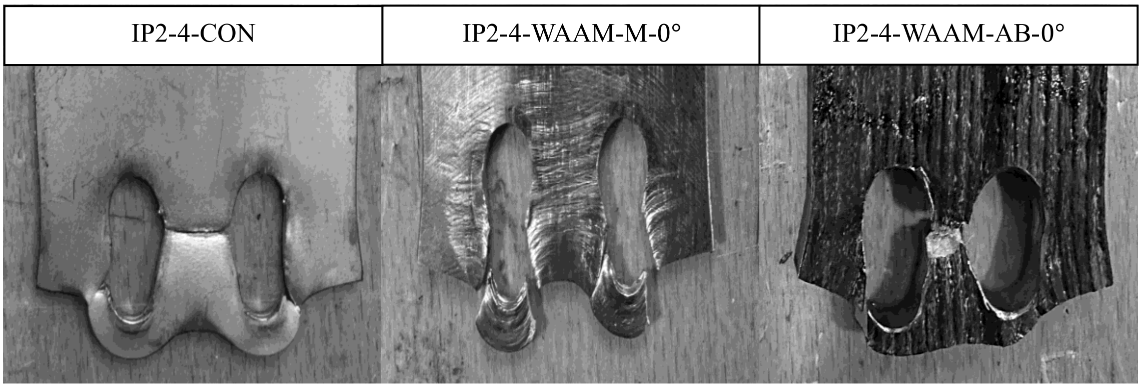

Figure 3.17: Failure modes for IP2-4 configuration of CON and AM plates.

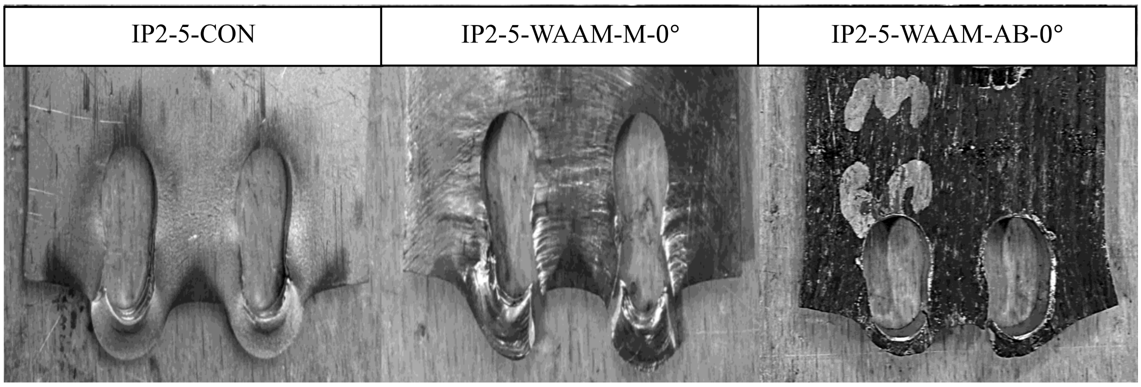

Figure 3.18: Failure modes for IP2-5 configuration of CON and AM plates.

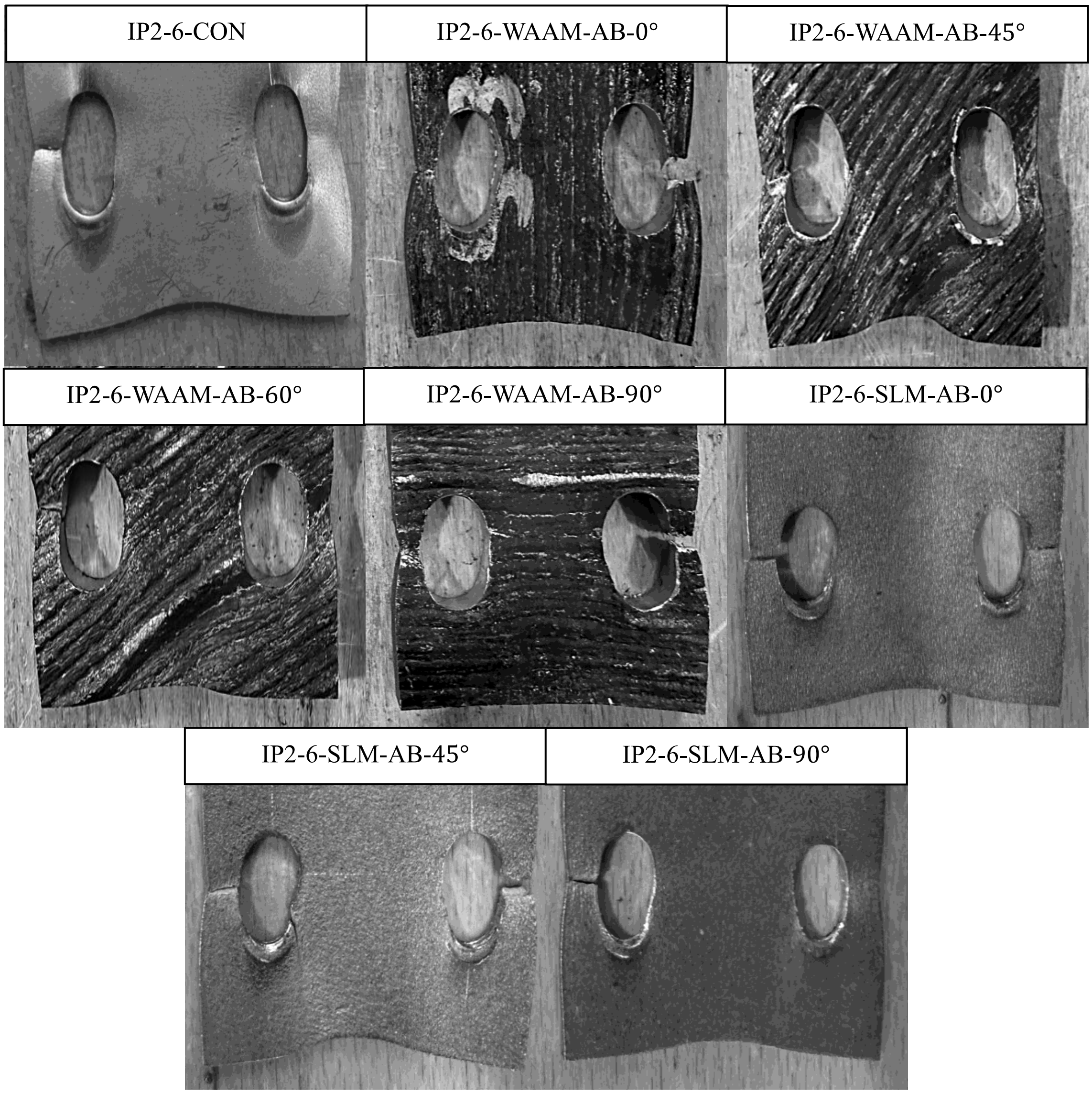

Figure 3.19: Failure modes for IP2-6 configuration of CON and AM plates.

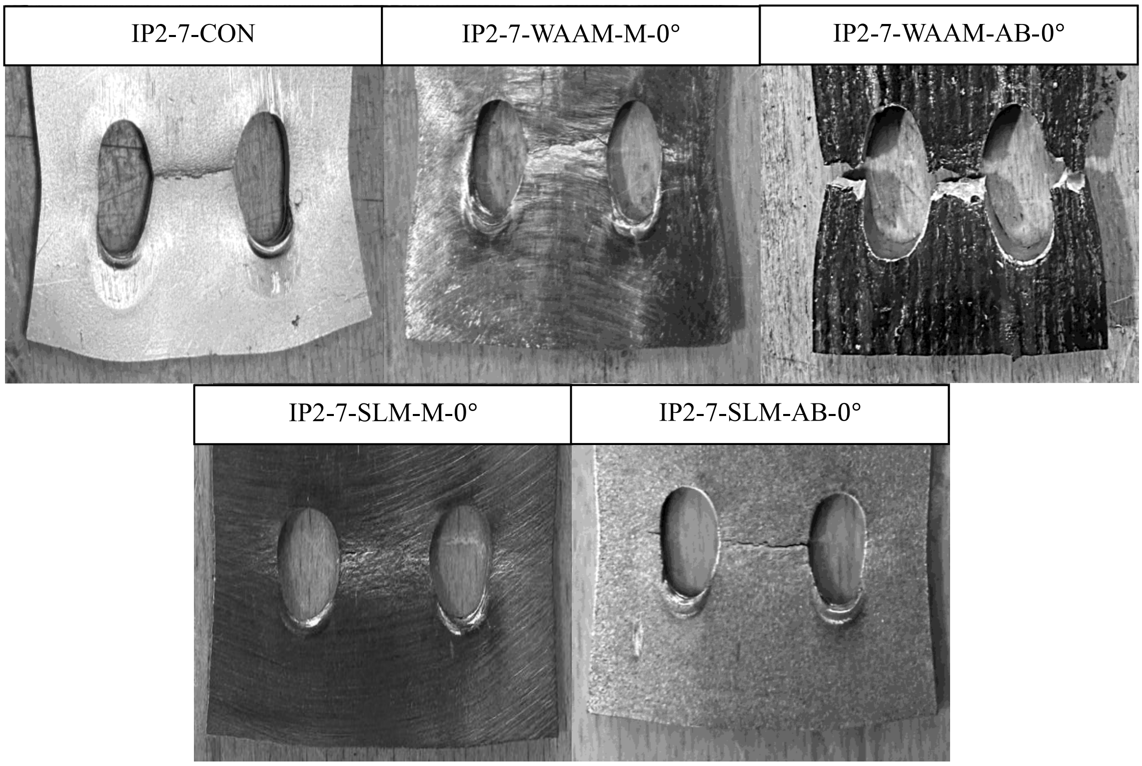

Figure 3.20: Failure modes for IP2-7 configuration of CON and AM plates.

3.5 Conclusions

Based on the mechanical behaviour of (CON) and AM 316L stainless steel coupons, as well as the failure modes in single- and double-bolted configurations of hybrid double-lap shear connections, the following conclusions were drawn:

a) CON coupon exhibited superior tensile properties, achieving the highest σ_u and ε_f, whereas WAAM specimens showed clear sensitivity to surface condition and extraction orientation, exhibiting improved properties at θ = 60° and 45° but significantly reduced ductility at θ = 90°. Meanwhile, SLM coupons achieved the highest $\sigma_{0.2}$ and yield ratio but exhibited notably low ductility, though still exceeding that of WAAM specimens extracted at θ = 90°.
b) When thickness is comparable, the load capacity of WAAM-M and SLM tests closely aligns with that of CON specimens, indicating that manufacturing method does not significantly affect global load-bearing performance.
c) Variations in geometric variables, such as e_1, e_2, b and p, predominantly influence the failure behaviour, reinforcing their critical role in the design of inner plates for double-lap bolted connections.
d) Crack initiation and propagation modes were broadly similar among CON and AM plates; however, WAAM machined and as-built plates extracted at θ = 45° and 60° displayed unique crack paths influenced by their layered microstructure and surface undulation, with

cracks propagating diagonally relative to the loading direction. In contrast, SLM specimens maintain consistent behaviour with minimal sensitivity to the surface condition and print orientation.

e) Overall, the majority of AM plates achieved similar failure modes to their CON counterparts. This demonstrates that selecting optimal printing orientations and standardised geometrical design variables can ensure reliable structural performance in hybrid 316L stainless steel double-lap shear connections incorporating AM metals.

f) While the present study focuses on the mechanical and failure behaviour aspects, further work is needed to establish a complete Process-Structure-Property-Performance (PSPP) relationship for the additively manufactured metals considered, with particular emphasis placed on grain morphology, texture, and anisotropy.

Chapter 4. Static Assessment of Hybrid Double-Lap Bolted Joints with Additively Manufactured 316L Plates

Forward Commentary

This article, titled "Static Assessment of Hybrid Double-Lap Bolted Joints With Additively Manufactured 316L Plates", was published in *Fatigue & Fracture of Engineering Materials & Structures* on 15 February 2026 [64]. The article examines the static response of hybrid double-lap shear bolted connections with conventional and additively manufactured 316L inner plates and evaluates the accuracy of codified and literature-based design equations for estimating their load capacity. Hasan Almuhanna conducted the overall work, including the investigation, formal analysis, and writing the manuscript. Professor Luca Susmel and Dr Giacomo Torelli contributed through supervision, critical review, and editing, while Professor Luca Susmel also contributed to the conceptualisation and methodology of the study.

Abstract

The present study examines the static response and evaluates the accuracy of design standards and selected literature-based design criteria in estimating the load capacity of the inner plates of double-lap shear bolted connections in single- and double-bolt configurations. The analysis is based on 70 experiments previously reported by the authors, including conventional and additively manufactured inner plates produced by wire arc additive manufacturing and selective laser melting. While additively manufactured plates exhibited load capacities comparable to conventional plates, they generally showed reduced ductility. Experimental load capacities are compared against the European standards EC3-1-8 and EC3-1-4, and the American standard AISC 370. Although originally developed for carbon steel, EC3-1-8 provided the most accurate estimations, whereas EC3-1-4 and AISC 370 consistently overestimated the load capacity. Literature-based equations showed the closest agreement, highlighting limitations in current standards for additively manufactured bolted plates.

4.1 Introduction

Additive manufacturing (AM) is redefining structural engineering by enabling the production of complex, optimised geometries through layer-by-layer fabrication guided by digital design models [65]. The feasibility of this technology was demonstrated by the successful construction of the first full-scale AM footbridge, fabricated using grade 308Lsi austenitic stainless steel wire via wire arc additive manufacturing (WAAM). The bridge underwent extensive material, component, and structural testing, and was validated under serviceability design loads, showcasing the potential of AM for large-scale structural applications [66]. As the technology is rapidly advancing, especially in the use of metals such as steels and stainless steels, a growing body of research is focussing on reduced-scale specimens to address open questions related to mechanical performance, surface quality, and structural integrity [9].

Several experimental studies have examined the mechanical performance of WAAM plates integrated as a component in bolted connections in both single- and double-lap shear testing arrangements, covering metals including carbon steel, duplex stainless steel, and austenitic stainless steel [27–33]. These investigations have identified a range of failure modes such as shear-out, net-section tension, bearing, out-of-plane curling, and an unexpected failure of end-splitting. These studies also showed that the structural response was influenced by WAAM characteristics including material anisotropy, extraction direction, and surface conditions.

Among the studies investigating WAAM-produced bolted connections, four have specifically focused on double-lap shear arrangements and evaluated the accuracy of various established design specifications. WAAM carbon steel connections were examined in [28], covering several geometrical combinations and two distinct nominal plate thicknesses. The study in [28] assessed several design provisions; among these, the previous edition of Eurocode BS EN 1993-1-8 for steel joints [67] yielded a mean experimental-to-estimated resistance ratio of 1.11 with a coefficient of variation (COV) of 0.073 [28], where the COV, defined as the standard deviation divided by the mean, indicates good agreement with the test results. A slightly higher mean ratio of 1.15 with greater variability (COV = 0.13) using the same previous edition of Eurocode BS EN 1993-1-8 provision was observed in [29], which also studied WAAM carbon steel. Although the average resistance was estimated reasonably well, the higher COV indicates reduced reliability. The work in [30] extended this research by testing thick WAAM carbon steel plates (7.9-9.3 mm thickness) and employed the updated Eurocode BS EN 1993-1-8 provision for steel joints [1], reporting a mean ratio of 1.11 and a lower COV of 0.07, which is comparable to the results reported in [28], despite the use of an updated Eurocode provision. Meanwhile, experiments on WAAM-produced 316L stainless steel connections were conducted in [32], demonstrating that the American standard ANSI/AISC 370 [4] yielded a higher mean ratio of 1.45 but with relatively low variability (COV = 0.088). Collectively, these studies illustrate the varying degrees of conservatism and precision when applying traditional steel design codes to WAAM-manufactured steel connections.

While both WAAM and selective laser melting (SLM) have been widely studied in the context of 316L stainless steel, most research on SLM-produced 316L has focused on microstructural characteristics and basic material properties such as anisotropy, porosity, and plain material mechanical behaviour [25,26,68,69]. However, a recent study has examined its structural performance in bolted connections, and it was focused on conditions following fire exposure [34]. As a result, there remains limited data on how SLM 316L stainless steel behaves in structural applications or whether its performance aligns with established design estimations. This presents an opportunity to assess the connection-level capacity of SLM plates against existing design codes.

Despite growing interest in the structural use of additive manufacturing, the design of WAAM stainless steel bolted connections remains underexplored. As mentioned above, only a limited number of studies have investigated both single- and double-lap WAAM and SLM 316L stainless steel bolted connections, while most existing research has focused on carbon steels. Therefore, the existing research is insufficient to assess the reliability of design standards and literature-based equations for such additively manufactured plates. The present study provides new insight by experimentally evaluating both single- and double-bolted configurations produced using SLM and WAAM, considering variations in geometry, print direction, and surface condition. Their performance is then compared against established design standards and proposed bearing strength equations from recent literature.

4.2 Reference experiments

The 316L stainless steel specimens examined in this study include conventionally manufactured reference plates, as well as plates produced using two additive manufacturing methods: SLM and WAAM. The fabrication procedures are described in a previous study from the authors [41], where the same specimens were used to investigate failure modes. In the present work, the focus is on examining the load-displacement response and evaluating both codified design provisions and equations developed in the literature for estimating the failure mechanism of the bolted connections. WAAM plates were produced using a robotic welding system with 316L wire under argon shielding, extracted from tubular builds via wire electrical discharge machining (EDM). SLM plates were fabricated using a laser-based powder bed system in an inert gas atmosphere and printed directly to the final dimensions. The mechanical properties of the parent materials, summarised in Table 4.1, were also reported in the previous study [41], where the strength properties of these materials were obtained from coupon testing.

Table 4.1: Mechanical properties of CON and AM 316L stainless steel coupons [41].

Designation	Modulus of elasticity, E (Gpa)	Offset yield stress, $f_{y,0.2}$ (MPa)	Ultimate stress, f_u (MPa)
CON	184	488	667
WAAM-M-0°	143	288	521
WAAM-M-45°	185	324	552
WAAM-M-60°	160	297	530
WAAM-M-90°	103	281	562
WAAM-AB-0°	124	278	493
WAAM-AB-45°	119	282	544
WAAM-AB-60°	139	323	566
WAAM-AB-90°	91	273	493
SLM-AB-0°	160	520	627
SLM-AB-45°	126	422	562
SLM-AB-90°	120	419	554

Experimental testing employed a double-lap shear setup (Figure 4.1), conducted on a Shimadzu universal testing machine equipped with a 300 kN load cell. Displacement-controlled loading was applied at a constant rate of 1 mm/min until failure. The setup was configured to promote failure in the thinner inner plates, while the thicker outer plates were designed to remain elastic and reduce secondary bending effects. Two primary configurations were investigated, comprising inner plates with either single or double bolt holes. Within each configuration, variations in geometrical variables presented in Figure 4.1, including end distance, e_1, edge distance, e_2, and pitch distance, p, were used to promote different failure modes, namely shear-out (SO), edge bearing (EB), net-section tension (NST), and block tearing (BT), the latter occurring in double-bolt configurations. Due to the ductile behaviour of 316L stainless steel, stress concentrations associated with bolt-hole interaction and the resulting large plastic deformation led most inner plates to exhibit a combination of failure modes, typically involving precursor EB failure followed by a governing partial or complete SO, NST, or BT, with only the final governing mode reported here, as shown in Figure 4.2 [41].

The AM plates varied in build orientation: for SLM, this referred to the direction of printing, whereas for WAAM, it denoted the extraction direction. Specifically, the printing direction angle, θ, is here defined as the angle between the extraction/printing direction and the direction of applied load. The tested inner plates included: conventionally manufactured plates (CON); SLM-produced plates tested in the as-built (SLM-AB) and machined (SLM-M) conditions; and WAAM-produced plates tested in the machined (WAAM-M) and as-built (WAAM-AB) conditions. All CON, SLM-M, SLM-AB, and WAAM-M plates had a uniform thickness, t of

2 mm. In the case of WAAM-M plates, the term M indicates that the plates were machined down to 2 mm to remove surface undulations. For SLM-M, M denotes only the removal of the rough surface, as the as-built thickness was already close to 2 mm. WAAM-AB plates were fabricated with an average $t = 5.3$ mm due to printing constraints. As reported in [41], no variation in failure modes was expected compared to their WAAM-M counterparts, although a significant increase in load capacity was observed with increased thickness. Table 4.2 and Table 4.3 give an overview of the tested specimens with their unique designation [41]. For example, IP1-1-WAAM-M-0° refers to configuration 1-1, featuring inner plates produced via WAAM. M indicates that the plates were machined, while 0° denotes the extraction or printing direction, θ against the applied load.

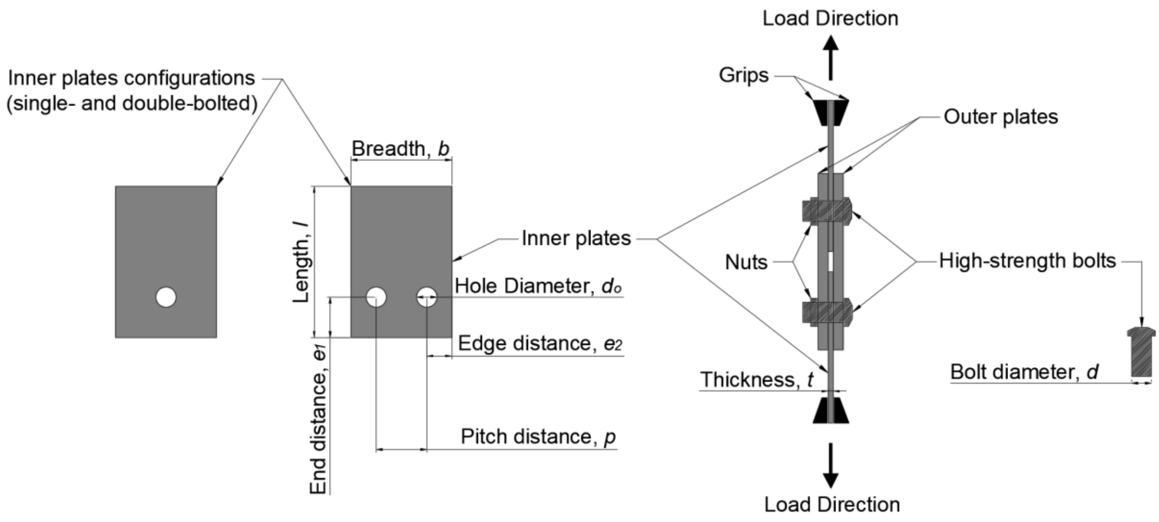

Figure 4.1: Test setup for double-lap shear bolted connections.

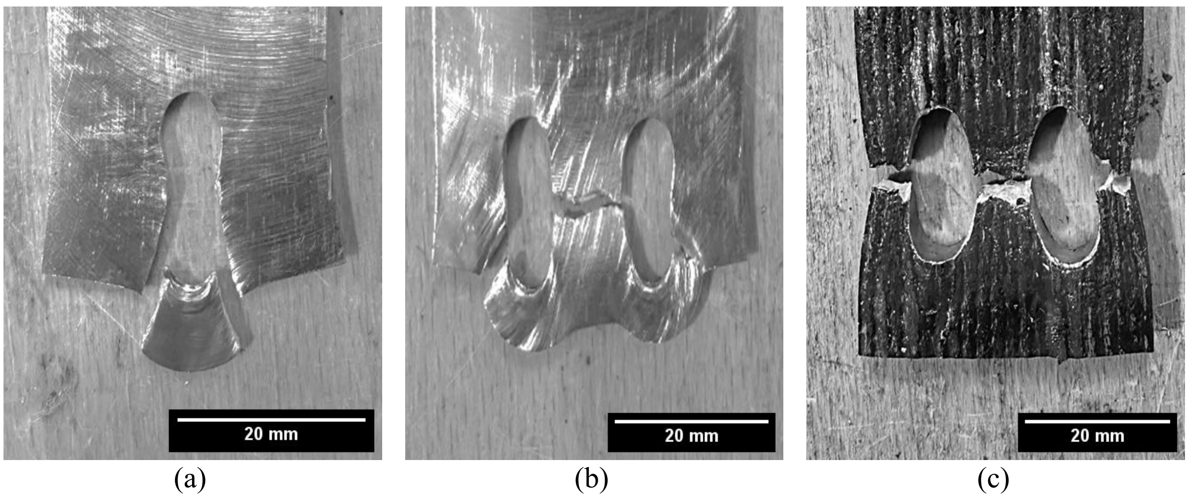

Figure 4.2: Representative governing failure modes observed in double-bolted configuration plates: (a) and (b) correspond to WAAM machined plates exhibiting SO and BT failures, respectively; (c) shows a WAAM as-built plate with NST failure [41].

Table 4.2: Tested specimens – single-bolt configuration [41].

Designation	Bolt type	Bolt grade	Hole diameter, d_o	Thickness, t (mm)	End distance, e_1 (mm)	Edge distance, e_2 (mm)	Breadth, b (mm)
IP1-1-CON	M6	10.9	6.6	2	14	15	30
IP1-2-CON	M6	10.9	6.6	2	13	15	30
IP1-3-CON	M6	10.9	6.6	2	11	15	30
IP1-4-CON	M6	10.9	6.6	2	8	15	30
IP1-5-CON	M6	10.9	6.6	2	15	8	16
IP1-1-WAAM-M-0°	M6	10.9	6.6	2	14	15	30
IP1-1-WAAM-M-45°	M6	10.9	6.6	2	14	15	30
IP1-1-WAAM-M-60°	M6	10.9	6.6	2	14	15	30
IP1-1-WAAM-M-90°	M6	10.9	6.6	2	14	15	30
IP1-2-WAAM-M-0°	M6	10.9	6.6	2	13	15	30
IP1-2-WAAM-M-45°	M6	10.9	6.6	2	13	15	30
IP1-2-WAAM-M-60°	M6	10.9	6.6	2	13	15	30
IP1-2-WAAM-M-90°	M6	10.9	6.6	2	13	15	30
IP1-3-WAAM-M-0°	M6	10.9	6.6	2	11	15	30
IP1-4-WAAM-M-0°	M6	10.9	6.6	2	8	15	30
IP1-1-WAAM-AB-0°	M8	12.9	8.4	5.4	14	15	30
IP1-2-WAAM-AB-0°	M8	12.9	8.4	5.4	13	15	30
IP1-2-WAAM-AB-45°	M8	12.9	8.4	5.3	13	15	30
IP1-2-WAAM-AB-60°	M8	12.9	8.4	5.2	13	15	30
IP1-2-WAAM-AB-90°	M8	12.9	8.4	5.2	13	15	30
IP1-3-WAAM-AB-0°	M8	12.9	8.4	5.3	11	15	30
IP1-4-WAAM-AB-0°	M8	12.9	8.4	5.4	8	15	30
IP1-5-WAAM-AB-0°	M8	12.9	8.4	5.2	15	8	16
IP1-5-WAAM-AB-45°	M8	12.9	8.4	5.4	15	8	16
IP1-5-WAAM-AB-60°	M8	12.9	8.4	5.3	15	8	16
IP1-5-WAAM-AB-90°	M8	12.9	8.4	5.3	15	8	16
IP1-1-SLM-M-0°	M6	10.9	6.6	2	14	15	30
IP1-1-SLM-AB-0°	M6	10.9	6.6	2	14	15	30
IP1-2-SLM-AB-0°	M6	10.9	6.6	2	13	15	30
IP1-2-SLM-AB-45°	M6	10.9	6.6	2	13	15	30
IP1-2-SLM-AB-90°	M6	10.9	6.6	2	13	15	30
IP1-5-SLM-AB-0°	M6	10.9	6.6	2	15	8	16
IP1-5-SLM-AB-45°	M6	10.9	6.6	2	15	8	16
IP1-5-SLM-AB-90°	M6	10.9	6.6	2	15	8	16

Table 4.3: Tested specimens – double-bolt configurations [41].

Designation	Bolt type	Bolt grade	Hole diameter, d_o	Thickness, t (mm)	End distance, e_1 (mm)	Edge distance, e_2 (mm)	Pitch distance, p (mm)	Breadth, b (mm)
IP2-1-CON	M6	10.9	6.6	2	12	12	16	40
IP2-2-CON	M6	10.9	6.6	2	11	12	16	40
IP2-3-CON	M6	10.9	6.6	2	8.2	12	16	40
IP2-4-CON	M6	10.9	6.6	2	8	12	16	40
IP2-5-CON	M6	10.9	6.6	2	7	12	16	40
IP2-6-CON	M6	10.9	6.6	2	16	8	24	40
IP2-7-CON	M6	10.9	6.6	2	15	11	18	40
IP2-1-WAAM-M-0°	M6	10.9	6.6	2	12	12	16	40
IP2-1-WAAM-M-45°	M6	10.9	6.6	2	12	12	16	40
IP2-1-WAAM-M-60°	M6	10.9	6.6	2	12	12	16	40
IP2-1-WAAM-M-90°	M6	10.9	6.6	2	12	12	16	40
IP2-2-WAAM-M-0°	M6	10.9	6.6	2	11	12	16	40
IP2-3-WAAM-M-0°	M6	10.9	6.6	2	8.2	12	16	40
IP2-3-WAAM-M-45°	M6	10.9	6.6	2	8.2	12	16	40
IP2-3-WAAM-M-60°	M6	10.9	6.6	2	8.2	12	16	40
IP2-3-WAAM-M-90°	M6	10.9	6.6	2	8.2	12	16	40
IP2-4-WAAM-M-0°	M6	10.9	6.6	2	8	12	16	40
IP2-5-WAAM-M-0°	M6	10.9	6.6	2	7	12	16	40
IP2-7-WAAM-M-0°	M6	10.9	6.6	2	15	11	18	40
IP2-2-WAAM-AB-0°	M8	12.9	8.4	5.5	11	12	16	40
IP2-3-WAAM-AB-0°	M8	12.9	8.4	5.6	8.2	12	16	40
IP2-3-WAAM-AB-45°	M8	12.9	8.4	5.2	8.2	12	16	40
IP2-3-WAAM-AB-60°	M8	12.9	8.4	5.5	8.2	12	16	40
IP2-3-WAAM-AB-90°	M8	12.9	8.4	5.3	8.2	12	16	40
IP2-4-WAAM-AB-0°	M8	12.9	8.4	5.0	8	12	16	40
IP2-5-WAAM-AB-0°	M8	12.9	8.4	5.3	7	12	16	40
IP2-6-WAAM-AB-0°	M8	12.9	8.4	5.4	16	8	24	40
IP2-6-WAAM-AB-45°	M8	12.9	8.4	5.0	16	8	24	40
IP2-6-WAAM-AB-60°	M8	12.9	8.4	5.3	16	8	24	40
IP2-6-WAAM-AB-90°	M8	12.9	8.4	5.0	16	8	24	40
IP2-7-WAAM-AB-0°	M8	12.9	8.4	5.4	15	11	18	40
IP2-7-SLM-M-0°	M6	10.9	6.6	2	15	11	18	40
IP2-6-SLM-AB-0°	M6	10.9	6.6	2	16	8	24	40
IP2-6-SLM-AB-45°	M6	10.9	6.6	2	16	8	24	40
IP2-6-SLM-AB-90°	M6	10.9	6.6	2	16	8	24	40
IP2-7-SLM-AB-0°	M6	10.9	6.6	2	15	11	18	40

4.3 Comparison of global load-displacement response across manufacturing methods

In addition to the interpretation of the failure modes and crack behaviour of the inner plates previously reported in [41], this section presents further analysis of the global load-displacement response of the tested connections. The load-displacement curves provide direct insight into the ductility of additively manufactured (AM) plates relative to their conventional (CON) counterparts. Since ductility is a key design parameter alongside strength, these curves provide a more complete understanding of the mechanical response of the connections before assessing the code-based estimations.

A comparative assessment of the 2 mm thick plates based on the global load-displacement curves across CON and AM tests can be seen in Figure 4.3a-e for the single-bolt configuration and Figure 4.4a-g for double-bolt configuration. The comparison reveals noticeable differences between the CON and AM specimens. Based on these figures, the load capacity of AM plates is broadly comparable to that of CON plates, with only minor variations observed. However, a clear difference is seen in terms of displacement at failure, δ, where AM plates consistently failed at lower δ values. For instance, in Figure 4.3a, IP1-1-CON reached a total $\delta = 19.5$ mm, whereas the highest displacements for WAAM-M and SLM-M and SLM-AB were $\delta = 12.8$, 11.2, and 9.2 mm respectively. This trend is also evident in the double-bolt configurations (Figure 4.4a-g), where CON plates again demonstrated greater displacement before failure. This indicates that AM plates have a detrimental effect in terms of elongation before failure, and they are less ductile than CON. Nevertheless, AM plates exhibited a steeper initial slope compared to CON plates, indicating enhanced connection stiffness. For similar geometries, the AM curves reached their peak loads over a shorter global displacement range, whereas the CON curves continued to develop load more gradually over a wider nonlinear region. This suggests that the CON connections sustained a more extended nonlinear response before the governing crack developed, while the AM connections reached similar load levels with less overall deformation. This could be attributed to differences in bolt-plate interaction, including increased friction due to surface roughness in SLM plates and the inherently higher bearing stiffness of both WAAM and SLM plates. The steeper initial slope also indicates that the AM connections underwent less elastic deformation before the onset of plastic behaviour. Additionally, the extraction orientation of $\theta = 45°$ and 60° in WAAM-M appeared to influence ductility, as these orientations exhibited slightly improved elongation. This observation aligns with coupon testing observed in [41], which showed that the diagonal printing orientation is beneficial to ductility. This further indicates that, despite the undulations being removed from the surface, the influence of the printing process persisted at the microstructural level, suggesting that the underlying grain structure and layer orientation contribute to this behaviour. For SLM tests, no clear consistency in behaviour was observed across different θ and surface conditions. This may imply that these variables have a less significant effect on mechanical performance in SLM compared to WAAM, where printing orientation and surface condition exhibit a more pronounced influence.

Beyond differences related to manufacturing extraction/print direction, θ, the influence of geometrical variables on load-bearing capacity and displacement was also evident. A decrease in end distance, e_1 from 14 mm to 8 mm for single-bolt configurations and from 14 mm to 8 mm for double-bolt configurations led to a noticeable reduction in both load capacity and ultimate displacement before failure. This trend was observed across all AM and CON plates, where specimens with shorter end distances exhibited earlier failure. Furthermore, the lower breadth, b value in IP1-5 (Figure 4.3e) resulted in a significant reduction in load capacity, despite e_1 having an adequate value of 15 mm. In contrast, IP2-7 (Figure 4.4g), which had large e_1, pitch distance, p, and sufficient edge distance, e_2, demonstrated improved overall performance. While these values were intentionally selected to ensure specific failure modes in the tested plates, the observed variations highlight the importance of adhering to design standard thresholds to achieve optimal structural performance.

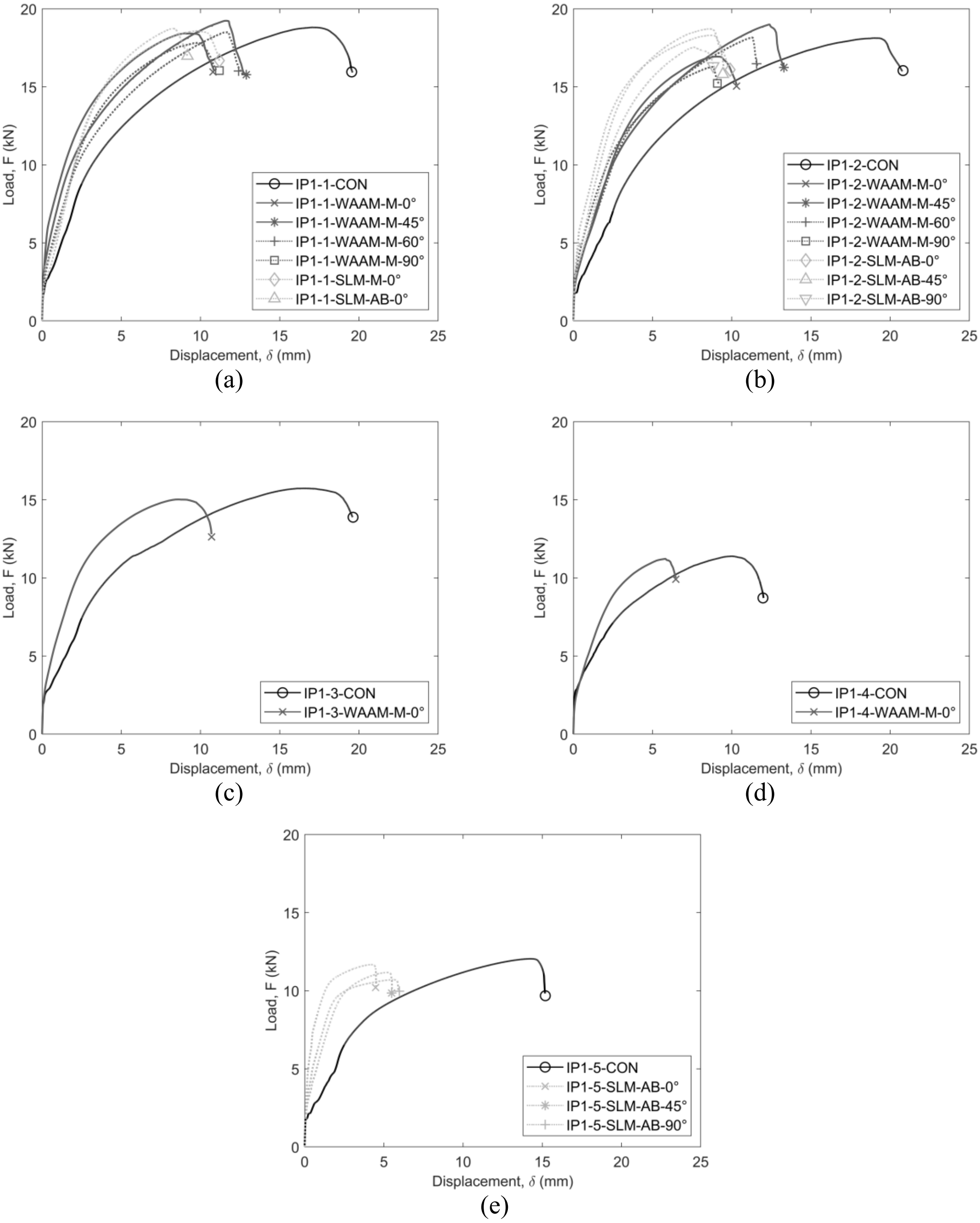

Figure 4.3: Load-displacement curves for single-bolt configurations with a consistent $t = 2$ mm: comparison between CON and AM plates.

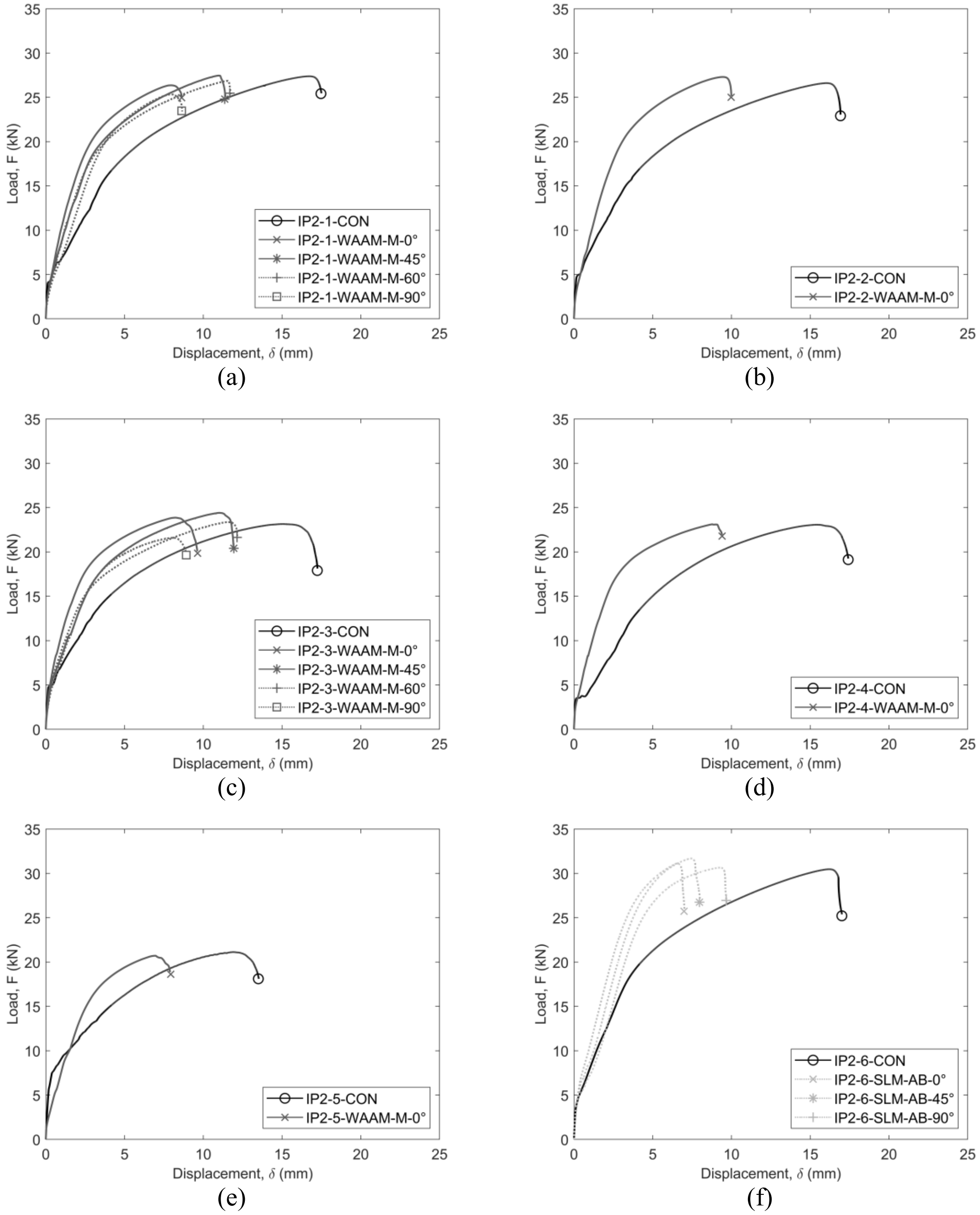

Figure 4.4: Load-displacement curves for double-bolt configurations with a consistent $t = 2$ mm: comparison between CON and AM plates.

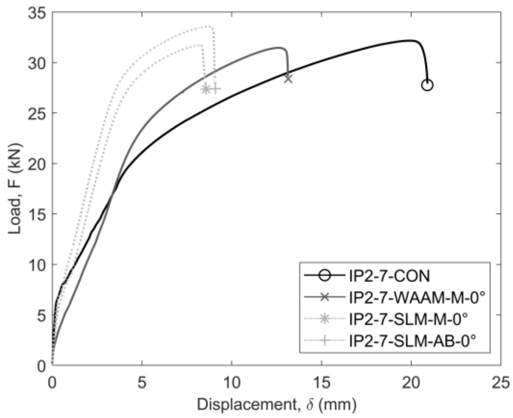

(g)

Figure 4.4: Load-displacement curves for double-bolt configurations with a consistent t=2 mm: comparison between CON and AM plates (continued).

In the case of WAAM-AB, the results for both single- and double-bolt configurations are shown in Figure 4.5a-e and Figure 4.6a-f, respectively. The curves differ markedly from those of the other specimens due to a significant increase in load-bearing capacity, primarily attributed to increased thickness, t. Despite surface undulations causing local variation in thickness, t, its overall increase played a key role in enhancing plate performance. However, this cannot be attributed to thickness alone because the bolt size and hole diameter, d_o were also changed. Furthermore, comparisons of extraction direction in Figure 4.5b,e and Figure 4.6b,e reinforced that a diagonal orientation (e.g., $\theta = 45°$ and 60°) is beneficial, noting that the performance of IP1-2-WAAM-AB-90° in Figure 4.5b did not follow this trend and was deemed to be an outlier.

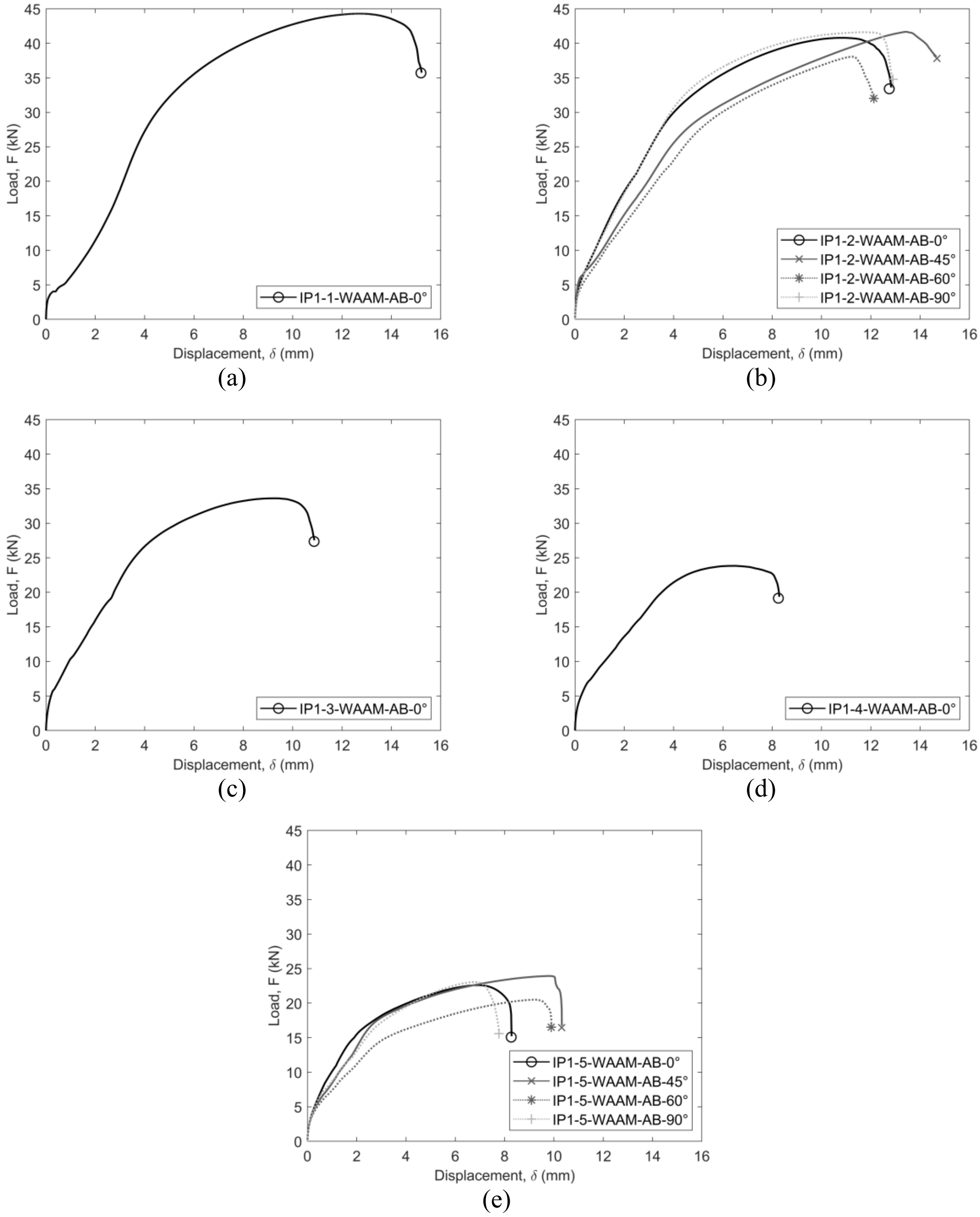

Figure 4.5: Load-displacement curves for single-bolt WAAM-AB configurations with non-uniform t and larger d_o.

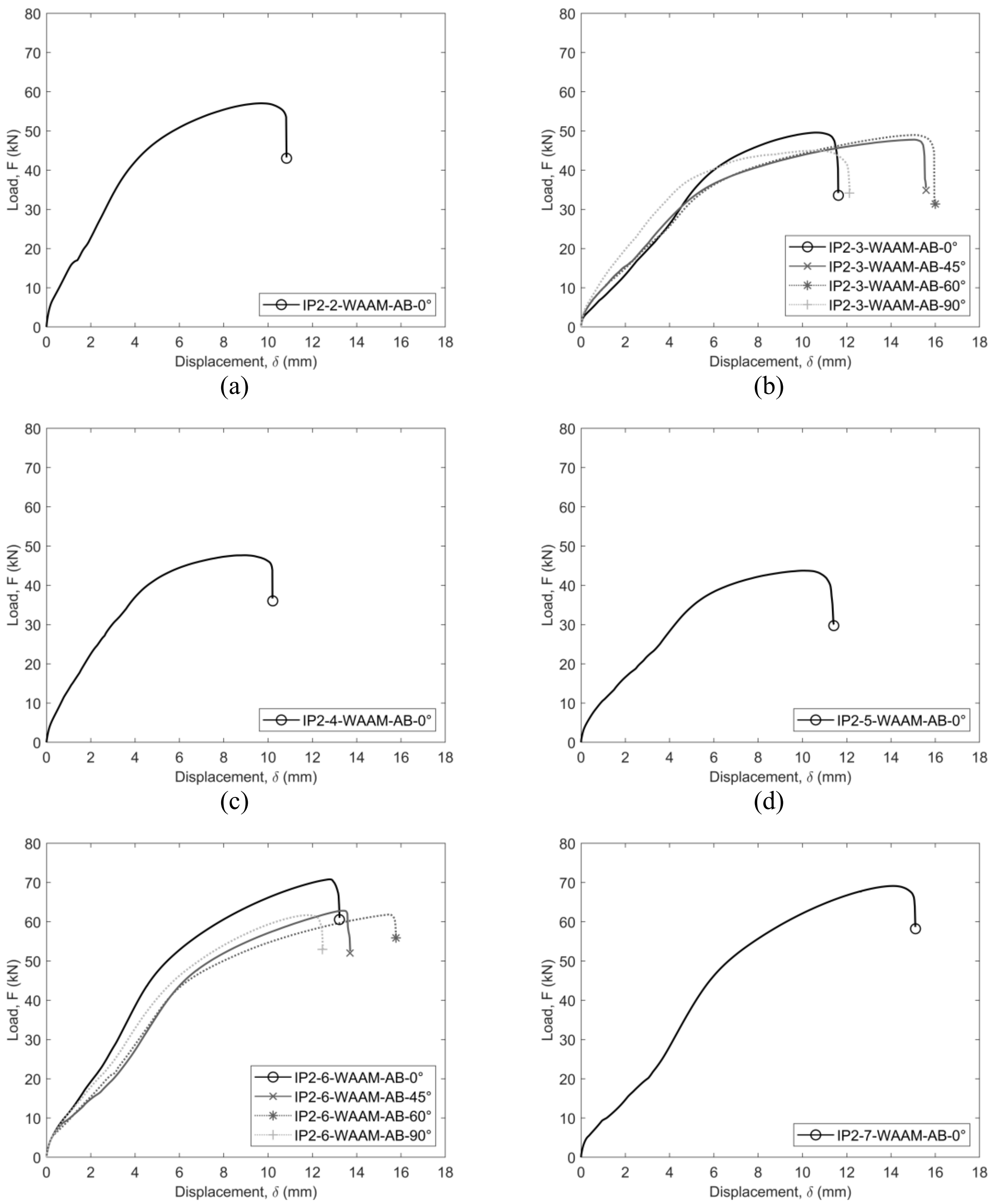

Figure 4.6: Load-displacement curves for double-bolt WAAM-AB configurations with non-uniform t and larger d_o.

4.4 Evaluation of design estimations

4.4.1 General

This section presents the equations used to estimate the design loads of double-lap shear bolted connections, as provided by the most commonly adopted design standards: BS EN 1993-1-8 [1], BS EN 1993-1-4 [2], and ANSI/AISC 370 [4], hereafter referred to as EC3-1-8, EC3-1-4, and AISC370 respectively. In addition to these standards, literature-based equations (LBE) specifically developed for AM bolted connections are also considered. All equations are applied using a strength-based criterion without the inclusion of partial safety factors, enabling direct comparison with the experimental failure loads of CON and AM plates under controlled test conditions.

4.4.2 EC3-1-8

The European standard EC3-1-8 [1], which is specified for carbon steel bolted connections, defines the design bearing resistance, $F_{b,EC3}$ to be calculated using Equation (4.1):

$$F_{b,EC3} = n_b k_m a_b f_u d t \tag{4.1}$$

Where, n_b is the number of bolts, k_m is a factor depends on the steel grade of the plate, f_u is the nominal material ultimate tensile strength of the plate, and a_b is taken as the minimum of three values; e_1/d_o (associated with edge bearing), $3 \times f_{ub}/f_u$ (associated with bolt bearing) and 3 (calibration limit). The notation f_{ub} is the nominal ultimate tensile strength of the bolt. The smallest of these values reflects the governing bearing mode in the connection.

For calculating the design net-section tension resistance, EN 1993-1-8 [1] refers to Equations (4.2), (4.3), (4.4), (4.5), and (4.6):

$$F_{t,Rd} = min[F_{pl,EC3}; F_{n,EC3}] \tag{4.2}$$

$$F_{pl,EC3} = A_g f_y \tag{4.3}$$

$$F_{n,EC3} = k A_{net} f_u \tag{4.4}$$

$$A_{net} = A_g - \Delta A_{net} \tag{4.5}$$

$$\Delta A_{net} = n_b d_o t \tag{4.6}$$

As shown in Equation (4.2), the design net-section tension resistance, $F_{t,EC3}$ of the plate is the minimum value of two; the design plastic resistance of the gross cross-section, $F_{pl,EC3}$ or the design ultimate resistance of the net cross-section, $F_{n,EC3}$. Equation (4.3) is used to calculate $F_{pl,EC3}$, where A_g is the cross-sectional area of the plate and f_y is the nominal yield strength of the inner plate material. To calculate $F_{u,EC3}$, Equation (4.4) is applied, considering that k is a value depends on the hole fabrication method, and A_{net} is the net cross-sectional area. A_{net} is obtained using Equation (4.5) where, ΔA_{net} represents the section area deducted due to the presence of hole/s. The value of ΔA_{net} can be directly calculated by using Equation (4.6).

The EN 1993-1-8 standard [1] further recommends applying Equation (4.7) to estimate the design block shear resistance, $F_{eff,EC3}$ for plates with two or more bolts.

$$F_{eff,EC3} = (A_{nt} f_u) + min\left[\frac{A_{gv} f_y}{\sqrt{3}}; \frac{A_{nv} f_u}{\sqrt{3}}\right] \tag{4.7}$$

The terms A_{nt}, A_{gv}, and A_{nv} refer to the net area subjected to tension, the gross area subjected to shear, and the net area subjected to shear, respectively.

4.4.3 EC3-1-4

EC3-1-4 [2] refers to EC3-1-8 [1] for the general design of bolted connections, including lap-shear configurations. That said, there is an adjustment to the bearing resistance equation, as EC3-1-4 [2] introduces specific provisions for stainless steel. The bearing resistance for stainless steel, $F_{b,EC3*}$ is determined using Equation (4.8) with specific considerations defined in EC3-1-4 [2].

$$F_{b,EC3*} = n_b a_b k_1 f_u dt \tag{4.8}$$

The notation a_b represents the bearing coefficient in the direction of the load transfer, while k_1 is the bearing coefficient in the direction perpendicular to the load transfer. The values of k_1 and a_b for edge bolts are calculated depending on the thickness of the plate and the chosen failure criterion. Since these tests aim to estimate failure at the ultimate state, the strength criterion is selected, and its corresponding a_b and k_1 values are calculated using equations (4.9) and (4.10). The lowest value of a_b is the value associated with the bearing type that occurs in the connections.

$$a_b = min\left[2.5; \frac{5e_1}{6d_o}\right] \tag{4.9}$$

$$k_1 = \begin{cases} 1 & if\ min\left[\frac{e_2}{d_o}; \frac{p}{2d_o}\right] > 1.5 \\ 0.8 & if\ min\left[\frac{e_2}{d_o}; \frac{p}{2d_o}\right] \leq 1.5 \end{cases} \tag{4.10}$$

4.4.4 AISC 370

The American standard AISC 370 [4] serves as the reference standard for the design of stainless steel bolted connections. Similar to EC3-1-8 [1] and EC3-1-4 [2], it provides a series of equations to estimate the failure capacity of shear bolted connections, but with different coefficient values depending on the adopted design criterion. The bearing resistance, $F_{b,AISC370}$ is determined using Equation (4.11), where the coefficient C_b is taken as 2.5 for $l_2/d_o > 1.5$ or 2 for $l_2/d_o \leq 1.5$. Here, the parameter l_2 is the distance from the centre of the hole to the centre of the adjacent hole or the edge of the plate perpendicular to the direction of the applied load.

$$F_{b,AISC370} = n_b C_b f_u dt \tag{4.11}$$

Equation (4.12) defines the net-section tension design resistance, $F_{t,AISC370}$. It follows the same formulation as that in EC3-1-8 [1] with slight modification, as it does not account for the effect of the fabrication method. The values of $N_{pl,AISC370}$ and $N_{n,AISC370}$ are calculated using Equations (4.13), and (4.14), respectively.

$$F_{t,AISC370} = min[F_{pl,AISC370}; F_{n,AISC370}] \tag{4.12}$$

$$F_{pl,AISC370} = A_g f_y \tag{4.13}$$

$$F_{n,AISC370} = A_{net} f_u \tag{4.14}$$

For the design resistance against block tearing, $F_{eff,AISC370}$, Equation (4.15) shows that AISC 370 [4] adopts the same formulation as EC3-1-8 [1], except for a constant factor, which is 0.6 in AISC 370 [4], resulting in a slight variation in the estimated capacity.

$$F_{eff,AISC370} = \left[(A_{nt} f_u) + min(0.6 A_{gv} f_y; 0.6 A_{nv} f_u)\right] \tag{4.15}$$

Unlike EC3-1-8 [1] and EC3-1-4 [2], AISC370 [4] provides an explicit equation to estimate the design capacity estimation for shear-out failure, $F_{so,AISC370}$ given in Equation (4.16). The coefficients (C_t) and (C_h) are 2.5 and 3, respectively under the strength criterion. The parameter l_1 refers to the distance from the centre of the hole to the centre of the adjacent hole or the edge of the plate parallel to the force.

$$F_{so,AISC370} = n_b C_t f_u dt \left(\frac{l_1}{C_h d_o}\right) \tag{4.16}$$

4.4.5 Literature-Based Equations (LBE)

The previously mentioned study [32], which investigated 316L stainless steel double-lap shear bolted connections, demonstrated that applying the shear-out and bearing resistance equations originally formulated by [70] and [71], respectively, yielded more accurate estimations than those obtained from codified design equations, with a reported mean estimation ratio of 1.06 and a coefficient of variation (COV) of 0.088. Subsequent work [72] introduced a modification to the shear-out equation to account for the bolt diameter, which was further refined by [28] to incorporate the effects of WAAM-produced carbon steel plates. Accordingly, the shear-out equation adopted in this study is that of [28], presented in equation (4.17). The term l_{av}

representing the length of active shear-out, is calculated using Equation (4.18), where l_c is the distance from the hole edge to the plate edge. The bearing resistance equation used remains that of [71], shown in equation (4.19). The LBE final load estimations, denoted as F_{LBE}, were used for all specimens except those designed with variations in geometric parameters e_2 and p , as the equations do not account for these changes [28,71].

$$F_{s,Guo} = 1.2 n_b l_{av} t f_u \left(\frac{3d}{e_1}\right)^{0.1} \tag{4.17}$$

$$l_{av} = l_c + \frac{d_o}{4} \tag{4.18}$$

$$F_{b,Teh\&Uz} = 3.5 n_b d t f_u \tag{4.19}$$

The aforementioned equations were specifically selected due to their refined formulations, enhancing the accuracy of estimating the failure mechanisms for WAAM-produced plates. Moreover, the selected equations are considered potentially suitable for estimating failures in SLM-produced specimens.

4.5 Results and discussion

The design provisions [1,2,4] and LBE [28,71] estimations for single-bolted configurations are summarised in Table 4.4 and Table 4.5, noting that inner plates governed by NST failures were excluded from these LBE estimations, since the equations are not defined for this mode. Figure 4.7a,c compares the experimental-to-estimated failure load ratios for CON and AM plates in the single-bolted configuration, showing a reduced variability of the ratios for CON plates. The most conservative results were from standards specifically tailored to stainless steel, with peak ratios of experimental-to-estimated failure loads reaching 1.85 in EC3-1-4 [2] and 1.78 under AISC 370 [4], indicating a pronounced tendency toward overdesign. Conversely, EC3-1-8 [1] provided more accurate estimations. This may reflect the more generalised nature of the bearing resistance equation adopted from EC3-1-8 [1], which, despite being developed for carbon steel, appears to align more closely with the load-bearing response of the AM plates. The LBE [28,71] estimations, primarily governed by SO failures, yielded the most accurate results, as clearly illustrated in Figure 4.7c. The mean ratio of experimental-to-estimated failure loads obtained from LBE estimations for AM plates was 1.10, accompanied by a low coefficient of variation (COV) of 0.087. This finding aligns closely with the observations reported in [32]. In contrast, AISC 370 [4] showed the highest mean ratio and variability, with values of 1.43 and

0.178, respectively. Furthermore, most observed failures involved a governing SO failure, which in EC3-1-8 [1] and EC3-1-4 [2], is accounted for under the bearing resistance check, where capacity decreases with reducing e_1 and therefore their estimations correspond to EB, whereas AISC 370 [4] includes an explicit shear-out resistance equation. As shown in Figure 4.8, the distinction between EB and SO can be illustrated using the e_1/d_o<3 condition derived from the definition of a_b in [28], which interpreted SO in EC3-1-8 [1] as being covered by the bearing resistance check. However, since stainless steel ductility makes the plate tend to have a mix of both failures, this approach provides a clarification on whether SO will occur to plates after the initial EB failure. This is why it was mentioned earlier that the failure is EB+SO with SO governing.

For double-bolted configurations, Table 4.6 and Table 4.7 present the corresponding design provisions [1,2,4] and LBE [28,71] estimations. Similar to the single-bolted configurations, specimens governed by NST failures were excluded from the LBE [28,71] estimations. Given the complexity introduced by the interaction of two bolt holes, significant variability was noted in the ratios for EC3-1-4 [2] and AISC 370 [4], with mean ratios of 1.65 and 1.39 and respective COV values of 0.234 and 0.201 (Figure 4.7d). The design standard EC3-1-8 [1] exhibited lower mean ratios (1.33) and reduced variability (COV = 0.160) compared to EC3-1-4 [2] yet still demonstrated considerable conservatism. The LBE [28,71] estimations again proved the most accurate, yielding a mean ratio of 1.12. However, the higher COV of 0.150 reflects a modest reduction in consistency compared to the single-bolted results. For CON plates, the corresponding double-bolt configuration results (Figure 4.7b) show improved agreement and lower scatter relative to AM plates, although EC3-1-4 [2] still leads to pronounced conservatism. The associated failure modes of the double-bolted configurations were not consistently captured by the design standards [1,2,4] or the LBE [28,71], with several cases showing clear discrepancies between predicted and observed modes. In particular, EC3-1-4 [2] predominantly predicted EB, while the governing failures were SO, NST, and BT. Since the LBE [28,71] equations are defined only for SO and EB, all cases of BT were predicted as SO.

Collectively, these results highlight the significant conservatism inherent in current stainless steel-specific design provisions when applied to WAAM and SLM-produced plates in bolted connections, while their application to CON plates remains generally reliable and conservative. The consistent accuracy and lower variability of the LBE [28,71] estimations suggest that these equations, explicitly formulated for AM, are more suitable than traditional, generalised stainless steel guidelines. This implies that current design codes may require calibration or the introduction of appropriate adjustment factors to adequately capture the unique mechanical response of WAAM and SLM fabricated components, achievable through further experimental and numerical research on AM bolted connections.

Table 4.4: Comparison between experimental results and design provision estimations [1,2,4] for the failure mechanisms of single-bolt configurations.

Designation	Experimental ultimate load, F_{Exp} (kN)	Governing failure mode	Design resistance to EC3-1-8, $F_{EC3-1-8}$ (kN)	Ratio to EC3-1-8, $\frac{F_{Exp}}{F_{EC3-1-8}}$	Failure mode (EC3-1-8)	Design resistance to EC3-1-4, $F_{EC3-1-4}$ (kN)	Ratio to EC3-1-4, $\frac{F_{Exp}}{F_{EC3-1-4}}$	Failure mode (EC3-1-4)	Design resistance to AISC370, $F_{AISC370}$ (kN)	Ratio to AISC370, $\frac{F_{Exp}}{F_{AISC370}}$	Failure mode (AISC370)
IP1-1-CON	18.8	SO	17.0	1.11	EB	14.1	1.33	EB	14.1	1.33	SO
IP1-1-WAAM-M-0°	18.4	SO	13.3	1.38	EB	11.1	1.66	EB	11.1	1.66	SO
IP1-1-WAAM-M-45°	19.2	SO	14.1	1.36	EB	11.7	1.64	EB	11.7	1.64	SO
IP1-1-WAAM-M-60°	18.5	SO	13.5	1.37	EB	11.2	1.65	EB	11.2	1.65	SO
IP1-1-WAAM-M-90°	17.8	SO	14.3	1.24	EB	11.9	1.50	EB	11.9	1.50	SO
IP1-1-WAAM-AB-0°	44.3	SO	35.5	1.25	EB	29.6	1.50	EB	29.6	1.50	SO
IP1-1-SLM-M-0°	18.5	SO	16.0	1.16	EB	13.3	1.39	EB	13.3	1.39	SO
IP1-1-SLM-AB-0°	18.7	SO	16.0	1.17	EB	13.3	1.41	EB	13.3	1.41	SO
IP1-2-CON	18.1	SO	15.8	1.15	EB	13.1	1.38	EB	13.1	1.38	SO
IP1-2-WAAM-M-0°	16.9	SO	12.3	1.37	EB	10.3	1.64	EB	10.3	1.64	SO
IP1-2-WAAM-M-45°	19.0	SO	13.0	1.46	EB	10.9	1.74	EB	10.9	1.74	SO
IP1-2-WAAM-M-60°	18.1	SO	12.5	1.45	EB	10.4	1.74	EB	10.4	1.74	SO
IP1-2-WAAM-M-90°	16.2	SO	13.3	1.22	EB	11.1	1.46	EB	11.1	1.46	SO
IP1-2-WAAM-AB-0°	40.8	SO	33.0	1.24	EB	27.5	1.48	EB	27.5	1.48	SO
IP1-2-WAAM-AB-45°	41.6	SO	35.7	1.17	EB	29.7	1.40	EB	29.7	1.40	SO
IP1-2-WAAM-AB-60°	38.0	SO	36.4	1.04	EB	30.4	1.25	EB	30.4	1.25	SO
IP1-2-WAAM-AB-90°	41.6	SO	31.7	1.31	EB	26.4	1.58	EB	26.4	1.58	SO
IP1-2-SLM-AB-0°	18.3	SO	14.8	1.24	EB	12.4	1.48	EB	12.4	1.48	SO
IP1-2-SLM-AB-45°	18.7	SO	13.3	1.41	EB	11.1	1.68	EB	11.1	1.68	SO
IP1-2-SLM-AB-90°	17.5	SO	13.1	1.34	EB	10.9	1.61	EB	10.9	1.61	SO
IP1-3-CON	15.7	SO	13.3	1.18	EB	11.1	1.41	EB	11.1	1.41	SO
IP1-3-WAAM-M-0°	15.0	SO	10.4	1.44	EB	8.7	1.72	EB	8.7	1.72	SO
IP1-3-WAAM-AB-0°	33.6	SO	27.4	1.23	EB	18.2	1.85	EB	22.8	1.47	SO
IP1-4-CON	11.3	SO	9.7	1.16	EB	8.1	1.40	EB	8.1	1.40	SO
IP1-4-WAAM-M-0°	11.2	SO	7.6	1.47	EB	6.3	1.78	EB	6.3	1.78	SO
IP1-4-WAAM-AB-0°	23.8	SO	20.3	1.17	EB	13.5	1.76	EB	16.6	1.43	SO
IP1-5-CON	12.0	NST	12.5	0.96	NST	12.5	0.96	NST	12.5	0.96	NST
IP1-5-WAAM-AB-0°	22.6	NST	19.5	1.16	NST	19.5	1.16	NST	19.5	1.16	NST
IP1-5-WAAM-AB-45°	23.9	NST	22.3	1.07	NST	22.3	1.07	NST	22.3	1.07	NST
IP1-5-WAAM-AB-60°	20.5	NST	22.8	0.90	NST	22.8	0.90	NST	22.8	0.90	NST

Table 4.4: Comparison between experimental results and design provision estimations [1,2,4] for the failure mechanisms of single-bolt configurations (continued).

Designation	Experimental ultimate load, F_{Exp} (kN)	Governing failure mode	Design resistance to EC3-1-8, $F_{EC3-1-8}$ (kN)	Ratio to EC3-1-8, $\frac{F_{Exp}}{F_{EC3-1-8}}$	Failure mode (EC3-1-8)	Design resistance to EC3-1-4, $F_{EC3-1-4}$ (kN)	Ratio to EC3-1-4, $\frac{F_{Exp}}{F_{EC3-1-4}}$	Failure mode (EC3-1-4)	Design resistance to AISC370, $F_{AISC370}$ (kN)	Ratio to AISC370, $\frac{F_{Exp}}{F_{AISC370}}$	Failure mode (AISC370)
IP1-5-WAAM-AB-90°	23.0	NST	19.9	1.16	NST	19.9	1.16	NST	19.9	1.16	NST
IP1-5-SLM-AB-0°	11.6	NST	11.8	0.98	NST	11.8	0.98	NST	11.8	0.98	NST
IP1-5-SLM-AB-45°	11.1	NST	10.6	1.05	NST	10.6	1.05	NST	10.6	1.05	NST
IP1-5-SLM-AB-90°	10.7	NST	10.4	1.03	NST	10.4	1.03	NST	10.4	1.03	NST

Table 4.5: Estimated failure mechanisms and load capacity ratios for single-bolt configurations using LBE [28,71].

Designation	Design resistance to LBE, F_{LBE} (kN)	Ratio to LBE, $\frac{F_{Exp}}{F_{LBE}}$	Failure mode (F_{LBE})
IP1-1-CON	20.3	0.93	SO
IP1-1-WAAM-M-0°	15.8	1.16	SO
IP1-1-WAAM-M-45°	16.8	1.14	SO
IP1-1-WAAM-M-60°	16.1	1.15	SO
IP1-1-WAAM-M-90°	17.1	1.04	SO
IP1-1-WAAM-AB-0°	40.1	1.10	SO
IP1-1-SLM-M-0°	19.1	0.97	SO
IP1-1-SLM-AB-0°	19.1	0.98	SO
IP1-2-CON	18.8	0.96	SO
IP1-2-WAAM-M-0°	14.7	1.15	SO
IP1-2-WAAM-M-45°	15.5	1.23	SO
IP1-2-WAAM-M-60°	14.9	1.21	SO
IP1-2-WAAM-M-90°	15.8	1.03	SO
IP1-2-WAAM-AB-0°	37.0	1.10	SO
IP1-2-WAAM-AB-45°	40.1	1.04	SO
IP1-2-WAAM-AB-60°	40.9	0.93	SO
IP1-2-WAAM-AB-90°	35.7	1.17	SO
IP1-2-SLM-AB-0°	17.6	1.04	SO
IP1-2-SLM-AB-45°	15.8	1.18	SO
IP1-2-SLM-AB-90°	15.6	1.12	SO
IP1-3-CON	15.7	1.00	SO
IP1-3-WAAM-M-0°	12.3	1.22	SO
IP1-3-WAAM-AB-0°	30.2	1.11	SO
IP1-4-CON	11.0	1.03	SO
IP1-4-WAAM-M-0°	8.6	1.30	SO
IP1-4-WAAM-AB-0°	21.0	1.13	SO

Table 4.6: Comparison between experimental results and design provision estimations [1,2,4] for the failure mechanisms of double-bolt configurations.

Designation	Experimental ultimate load, F_{Exp} (kN)	Governing failure mode	Design resistance to EC3-1-8, $F_{EC3-1-8}$ (kN)	Ratio to EC3-1-8, $\frac{F_{Exp}}{F_{EC3-1-8}}$	Failure mode (EC3-1-8)	Design resistance to EC3-1-4, $F_{EC3-1-4}$ (kN)	Ratio to EC3-1-4, $\frac{F_{Exp}}{F_{EC3-1-4}}$	Failure mode (EC3-1-4)	Design resistance to AISC370, $F_{AISC370}$ (kN)	Ratio to AISC370, $\frac{F_{Exp}}{F_{AISC370}}$	Failure mode (AISC370)
IP2-1-CON	27.3	BT*	25.9	1.05	BT	19.4	1.41	EB	24.3	1.12	SO
IP2-1-WAAM-M-0°	26.3	BT*	17.8	1.48	BT	15.2	1.73	EB	18.1	1.45	BT
IP2-1-WAAM-M-45°	27.4	BT*	19.4	1.41	BT	16.1	1.70	EB	19.7	1.39	BT
IP2-1-WAAM-M-60°	26.8	BT*	18.2	1.47	BT	15.4	1.74	EB	18.5	1.45	BT
IP2-1-WAAM-M-90°	25.3	BT*	18.4	1.38	BT	16.3	1.55	EB	18.7	1.35	BT
IP2-2-CON	26.6	BT	24.4	1.09	BT	17.8	1.49	EB	22.2	1.20	SO
IP2-2-WAAM-M-0°	27.3	BT	17.1	1.60	BT	13.9	1.96	EB	17.4	1.57	SO+BT
IP2-2-WAAM-AB-0°	57.0	BT	40.0	1.43	BT	37.9	1.50	EB	42.6	1.34	BT
IP2-3-CON	23.1	SO	19.9	1.16	EB	13.3	1.74	EB	16.6	1.39	SO
IP2-3-WAAM-M-0°	23.8	SO	15.2	1.57	BT	10.4	2.29	EB	12.9	1.84	SO
IP2-3-WAAM-M-45°	24.4	BT	16.5	1.48	EB+BT	11.0	2.22	EB	13.7	1.78	SO
IP2-3-WAAM-M-60°	23.3	BT	15.6	1.49	BT	10.5	2.22	EB	13.2	1.77	SO
IP2-3-WAAM-M-90°	21.6	BT	15.9	1.36	BT	11.2	1.93	EB	12.3	1.76	SO
IP2-3-WAAM-AB-0°	49.5	BT	33.7	1.47	BT	28.7	1.72	EB	34.2	1.45	BT
IP2-3-WAAM-AB-45°	47.7	BT	34.6	1.38	BT	29.9	1.60	EB	35.1	1.36	BT
IP2-3-WAAM-AB-60°	48.9	SO	38	1.29	BT	30.4	1.61	EB	38.6	1.27	BT
IP2-3-WAAM-AB-90°	44.9	BT	31.9	1.41	BT	27.2	1.65	EB	32.4	1.39	BT
IP2-4-CON	23.0	BT	19.4	1.19	EB	12.9	1.78	EB	16.2	1.42	SO
IP2-4-WAAM-M-0°	23.1	SO	15.1	1.53	BT	10.1	2.29	EB	12.6	1.83	SO
IP2-4-WAAM-AB-0°	47.6	BT	29.6	1.61	BT	25.0	1.90	EB	30.0	1.59	BT
IP2-5-CON	21.1	SO	17.0	1.24	EB	11.3	1.87	EB	14.1	1.50	SO
IP2-5-WAAM-M-0°	20.7	SO	13.3	1.56	EB	8.8	2.35	EB	11.1	1.86	SO
IP2-5-WAAM-AB-0°	43.7	SO	28.3	1.54	BT	23.2	1.88	EB	28.6	1.53	BT
IP2-6-CON	30.4	NST*	35.8	0.85	NST	25.9	1.17	EB	32.0	0.95	EB
IP2-6-WAAM-AB-0°	70.8	NST*	60.0	1.18	NST	54.1	1.31	EB	60.0	1.18	NST
IP2-6-WAAM-AB-45°	62.8	NST*	56.4	1.11	NST	55.3	1.14	EB	56.4	1.11	NST
IP2-6-WAAM-AB-60°	61.8	NST*	68.4	0.90	NST	60.9	1.01	EB	68.5	0.90	NST
IP2-6-WAAM-AB-90°	61.7	NST*	54.6	1.13	NST	50.1	1.23	EB	54.6	1.13	NST
IP2-6-SLM-AB-0°	31.1	NST*	33.6	0.93	NST	24.3	1.28	EB	30.1	1.03	EB
IP2-6-SLM-AB-45°	31.6	NST*	30.1	1.05	NST	21.8	1.45	EB	27.0	1.17	EB

Table 4.6: Comparison between experimental results and design provision estimations [1,2,4] for the failure mechanisms of double-bolt configurations (continued).

Designation	Experimental ultimate load, F_{Exp} (kN)	Governing failure mode	Design resistance to EC3-1-8, $F_{EC3-1-8}$ (kN)	Ratio to EC3-1-8, $\frac{F_{Exp}}{F_{EC3-1-8}}$	Failure mode (EC3-1-8)	Design resistance to EC3-1-4, $F_{EC3-1-4}$ (kN)	Ratio to EC3-1-4, $\frac{F_{Exp}}{F_{EC3-1-4}}$	Failure mode (EC3-1-4)	Design resistance to AISC370, $F_{AISC370}$ (kN)	Ratio to AISC370, $\frac{F_{Exp}}{F_{AISC370}}$	Failure mode (AISC370)
IP2-6-SLM-AB-90°	30.6	NST*	29.7	1.03	NST	21.5	1.42	EB	26.6	1.15	EB
IP2-7-CON	32.1	BT*	32.1	1.00	BT	30.3	1.06	EB	30.3	1.06	SO
IP2-7-WAAM-M-0°	31.4	BT*	21.9	1.43	BT	21.9	1.43	BT	22.2	1.41	BT
IP2-7-WAAM-AB-0°	69.1	NST	51.6	1.34	BT	51.6	1.34	BT	52.6	1.31	BT
IP2-7-SLM-M-0°	31.7	BT*	31.2	1.02	BT	28.5	1.11	EB	31.9	0.99	BT
IP2-7-SLM-AB-0°	33.5	BT*	31.2	1.07	BT	28.5	1.18	EB	31.9	1.05	BT

BT* = Partial block tearing; NST* = Partial net-section tension.

Table 4.7: Estimated failure mechanisms and load capacity ratios for double-bolt configurations using LBE [28,71].

Designation	Design resistance to LBE, F_{LBE} (kN)	Ratio to LBE, $\frac{F_{Exp}}{F_{LBE}}$	Failure mode (F_{LBE})
IP2-1-CON	34.5	0.79	SO
IP2-1-WAAM-M-0°	27.0	0.97	SO
IP2-1-WAAM-M-45°	28.6	0.96	SO
IP2-1-WAAM-M-60°	27.4	0.98	SO
IP2-1-WAAM-M-90°	29.1	0.87	SO
IP2-2-CON	31.4	0.85	SO
IP2-2-WAAM-M-0°	24.6	1.11	SO
IP2-2-WAAM-AB-0°	62.6	0.91	SO
IP2-3-CON	22.7	1.02	SO
IP2-3-WAAM-M-0°	17.7	1.34	SO
IP2-3-WAAM-M-45°	18.8	1.30	SO
IP2-3-WAAM-M-60°	18.0	1.29	SO
IP2-3-WAAM-M-90°	19.1	1.13	SO
IP2-3-WAAM-AB-0°	45.0	1.10	SO
IP2-3-WAAM-AB-45°	46.1	1.03	SO
IP2-3-WAAM-AB-60°	50.7	0.96	SO
IP2-3-WAAM-AB-90°	42.6	1.05	SO
IP2-4-CON	22.0	1.05	SO
IP2-4-WAAM-M-0°	17.2	1.34	SO
IP2-4-WAAM-AB-0°	39.0	1.22	SO
IP2-5-CON	18.8	1.12	SO
IP2-5-WAAM-M-0°	14.7	1.41	SO
IP2-5-WAAM-AB-0°	34.8	1.26	SO

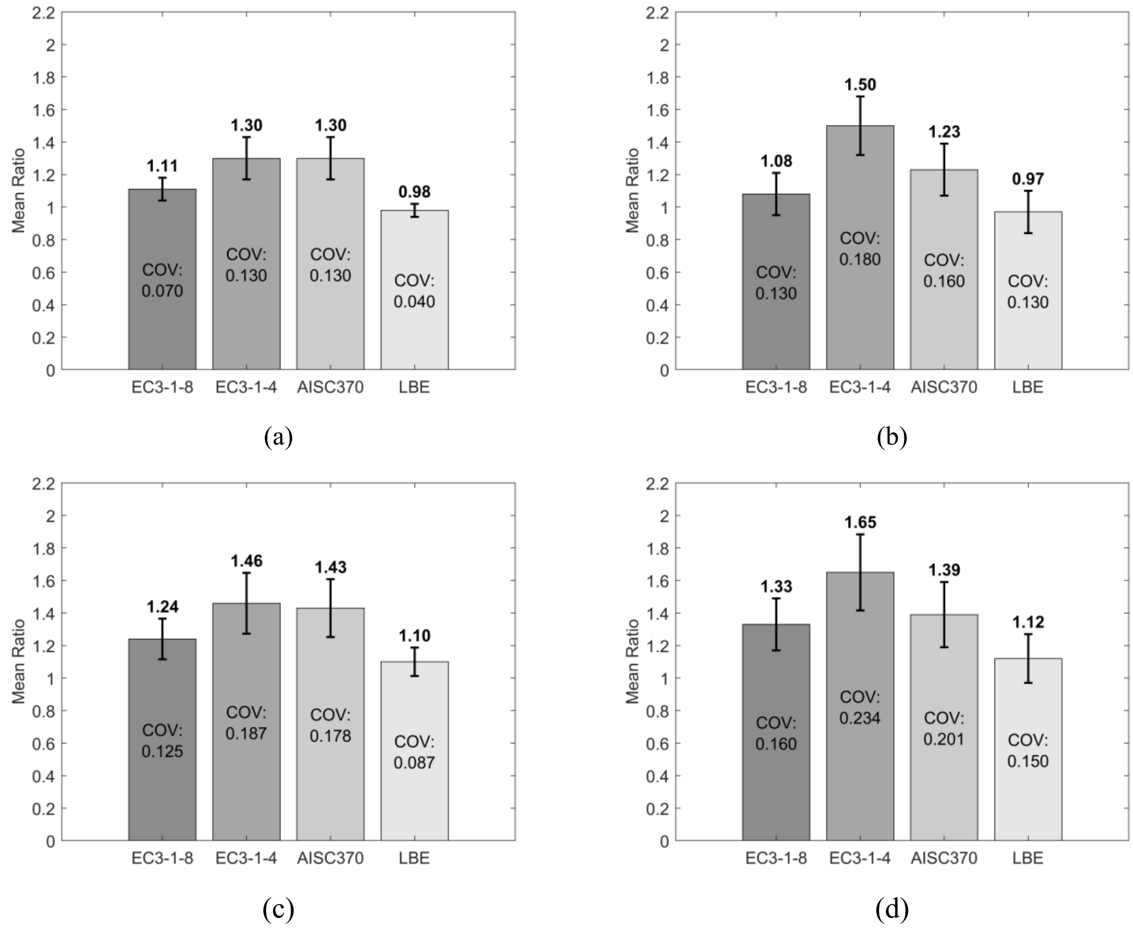

Figure 4.7: Comparison of design provisions [1,2,4] and LBE [28,71] estimations against experimental load capacity plates: mean ratios and COV of CON plates in (a) single-bolt and (b) double-bolt configurations, and for AM plates in (c) single-bolt and (d) double-bolt configurations.

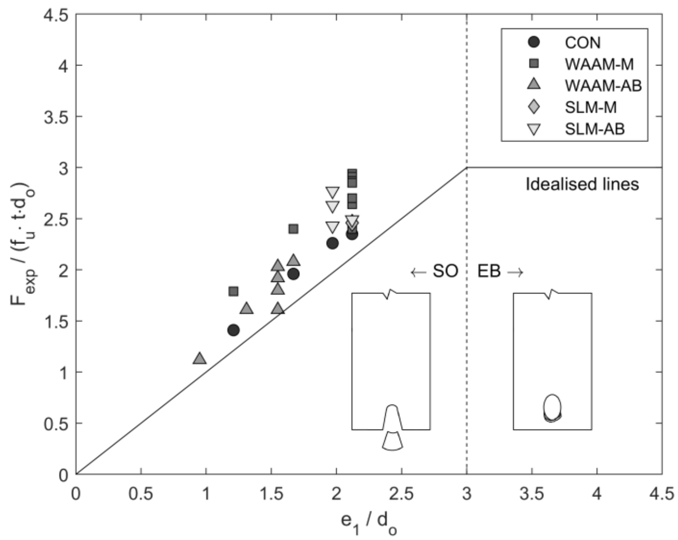

Figure 4.8: Indirect interpretation of EC3-1-8 [1] showing the threshold between EB and SO governing failures for single-bolted configurations connection results, using the condition e_1/d_o<3 as derived from the definition of a_b in [28].

4.6 Conclusions

The global load-displacement comparisons between CON and AM plates, together with the evaluation of load capacities against design provisions and LBE estimations for hybrid double-lap shear connections, led to the following conclusions:

a) Bolted connections with integrated AM inner plates exhibited lower displacement at failure compared to CON plates, indicating noticeably reduced ductility and elongation capacity across both single- and double-bolt configurations, despite no significant differences in load capacity. Therefore, special attention should be given to the design of connections to ensure a ductile and thus safe, structural response.

b) The diagonal extraction orientation clearly enhanced ductility in both WAAM-M and WAAM-AB plates, demonstrating its beneficial effect.

c) Design codes tailored to stainless steel, such as EC3-1-4 [2] and AISC 370 [4], were overly conservative, especially in AM applications, with high experimental-to-estimated failure loads mean ratios and COVs, suggesting potential for overdesign and inefficiency.

d) EC3-1-8 [1], although developed for carbon steel, performed better for AM plates due to its more generalised formulation, specifically in the bearing resistance equation, producing closer estimations with reduced variability in both single- and double-bolt configurations.
e) For CON plates, the assessed design standards generally provided conservative estimations, with ratios closer to unity and lower variability than those for AM plates.
f) LBE [28,71] consistently outperformed code provisions, showing the lowest deviation from experimental results and offering more accurate load capacity estimations.
g) Current design standards inadequately estimate the failure mechanisms in AM plates, underlining the need for updated equations or modification factors based on experimental and numerical data tailored to WAAM and SLM plates' specific behaviour.

Chapter 5. The Theory of Critical Distances for Predicting the Static Failure of Double-Lap Bolted Joints with Conventional and Additively Manufactured 316L Stainless Steel Inner Plates

Forward Commentary

This article, titled "The Theory of Critical Distances for Predicting the Static Failure of Double-Lap Bolted Joints With Conventional and Additively Manufactured 316L Stainless Steel Inner Plates", was published in *Fatigue & Fracture of Engineering Materials & Structures* on 01 July 2026 [73]. The article evaluates the accuracy of the Theory of Critical Distances, applied in the form of the Point Method, in predicting the static strength of double-lap shear bolted connections with conventional and additively manufactured 316L stainless steel inner plates. Hasan Almuhanna conducted the overall work, including formal analysis, and writing of the manuscript. The methodology was developed jointly by Hasan Almuhanna and Professor Luca Susmel. Professor Luca Susmel also contributed through conceptualisation, supervision, critical review, and input to the drafting of the manuscript. Dr Giacomo Torelli contributed through supervision and critical review of the manuscript.

Abstract

This study assesses the accuracy of the Theory of Critical Distances applied in the form of the Point Method in predicting the static strength of 316L stainless steel double-lap shear bolted connections under static tensile loading. Single- and double-bolt configurations were tested using inner plates manufactured from conventional material and from additively manufactured material, namely wire arc additive manufacturing and selective laser melting. The additively manufactured plates were assessed in both machined and as-built conditions and extracted at different printing orientations. Treating the bolt hole as a stress concentrator, linear elastic finite element stress fields were post-processed to determine the Point Method effective stress from stress-distance curves

extracted along different paths relative to the loading direction. The Point Method, calibrated using an inherent stress and a characteristic length estimated from 2 mm thick conventional notched plates, provided generally good predictions for both conventional and additively manufactured plates. However, the prediction accuracy decreased for thicker as-built wire arc additively manufactured plates. Recalibrating the Point Method using wire arc additive manufacturing notched specimens with a comparable mean thickness improved the predictions for the thicker wire arc additively manufactured plates; however, a non-conservative bias remained. These findings confirm that the Point Method parameters calibrated using plain and notched specimens can be transferred to bolted joint assemblies.

5.1 Introduction

The most common solutions for joining structural steel components are welding, bolts, and rivets. These typical connecting methods are robust in ensuring the overall reliability of structural assemblies. Nevertheless, the advantage of bolts over other solutions is that the structural parts connected by bolts can easily be disassembled and then reused. This further encouraged researchers in the field to investigate and utilise various innovative additive manufacturing (AM) techniques for the fabrication of bolted connections, leading to a growing body of research exploring their structural performance and potential applications [27,28,30–34,74]. In addition, these advances have opened new possibilities for optimising structural steel connections using AM technologies, allowing for tailored designs that were not feasible with conventional manufacturing approaches [75]. For example, topology-optimised wire arc additively manufactured (WAAM) bolted head plates [76] and optimised metal AM connections in lightweight steel framing [77] have been proposed, highlighting possible future applications involving complex connection geometries and improved stiffness and strength. A recent review has also identified metal AM, particularly wire arc additive manufacturing (WAAM), as a promising technology for steel construction, especially where large-scale automated fabrication, reduced material waste, and the production or strengthening of complex structural components are required [78]. However, wider adoption in structural steel applications remains limited by challenges associated with defects related to the manufacturing process, surface condition, residual stresses, anisotropic material behaviour, and the lack of structural design guidance [78]. In a previous work conducted by the authors [41], a comprehensive failure behaviour examination was carried out, starting with the assessment of conventionally produced (CON) 316L stainless steel inner plates as reference specimens. This was followed by testing inner plates produced through additive manufacturing, specifically using wire arc additive manufacturing (WAAM) and selective laser melting (SLM), in order to evaluate their potential as viable alternatives.

As far as design is concerned, evaluating the impact of various design variables on stress concentration and plate failure in bolted connections is crucial for ensuring structural integrity and durability. Traditionally, this evaluation has heavily relied on non-linear Finite Element (FE) models [79], which offer a detailed and accurate representation of complex stress distributions and failure mechanisms under different loading conditions. For instance, ductile fracture in bolted connections has been numerically simulated using non-linear FE analysis combined with a ductile fracture criterion and a damage evolution rule [80]. In contrast, the use of linear-elastic models, which simplify bolt holes as stress concentrators and treat bolted connections as notched components, has not yet been systematically explored. While linear-elastic models offer a computationally less demanding solution, they can nonetheless provide valuable insights into stress concentration phenomena, provided that the problem is addressed using a reliable methodology. To address this knowledge gap, the Theory of Critical Distances (TCD) was employed in this study to assess the static strength of double-lap shear bolted connections within a linear-elastic framework. The TCD is a set of approaches for predicting fracture at stress or strain concentrators of various types using a material-specific critical distance, and it provides a practical framework for evaluating strength and failure in engineering applications [35].

The TCD postulates that the static strength of notched and cracked components can be estimated by directly post-processing the stress fields near the stress raisers; under Mode I loading, the TCD states that fracture occurs when a critical distance-related effective stress, σ_{eff}, exceeds the material's inherent strength, σ_0 [81–87]. A distinctive feature of the TCD is that σ_{eff} can be evaluated using a linear-elastic constitutive law, thereby greatly simplifying the design problem. However, material-specific factors influence the relationship between σ_0 and the ultimate tensile strength, σ_{UTS}. For ductile materials with significant plastic deformation preceding final failure, σ_0 is typically higher than σ_{UTS} [82]. Brittle and quasi-brittle materials generally have σ_0 approaching σ_{UTS} [87].

There are four different ways to determine the effective stress according to the TCD, i.e. the Point Method (PM), Line Method, Area Method, and Volume Method [35]. To apply the TCD in the form of either the PM or the Line Method, the first step is to define the so-called focus path. The focus path is typically defined as a straight line emanating from the hot-spot (assumed to coincide with the crack initiation point) and aligned with the crack propagation direction, i.e. the direction experiencing the maximum damage extent [35].

Once the focus path has been defined, in the PM the critical stress is taken at a distance equal to $L/2$ from the hot-spot associated with the stress/strain concentrator under assessment, where L is the TCD material characteristic length (an experimentally determined material length scale). In contrast, the Line Method calculates σ_{eff} by averaging the stress along the focus path over a length equal to $2L$. Finally, the Area Method and the Volume Method calculate σ_{eff} by averaging the stress over a semicircular area (with radius $\approx 1.32L$) and a hemispherical volume (with radius $\approx 1.54L$), respectively [35].

In this study, the PM was selected because of its simplicity and suitability for ductile materials such as 316L stainless steel [86,88]. Following the shear tests, the PM was applied by post-processing the local linear-elastic FE stress fields obtained from numerical models replicating the bolted connection tests on CON inner plates. The stress-distance focus path for the PM was defined at the hole mid-thickness edge within the hot-spot region, centred on the experimentally observed crack-initiation location in the tested inner plates. To account for the observed variation in crack paths, stress-distance curves were extracted from the initiation point along three directions: perpendicular, diagonal, and parallel to the loading direction, and the PM predictions were evaluated for each path. Additionally, the path most closely aligned with the experimentally observed crack direction was identified and used for comparison.

The values of L and σ_0 were first calibrated from two notched specimens manufactured from the same material as the CON plates, following the standard procedure described in detail in Section 5.4.2. These material constants were then used in conjunction with the PM to post-process the FE models of the CON inner plates. The same L-σ_0 pairing was subsequently applied to the FE models of inner plates produced by WAAM and SLM to assess transferability across manufacturing methods. A further assessment was performed for the as-built WAAM (WAAM-AB) inner plates by calibrating an additional L-σ_0 pairing using WAAM notched specimens with a comparable mean thickness.

5.2 Reference experiments

This section presents the material properties, design and key results from an experimental program published in detail in [41]. The key goal of this initial experimental investigation was to perform a detailed failure analysis of bolted joints containing both conventional and AM plates. These results are then used in the following sections of the paper as a basis for assessment via TCD.

Prior to testing the bolted specimens, a series of coupon tests was conducted in accordance with ASTM E8/E8M [61], covering both CON specimens and AM specimens produced by WAAM and SLM. The coupons were tested in both machined and as-built conditions. For WAAM specimens, surface undulations and different extraction orientations were considered, whereas for SLM specimens, the effect of deposition direction was evaluated. The key mechanical properties of the tested materials, including elastic modulus, E, yield stress, $\sigma_{0.2}$, and ultimate tensile stress, σ_{UTS}, are summarised in Table 5.1. In the specimen designations, (M) refers to machined and (AB) indicates as-built. The reported angle specifies the orientation of the specimen relative to the deposition or extraction direction. It can be noted from Table 5.1 that some modulus of elasticity, E, values are relatively low. As discussed in detail in [41], the comparatively low E values measured for some AM specimens were mainly associated with manufacturing-related effects and specimen orientation.

Table 5.1: Mechanical properties from coupon tests [41].

Designation	Modulus of elasticity, E (Gpa)	Offset yield stress, $\sigma_{0.2}$ (MPa)	Ultimate stress, σ_{UTS} (Mpa)
CON	184	488	667
WAAM-M-0°	143	288	521
WAAM-M-45°	185	324	552
WAAM-M-60°	160	297	530
WAAM-M-90°	103	281	562
WAAM-AB-0°	124	278	493
WAAM-AB-45°	119	282	544
WAAM-AB-60°	139	323	566
WAAM-AB-90°	91	273	493
SLM-AB-0°	160	520	627
SLM-AB-45°	126	422	562
SLM-AB-90°	120	419	554

The experimental setup and procedures for the double-lap shear tests are described below. Each connection consisted of two 2 mm-thick inner test plates and two 4 mm-thick outer plates, assembled using fully threaded grade 10.9 M6 high-strength bolts. The bolt holes had a diameter of 6.6 mm to provide adequate clearance. The increased thickness of the outer plates was intended not only to withstand the applied loads, but also to minimise secondary bending during testing and ensure that failure occurred in the inner plates, which were the primary focus of the investigation. For the WAAM-AB plates, non-threaded grade 12.9 M8 bolts were used instead, with the hole size increased to 8.4 mm, and the outer plate thickness increased to 8 mm to accommodate the larger bolts and the increased mean thicknesses and surface undulations. For the SLM specimens, the designation M indicates that the rough surface was removed by machining, without altering the overall thickness. The test setup is illustrated in Figure 5.1, while the design details and the measured failure capacities for each configuration are summarised in Table 5.2 and Table 5.3 [41]. In these tables, the notation (IP) in the designation column refers to the inner plates: (IP1) indicates plates tested in the single-bolt configuration, whereas (IP2) denotes plates tested in the double-bolt configuration. The number that follows each designation identifies the specific specimen, corresponding to its unique set of geometrical variables. Similar to the coupons, additional identifiers specify the manufacturing method (CON, WAAM, or SLM) and, for AM plates, the deposition/extraction direction (e.g., 0°, 90°).

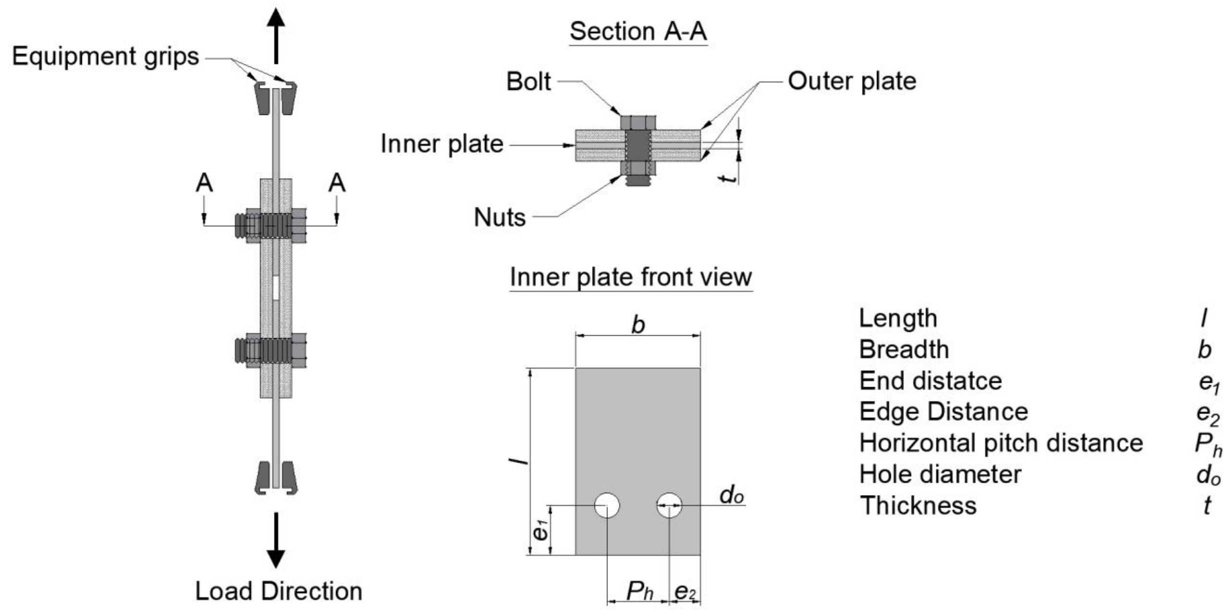

Figure 5.1: Test setup for double-lap shear bolted connections, illustrating the two-bolt configuration.

Table 5.2: Design details and ultimate load capacities of inner plates with single-bolt configuration [41].

Designation	Thickness, t (mm)	End distance, e_1 (mm)	Edge distance, e_2 (mm)	Breadth, b (mm)	Experimental ultimate load, F_{Exp} (Kn)
IP1-1-CON	2	14	15	30	18.8
IP1-2-CON	2	13	15	30	18.1
IP1-3-CON	2	11	15	30	15.7
IP1-4-CON	2	8	15	30	11.3
IP1-5-CON	2	15	8	16	12.0
IP1-1-WAAM-M-0°	2	14	15	30	18.4
IP1-1-WAAM-M-45°	2	14	15	30	19.2
IP1-1-WAAM-M-60°	2	14	15	30	18.5
IP1-1-WAAM-M-90°	2	14	15	30	17.8
IP1-2-WAAM-M-0°	2	13	15	30	16.9
IP1-2-WAAM-M-45°	2	13	15	30	19.0
IP1-2-WAAM-M-60°	2	13	15	30	18.1
IP1-2-WAAM-M-90°	2	13	15	30	16.2
IP1-3-WAAM-M-0°	2	11	15	30	15.0
IP1-4-WAAM-M-0°	2	8	15	30	11.2
IP1-1-WAAM-AB-0°	5.4	14	15	30	44.3
IP1-2-WAAM-AB-0°	5.4	13	15	30	40.8
IP1-2-WAAM-AB-45°	5.3	13	15	30	41.6
IP1-2-WAAM-AB-60°	5.2	13	15	30	38.0
IP1-2-WAAM-AB-90°	5.2	13	15	30	41.6
IP1-3-WAAM-AB-0°	5.3	11	15	30	33.6
IP1-4-WAAM-AB-0°	5.4	8	15	30	23.8
IP1-5-WAAM-AB-0°	5.2	15	8	16	22.6
IP1-5-WAAM-AB-45°	5.4	15	8	16	23.9
IP1-5-WAAM-AB-60°	5.3	15	8	16	20.5
IP1-5-WAAM-AB-90°	5.3	15	8	16	23.0
IP1-1-SLM-M-0°	2	14	15	30	18.5
IP1-1-SLM-AB-0°	2	14	15	30	18.7
IP1-2-SLM-AB-0°	2	13	15	30	18.3
IP1-2-SLM-AB-45°	2	13	15	30	18.7
IP1-2-SLM-AB-90°	2	13	15	30	17.5
IP1-5-SLM-AB-0°	2	15	8	16	11.6
IP1-5-SLM-AB-45°	2	15	8	16	11.1
IP1-5-SLM-AB-90°	2	15	8	16	10.7

Table 5.3: Design details and ultimate load capacities of inner plates with double-bolt configuration [41].

Designation	Thick-ness, t (mm)	End distance, e_1 (mm)	Edge distance, e_2 (mm)	Horizontal pitch distance, p_h (mm)	Breadth, b (mm)	Experimental ultimate load, F_{Exp} (Kn)
IP2-1-CON	2	12	12	16	40	27.3
IP2-2-CON	2	11	12	16	40	26.6
IP2-3-CON	2	8.2	12	16	40	23.1
IP2-4-CON	2	8	12	16	40	23.0
IP2-5-CON	2	7	12	16	40	21.1
IP2-6-CON	2	16	8	24	40	30.4
IP2-7-CON	2	15	11	18	40	32.1
IP2-1-WAAM-M-0°	2	12	12	16	40	26.3
IP2-1-WAAM-M-45°	2	12	12	16	40	27.4
IP2-1-WAAM-M-60°	2	12	12	16	40	26.8
IP2-1-WAAM-M-90°	2	12	12	16	40	25.3
IP2-2-WAAM-M-0°	2	11	12	16	40	27.3
IP2-3-WAAM-M-0°	2	8.2	12	16	40	23.8
IP2-3-WAAM-M-45°	2	8.2	12	16	40	24.4
IP2-3-WAAM-M-60°	2	8.2	12	16	40	23.3
IP2-3-WAAM-M-90°	2	8.2	12	16	40	21.6
IP2-4-WAAM-M-0°	2	8	12	16	40	23.1
IP2-5-WAAM-M-0°	2	7	12	16	40	20.7
IP2-7-WAAM-M-0°	2	15	11	18	40	31.4
IP2-2-WAAM-AB-0°	5.5	11	12	16	40	57.0
IP2-3-WAAM-AB-0°	5.6	8.2	12	16	40	49.5
IP2-3-WAAM-AB-45°	5.2	8.2	12	16	40	47.7
IP2-3-WAAM-AB-60°	5.5	8.2	12	16	40	48.9
IP2-3-WAAM-AB-90°	5.3	8.2	12	16	40	44.9
IP2-4-WAAM-AB-0°	5.0	8	12	16	40	47.6
IP2-5-WAAM-AB-0°	5.3	7	12	16	40	43.7
IP2-6-WAAM-AB-0°	5.4	16	8	24	40	70.8
IP2-6-WAAM-AB-45°	5.0	16	8	24	40	62.8
IP2-6-WAAM-AB-60°	5.3	16	8	24	40	61.8
IP2-6-WAAM-AB-90°	5.0	16	8	24	40	61.7
IP2-7-WAAM-AB-0°	5.4	15	11	18	40	69.1
IP2-7-SLM-M-0°	2	15	11	18	40	31.7
IP2-6-SLM-AB-0°	2	16	8	24	40	31.1
IP2-6-SLM-AB-45°	2	16	8	24	40	31.6
IP2-6-SLM-AB-90°	2	16	8	24	40	30.6
IP2-7-SLM-AB-0°	2	15	11	18	40	33.5

5.3 Observed cracking behaviour and definition of the TCD focus paths

The location of crack initiation and propagation directions were identified by post-test inspection of CON, WAAM, and SLM specimens [41]. In all cases, the crack initiation occurred at the bolt hole edge on the loaded side within the bearing zone, where the bolt-to-hole contact produces localised damage and the highest stress concentration (Figure 5.2a-c). For CON plates, crack propagation typically followed the weakest ligament defined by the specimen geometry and relative dimensions, producing mainly straight tearing paths either parallel or perpendicular to the loading direction. Accordingly, the crack direction was not random but largely governed by the geometrical design of the specimen, which determined the weakest ligament and in turn led to well-defined, typical failure modes and tearing paths. For WAAM plates, cracking could deviate from this tendency, with several specimens additively manufactured at raster angles of 45° and 60° exhibiting a diagonal crack trajectory. This is attributed to the WAAM layer morphology and its orientation relative to the loading direction, which can guide crack growth and promote inclined propagation. In contrast, the SLM specimens showed cracking behaviour more consistent with that of the CON specimens, with the crack initiation location and propagation direction remaining broadly similar across the tested configurations and showing minimal sensitivity to surface condition and print direction. Based on the observed cracking behaviour, three representative focus paths were considered for each specimen in the TCD analyses discussed below: perpendicular, diagonal, and parallel. The link between the observed cracking behaviour and the focus path directions is illustrated schematically in Figure 5.2d.

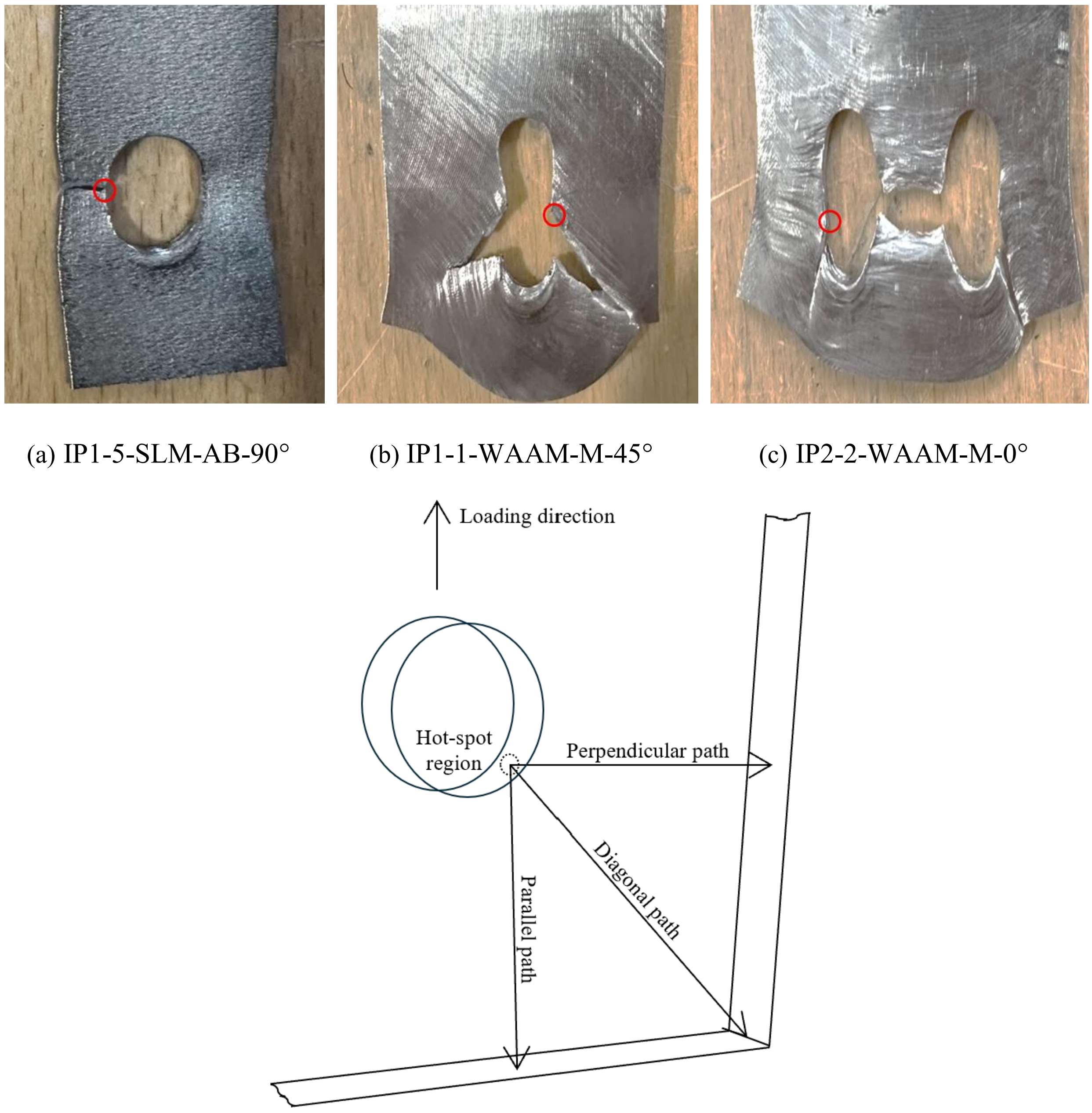

(d)

Figure 5.2: Representative experimentally observed failures for selected (a) SLM and (b, c) WAAM specimens, showing the crack initiation point at the bolt hole edge (red circles) and the resulting crack paths [41]; (d) corresponding TCD focus paths from the crack initiation point relative to the loading direction.

5.4 Application of the Theory of Critical Distances

5.4.1 Methodology

In the standard formulation of the PM, once the material's characteristic length, L, and the focus path are determined, the effective stress, σ_{eff}, is defined as the stress value located at a distance of $L/2$ from the tip of the notch or crack being assessed [82,89] (Figure 5.3a,b):

$$\sigma_{eff} = \sigma_{VM}\left(\theta = 0, r = \frac{L}{2}\right) \tag{5.1}$$

In definition (5.1), σ_{VM} is von Mises equivalent stress, while θ and r are polar coordinates. Von Mises stress was employed in this study since previous work reported that, for ductile materials modelled by using a linear-elastic constitutive law, it provides more accurate predictions than Tresca's criterion and the maximum principal stress criterion [84]. The characteristic length, L, can directly be estimated via the following well-known definition:

$$L = \frac{1}{\pi}\left(\frac{K_{IC}}{\sigma_0}\right)^2 \tag{5.2}$$

with K_{IC} being the plane-strain fracture toughness, which is recommended to be determined experimentally in accordance with ASTM E399 [90].

As defined by Eq. (5.2), determining the value of L is straightforward only when the inherent material strength, σ_0, is assumed equal the ultimate tensile strength, σ_{UTS}, and the value of K_{IC} is available. If this condition is not satisfied, a well-established alternative approach consists of calibrating the parameters from experimental results obtained by testing specimens containing notches of different sharpness [82]. This procedure is illustrated in Figure 5.3. According to the PM argument, the intersection point of two linear-elastic stress-distance curves at incipient failure, derived from tests on notches of different sharpness, allows the direct estimation of σ_0 and L. The procedure summarised in Figure 5.3c was used in the present investigation to determine L.

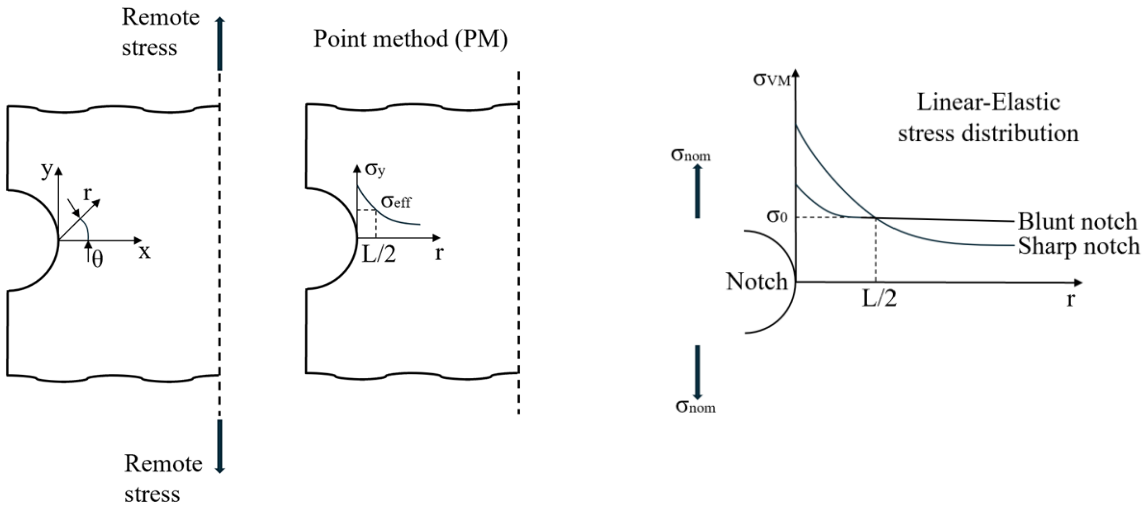

(a) (b) (c)

Figure 5.3: Illustration of the Point Method (PM); (a) local polar coordinates, (b) effective stress evaluation at a distance $L/2$ from the notch root, and (c) determination of σ_0 and L from the intersection of the linear elastic stress curves for two notch types. (a) and (b) are adapted from [91], while (c) is adapted from [82].

5.4.2 Characterisation of σ_0 and L via the two-notch approach

Two U-notched specimens were prepared using CON 316L stainless steel: one with a sharp notch with root radius, r_n, equal to 0.5 mm and the other with a blunt notch with r_n = 1.5 mm, as shown in Figure 5.4. Uniaxial tensile tests were conducted with a displacement rate of 1 mm/min. Two global load-displacement curves for the representative sharp notch test and the blunt notch test are shown in Figure 5.5a,b. These tests were followed by linear-elastic three-dimensional FE simulations performed using FE commercial software ANSYS Mechanical [92]. The elastic modulus, $E = 184$ Gpa, obtained from the CON coupon tests was used in the numerical analyses. Each specimen type was then modelled by progressively refining the mesh in the vicinity of the notch tip until convergence was achieved. A direct stiffness comparison using the global load-displacement curves from the experimental and FE responses was considered. However, the experimental stiffness was derived from the testing equipment crosshead displacement, which included the combined compliance of the equipment, grips, and specimen, whereas the FE displacement represented the specimen response only. The two stiffness values were therefore not directly comparable and could not provide a reliable basis for validation.

The linear-elastic stress-distance curves (in terms of von Mises equivalent stress) along the notch bisectors at the incipient failure condition were extracted for both specimens. These curves were then combined (see Figure 5.5c), and the values of σ_0 and $L/2$ at the intersection were determined to be 1441 MPa and 0.22 mm, respectively. The obtained value of σ_0 is about twice the ultimate tensile stress, $\sigma_{UTS} = 667$ MPa, measured from the CON 316L stainless steel coupon tests. The obtained ratio between σ_0 and σ_{UTS}, of about 2, is consistent with the observations reported in David Taylor's book [35]. The values of σ_0 and $L/2$ obtained through this procedure were then used in the TCD assessment of the bolted connections. The suitability of the linear-elastic models analysis was assessed through convergence of the local stress fields, as shown in Appendix B, and the accuracy of the resulting failure-load predictions presented in Section 5.4.7.

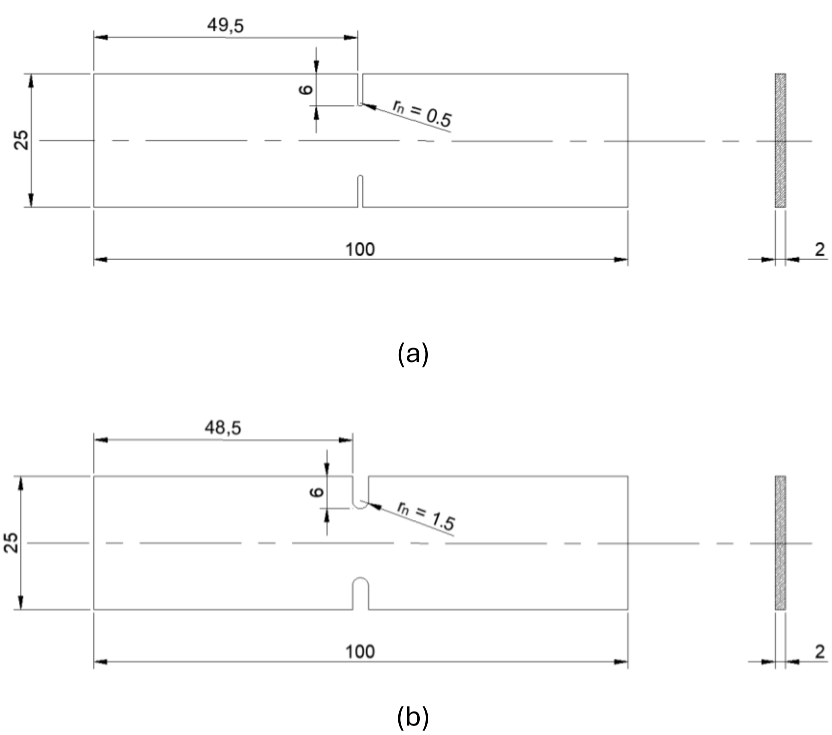

Figure 5.4: Geometrical dimensions of the notched specimens (in mm); (a) sharp notch and (b) blunt notch.

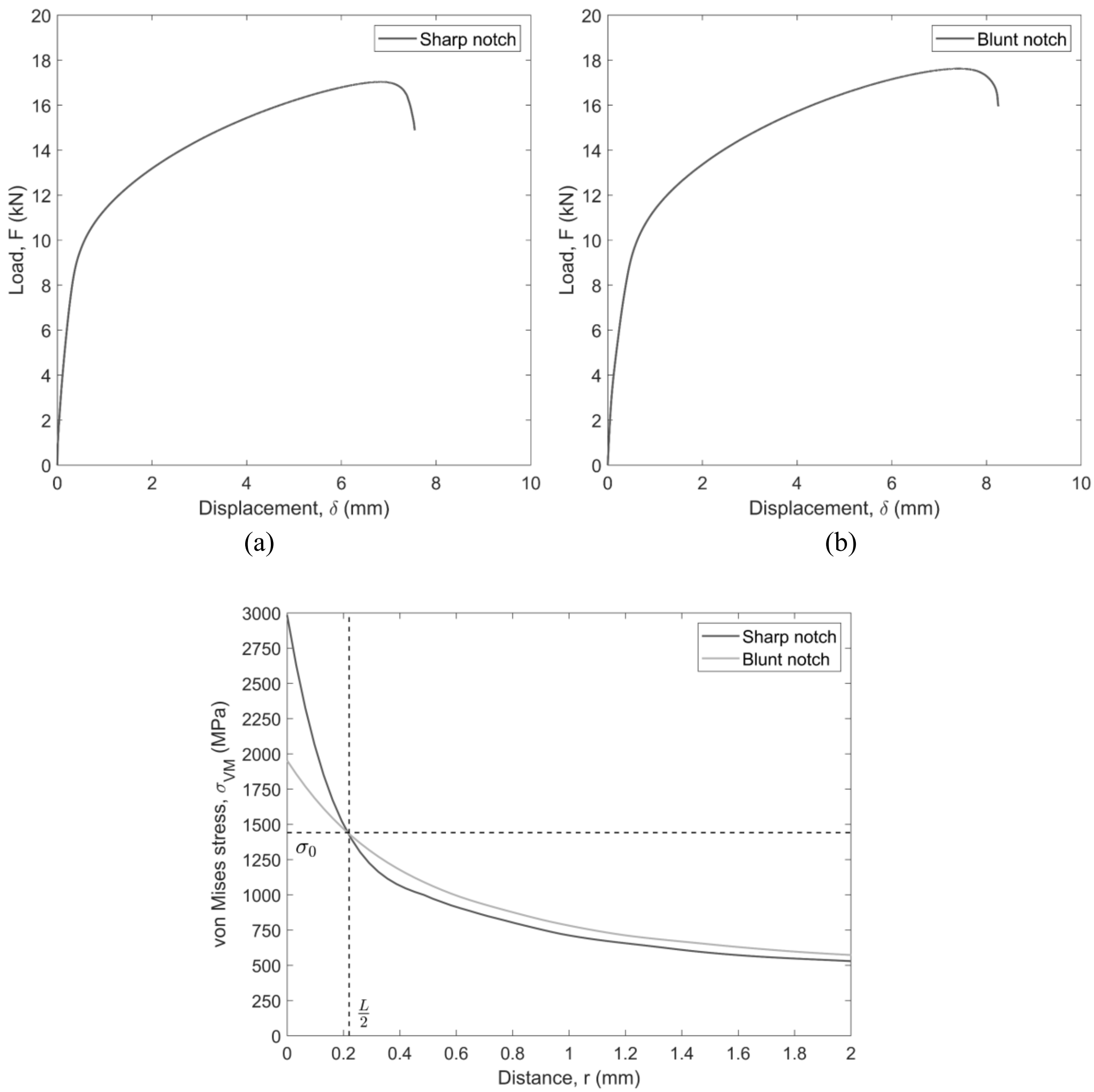

(a) (b)

(c)

Figure 5.5: Load-displacement curves for the CON notched specimens with a uniform thickness of 2 mm; (a) sharp notch and (b) blunt notch; (c) corresponding FE stress-distance curves.

To enable a further assessment under matching AM conditions, the same two-notch calibration procedure was also applied to WAAM-AB material. Two notched WAAM-AB plates, with the same dimensions as those of CON notched specimens were tested. The specimens were extracted and tested only in the 0° direction. The mean measured thickness was 5.3 mm for the plate containing the blunt notch and 5.2 mm for the plate with the sharp notch.

The corresponding global load-displacement curves for the sharp and blunt notched specimens are shown in Figure 5.6a,b, respectively. The FE-derived stress-distance curves are reported in Figure

5.6c, from which the values of σ_0 and *L/2* were estimated to be approximately 1345 MPa and 0.31 mm, respectively. Due to limited material availability, only two AM specimens could be tested. Although this did not allow any statistical assessment of variability, it was nevertheless possible to obtain an approximate estimate of the above parameters. The resulting ratio of σ_0 and σ_{UTS} is also higher than that obtained for the CON material, ranging from approximately 2.4 to 2.7 based on the WAAM-AB ultimate tensile stress values reported in Table 5.1. However, this range is considered reasonable, since the ratio of σ_0, and σ_{UTS}, is expected to increase from unity for a fully brittle material as material ductility increases. Therefore, the value of approximately 2 reported by Taylor [35] should be regarded as a reference value rather than a fixed limit. The higher ratio obtained for the WAAM-AB specimens may also be influenced by the specific as-built morphology of the material, including surface undulations and local geometric irregularities. These parameters were subsequently used for the PM predictions of the WAAM-AB bolted joints.

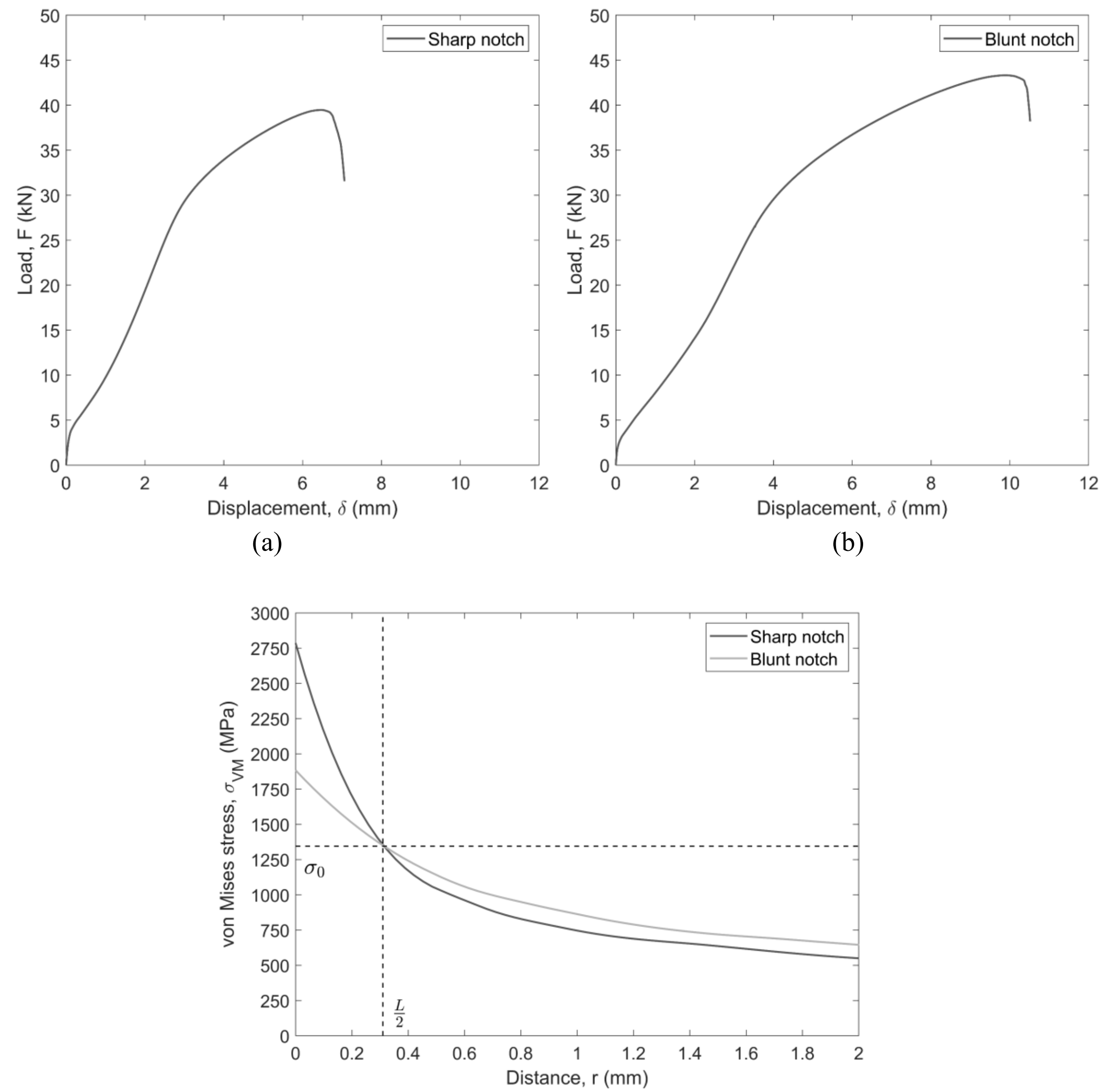

(a) (b)

(c)

Figure 5.6: Load-displacement curves for the WAAM-AB notched specimens; (a) sharp notch and (b) blunt notch; (c) corresponding FE stress-distance curves.

5.4.3 Finite element model setup for bolted connections

The linear-elastic stress fields in the vicinity of the bolt holes were obtained from three-dimensional FE models developed in ANSYS Mechanical (see Figure 5.7a and b) [92]. The reason for adopting 3D models was that, as mentioned in the previous section, the stress analysis was carried out in terms of von Mises equivalent stress. Accordingly, the relevant stress fields and the corresponding stress-distance curves were determined at the mid-section of the tested plates, i.e.

at those sections experiencing the highest degree of stress triaxiality (although this remained limited due to the small thickness of the plates).

Initially, a standard detailed contact-based assembly model was adopted to replicate the experimental configuration as closely as practicable and to verify the sensitivity of the near-hole stress field to modelling assumptions. The model comprised the complete plate-bolt-nut assembly, with all interfaces represented through contact definitions. The IP1-1-CON configuration was used as the base model for the sensitivity studies on friction and mesh refinement. By using the assembly tool available in ANSYS [92], these components were combined into a full model without merging, enabling the specification of contact interactions. All relevant interfaces were defined as frictional, except between the bolt and nut where a bonded contact was applied. The frictional contact definitions allowed separation while transmitting compressive contact forces and resisting relative tangential sliding. The Augmented Lagrange formulation was used, while the penetration tolerance and normal contact stiffness were left as program controlled. This choice corresponded to the experimental setup, where a minimal tightening torque was used to align the plates and restrict movement in directions other than the applied load. Therefore, in the model, this bonded bolt-nut definition both prevented slip at the interface and provided adequate clamping without the need to model minimal bolt preload. This reduced unnecessary detail in the connection representation and ensured stable analysis, as the study focused on plate stress distribution rather than detailed preload behaviour. The friction coefficient, μ, was investigated through a sensitivity study comparing μ = 0.15, 0.20, and 0.25, which showed mean σ_{VM} differences below 1.7% over the stress-distance range from the edge of the inner plate hole. Due to the limited variability observed in the sensitivity study, and consistent with earlier finite element studies on steel bolted joints [93,94], the value of μ was taken as 0.20 for all models. The bolt shanks were designed as smooth cylinders with diameters equal to the nominal size, and the clearance between bolts and holes was omitted to avoid introducing contact errors. This simplification was adopted to obtain a stable and repeatable local stress field for the TCD assessment, although it may affect the initial bearing contact, local load transfer, and near-hole stress distribution.

As shown in Figure 5.7c, the mesh refinement tool was applied directly to the bolt-hole edges. The circular geometry enabled the generation of a uniform, radially distributed fine mesh without the need for bias lines. A mesh sensitivity study was conducted on the IP1-1-CON inner plate model, with global element sizes of 1.2 mm, 1.0 mm, and 0.8 mm. The 0.8 mm mesh significantly increased computational time with only a 0.3% mean change in σ_{VM} over the stress-distance range between 1.0 and 0.8 mm mesh sizes. Therefore, a global element size of 1.0 mm was adopted, which, after local refinement, reduced the element size to approximately 0.3 mm around the holes. The outer plates, bolts, and nuts were meshed with a 2.0 mm element size.

Although the detailed contact-based assembly model provided a rigorous representation of the experimental configuration, it required long run times, which would have made processing the full dataset inefficient. A simplified model was therefore implemented to achieve a substantial reduction in run time while retaining the accuracy required for the TCD-based assessment. The simplified model (see Figure 5.8) consisted of a single inner plate with a cylindrical solid inserted through the bolt hole to represent the bolt shank. The frictional contact between the shank and the plate was kept at 0.2. The shank end faces were fully fixed, and the end face of the plate was subjected to the experimental load. The shank was extended by 1 mm beyond both plate faces so that the boundary conditions were applied away from the hole edge, avoiding artificial surface stress spikes and allowing a representative stress field through the hole thickness to develop.

Stress-distance curves were extracted through the plate mid-thickness along three paths relative to the loading direction: perpendicular, diagonal, and parallel (Figure 5.2d). For each path, the origin was defined at the experimentally observed crack initiation point on the hole edge, which was consistent with the FE hot-spot corresponding to the maximum stress location. A direct comparison of the equivalent von Mises stress, σ_{VM}, along each path showed very close agreement between the full and simplified FE models (Figure 5.9). Along the perpendicular path, the simplified model differed from the full model at $L/2$ by only about 0.3%. Similar differences were observed for the other directions, with $\sigma_{VM}(L/2)$ differing by 0.3% for the diagonal path and by 1.0% for the parallel path. When averaged over a distance equal to L, the mean difference between the simplified and full models remained below 1% for all three focus path directions, with an overall mean absolute difference of about 0.6%. This simplified model therefore eliminates most of the contact-related complexity and reduces the run time by approximately 83%, while preserving the governing stress fields. Accordingly, the simplified numerical approach was adopted for all subsequent models.

Using the focus path definition introduced in Section 5.3 (Figure 5.2d), stress-distance curves for each specimen were extracted at the plate mid-thickness. The predicted hot-spot was consistently located at the loaded hole edge, in good agreement with the experimentally observed crack initiation point. For each specimen, this experimentally identified point was therefore selected as the origin of the TCD focus paths. Figure 5.10 shows the corresponding FE contours for representative specimen cases, illustrating that this experimentally identified point lies within the hot-spot location. The resulting effective stress, σ_{eff}, and the corresponding PM prediction accuracy were compared for each path. This will be discussed in the next sections.

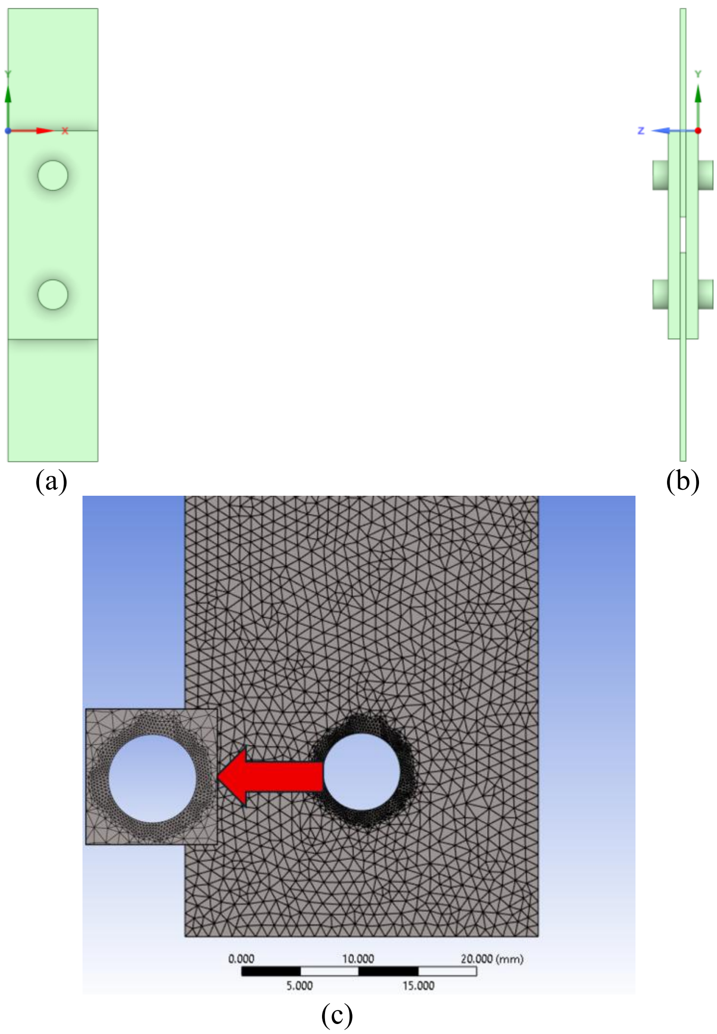

Figure 5.7: A full 3D finite element model of the double-bolted connections; (a) front view, (b) side view, and (c) inner plate's tetrahedral mesh with a zoom into the refinement around the holes.

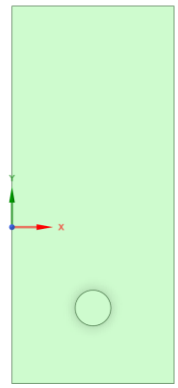

(a)

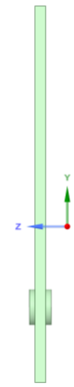

(b)

Figure 5.8: Simplified model showing a single inner plate with a cylindrical bolt shank inserted through the hole; (a) front and (b) side view.

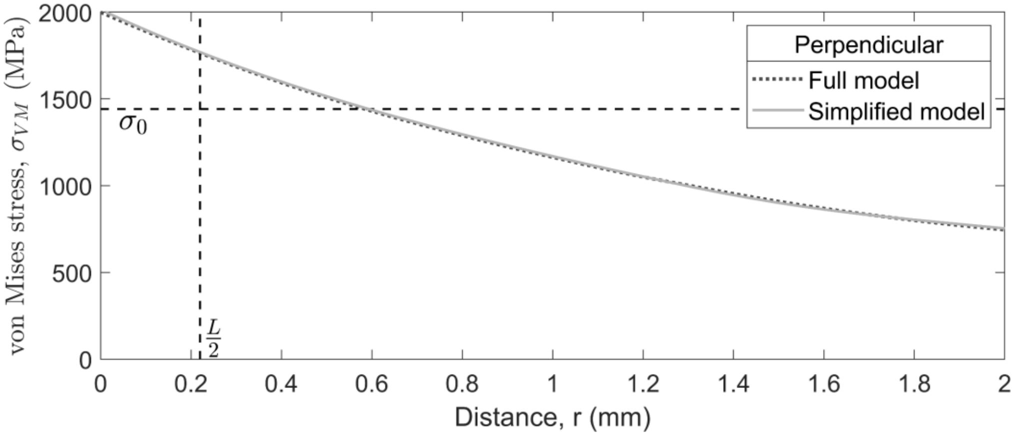

(a)

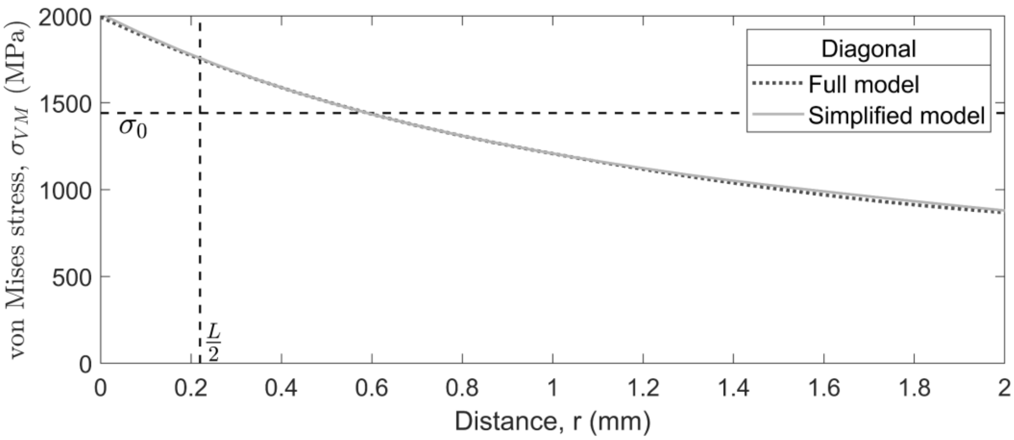

(b)

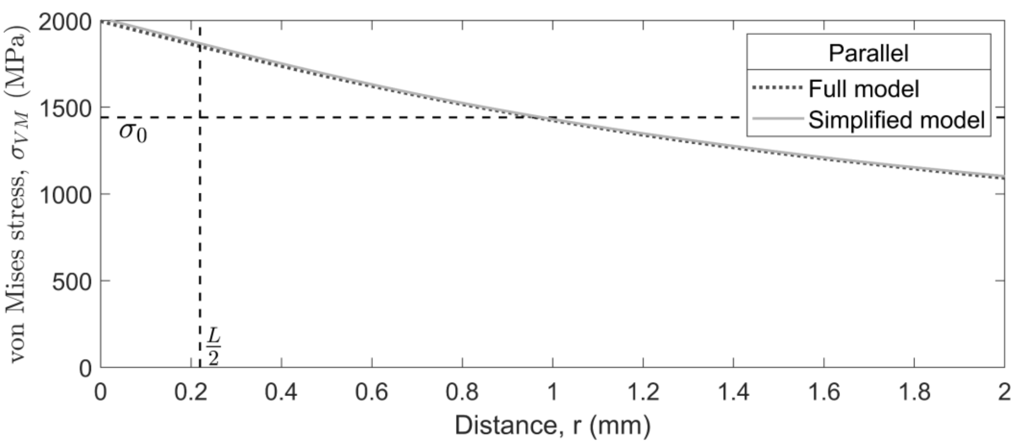

(c)

Figure 5.9: Comparison of the full and simplified FE models for IP1-1-CON: (a) perpendicular, (b) diagonal, and (c) parallel paths.

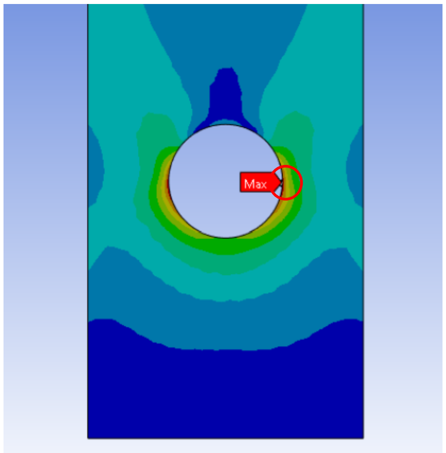

(a) IP1-5-SLM-AB-90°

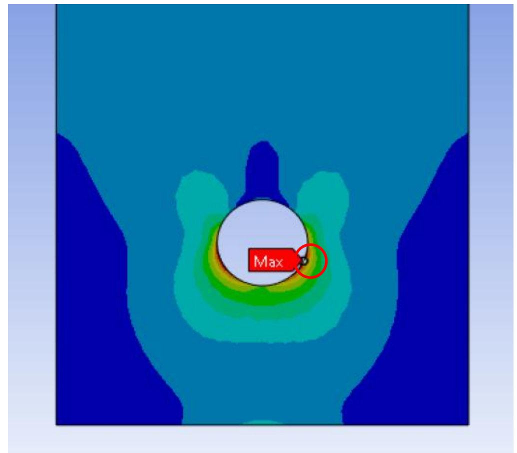

(b) IP1-1-WAAM-M-45°

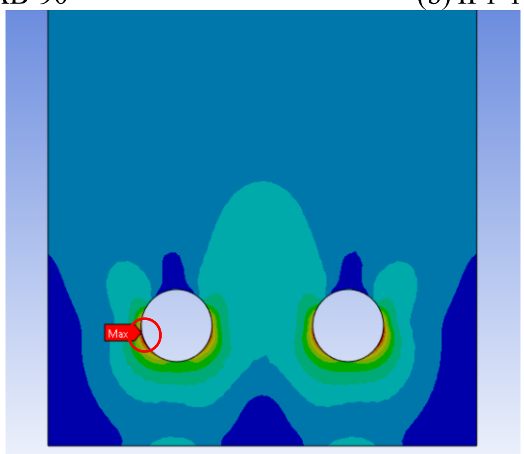

(c) IP2-2-WAAM-M-0°

Figure 5.10: The corresponding FE equivalent von Mises stress contours for representative specimen cases. The 'Max' label indicates the location of the maximum σ_{VM} and is shown for reference, while the red circles mark the experimentally observed crack initiation point at the bolt hole edge.

5.4.4 TCD-PM assessment of CON inner plates

Following the results of Section 5.4.2, where the values of σ_0 and L were determined using the standard two-notch approach based on two CON specimens containing sharp and blunt notches, the predictive accuracy of the PM was assessed initially for the CON inner plates. The PM was applied to the corresponding stress-distance curves to evaluate the signed relative prediction error defined as follows:

$$\text{Relative prediction error } (\%) = \frac{\sigma_{eff} - \sigma_0}{\sigma_0} \times 100 \quad (5.3)$$

A representative example for the CON inner plates' plots (IP2-1-CON) is shown in Figure 5.11. The results, summarised in Table 5.4, report the crack path orientation predicted from the failure mode according to BS EN 1993-1-8 (hereafter referred to as EC3-1-8) [1], the experimentally observed crack paths, and the stress-distance results obtained from the perpendicular, diagonal, and parallel focus paths. The values corresponding to the observed crack paths are highlighted in dark grey. Across all CON plates, the extraction path parallel to the loading direction consistently produced the highest effective stress, σ_{eff}. This is largely in agreement with both the EC3-1-8 predictions [1] and the observed crack paths (Table 5.4).

The overall accuracy of the PM associated with the considered focus paths was assessed in terms of the mean absolute error (MAE), defined as follows:

$$\mathrm{MAE}(\%) = \frac{1}{n}\sum_{i=1}^{n}|\text{Relative prediction error}_i| \tag{5.4}$$

where n is the number of estimates. Based on the error index, the perpendicular path provided the highest level of accuracy with a combined MAE across all single- and double-bolted configurations of 8.0%, outperforming the diagonal path with MAE of 9.1% and the parallel path with MAE of 12.8%. However, the perpendicular direction showed a slightly higher tendency towards non-conservative predictions, particularly for several double-bolted configuration specimens. It was also evident that selecting the extraction direction to match the observed crack propagation direction did not improve the overall accuracy (combined MAE = 8.7%), relative to using the perpendicular direction.

Regarding the obtained accuracy as a function of the adopted focus path, it is important to note that the TCD generally provides estimates that fall within an error interval of ±20% [82,85]. Since, apart from a small number of outliers, most results across all directions lie within this ±20% error band (Table 5.4), this indicates that the differences between the effective stresses associated with the three potential directions fall within the intrinsic accuracy of the TCD. This suggests that the most appropriate way to apply the TCD is to identify the focus path associated with the maximum damage extent, which generally returns a crack propagation direction that is well aligned with the one identified using the EC3-1-8 standard approach [1] (Table 5.4).

Turning back to the calibration of the TCD, the relatively low MAE suggests that the values of σ_0 and L derived from idealised CON notched specimens are adequate for the CON inner plate connections, despite the greater complexity of the local stress distributions characterising the tested bolted specimens. That said, coupon tests showed that the material properties differ between manufacturing procedures, and AM-specific process and surface conditions were found to influence crack propagation in WAAM specimens extracted in the diagonal direction [41]. Therefore, the applicability of the adopted σ_0-L pairing to inner plates manufactured by WAAM and SLM deserves to be explored in detail. This will be addressed in the following section.

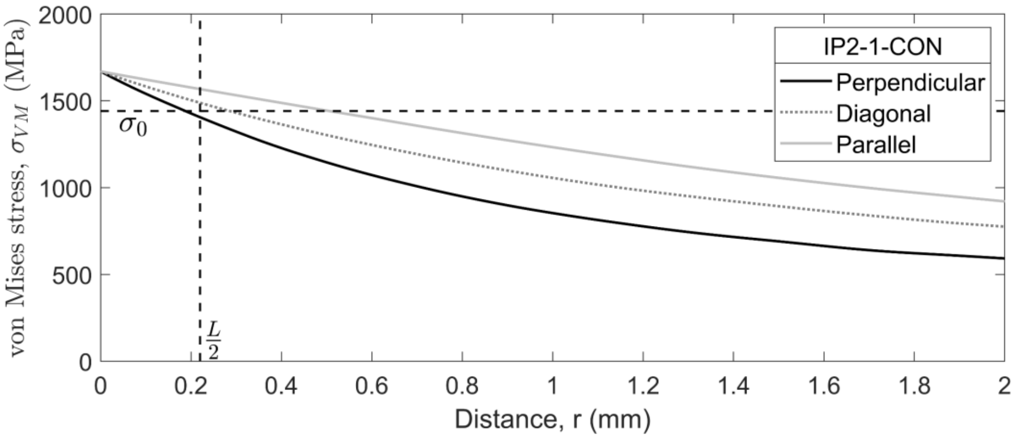

Figure 5.11: Application of the TCD-PM to the stress-distance curves extracted along different focus path directions for representative CON inner plate.

.

Table 5.4: Accuracy of TCD-PM applied to the CON inner plates (EB: edge bearing; NST: net-section tension; BT: block tearing); the dark grey highlighted values indicate the results corresponding to the experimentally observed crack path for each specimen.

Designation	Predicted crack path according to EC3-1-8		Perpendicular Path Direction		Diagonal Path Direction		Parallel Path Direction	
	Failure mode/Crack path	Actual crack Path	Effective stress, σ_{eff} (MPa)	Relative prediction error, %	Effective stress, σ_{eff} (MPa)	Relative prediction error, %	Effective stress, σ_{eff} (MPa)	Relative prediction error, %
IP1-1-CON	EB/ Parallel	Parallel	1769	22.8	1758	22.0	1868	29.6
IP1-2-CON	EB/ Parallel	Perpendicular	1721	19.4	1682	16.7	1759	22.1
IP1-3-CON	EB/ Parallel	Parallel	1598	10.9	1571	9.0	1664	15.4
IP1-4-CON	EB/ Parallel	Parallel	1357	−5.8	1335	−7.3	1420	−1.5
IP1-5-CON	NST/ Perpendicular	Perpendicular	1373	−4.7	1562	8.1	1642	14.0
IP2-1-CON	BT/ Perpendicular & Parallel	Perpendicular*	1406	−2.5	1489	3.3	1568	8.8
IP2-2-CON	BT/ Perpendicular & Parallel	Perpendicular*	1376	−4.5	1473	2.2	1567	8.8
IP2-3-CON	EB/ Parallel	Parallel	1390	−3.5	1408	−2.3	1557	8.0
IP2-4-CON	EB/ Parallel	Perpendicular*	1408	−2.3	1403	−2.7	1482	2.8
IP2-5-CON	EB/ Parallel	Parallel	1365	5.3	1356	−5.9	1463	1.5
IP2-6-CON	NST/ Perpendicular	Perpendicular	1514	5.1	1689	17.2	1770	22.9
IP2-7-CON	BT/ Perpendicular & Parallel	Perpendicular*	1582	9.8	1628	12.9	1704	18.2

*The visible crack initiation/propagation is between the holes.

5.4.5 TCD-PM assessment of WAAM and SLM inner plates using the σ_0-L pairing calibrated from CON notched specimens

This section examines the accuracy of the PM, calibrated using the σ_0 and L values obtained from the CON notched specimens, in estimating the static strength of bolted joints containing additively manufactured inner plates. This validation exercise is particularly challenging, since the PM was used to post-process the results from FE models in which the material was modelled as homogeneous and isotropic, i.e. without accounting for the manufacturing direction in the stress analysis.

Representative stress-distance plots are shown in Figure 5.12 for the 2 mm AM plates, including machined WAAM (WAAM-M), machined SLM (SLM-M), and as-built SLM (SLM-AB). Figure 5.13 presents the corresponding plots for the as-built WAAM (WAAM-AB) plates. The associated TCD prediction results are summarised in Table 5.5 for the 2 mm AM plates and in Table 5.6 for the WAAM-AB plates. Additional TCD analysis plots are provided in Appendix B.

In terms of predictive performance for the 2 mm AM plates, the diagonal direction produced the lowest error, with an MAE of 11.7%, closely followed by the perpendicular direction with an MAE of 11.8%, while the parallel direction showed a higher error, with an MAE of 15.7%. Consistent with the CON assessment, the perpendicular direction exhibited the strongest tendency towards non-conservative predictions. In addition, selecting the extraction direction to follow the observed crack path slightly lowered the overall accuracy, giving an MAE of 12.9%. Furthermore, it was evident that a small number of prediction errors across all paths fall outside the $\pm$20% interval, with the outliers predominantly positive, indicating conservative predictions. Compared with the CON plates, the 2 mm AM results show a modest increase in error. However, the level of accuracy remains comparable, indicating that the CON calibrated TCD-PM provides an acceptable prediction for AM inner plates of matched thickness.

In contrast, the WAAM-AB plates with thicknesses exceeding 2 mm showed a reduction in accuracy. The MAE exceeded 20% threshold for both the perpendicular and diagonal extraction paths, reaching 21.9% and 20.8%, respectively. Although the parallel path showed a slightly lower MAE of 18.4%, all predictions remained non-conservative. A further increase in error was observed for the double-bolt configurations, with MAE rising from 18.6%, 17.5%, and 14.6% for IP1 to 24.9%, 23.8%, and 21.9% for IP2 in the perpendicular, diagonal, and parallel paths, respectively, confirming an evident effect of joint configuration in the as-built plates. When the extraction path corresponding to the experimentally observed crack path was considered, the resulting MAE was approximately 21.1%.

Overall, the accuracy in estimating the static strength of bolted joints containing AM plates was found to decrease. This reduction can be attributed to two main factors: first, AM metals exhibit mechanical properties and micro/meso-structural morphologies that differ from those of their conventionally manufactured counterparts, leading to different values of the TCD material constants; second, the FE models did not explicitly account for the micro/meso-structural variations associated with the AM process. This is particularly evident for the WAAM-AB plates, where the as-built surface condition induces local geometric irregularities that, together with the anisotropic material response arising from the AM micro/meso-structural morphology, may influence the local process zone ahead of the crack initiation region. These features are not explicitly represented in the simplified linear elastic FE models, which treat the material as homogeneous and isotropic and idealise the local geometry around the bolt hole. Therefore, the remaining non-conservatism should not be interpreted as a thickness effect alone, but rather as a consequence of the WAAM-AB morphology and its associated anisotropic material behaviour not being fully captured by the adopted FE/TCD framework. Nevertheless, despite these complexities and modelling limitations, the accuracy obtained using TCD parameters calibrated from conventionally manufactured material remains remarkable, with prediction errors still close to the typical ±20% range commonly observed when the TCD is applied to a variety of structural integrity problems [82,85].

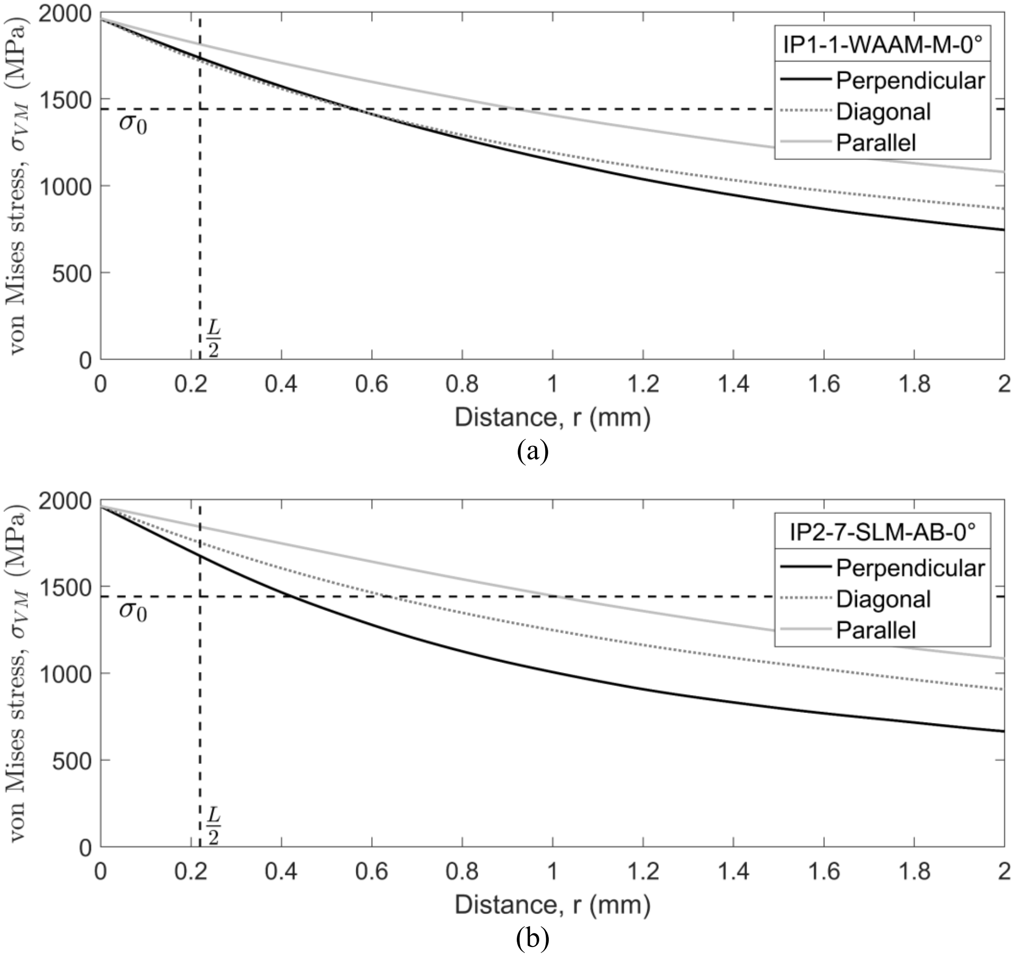

Figure 5.12: TCD-PM applied to the stress-distance curves extracted along different focus path directions for AM inner plates with a consistent thickness of 2 mm; (a) IP1-1-WAAM-M-0°, representing a single-bolted inner plate, and (b) IP2-7-SLM-M-0°, representing a double-bolted inner plate.

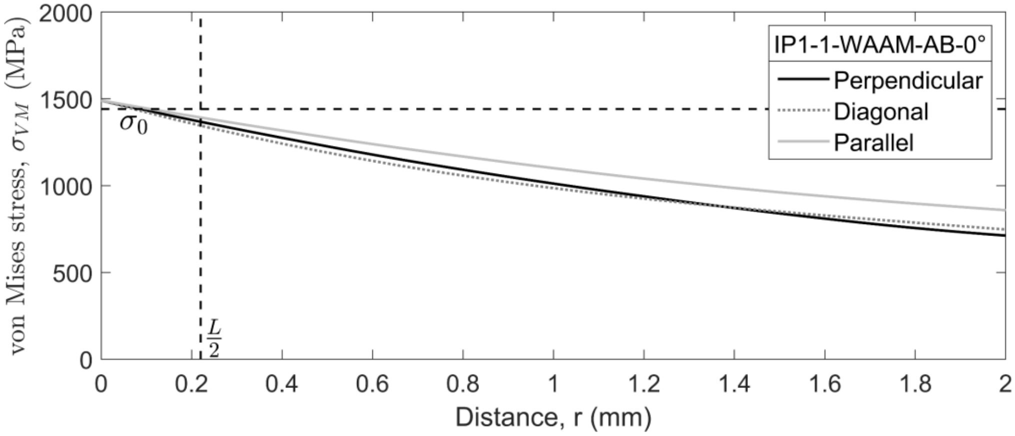

(a)

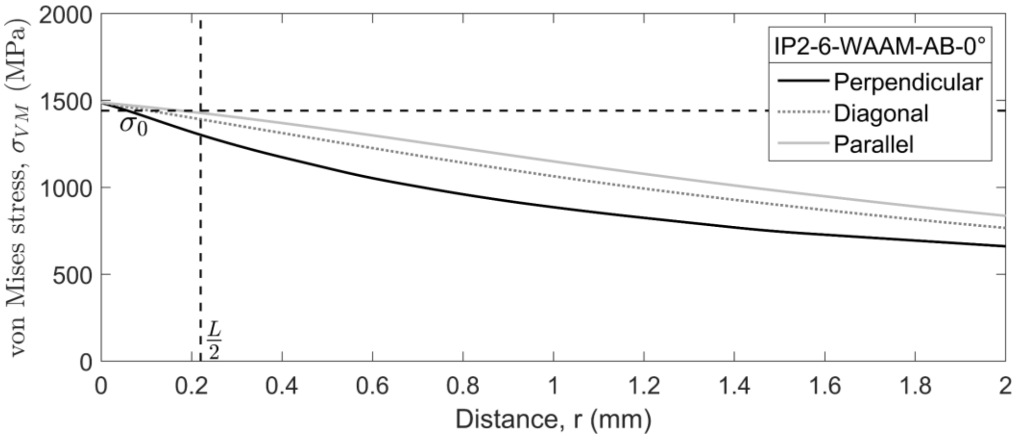

(b)

Figure 5.13: TCD-PM applied to the stress-distance curves extracted along different focus path directions for WAAM-AB inner plates with thicknesses greater than 2 mm; (a) IP1-1-WAAM-AB-0°, representing a single-bolted inner plate, and (b) IP2-7-WAAM-AB-0°, representing a double-bolted inner plate.

Table 5.5: Accuracy of TCD-PM applied to the AM inner plates with a consistent thickness of 2 mm (EB: edge bearing; NST: net-section tension; BT: block tearing); the dark grey highlighted values indicate the results corresponding to the experimentally observed crack path for each specimen.

Designation	Predicted crack path according to EC3-1-8		Perpendicular Path Direction		Diagonal Path Direction		Parallel Path Direction	
	Failure mode/Crack path	Actual crack Path	Effective stress, σ_{eff} (MPa)	Relative prediction error, %	Effective stress, σ_{eff} (MPa)	Relative prediction error, %	Effective stress, σ_{eff} (MPa)	Relative prediction error, %
IP1-1-WAAM-M-0°	EB/Parallel	Parallel	1737	20.6	1718	19.2	1816	26.1
IP1-1-WAAM-M-45°	EB/Parallel	Diagonal	1807	25.4	1786	23.9	1890	31.2
IP1-1-WAAM-M-60°	EB/Parallel	Diagonal	1744	21.1	1725	19.7	1825	26.6
IP1-1-WAAM-M-90°	EB/Parallel	Parallel	1691	17.4	1673	16.1	1767	22.6
IP1-2-WAAM-M-0°	EB/Parallel	Parallel	1614	12.0	1579	9.6	1649	14.5
IP1-2-WAAM-M-45°	EB/Parallel	Diagonal	1803	25.2	1763	22.4	1843	27.9
IP1-2-WAAM-M-60°	EB/Parallel	Diagonal	1724	19.6	1686	17.0	1762	22.3
IP1-2-WAAM-M-90°	EB/Parallel	Parallel	1558	8.1	1525	5.8	1591	10.4
IP1-3-WAAM-M-0°	EB/Parallel	Parallel	1532	6.3	1506	4.5	1593	10.5
IP1-4-WAAM-M-0°	EB/Parallel	Parallel	1346	−6.6	1325	−8.1	1406	−2.4
IP1-1-SLM-M-0°	EB/Parallel	Parallel	1744	21.1	1725	19.7	1825	26.6
IP1-1-SLM-AB-0°	EB/Parallel	Parallel	1763	22.4	1743	21.0	1844	28.0
IP1-2-SLM-AB-0°	EB/Parallel	Parallel	1743	20.9	1705	18.3	1781	23.6
IP1-2-SLM-AB-45°	EB/Parallel	Parallel	1788	24.1	1750	21.5	1827	26.8
IP1-2-SLM-AB-90°	EB/Parallel	Parallel	1676	16.3	1640	13.8	1712	18.8
IP1-5-SLM-AB-0°	NST/Perpendicular	Perpendicular	1331	−7.7	1510	4.8	1591	10.4
IP1-5-SLM-AB-45°	NST/Perpendicular	Perpendicular	1272	−11.7	1444	0.2	1519	5.4
IP1-5-SLM-AB-90°	NST/Perpendicular	Perpendicular	1224	−15.0	1390	−3.6	1462	1.5
IP2-1-WAAM-M-0°	BT/ Perpendicular & Parallel	Perpendicular*	1333	−7.5	1370	−4.9	1437	−0.3
IP2-1-WAAM-M-45°	BT/ Perpendicular & Parallel	Diagonal	1495	3.7	1516	5.2	1623	12.7
IP2-1-WAAM-M-60°	BT/ Perpendicular & Parallel	Diagonal*	1356	−5.9	1395	−3.2	1464	1.6
IP2-1-WAAM-M-90°	BT/ Perpendicular & Parallel	Perpendicular*	1287	−10.7	1323	−8.2	1386	−3.8

Table 5.5: Accuracy of TCD-PM applied to the AM inner plates with a consistent thickness of 2 mm (EB: edge bearing; NST: net-section tension; BT: block tearing); the dark grey highlighted values indicate the results corresponding to the experimentally observed crack path for each specimen (continued).

Designation	Predicted crack path according to EC3-1-8		Perpendicular Path Direction		Diagonal Path Direction		Parallel Path Direction	
	Failure mode/Crack path	Actual crack Path	Effective stress, σ_{eff} (MPa)	Relative prediction error, %	Effective stress, σ_{eff} (MPa)	Relative prediction error, %	Effective stress, σ_{eff} (MPa)	Relative prediction error, %
IP2-2-WAAM-M-0°	BT/ Perpendicular & Parallel	Parallel	1511	4.8	1509	4.7	1613	12.0
IP2-3-WAAM-M-0°	BT/ Perpendicular & Parallel	Parallel	1452	0.7	1452	0.7	1572	9.1
IP2-3-WAAM-M-45°	EB+BT/ Perpendicular & Parallel	Diagonal	1483	2.9	1483	2.9	1610	11.7
IP2-3-WAAM-M-60°	BT/ Perpendicular & Parallel	Diagonal	1419	−1.5	1419	−1.5	1538	6.7
IP2-3-WAAM-M-90°	BT/ Perpendicular & Parallel	Parallel	1324	−8.1	1324	−8.1	1430	−0.7
IP2-4-WAAM-M-0°	BT/ Perpendicular & Parallel	Parallel	1411	−2.1	1409	−2.2	1529	6.1
IP2-5-WAAM-M-0°	EB/Parallel	Parallel	1309	−9.2	1277	−11.4	1328	−7.8
IP2-7-WAAM-M-0°	BT/ Perpendicular & Parallel	Perpendicular*	1575	9.3	1643	14.0	1731	20.2
IP2-7-SLM-M-0°	BT/ Perpendicular & Parallel	Perpendicular*	1588	10.2	1656	14.9	1747	21.2
IP2-6-SLM-AB-0°	NST/ Perpendicular	Perpendicular	1537	6.6	1707	18.4	1787	24.0
IP2-6-SLM-AB-45°	NST/ Perpendicular	Perpendicular	1563	8.4	1734	20.4	1814	25.9
IP2-6-SLM-AB-90°	NST/ Perpendicular	Perpendicular	1514	5.0	1680	16.6	1757	21.9
IP2-7-SLM-AB-0°	BT/ Perpendicular & Parallel	Perpendicular*	1678	16.5	1750	21.5	1845	28.1

*The visible crack initiation/propagation is between the holes.

Table 5.6: Accuracy of TCD-PM applied to the AM inner plates with thicknesses greater than 2 mm (EB: edge bearing; NST: net-section tension; BT: block tearing); the dark grey highlighted values indicate the results corresponding to the experimentally observed crack path for each specimen.

Designation	Predicted crack path according to EC3-1-8		Perpendicular Path Direction		Diagonal Path Direction		Parallel Path Direction	
	Failure mode/Crack path	Actual crack Path	Effective stress, σ_{eff} (MPa)	Relative prediction error, %	Effective stress, σ_{eff} (MPa)	Relative prediction error, %	Effective stress, σ_{eff} (MPa)	Relative prediction error, %
IP1-1-WAAM-AB-0°	EB/Parallel	Parallel	1368	−5.1	1345	−6.6	1393	−3.3
IP1-2-WAAM-AB-0°	EB/Parallel	Parallel	1299	−9.8	1275	−11.5	1322	−8.3
IP1-2-WAAM-AB-45°	EB/Parallel	Diagonal	1354	−6.0	1327	−7.9	1377	−4.4
IP1-2-WAAM-AB-60°	EB/Parallel	Diagonal	1255	−12.9	1232	−14.5	1279	−11.2
IP1-2-WAAM-AB-90°	EB/Parallel	Parallel	1386	−3.8	1362	−5.5	1411	−2.1
IP1-3-WAAM-AB-0°	EB/Parallel	Parallel	1183	−17.9	1157	−19.7	1204	−16.5
IP1-4-WAAM-AB-0°	EB/Parallel	Parallel	1011	−29.8	997	−30.8	1039	−27.9
IP1-5-WAAM-AB-0°	NST/Perpendicular	Perpendicular	1035	−28.2	1122	−22.1	1159	−19.6
IP1-5-WAAM-AB-45°	NST/Perpendicular	Perpendicular	1055	−26.8	1144	−20.6	1178	−18.3
IP1-5-WAAM-AB-60°	NST/Perpendicular	Perpendicular	920	−36.1	996	−30.9	1028	−28.7
IP1-5-WAAM-AB-90°	NST/Perpendicular	Perpendicular	1033	−28.3	1121	−22.2	1155	−19.8
IP2-2-WAAM-AB-0°	BT/ Perpendicular & Parallel	Perpendicular*	1045	−27.5	1045	−27.5	1072	−25.6
IP2-3-WAAM-AB-0°	BT/ Perpendicular & Parallel	Parallel	951	−34.0	926	−35.7	943	−34.6
IP2-3-WAAM-AB-45°	BT/ Perpendicular & Parallel	Diagonal	994	−31.0	965	−33.0	984	−31.7
IP2-3-WAAM-AB-60°	BT/ Perpendicular & Parallel	Diagonal	957	−33.6	929	−35.5	949	−34.2
IP2-3-WAAM-AB-90°	BT/ Perpendicular & Parallel	Parallel	881	−38.8	856	−40.6	873	−39.4
IP2-4-WAAM-AB-0°	BT/ Perpendicular & Parallel	Parallel	1040	−27.9	1010	−29.9	1032	−28.4
IP2-5-WAAM-AB-0°	BT/ Perpendicular & Parallel	Parallel	973	−32.5	952	−33.9	972	−32.5
IP2-6-WAAM-AB-0°	NST/Perpendicular	Perpendicular	1301	−9.7	1392	−3.4	1427	−1.0
IP2-6-WAAM-AB-45°	NST/Perpendicular	Perpendicular	1251	−13.2	1336	−7.3	1373	−4.7

Table 5.6: Accuracy of TCD-PM applied to the AM inner plates with thicknesses greater than 2 mm (EB: edge bearing; NST: net-section tension; BT: block tearing); the dark grey highlighted values indicate the results corresponding to the experimentally observed crack path for each specimen (continued).

Designation	Predicted crack path according to EC3-1-8		Perpendicular Path Direction		Diagonal Path Direction		Parallel Path Direction	
	Failure mode/Crack path	Actual crack Path	Effective stress, σ_{eff} (MPa)	Relative prediction error, %	Effective stress, σ_{eff} (MPa)	Relative prediction error, %	Effective stress, σ_{eff} (MPa)	Relative prediction error, %
IP2-6-WAAM-AB-60°	NST/Perpendicular	Perpendicular	1156	−19.8	1241	−13.9	1274	−11.6
IP2-6-WAAM-AB-90°	NST/Perpendicular	Perpendicular	1227	−14.8	1308	−9.2	1342	−6.8
IP2-7-WAAM-AB-0°	BT/ Perpendicular & Parallel	Perpendicular	1215	−15.7	1222	−15.2	1265	−12.2

*The visible crack initiation/propagation is between the holes

5.4.6 TCD-PM assessment of WAAM-AB inner plates using σ_0-L under the same AM conditions

With the decrease in PM prediction accuracy observed for the combined results of both single- and double-bolt configurations of the WAAM-AB plates, a further investigation was carried out by exploring an alternative calibration strategy. As shown in Table 5.7, calibrating the σ_0-L pairing from the WAAM-AB notched specimens slightly improved the PM accuracy. The MAE decreased to 19.7%, 18.1%, and 15.3% for the perpendicular, diagonal, and parallel extraction paths, respectively, meaning that the majority of the results from all three directions fall within the ±20% interval. However, the double-bolt configurations generally showed larger errors than the single-bolt plates, indicating that the joint configuration in WAAM-AB specimens still affects the prediction accuracy even after calibration based on matching mean thickness. Moreover, the predictions remained predominantly non-conservative, with negative accuracy values governing the results, although a few cases became slightly conservative, reaching up to 4.1%. Despite these complexities, the results discussed in this section indicate that using a σ_0-L pairing calibrated from notched WAAM-AB specimens yields a modest improvement in prediction accuracy.

To account for the limited number of WAAM-AB notched specimens used for calibration, a sensitivity check was also performed by varying σ_0 by ±5%, while keeping L unchanged. This analysis showed a noticeable shift in the prediction errors, confirming that the recalibrated predictions are sensitive to the selected value of σ_0. However, the predictions remained predominantly non-conservative and the overall trend was not removed. Therefore, the recalibrated assessment should be interpreted as an indicative evaluation of the benefit of using WAAM-AB specific calibration parameters, rather than as a statistically robust calibration.

Table 5.7: Accuracy of TCD-PM applied to the AM inner plates with thicknesses greater than 2 mm using the WAAM-AB calibrated σ_0-L pairing (EB: edge bearing; NST: net-section tension; BT: block tearing); the dark grey highlighted values indicate the results corresponding to the experimentally observed crack path for each specimen.

Designation	Predicted crack path according to EC3-1-8		Perpendicular Path Direction		Diagonal Path Direction		Parallel Path Direction	
	Failure mode/Crack path	Actual crack Path	Effective stress, σ_{eff} (MPa)	Relative prediction error, %	Effective stress, σ_{eff} (MPa)	Relative prediction error, %	Effective stress, σ_{eff} (MPa)	Relative prediction error, %
IP1-1-WAAM-AB-0°	EB/Parallel	Parallel	1321	−1.8	1292	−3.9	1354	0.7
IP1-2-WAAM-AB-0°	EB/Parallel	Parallel	1255	−6.7	1225	−9.0	1285	−4.5
IP1-2-WAAM-AB-45°	EB/Parallel	Diagonal	1307	−2.8	1275	−5.2	1339	−0.5
IP1-2-WAAM-AB-60°	EB/Parallel	Diagonal	1212	−9.9	1183	−12.1	1243	−7.6
IP1-2-WAAM-AB-90°	EB/Parallel	Parallel	1341	−0.3	1310	−2.6	1374	2.1
IP1-3-WAAM-AB-0°	EB/Parallel	Parallel	1142	−15.1	1113	−17.2	1170	−13.0
IP1-4-WAAM-AB-0°	EB/Parallel	Parallel	974	−27.6	956	−28.9	1012	−24.8
IP1-5-WAAM-AB-0°	NST/Perpendicular	Perpendicular	976	−27.4	1088	−19.1	1135	−15.6
IP1-5-WAAM-AB-45°	NST/Perpendicular	Perpendicular	993	−26.2	1111	−17.4	1157	−13.9
IP1-5-WAAM-AB-60°	NST/Perpendicular	Perpendicular	867	−35.5	970	−27.9	1010	−24.9
IP1-5-WAAM-AB-90°	NST/Perpendicular	Perpendicular	973	−27.7	1091	−18.9	1136	−15.6
IP2-2-WAAM-AB-0°	BT/ Perpendicular & Parallel	Perpendicular*	1005	−25.3	1007	−25.2	1043	−22.5
IP2-3-WAAM-AB-0°	BT/ Perpendicular & Parallel	Parallel	925	−31.2	892	−33.7	914	−32.0
IP2-3-WAAM-AB-45°	BT/ Perpendicular & Parallel	Diagonal	965	−28.2	930	−30.9	955	−29.0
IP2-3-WAAM-AB-60°	BT/ Perpendicular & Parallel	Diagonal	930	−30.8	895	−33.5	918	−31.7
IP2-3-WAAM-AB-90°	BT/ Perpendicular & Parallel	Parallel	858	−36.2	826	−38.6	846	−37.1
IP2-4-WAAM-AB-0°	BT/ Perpendicular & Parallel	Parallel	1009	−25.0	973	−27.7	1000	−25.7
IP2-5-WAAM-AB-0°	BT/ Perpendicular & Parallel	Parallel	944	−29.8	916	−31.9	943	−29.9
IP2-6-WAAM-AB-0°	NST/Perpendicular	Perpendicular	1234	−8.3	1352	0.5	1400	4.1
IP2-6-WAAM-AB-45°	NST/Perpendicular	Perpendicular	1185	−11.9	1298	−3.5	1345	0

Table 5.7: Accuracy of TCD-PM applied to the AM inner plates with thicknesses greater than 2 mm using the WAAM-AB calibrated σ_0-L pairing (EB: edge bearing; NST: net-section tension; BT: block tearing); the dark grey highlighted values indicate the results corresponding to the experimentally observed crack path for each specimen (Continued).

Designation	Predicted crack path according to EC3-1-8		Perpendicular Path Direction		Diagonal Path Direction		Parallel Path Direction	
	Failure mode/Crack path	Actual crack Path	Effective stress, σ_{eff} (MPa)	Relative prediction error, %	Effective stress, σ_{eff} (MPa)	Relative prediction error, %	Effective stress, σ_{eff} (MPa)	Relative prediction error, %
IP2-6-WAAM-AB-60°	NST/Perpendicular	Perpendicular	1095	−18.6	1203	−10.6	1247	−7.3
IP2-6-WAAM-AB-90°	NST/Perpendicular	Perpendicular	1164	−13.5	1271	−5.5	1316	−2.2
IP2-7-WAAM-AB-0°	BT/ Perpendicular & Parallel	Perpendicular	1164	−13.5	1177	−12.5	1236	−8.1

*The visible crack initiation/propagation is between the holes.

5.4.7 Comparison between TCD-PM and EC3-1-8 resistance predictions

A detailed assessment of resistance predictions according to EC3-1-8 [1] for the tested hybrid bolted joints was reported in a separate study [64], where the relevant resistance equations, failure estimations, and comparisons with other design provisions were discussed. Therefore, the present section compares the EC3-1-8 [1] resistance predictions with the TCD-PM predictions in terms of failure load. The comparison is based on the experimental-to-predicted failure load ratio, where values greater than unity indicate conservative predictions and values lower than unity indicate non-conservative predictions.

As seen in Figure 5.14a and b, the TCD-PM predictions, in terms of mean load ratios, were close to unity for the CON plates. However, except for the perpendicular path in the double-bolt configuration, all paths showed non-conservative predictions compared with EC3-1-8 [1]. Moreover, the TCD-PM predictions had a slightly higher coefficient of variation (COV) for the single-bolt configuration, but an evidently lower COV for the double-bolt configuration.

In contrast, the TCD-PM predictions for the AM plates, shown in Figure 5.14c and d, were generally slightly conservative, with mean ratios mostly higher than unity for the single-bolt AM plates and between 1.06 and 1.12 for the double-bolt AM plates. However, the TCD-PM results showed greater scatter, especially for the perpendicular path in the single-bolt configuration, reflecting the sensitivity of the method to the selected extraction path and to local material and geometrical variability. Overall, EC3-1-8 [1] provides a conservative design baseline, whereas TCD-PM gives closer mean failure load predictions.

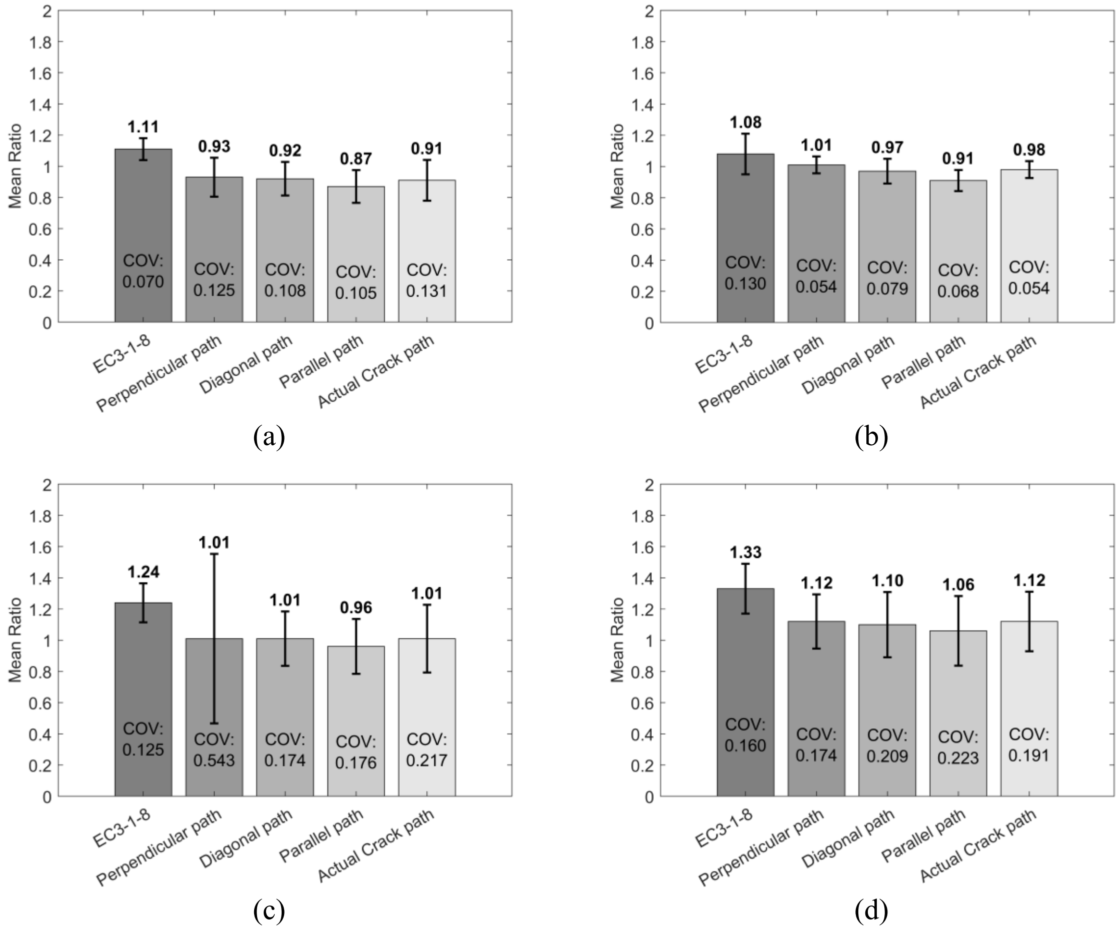

Figure 5.14 Comparison between EC3-1-8 [1] and TCD-PM failure load predictions using different stress extraction paths against experimental failure loads: mean experimental-to-predicted load ratios and COV of CON plates in (a) single-bolt and (b) double-bolt configurations and AM plates in (c) single-bolt and (d) double-bolt configurations.

5.5 Concluding remarks

Based on the static tests, linear elastic finite element models, and the Point Method analysis, it can be concluded that:

a) Linear elastic finite element models of the conventional and additively manufactured notched specimens and bolted joints captured the stress fields required for the Theory of Critical Distances assessments. The predictions were also insensitive to reasonable variations in mesh density and friction.

b) Applying the Point Method, when calibrated using the conventional notched plates, provided broadly acceptable predictions for additively manufactured inner plates of matched thickness.

c) For the as-built wire arc additively manufactured inner plates with mean thicknesses greater than 2 mm, using the calibration obtained from the conventional notched plates led to a clear reduction in accuracy and non-conservative predictions for all specimens. This confirms that the Point Method formulation is sensitive to the values of the calibration material properties being used.
d) Recalibrating the material parameters using as-built wire arc additively manufactured notched specimens improved the predictions for the as-built wire arc additively manufactured inner plates and moved the overall mean absolute error across all stress-distance paths back within an acceptable error range, although a non-conservative tendency remained.
e) Double-bolt configuration as-built wire arc additively manufactured inner plates showed larger errors than the single-bolt specimens even after the recalibration process, indicating that joint configuration influences prediction accuracy.
f) The most accurate stress extraction path varied between specimen groups, with no single path giving both the lowest error and consistently conservative predictions. Therefore, when the actual cracking behaviour is not known, the path providing the most conservative results should be adopted.
g) Compared with EC3-1-8 [1], the Point Method gave mean ratios closer to unity, but was generally less conservative and sensitive to the selected extraction path.

Chapter 6. Machine Learning Models to Predict the Static Failure of Double-Lap Shear Bolted Connections

Forward Commentary

This article titled "Machine Learning Models to Predict the Static Failure of Double-Lap Shear Bolted Connections" was published in *Fatigue and Fracture of Engineering Materials and Structures* on 28 June 2025 [95]. The article evaluates several machine learning models within a unified training and validation framework and reports, for each model, the best predictive capability demonstrated on the dataset, highlighting its potential for this application. The initial concept of integrating machine learning into this work was developed jointly by Hasan Almuhanna and Professor Luca Susmel, and Dr Giacomo Torelli motivated by the increasing use of machine learning as an alternative to traditional prediction methods in structural engineering. Hasan Almuhanna conducted the overall work, including reviewing relevant machine learning methods, compiling the dataset, developing and running the scripts, and writing the manuscript. Professor Luca Susmel and Dr Giacomo contributed through critical review, editing, and technical suggestions throughout the drafting process.

Additional, unpublished work was included as a new section (Section 6.8) to link this paper more directly to the wider study. This section integrates results from the tested specimens and expands the dataset using additional literature data, with particular emphasis on additively manufactured inner plates. This extension demonstrates that machine learning can be a useful alternative predictive approach and that its predictive capability is comparable to codified design-based estimations.

Abstract

This study investigates the potential of machine learning models to predict the failure load and mode of double-lap shear bolted connections. Five algorithms were evaluated: adaptive boosting, artificial neural network, decision trees, support vector machines with radial basis function kernel, and k-nearest neighbours. A dataset comprising 221 experimental and numerical tests with varying input parameters, including different grades of stainless and carbon steel, was used to train the models. Unlike previous studies, the inclusion of diverse

materials enabled the development of more generalizable models. To address data limitations, reduce biases associated with data split, and mitigate overfitting, k-fold cross-validation was adopted instead of the conventional 80/20 split. Results show that both regression and classification models achieved high coefficients of determination across most algorithms. Adaptive boosting delivered the most accurate failure load predictions, while artificial neural network achieved the highest accuracy in classifying failure modes. The findings highlight the potential of well-trained machine learning models to outperform traditional codified methods in accurately predicting the structural response of bolted connections, especially when trained on diverse datasets.

6.1 Introduction

Joining steel frames in structures using bolted connections requires a careful design procedure illustrated in relevant design standards such as BS EN 1993-1-8 [1] or ANSI/AISC 360-22 [3]. The codified design equations considered in these standard codes estimate the failure loads of bolted connections by adopting safety factors that ensure a robust structural performance of the designed joints. The procedure consists of estimating the final design failure load by using simplistic equations to calculate the failure corresponding to several specific modes and then taking the lowest of the obtained values. The methodology recommended by these standard codes results in conservative estimations for the failure mechanism, which may not reflect the failure mechanism accurately [96,97]. While past studies generally indicate conservative estimations, some studies have demonstrated that standard approaches can be non-conservative under specific circumstances [98]. Furthermore, the increasing use of bolted connections with different materials including different grades of steel and stainless steel broadens the range of possible failure mechanisms, thus making codified equations more prone to errors. This issue was observed in past studies where authors noticed cases of underestimations and proposed and validated adjusted design equations that yield a better estimation for the specific material used in the test [79,99–103]. In order to overcome all these issues, innovative tools such as machine learning models can be trained and be turned into reliable design tools suitable for accurately estimating the failure mechanism of such a complex structural part.

Machine learning is a specialised tool under the artificial intelligence umbrella that leverages collected data to analyse complex situations or problems. It learns from the data to build accurate models that can predict outcomes or generate meaningful insights [104]. Jiang et al. [39] and Jiang and Zhao [40] utilized eight machine learning models (see list in Table 6.1) to predict the design failure loads and modes of high-strength and stainless steel bolted connections respectively. These studies collected numerical and experimental design data from past papers, trained the models and tested/validated them to find the one with the best performance. The overall framework adopted by the authors is reported in the flowchart of Figure 6.1. It is worth noting that these authors described adaptive boosting (AdaBoost), light gradient boosting machine (LightGBM), extreme gradient boosting (XGBoost), and cat boosting (CatBoost) as sub-models developed from the decision tree algorithm (DT). Jiang et al. [39] found that all the models gave reliable predictions of failure mechanism, with support vector machine learning model with radial basis function kernel (SVM-RBF) yielding the highest accuracy of predictions for both failure loads and modes. Moreover, the study concluded that as far as failure modes prediction is concerned, the accuracy of the models surpassed the accuracy of estimations obtained through standard approaches, which ranged from 67.9%-85.3%. Similarly, Jiang and Zhao [40] found that all machine learning models yield high accuracy, with SVM giving the best results.

In a similar study, Zakir Sarothi et al. [38] evaluated the performance of 11 different algorithms to predict the failure of double-lap shear bolted connections. In contrast to Jiang et al. [39] and Jiang and Zhao [40] the results reported in Zakir Sarothi et al. study found that random forest (RF) model gave the highest accuracy of predictions. This suggests that the model accuracy may depend on the input variables and quality of collected data, as well as the variation of sources used for the dataset.

This paper collects a dataset of double-lap shear bolted connections and uses it to train five different machine learning models to predict both failure loads and modes using MATLAB software [105]. In contrast to the studies mentioned above, this work incorporates an expanded set of input variables, including material type and yield ratio. These additional variables are added to better describe the dataset, which covers various material types, including different grades of steel and stainless steel. This adjustment ensures that the models effectively capture the complexities associated with these diverse materials and material grades.

Table 6.1: Machine learning models used in previous double-lap shear bolted connections failure predictions.

Machine learning model	Designation	Reference
Decision tree	DT	[38–40]
Random forest	RF	
Support vector machine with radial basis function kernel	SVM-RBF	
K-nearest neighbours	K-NN	
Adaptive boosting	AdaBoost	
Light gradient boosting machine	LightGBM	
Extreme gradient boosting	XGBoost	
Linear regression	LR	[38]
Ridge regression	RR	
Lasso regression	LAR	
Artificial neural network	ANN	

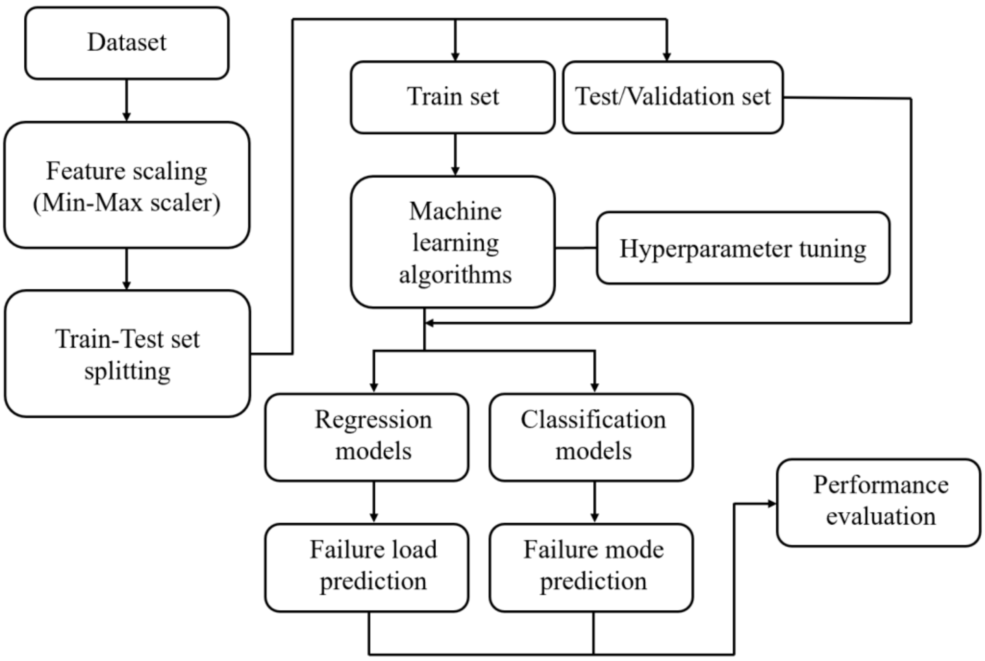

Figure 6.1: Flowchart for constructing the machine learning models. Adapted from [39].

6.2 Dataset

A combination of 221 experimental and numerical tests data were collected from the technical literature (Table 6.2). The collected data consisted of various types of carbon steel, including mild and high-strength grades, and different types of stainless steel. Additionally, three types of bolted connections were included, based on one, two, and four bolts respectively, as schematized in Figure 6.2. The number of bolts in a connection is here denoted as n_b. The considered geometrical variables included (see Figure 6.2) the thickness, t; length, l; breadth, b; end distance, e_1; edge distance, e_2; horizontal pitch distance, p_h; and vertical pitch distance, p_v. Note that, for illustrative purposes, geometrical variables, including the edge distance e_2, are shown symmetric about the centreline; however, the actual test specimens differ from this idealised symmetry. The arrangement of plates with two bolts is not always horizontal. Several specimens have a vertical bolt configuration. Consequently, either p_h or p_v is equal to zero depending on the specific arrangement. Furthermore, mechanical properties obtained from both the parent material characterization and the tests run using bolted connections were considered, namely failure load, F_u; yield ratio, F_y/F_u; and Failure Mode. The use of the yield ratio allowed the models' ability to distinguish between different material types and grades to be enhanced. Other strength-related properties, such as fracture strain or elongation at fracture, were excluded due to inconsistent reporting across sources. Similarly, elastic modulus was omitted given its limited variation and negligible influence on model performance. Figure 6.3 illustrates a general test setup for double-lap shear bolted connections. Since in a test the two inner plates are virtually identical, it is common practice to replace one of them with an auxiliary plate with increased capacity to ensure one single plate is damaged, with this strategy reducing material waste and experiment costs.

The collected data covered three general failure modes including block tearing (BT), edge bearing (EB) of the hole, and net-section tension (NST) – see Figure 6.4. These are the primary failure modes as defined in design standards EN 1993-1-8 [1] and ANSI/AISC 360 [3]. While shear-out is also addressed in ANSI/AISC 360 [3], it can be generally considered a form of bearing failure that occurs when the end distance is insufficient to prevent tearing along the shear planes. Normally, the plates suffer these failure modes at the ultimate load, F_u. However, past studies indicate that additional failure modes, such as end splitting and out-of-plane deformation (curling), particularly during the post-necking stage of testing can occur [79,96,99–103]. The curling failure was especially observed when the weaker plate was placed as an outer rather than an inner plate in double-lap bolted connection tests [79]. However, for the uniformity of the dataset and to be able to use learning models consistently, only the primary failure modes BT, EB, and NST were included. Cases of shear-out were accordingly grouped under EB.

To summarise, the input variables comprised both categorical variables (type of material and failure mode) and numerical variables (n_b, t, l, b, e_1, e_2, P_h, P_v, F_u, and F_y/F_u). The categorical variables were converted into categorical types in the model. This conversion was necessary because machine learning models cannot process text directly. By encoding these variables as categorical types, the model could correctly interpret and distinguish between different categories during prediction.

Table 6.2: Summary of the literature data on double-lap shear bolted connections.

Source of data	Reference	Material	Number of tests, n	Bolted connection type	Primary Failure mode
Experiment	[96]	Grade S235 Mild steel	19	1-bolt and 2-bolts	BT, EB, and NST
Experiment	[99]	S690QL ultra high-strength steel	38	1-bolt and 2-bolts	EB and NST
Experiment	[100]	S550Q high-strength steel	8	1-bolt	EB and NST
		S690Q high-strength steel	8	1-bolt	EB and NST
		S890Q high-strength steel	8	1-bolt	EB and NST
Experiment	[101]	Grade EN 1.4301 austenitic stainless steel	3	1-bolt and 2-bolts	EB
		Grade EN 1.4162 lean duplex stainless steel	2	1-bolt and 2-bolts	EB and NST
Experiment	[102]	S550Q high-strength steel	12	2-bolts	EB
		S690Q high-strength steel	12	2-bolts	EB
		S890Q high-strength steel	12	2-bolts	EB
Numerical modelling	[103]	Grade EN 1.4162 duplex stainless steel	84	1-bolt, 2-bolts, and 4-bolts	EB and NST
Experiment	[79]	Grade EN 1.4512 ferritic stainless steel	15	1-bolt and 2-bolts	EB

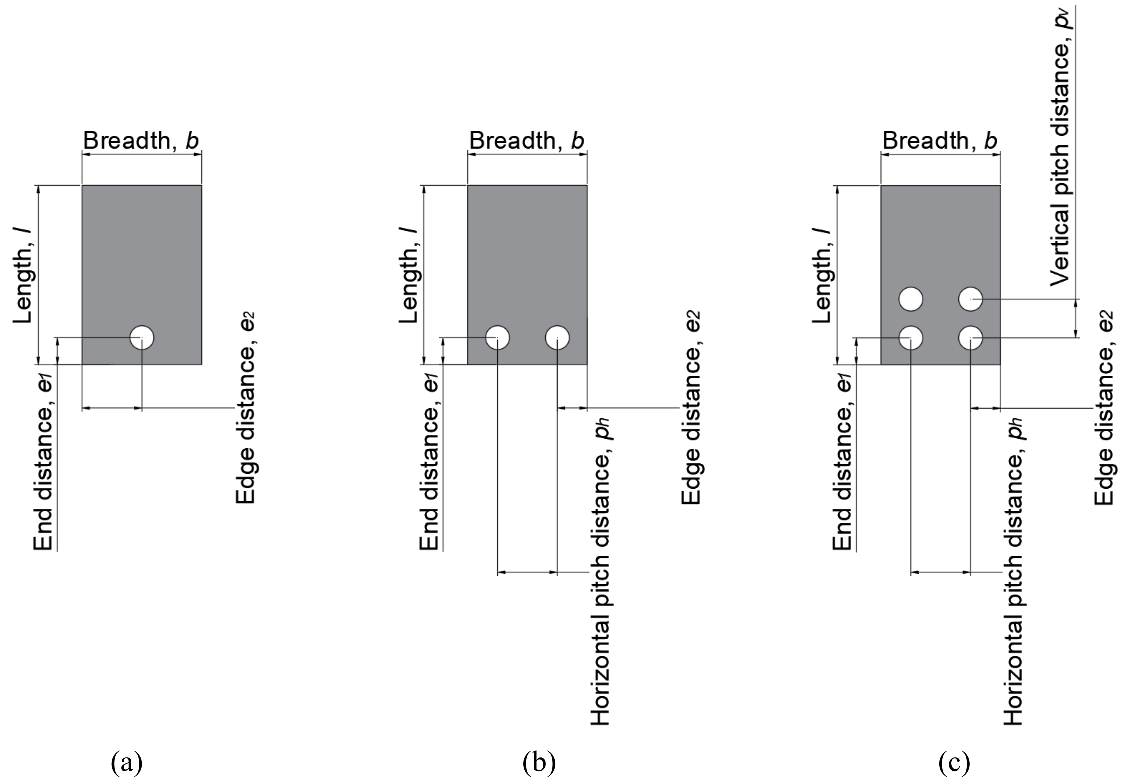

Figure 6.2: Notation for geometrical parameters of the inner plate based on (a) 1-bolt, (b) 2-bolts, and (c) 4-bolts.

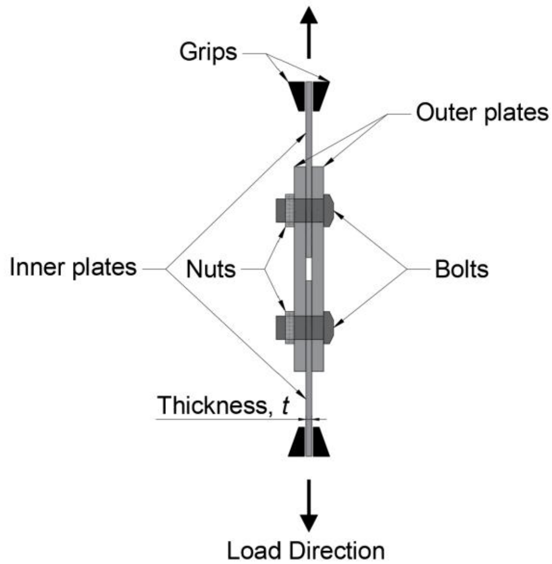

Figure 6.3: Test setup for double-lap shear bolted connections.

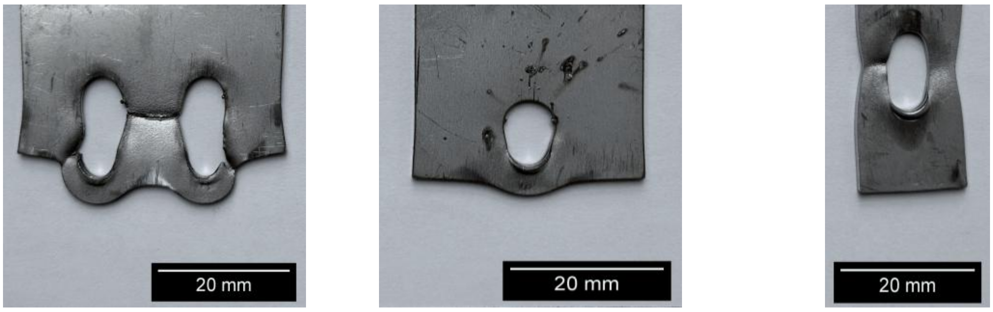

(a) (b) (c)

Figure 6.4: Failure modes of double-lap shear bolted connections: (a) block tearing, (b) edge bearing/shear-out, and (c) net-section tension.

6.3 Machine learning models

6.3.1 Review and pre-processing of the dataset

To characterise the correlation between all input and output variables of the dataset used in the machine learning models, a correlation matrix was created (Figure 6.5). The matrix illustrates the relationships between the variables, with correlation coefficients ranging from +1 to -1. A coefficient of +1 indicates a perfect positive correlation, meaning that as one variable increases, the other increases proportionally. Conversely, a coefficient of -1 indicates a perfect negative correlation, meaning that as one variable increases, the other variable decreases. A coefficient of zero indicates no correlation, meaning that the two variables have no relation. In the collected dataset, there were no coefficients equal to zero, indicating that all variables affect each other. An example of a strong positive relation can be seen between the thickness, t and the diameter of the hole, d_o with a coefficient equal to 0.85. This reflects the fact that larger applied loads require both thicker plates and larger diameter bolts (and thus larger holes) to safely transfer the load. As a result, plate thickness, t, is also highly correlated with the failure force, F_u, as shown in the matrix. This correlation aligns with the codified design equations in Section 4, where the failure force increases proportionally with increasing thickness.

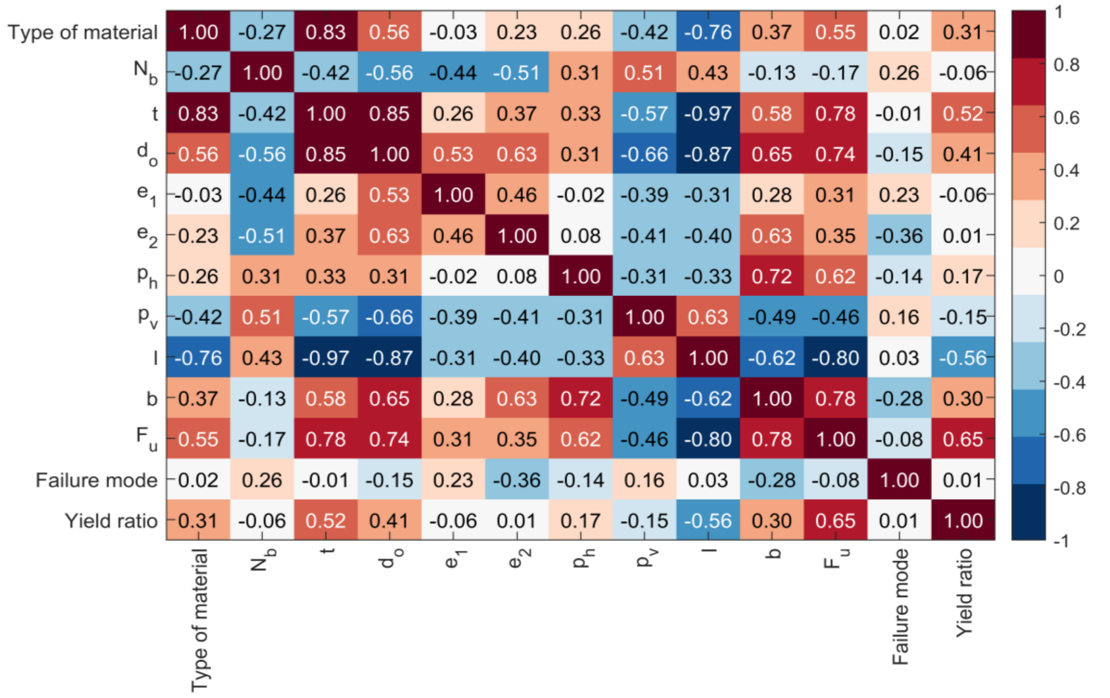

Figure 6.5: Correlation matrix of dataset variables.

Table 6.3 presents the statistics for the geometrical variables, including the coefficient of variation (COV), which is calculated as the ratio of the standard deviation to the mean. The COV provides a measure of relative variability in the data, with higher values indicating greater variation. It is evident that the vertical pitch distance p_v and the horizontal pitch distance p_h show the highest COV. This is largely because, in the dataset, these distances are considered zero for configurations where they do not exist. Specifically, for single-bolted connections, both p_v and p_h are zero, and for double-bolted connections, only p_v is zero. The length of the plates showed the lowest COV since it is almost consistent for the collected dataset. While the length of the plates shows low variability, it does not have a significant influence on the failure mechanisms, as the primary factors driving failure are strongly related to the other geometrical variables and material properties. It is evident that since the thickness in the dataset ranges from 0.77 to 12 mm, making it have relatively high COV reaching 0.68.

Table 6.3: Geometrical variables statistics.

Geometrical variables	Minimum (mm)	Maximum (mm)	Mean (mm)	Median (mm)	COV
Thickness, t	0.77	12.00	6.39	9.90	0.68
Diameter of hole, d_o	9.00	30.00	19.69	22.00	0.38
End distance, e_1	9.00	106.20	40.40	38.74	0.55
Edge distance, e_2	14.00	78.04	36.51	31.08	0.48
horizontal pitch distance, p_h	0	104.00	23.81	0	1.41
Vertical pitch distance, p_v	0	70.00	10.58	0	1.73
Length, l	200.00	440.70	285.80	200.00	0.32
Breadth, b	41.44	216.00	98.24	72.00	0.53

Figure 6.6 displays the frequency (number of occurrences) of different variables of the machine learning dataset. Figure 6.6a indicates a high frequency of edge bearing failure making it the dominant failure mode. In comparison, the net-section tension frequency is approximately half that of the edge bearing. The low occurrence of block tearing is attributed to the relatively low number of 4-bolt configurations, as shown in Figure 6.6b. Additionally, Figure 6.6c represents the types of materials used, with plates produced from duplex stainless steel being the most prevalent within the dataset.

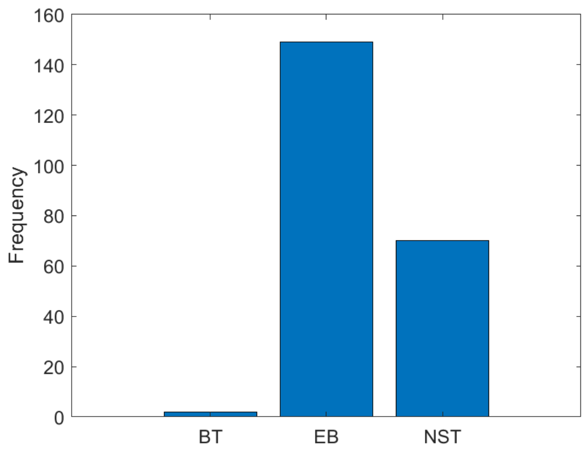

(a)

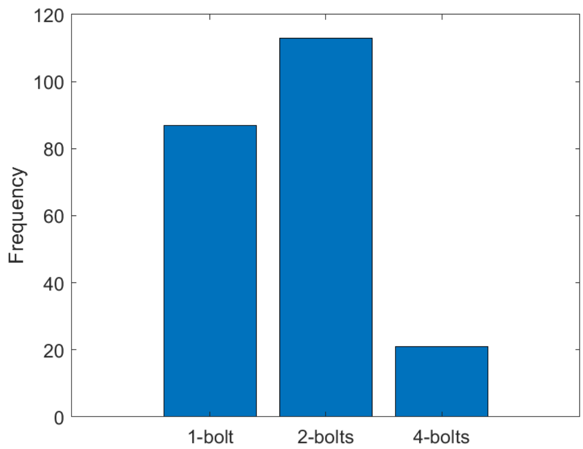

(b)

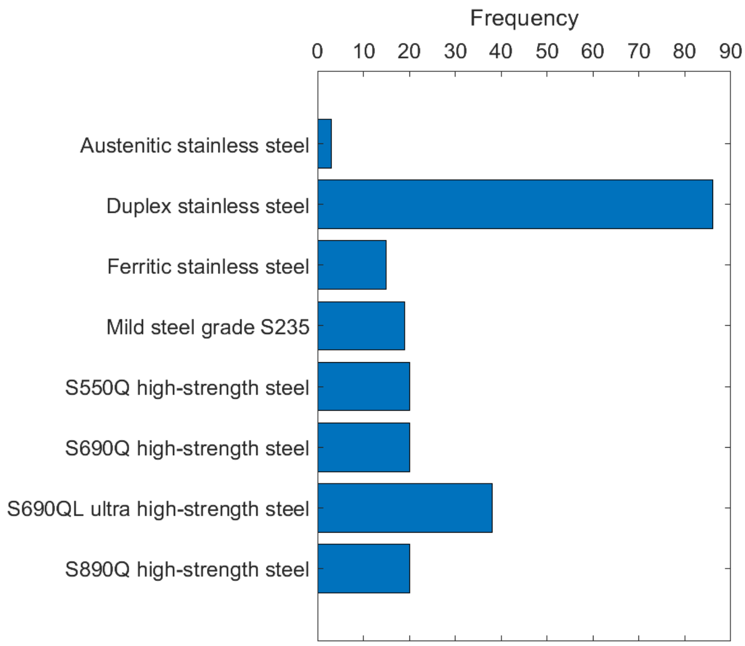

(c)

Figure 6.6: Frequency percentage (%) of input data; (a) failure mode, (b) number of bolts, and (c) material type.

6.3.2 Overview of the used machine learning algorithms

This study explored the predictive capabilities of five different Machine Learning algorithms: adaptive boosting (AdaBoost), decision tree (DT), support vector machine (SVM), k-nearest neighbors (K-NN), and artificial neural network (ANN). The following sections provide an overview of these algorithms, together with a discussion on the implemented cross-validation method.

6.3.2.1 Adaptive boosting (AdaBoost)

Adaptive boosting algorithm (AdaBoost) is a robust ensemble learning technique that improves the accuracy of weak learners, which are simple models that perform slightly better than random guessing. As illustrated in Figure 6.7, AdaBoost ensembling begins by training a weak classifier and then adjusting the distribution of the data, where the classifier with the highest errors is given larger date to enhance the performance of the next weak classifier in subsequent rounds. Then, the classifiers are combined, and weights based on their performance are assigned to create a strong classifier [106]. Because of its demonstrated robustness, AdaBoost is here chosen over other machine learning models, including RF, LightGBM, XGBoost, and CatBoost, as they take a similar approach [107]. In MATLAB, Adaboost sub-models LSBoost and RUSBoost are used as they are specified for regression, and classification models, respectively.

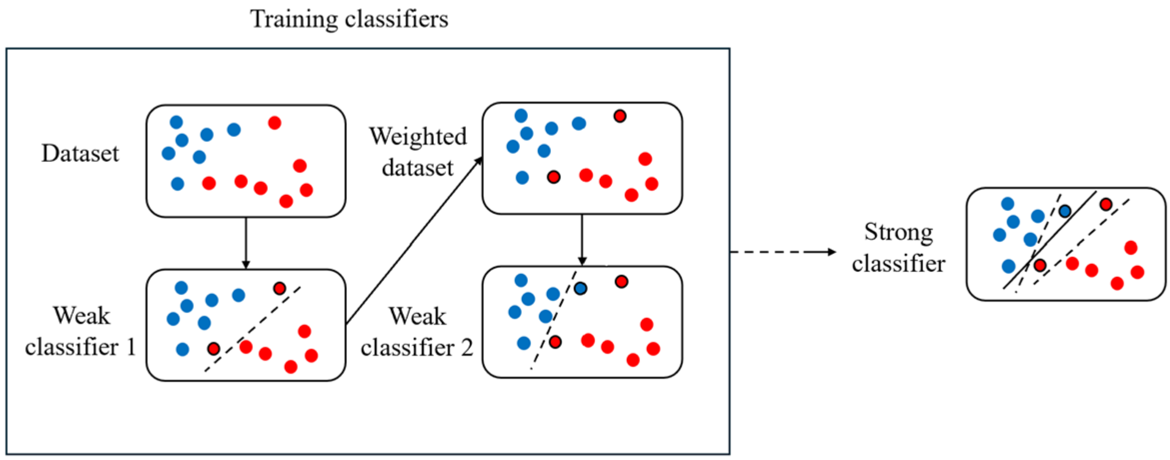

Figure 6.7: Graphical illustration of adaptive boosting (AdaBoost) machine learning model adapted from [108].

6.3.2.2 Decision tree (DT)

The decision tree (DT) model (Figure 6.8) works as a tree-like flowchart that starts with a root node connected with internal nodes by branches. Each node represents an examination of a particular variable, and its corresponding leaf node shows the classification. Based on the outcome of these examinations, the process moves through the branches to reach the leaf node that provides final classification [38]. Although DT is not considered the most effective machine learning algorithm, it is selected in this study because of its simplicity and interpretability, given by the fact that each path from root to leaf can be seen as a clear decision-making process [109].

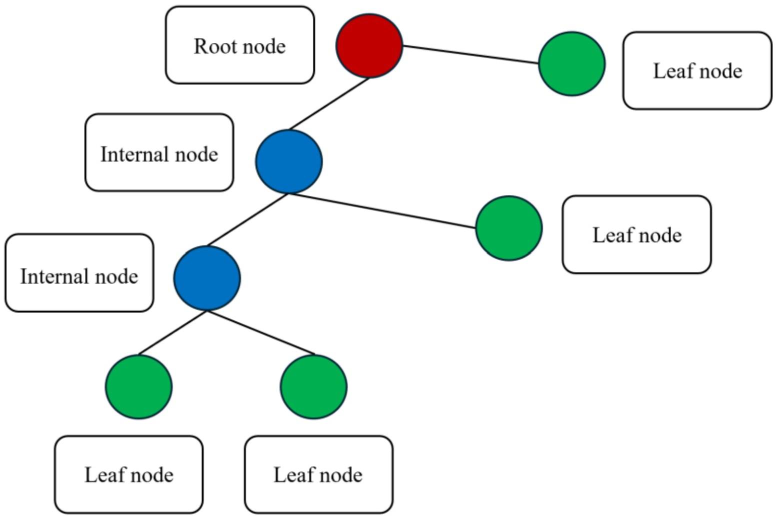

Figure 6.8: Simplified schematic of decision tree (DT) machine learning model.

6.3.2.3 Support vector machine with radial basis function kernel (SVM-RBF)

Support vector machine (SVM) is a type of machine learning model that separates different classes by hyperplanes to create an optimal classifier (Figure 6.9). The boundaries, known as support vectors, are selected to maximise the margin between the hyperplanes and the nearest training data points from each class to reduce the classification error [110]. As seen in Figure 6.10, the purpose of the radial basis function kernel (RBF) is to separate classes for a nonlinear problem when a linear boundary is not possible by transforming the data into higher-dimensional space [111]. SVM is selected in this work owing to its proven effectiveness in high-dimensional spaces and its robustness against overfitting [112,113].

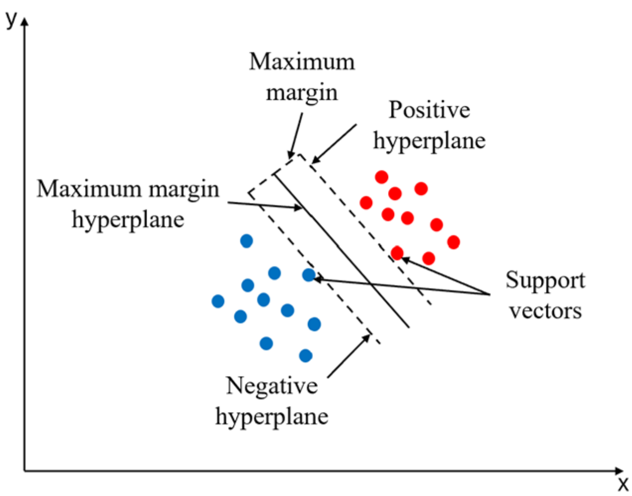

Figure 6.9: Schematic visualisation of one-dimensional support vector machine (SVM) model.

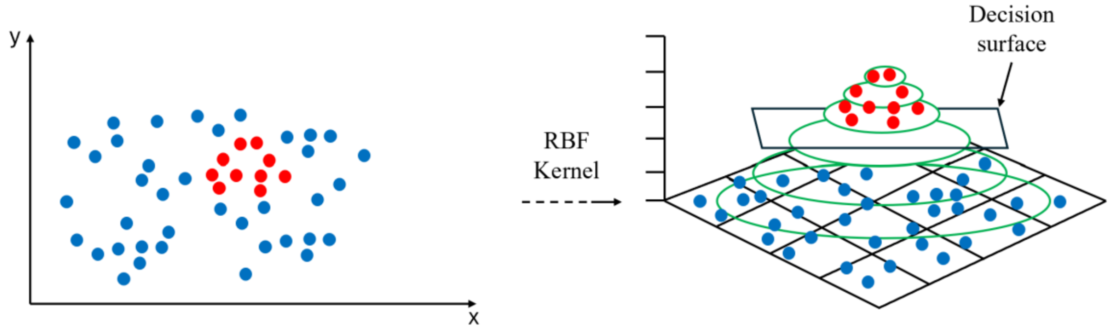

Figure 6.10: Schematics of the use of radial basis function kernel (RBF) for nonlinear problem adapted from [111].

6.3.2.4 K-nearest neighbours (K-NN)

The k-nearest neighbours (K-NN) machine learning model is categorised as a non-parametric since its technique is based on identifying patterns for classifications and predictions, in contrast to other models that depend on applying equations to data [114]. K-NN classifies the unknown variable based on the characteristics of its nearest neighbours, where the neighbourhood closeness is defined by a measure such as the Euclidean distance (Figure 6.11). Noting that major setbacks of this model include the fact that the K value is user-defined input, which can lead to lower accuracy, and the high computational cost associated with its use [115].

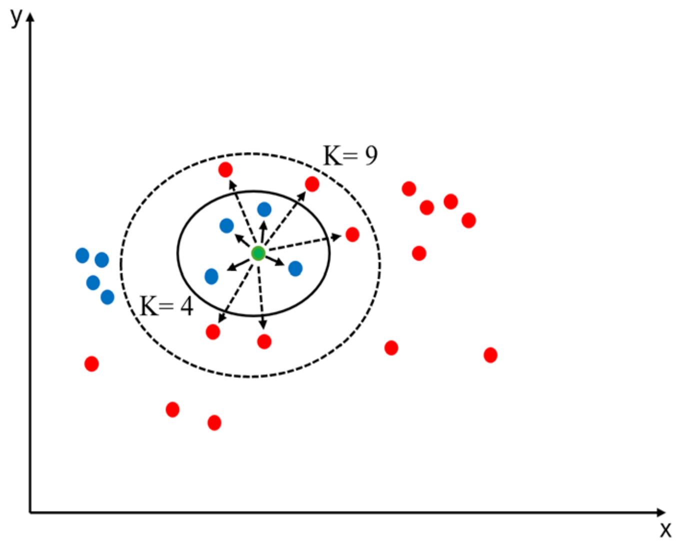

Figure 6.11: Representation of the k-nearest neighbours (K-NN) model adapted from [115].

6.3.2.5 Artificial neural network (ANN)

Artificial neural network (ANN) is a computational model inspired by the functioning of the human brain (Figure 6.12). They consist of layers of interconnected nodes, analogous to neurons, that work together to process information and solve complex tasks. This network takes in input data, process it through hidden layers, and adjust the strength of connections based on detecting patterns in the input data [116]. ANN has proven to be reliable tools in various applications including structural engineering, as evidenced by several studies, see for instance [117–119].

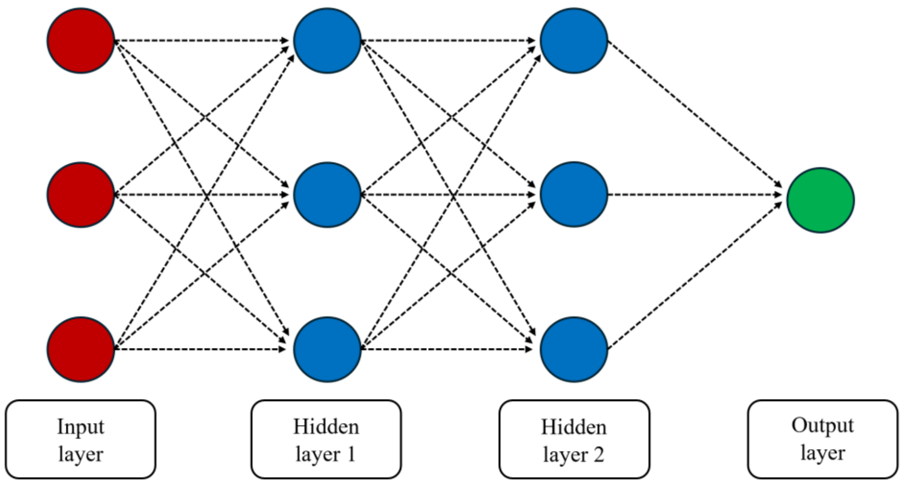

Figure 6.12: Schematic of artificial neural network (ANN). Adapted from [117].

6.3.3 Training the data with cross-validation and setting hyperparameters

MATLAB was the software used to train the models. The common practice of training data is using the hold-out method, splitting them by 80% for training and 20% for testing, with this split remaining fixed. However, k-fold cross-validation is often adopted as a more robust approach that uses all the data for training and validation in each iteration, resulting in improving the accuracy of results for both prediction and classification models [120]. In this study, k-fold cross-validation was implemented for all models by partitioning the data into five k-folds. This means that in each iteration, one-fold (equivalent to 20% of the dataset) was used as the validation set, while the remaining four folds were used for training. It is important to note that increasing the number of folds to higher than five in cross-validation did not lead to significant improvements in models' performance. Therefore, the five folds were considered optimal configuration. Each k-fold was evaluated separately, and the final performance of the regression and classification models was determined based on the validation results from all k-fold trials, specifically reporting the best overall performance across multiple cross-validation runs. This approach helps ensure an unbiased and robust assessment of model performance by reducing the influence of any single fold that may overperform or underperform relative to the others. The hyperparameters used to tune the models were selected after multiple trials to ensure optimal prediction performance while minimising the risk of overfitting. Table 6.4 displays the most important hyperparameters for each model.

Table 6.4: Hyperparameters for each model

Machine learning algorithm	Hyperparameter	Value
SVM-RBF	Regularisation parameter	1000
	Kernel function coefficient	0.8
DT	Maximum number of splits	35
K-NN	Number of neighbours	3
AdaBoost	Number of learning cycles	30
	Learning rate	0.1
ANN	Number of hidden layers	20
	Number of epochs	50

6.4 Codified design estimations

This section presents the equations to estimate the design loads of double-lap shear bolted connections obtained from the most-commonly adopted standard codes, including EN 1993-1-8 [1] and ANSI/AISC 360 [3] for carbon steel, and ANSI/AISC 370-21 [4] for stainless steel. This allows to highlight the differences and similarities between the standards and give a comprehensive understanding of their approaches.

6.4.1 EN 1993-1-8

The reference European standard for the design of steel bolted connection is code EN 1993-1-8 [1]. According to this code, the design bearing resistance, $F_{b,EC3}$ is calculated using Equation (6.1):

$$F_{b,EC3} = n_b \times \frac{k_m \times a_b \times f_u \times d \times t}{\gamma_{M2}} \tag{6.1}$$

Where, k_m is a reduction factor that depends on the steel grade of the plate, f_u is the nominal ultimate tensile strength of the plate, d is the nominal diameter of the bolt, and $\mathrm{a_b}$ is defined as the minimum value between e_1/d_o (edge bearing limit), $3 \times f_{ub}/f_u$ (bolt bearing limit) and 3 (plate bearing/shear-out limit). It is evident that the lowest value of a_b is the value associated with the bearing type that occurs in the connections. The notation γ_{M2} is the partial safety factor for the bolt's resistance

For calculating the design net-section tension resistance, $F_{t,Rd}$, EN 1993-1-8 [1] refers to Equations (6.2), (6.3), (6.4), (6.5), and (6.6):

$$F_{t,Rd} = min[F_{pl,EC3}; F_{n,EC3}] \tag{6.2}$$

$$F_{pl,EC3} = \frac{A_g \times f_y}{\gamma_{M0}} \tag{6.3}$$

$$F_{n,EC3} = \frac{k \times A_{net} \times f_u}{\gamma_{M2}} \tag{6.4}$$

$$A_{net} = A_g - \Delta A_{net} \tag{6.5}$$

$$\Delta A_{net} = n_b \times d_o \times t \tag{6.6}$$

As seen in Equation (6.2), the design net-section tension resistance, $F_{t,EC3}$ of the plate is the minimum value of the design plastic resistance of the gross cross-section, $F_{pl,EC3}$ or the design ultimate resistance of the net cross-section, $F_{n,EC3}$. Equation (6.3) is used to calculate $F_{pl,EC3}$, noting that A_g is the cross-sectional area of the plate and γ_{M0} is the partial safety factor for the resistance of cross sections. For calculating $F_{n,EC3}$, Equation (6.4) is used considering that k is a value that depends on the method implemented for fabricating the hole of the plate, and A_{net} is the net area of the plate cross-section, which is calculated by Equation (6.5) where, ΔA_{net} is the section area deducted considering the presence of the hole/s. The value of ΔA_{net} can be calculated by using Equation (6.6).

The code EN 1993-1-8 [1] standard also recommends that Equation (6.7) is used to estimate the design block tearing resistance of a plate with two or more bolts, $F_{eff,EC3}$.

$$F_{eff,EC3} = \frac{(A_{nt} \times f_u) + min\left[\frac{A_{gv} \times f_y}{\sqrt{3}}; \frac{A_{nv} \times f_u}{\sqrt{3}}\right]}{\gamma_{M2}} \tag{6.7}$$

The parameter A_{nt} is the net area subjected to tension, A_{gv} is the gross area subjected to shear, A_{nv} is the net area subjected to shear, and f_y is the yield strength of the plate.

6.4.2 ANSI/AISC 360 & 370

ANSI/AISC 360 [3] and ANSI/AISC 370 [4] are the reference standards for the design of carbon steel and stainless steel bolted connections, respectively. Similar to EN 1993-1-8 [1], ANSI/AISC 360 [3] gives a set of equations to estimate the failure estimations shear bolted connection, though including additional considerations and different partial safety factors. For instance, equation (6.8) is used to estimate the design bearing capacity, $F_{b,AISC360}$ obtained by either including a Load and Resistance Factor Design (LRFD) in the numerator or an Allowable Strength Design (ASD) partial safety factor in the denominator, with LRFD and ASD having values of 0.75 and 2, respectively. Noting the values of ASD and LRFD are same for all design estimation equations presented for carbon steel.

$$F_{b,AISC360} = n_b \times C_b \times f_u \times d \times t \times (\,LRFD\ or\,\frac{1}{ASD}) \tag{6.8}$$

In Equation (6.8) the coefficient C_b is to be taken as equal to 3 if the bolt-hole deformation at the serviceability limit state is not considered, or 2.4 if it is a design consideration.

Equation (6.9) represents the net-section tension design resistance, $F_{t,AISC360}$ according to ANSI/AISC 360 [3]. Note that this is the same equations represented in EN 1993-1-8 [1] but with different partial safety factors. The values of $N_{pl,AISC360}$ and $N_{n,ASCI360}$ are calculated using Equations (6.10), and (6.11), respectively.

$$F_{t,AISC360} = min[F_{pl,AISC360}; F_{n,AISC360}] \tag{6.9}$$

$$F_{pl,AISC360} = A_g \times f_y \times (\,LRFD\ or\,\frac{1}{ASD}) \tag{6.10}$$

$$F_{n,AISC360} = A_{net} \times f_u \times (\,LRFD\ or\,\frac{1}{ASD}) \tag{6.11}$$

For block tearing design resistance, $F_{eff,AISC360}$, as shown in Equation (6.12) that ANSI/AISC 360 [3] uses the same equation used in EN 1993-1-8 [1] but with the different partial safety factors. Note that the constant factor, which is equal to 0.6, slightly differs from EN 1993-1-8 [1].

$$F_{eff,AISC360} = \big[(A_{nt} \times f_u) + min(0.6 \times A_{gv} \times f_y; 0.6 \times A_{nv} \times f_u)\big] \times (\,LRFD\ or\,\frac{1}{ASD}) \tag{6.12}$$

For stainless steel bolted connections, ANSI/AISC 370 [4] provides similar equations. The only slight adjustment, in relation to the provisions of ANSI/AISC 360 [3] for carbon steel, is for the bearing resistance equation where C_b value is 2.5 for $l_2/d_o > 1.5$ or 2 for $l_2/d_o \leq 1.5$. Note that the parameter l_2 is the distance from the centre of the hole to the centre of the adjacent hole or the edge of the plate.

Overall, EN 1993-1-8 [1] and ANSI/AISC 360&370 [3,4] adopt broadly similar approaches for calculating design resistance, although they differ in the formulation and value of the partial safety factors applied. Both standards are intentionally conservative, incorporating these safety factors to account for uncertainties and to ensure the safe design of structural components. For certain connection configurations where design predictions were not reported in the literature, the missing values were manually calculated using the respective code equations without applying partial safety factors, in order to reflect the nominal resistance and allow for consistent comparison with experimental results. As discussed in Section 5, EN 1993-1-8 [1] generally produced more conservative estimates than ANSI/AISC 360&370 [3,4]. However, due to the omission of safety factors in the manual calculations, the predictions based on ANSI/AISC 360&370 [3,4] in particular tended to overestimate the failure loads, especially in the mid-to-high load range.

6.5 Performance analysis

6.5.1 Regression models

The regression models and the codes' estimations were evaluated by three general metrics, namely the mean absolute error (MAE), the root mean square error (RMSE), and the Coefficient of Determination (R^2), using Equations (6.13), (6.14), and (6.15), respectively. Noting that notation n in the equations represents the amount of data. All reported training metrics for the regression models represent the average performance across the training folds in the k-fold cross-validation. Validation metrics are calculated based on the aggregated predictions from all validation folds, providing an overall assessment of each model's generalisation performance. The regression plots are also based on these aggregated validation predictions.

As shown in Table 6.5, the performance of AdaBoost surpassed that of the other models and codes across all three metrics for both training and validation sets. Notably, AdaBoost achieved a high validation R^2 value of 0.96, indicating strong agreement with experimental results. Figure 6.13a shows that AdaBoost produced a well-fitted regression model when comparing the experimental failure loads, F_u with the predicted values, F_{est}. ANN and DT also performed well, with relatively low prediction errors and R^2 values of 0.95, indicating good model fitness (Figure 6.13b and Figure 6.13c). Although SVM-RBF and K-NN both achieved an R^2 of 0.90, their error patterns differed. The SVM-RBF model exhibited the highest MAE among all models, indicating a considerable average prediction error. As shown in Figure 6.13d, the

SVM-RBF predictions are widely scattered around the ideal line, with noticeable deviations in both directions across the mid and upper load ranges. This dispersion reflects a lack of consistency in prediction, despite reasonable correlation with experimental values. Similarly, the K-NN model reached the highest RMSE, possibly due to poor performance on extreme values. As illustrated in Figure 6.13e, K-NN tended to systematically underestimate the failure loads, particularly at higher values. This bias, along with its high error, demonstrates the model's limited generalization capability compared to the other machine learning approaches.

The codified predictions in EN 1993-1-8 [1] consistently underestimated the failure loads, as shown in Figure 6.13f. In contrast, the ANSI/AISC 360&370 [3,4] predictions exhibited greater scatter and tended to overestimate several values, especially in the mid-to-high load range (Figure 6.13g). This variability contributed to its relatively lower R^2 and higher error values. Overall, Table 6.5 and Figure 6.13 demonstrate that AdaBoost outperformed both code-based approaches in terms of accuracy and consistency, with fewer instances of failure load misprediction. The ANN and DT models, although comparable to EN 1993-1-8 [1] in overall error metrics, provided more balanced predictions with reduced underestimation bias.

$$\text{MAE} = \frac{1}{n}\sum_{i=1}^{n}|F_u - F_{est}| \tag{6.13}$$

$$\text{RMSE} = \sqrt{\frac{1}{n}\sum_{i=1}^{n}(F_u - F_{est})^2} \tag{6.14}$$

$$\text{R}^2 = 1 - \frac{\sum_{i=1}^{n}(F_u - F_{est})^2}{\sum_{i=1}^{n}(F_u - \frac{1}{n}\sum F_u)^2} \tag{6.15}$$

Table 6.5: Evaluation metrics for the models and codes performance.

Machine learning model designation	Train Set			Validation set		
	RMSE (kN)	MAE (kN)	R^2	RMSE (kN)	MAE (kN)	R^2
AdaBoost	28.82	18.61	0.99	46.21	27.71	0.96
ANN	32.52	18.88	0.98	55.98	33.36	0.95
DT	36.04	19.13	0.98	56.31	32.58	0.95
SVM-RBF	33.57	28.28	0.98	76.30	56.12	0.90
K-NN	69.83	36.97	0.92	77.27	48.21	0.90
Codified design estimations	RMSE	MAE	R^2			
EN 1993-1-8	56.64	37.70	0.95			
ANSI/AISC 360&370	95.18	55.61	0.85			

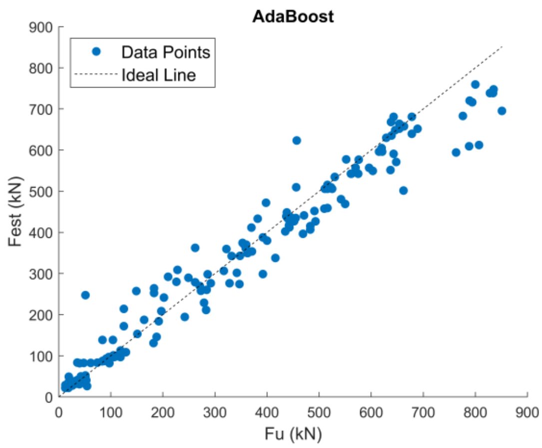

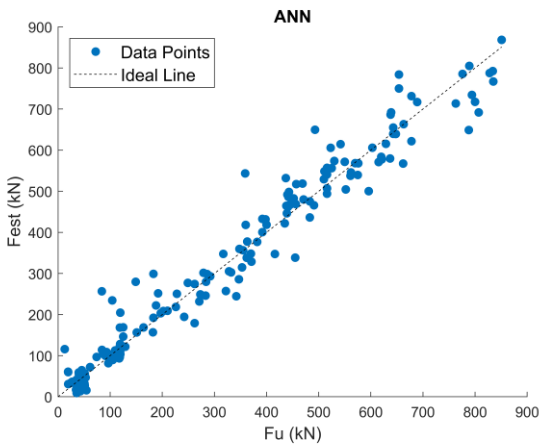

(a) (b)

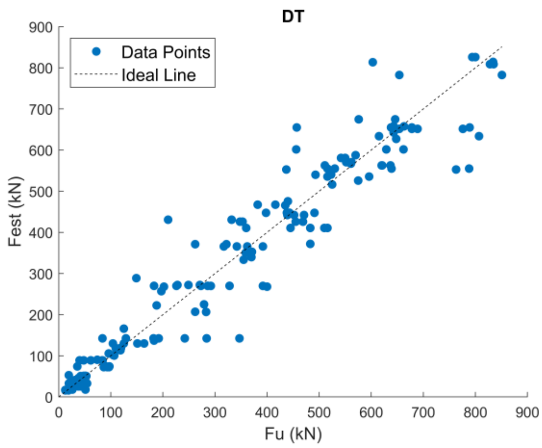

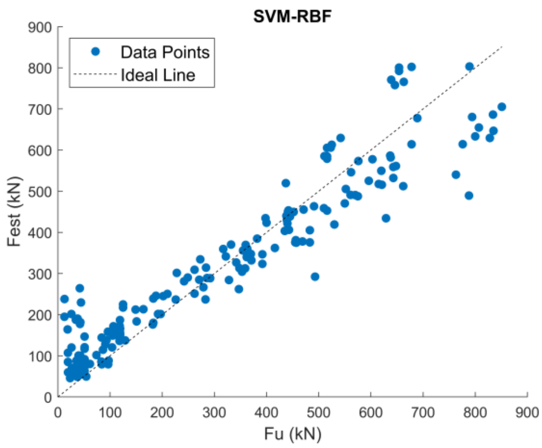

(c) (d)

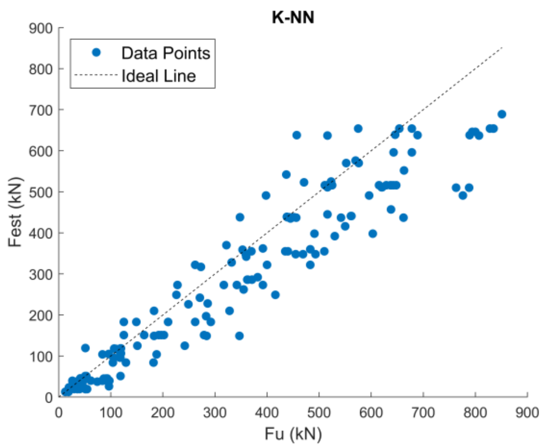

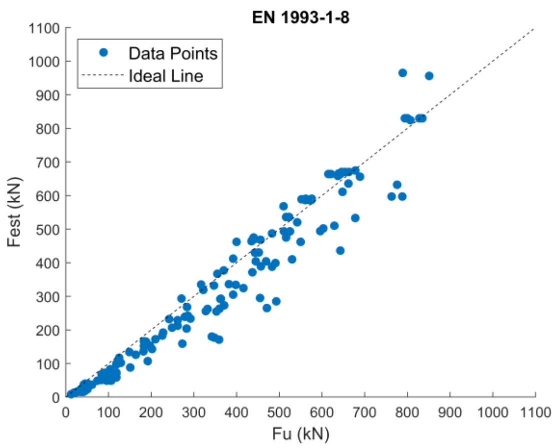

(e) (f)

Figure 6.13: Comparison between actual failure loads, F_u and predicted values, F_{est} by machine learning models and design standards.

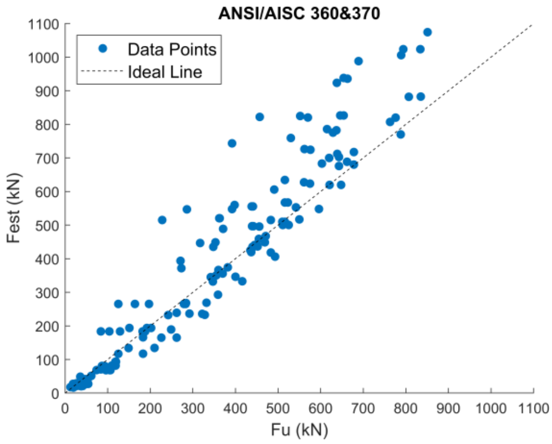

(g)

Figure 6.13: Comparison between actual failure loads, F_u and predicted values, F_{est} by machine learning models and design standards (continued).

6.5.2 Classification models

Figure 6.14 presents the aggregated performance across the validation sets of k-fold cross-validation for the classification models, shown in the form of confusion matrices. The diagonal blue brackets indicate the correctly predicted failure modes, while the light orange brackets highlight the misclassified instances. As described in [121], recall refers to the percentage of actual failure modes that the model correctly identifies, while precision represents the percentage of predicted failure modes that are correct. Accuracy reflects the overall proportion of correct predictions across all failure modes. Among the models, the ANN demonstrated the best overall performance, achieving the highest accuracy of 91.0%, with partial but improved classification of the rare BT failure mode and strong recall and precision scores for EB and NST. The DT and SVM-RBF models also performed well, with accuracies of 90.0% and 89.1%, respectively, showing consistent results for the dominant failure modes EB and NST, but struggling with the rare BT failure mode. The K-NN model achieved an accuracy of 83.7%, correctly identifying one BT case but showing slightly lower recall for the NST failure mode. In contrast, the AdaBoost model underperformed, with a reduced accuracy of 67.9%, primarily due to frequent misclassifications between EB and NST and a complete failure to correctly classify any BT instances. Overall, the results indicate that ANN, followed by DT and SVM-RBF, offered the most reliable classification of failure modes, while AdaBoost’s performance was notably weaker in this task.

AdaBoost Model

Predicted mode \ Actual mode	BT	EB	NST	Recall
BT	0	2	0	0%
EB	26	94	29	63.1%
NST	5	9	56	80.0%
Precision	0%	89.5%	65.9%	67.9% (Accuracy)

(a)

DT Model

Predicted mode \ Actual mode	BT	EB	NST	Recall
BT	0	2	0	0%
EB	1	138	10	92.6%
NST	0	9	61	87.1%
Precision	0%	92.6%	85.9%	90.0% (Accuracy)

(b)

SVM-RBF Model

Predicted mode \ Actual mode	BT	EB	NST	Recall
BT	0	2	0	0%
EB	0	137	12	91.9%
NST	0	10	60	85.7%
Precision	0%	91.9%	83.3%	89.1% (Accuracy)

(c)

K-NN Model

Predicted mode \ Actual mode	BT	EB	NST	Recall
BT	1	1	0	50.0%
EB	0	138	11	92.6%
NST	0	24	46	65.7%
Precision	100%	84.7%	80.7%	83.7% (Accuracy)

(d)

ANN Model

Predicted mode \ Actual mode	BT	EB	NST	Recall
BT	1	1	0	50.0%
EB	0	142	7	95.3%
NST	0	12	58	82.9%
Precision	100%	91.6%	89.2%	91.0% (Accuracy)

(e)

Figure 6.14: Confusion matrices summarising the performance of the classification models for failure mode predictions.

6.6 Discussion of results

The results presented in the previous section show that machine learning approaches offer a robust alternative to traditional codified methods for predicting failure loads and modes in bolted connections. While EN 1993-1-8 [1] generally produced conservative estimates, tending to underestimate failure loads, the ANSI/AISC 360&370 [3,4] predictions, particularly when calculated without safety factors, were observed to overestimate the failure loads in several cases. In contrast, regression models such as AdaBoost, ANN, and DT, as well as classification models including ANN, SVM-RBF, and DT yielded more accurate and balanced predictions. Hence these machine learning tools have a significant potential in the design of bolted connections, where accuracy is critical for achieving a design that is both material-efficient and safe.

The regression and classification analyses provided a clear understanding of the performance of the five models used for the design predictions of double-lap shear bolted connections. AdaBoost stood out as the best-performing model for failure load predictions, achieving the lowest prediction errors and highest R^2 value. The regression analysis highlighted a significant variation in the models' performance for predicting failure loads, reflecting the complexity of estimations for such a large quantity of input variables. For classification, the ANN model achieved the highest accuracy, correctly identifying one of the few instances of the BT failure mode and performing strongly across the other failure modes. The DT and SVM-RBF models also performed reliably, while AdaBoost showed the weakest classification performance. The difference in model rankings between regression and classification tasks suggests that some algorithms are better suited to numerical prediction than categorical classification, depending on how the learning algorithm interacts with the data structure. These findings emphasize the importance of selecting machine learning models that are appropriate to the nature of the prediction task to maximise reliability.

6.7 Conclusions

This study evaluated the effectiveness of machine learning approaches as an alternative to traditional codified design methods for predicting the failure loads and modes of double-lap shear bolted connections across various types of steel and stainless steel materials. Data from experimental results and numerical analyses were collected from past papers and used to train five different models, including adaptive boosting (AdaBoost), decision tree (DT), support vector machine with radial basis function kernel (SVM-RBF), k-nearest neighbours (K-NN), and artificial neural network (ANN). K-fold cross-validation was used, with five folds identified as optimal. Based on the results and discussions, the following conclusions are drawn:

a) Most of the evaluated machine learning models outperformed traditional codified approaches in accuracy for failure load predictions. In particular, AdaBoost, ANN, and DT demonstrated strong performance in this task.
b) AdaBoost achieved the highest R^2 value of 0.96 and the lowest prediction errors across both training and validation sets, indicating excellent fit and generalization.
c) The ANN and DT models showed comparable performance to EN 1993-1-8 [1] in regression, with similar R^2 values (0.95) and slightly lower MAE. Although not the top-performing machine learning models, both ANN and DT outperformed the ANSI/AISC 360&370 [3,4] predictions across all metrics. Both models also provided more balanced predictions and exhibited reduced underestimation bias compared to the conservative trend observed in EN 1993-1-8 [1].
d) Despite its superiority in regression, AdaBoost was the weakest among the machine learning models in classifying failure modes. It misclassified nearly all BT cases and confused EB and NST modes, resulting in the lowest classification accuracy (67.9%). This contrast highlights its limitation in handling imbalanced categorical data and suggests that model suitability varies significantly by prediction type.
e) ANN provided a strong balance between accuracy and robustness. It not only achieved one of the lowest regression errors, rivalling AdaBoost, but also achieved the highest classification accuracy at 91.0%. This highlights its adaptability for both numerical and categorical predictions in structural engineering applications, such as double-lap shear bolted connections.
f) Although hyperparameter tuning values remained consistent across both regression and classification analyses, the models exhibited notable differences in performance. This shows that model performance is strongly influenced by the type of prediction problem.
g) Overall, the study revealed that AdaBoost is the most reliable model for predicting failure loads, while the ANN model demonstrated the best collective performance across both regression and classification tasks. Although this study is limited to static loading, the machine learning framework applied is adaptable and could be extended to predict fatigue-related failure, provided suitable cyclic loading data is available.

6.8 Incorporating AM dataset

6.8.1 Introduction

Building on the published manuscript, the evaluation of the machine learning models was extended by incorporating both CON and AM inner plates from the experimentally tested double-lap shear connections, along with additional AM data collected from the literature. This expanded dataset ensures that the models are trained across all manufacturing conditions of the inner plates, therefore enhancing their predictive capability. In addition, a fixed random seed was introduced into the machine learning script to ensure reproducibility of the modelling results, particularly because the ANN showed noticeable run-to-run variability with the expanded dataset. The full expanded dataset and scripts used for the analysis are provided in Appendix C.

6.8.2 New dataset

In addition to the tested double-lap shear connections, data from the literature on AM and CON plates were incorporated, adding a total of 239 new data points. Of these, 12 correspond to the CON pilot tests of this study, while all the remaining are AM tests from this study and from the literature. This expansion increased the overall dataset to 460. To be consistent with the published work, SO and EB failures in AM plates were grouped under EB, following the same simplification. A distinct failure mode, end splitting (ES), was also introduced, as it was observed exclusively in WAAM plates [28–30]. A summary of the additional collected dataset is presented in Table 6.6. Figure 6.15a-c illustrates the distribution of failure modes, number of bolts, and material types, respectively, after the inclusion of AM data from both the literature, alongside the CON and AM bolted connections tests used in the pilot study.

The CON and AM data were combined since they represented the same type of bolted connection and shared the same core input variables. Material type was retained, while surface condition and print/extraction direction were added as input variables to account for AM-related differences. However, some AM material types and failure modes were represented by fewer cases, which may have affected the prediction and classification accuracy for those categories.

Table 6.6: Summary of the additional literature data on AM double-lap shear bolted connections.

Source of data	Reference	Material	Number of tests, n	Bolted connection type	Primary Failure mode
Experiment	own tests	Austenitic stainless steel	12	1-bolt and 2-bolts	BT, EB, and NST
Experiment	own tests	WAAM austenitic stainless steel (ER316L wire)	45	1-bolt and 2-bolts	BT, EB, and NST
Experiment	own tests	SLM Austenitic stainless steel (powder)	13	1-bolt and 2-bolts	BT, EB, and NST
Experiment	[28]	WAAM Carbon steel (ER70S-6 wire)	60	1-bolt	EB, ES, and NST
Experiment	[29]	WAAM Carbon steel (ER50-6 wire)	36	1-bolt	EB, ES, and NST
Experiment	[32]	WAAM austenitic stainless steel (ER316L wire)	43	1-bolt	EB and NST
Experiment	[30]	WAAM Carbon steel (ER50-6 wire)	30	1-bolt	EB, ES, and NST

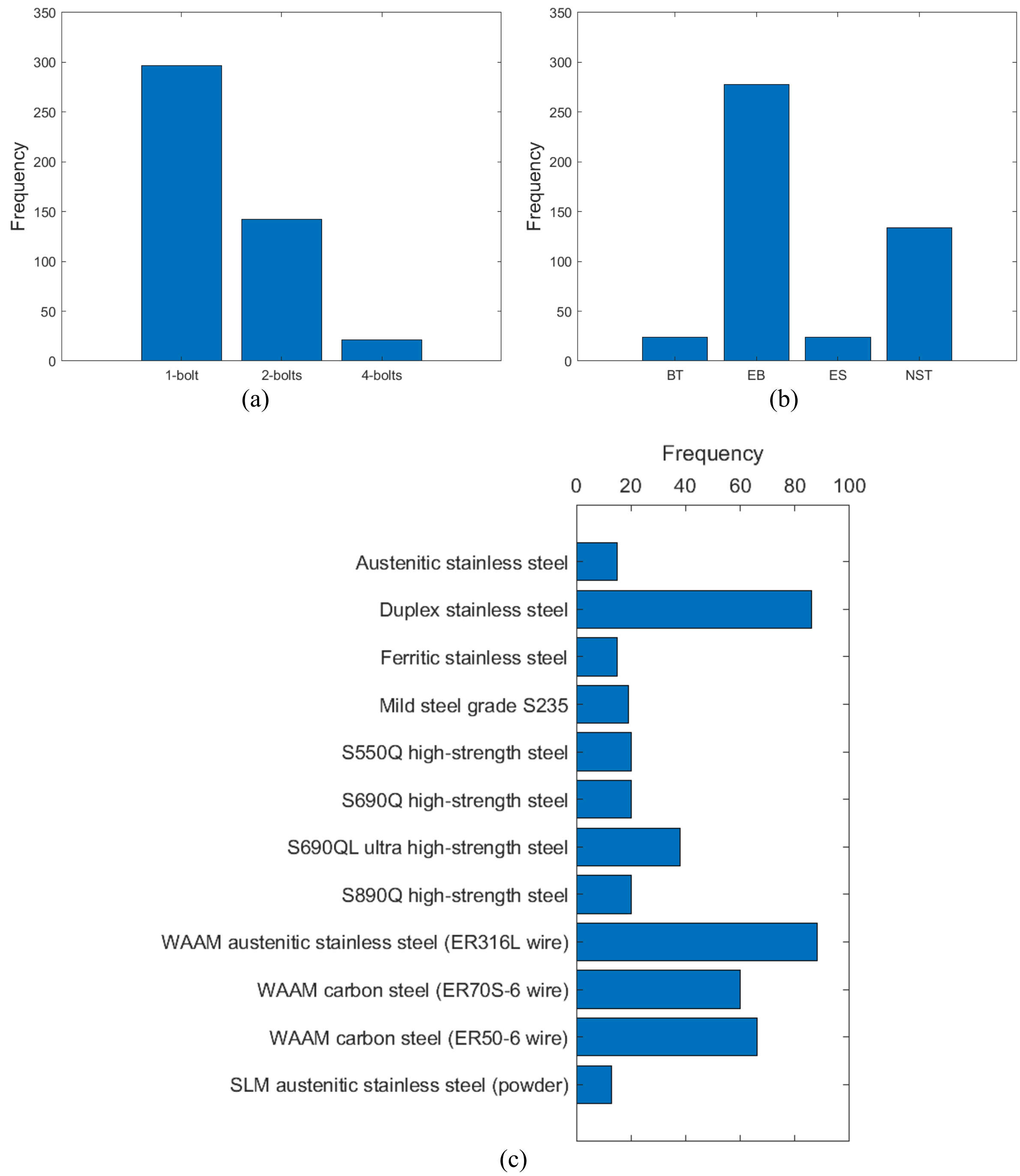

Figure 6.15: Frequency percentage (%) of input data dataset expansion; (a) failure mode, (b) number of bolts, and (c) material type.

6.8.3 Geometrical statistics and correlation matrix of the AM data

Table 6.7 shows the statistics for the geometrical variables for the dataset of both AM tests of the literature and the AM tests of this study. The geometric dataset shows consistent variation for most parameters (COV ranging around 0.4-0.6), but p_h stands out with a COV of 2.67 due to the dominance of single-bolt configurations with zero horizontal pitch and a few double-bolted configurations with large values. It can be observed that p_v is absent from the table because none of the tested AM plates in the collected dataset used bolt configuration that requires a vertical pitch distance.

Figure 6.16 represents the correlation matrix for AM dataset. Noting that for cases where plate lengths were not reported in the literature, they were assumed to be three times the breadth. Similar to the conventional dataset, strong positive relation is evident among the geometric variables, particularly between t and d_o, and between e_1 and e_2, with coefficients above 0.6. This shows the geometric constraints of the plate layout, where adjustments in one parameter necessitate the changes in the others. Furthermore, a correlation between the failure load, F_u and t is also observed in AM plates, with a positive coefficient value of 0.8. In contrast, failure mode shows only weak direct correlations with individual variables, which is consistent with its stronger dependence on combined effects rather than single dimensions. In addition, surface condition and print/extraction direction show negligible correlations with either geometric variables or failure mechanism, suggesting that their influence is secondary compared with geometry and other material conditions. However, these overall findings indicate that while plate design can largely be described through direct geometric relationships, the accurate prediction of failure requires capturing the interaction between multiple geometric and material factors rather than relying on single variable relations alone.

Table 6.7: Geometrical variables statistics for the AM plates.

Geometrical variables	Minimum (mm)	Maximum (mm)	Mean (mm)	Median (mm)	COV
Thickness, t	2.00	9.30	4.52	3.40	0.51
Diameter of hole, d_o	2.00	30.00	18.24	19.71	0.42
End distance, e_1	7.00	118.40	42.77	39.10	0.63
Edge distance, e_2	8.00	74.00	37.74	39.75	0.53
horizontal pitch distance, p_h	0.00	24.00	2.33	0.00	2.67
Length, l	70.00	444.00	237.29	240.30	0.54
Breadth, b	16.00	148.00	81.64	80.10	0.49

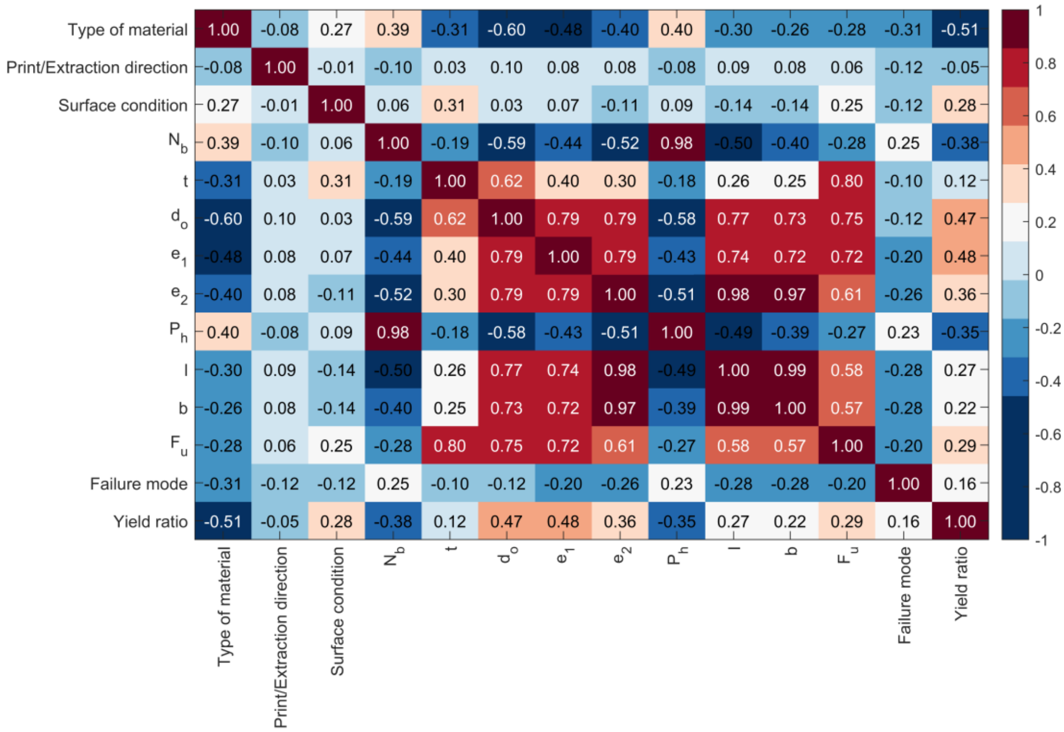

Figure 6.16: Correlation matrix of the new AM dataset variables.

6.8.4 Performance analysis

6.8.4.1 Regression models

Across the training and validation sets, the inclusion of the AM results in the dataset reduced the MAE and RMSE values for most of the machine learning models, although a slight MAE increase was observed for the ANN model. (Table 6.8 and Figure 6.17). AdaBoost remained the best performing model, reaching a validation R^2 of 0.97 and showing strong predictive capability for dataset both without and with the AM results. SVM-RBF appeared to benefit the most from the dataset expansion, with lower training and validation errors and an increase in validation R^2 from 0.90 to 0.94, suggesting that the additional AM data helped define a better regression fit for the RBF kernel. In contrast, the ANN model showed a slight reduction in validation R^2, indicating that its performance was relatively insensitive to the increase in dataset size. The DT model also showed a small reduction in validation R^2, although its error measures improved with the expanded dataset. K-NN remained the weakest model overall, with only limited improvement and the lowest validation R^2 of 0.84. The codified design estimations based on EN 1993-1-8 [1], ANSI/AISC 360 [3], and ANSI/AISC 370 [4] also improved slightly after the inclusion of the AM plates, although they continued to show the same general bias patterns observed previously and remained less accurate than the best performing machine learning models. Overall, the expanded dataset improved the performance of the stronger models, with AdaBoost showing the best agreement with the experimental failure loads and SVM-RBF also benefiting clearly from the inclusion of the AM data.

Table 6.8: Evaluation metrics for the models and codes performance after expanding the dataset with AM bolted connections results.

Machine learning model designation	Train Set			Validation set		
	RMSE (kN)	MAE (kN)	R^2	RMSE (kN)	MAE (kN)	R^2
AdaBoost	23.53	14.78	0.99	36.53	21.20	0.97
ANN	34.62	20.04	0.97	49.81	31.87	0.94
DT	26.10	15.36	0.98	46.81	25.62	0.94
SVM-RBF	17.23	14.24	0.99	46.87	29.80	0.94
K-NN	59.14	29.14	0.91	79.06	44.59	0.84
Codified design estimations	RMSE	MAE	R^2			
EN 1993-1-8	42.92	26.69	0.95			
ANSI/AISC 360&370	69.29	35.84	0.88			

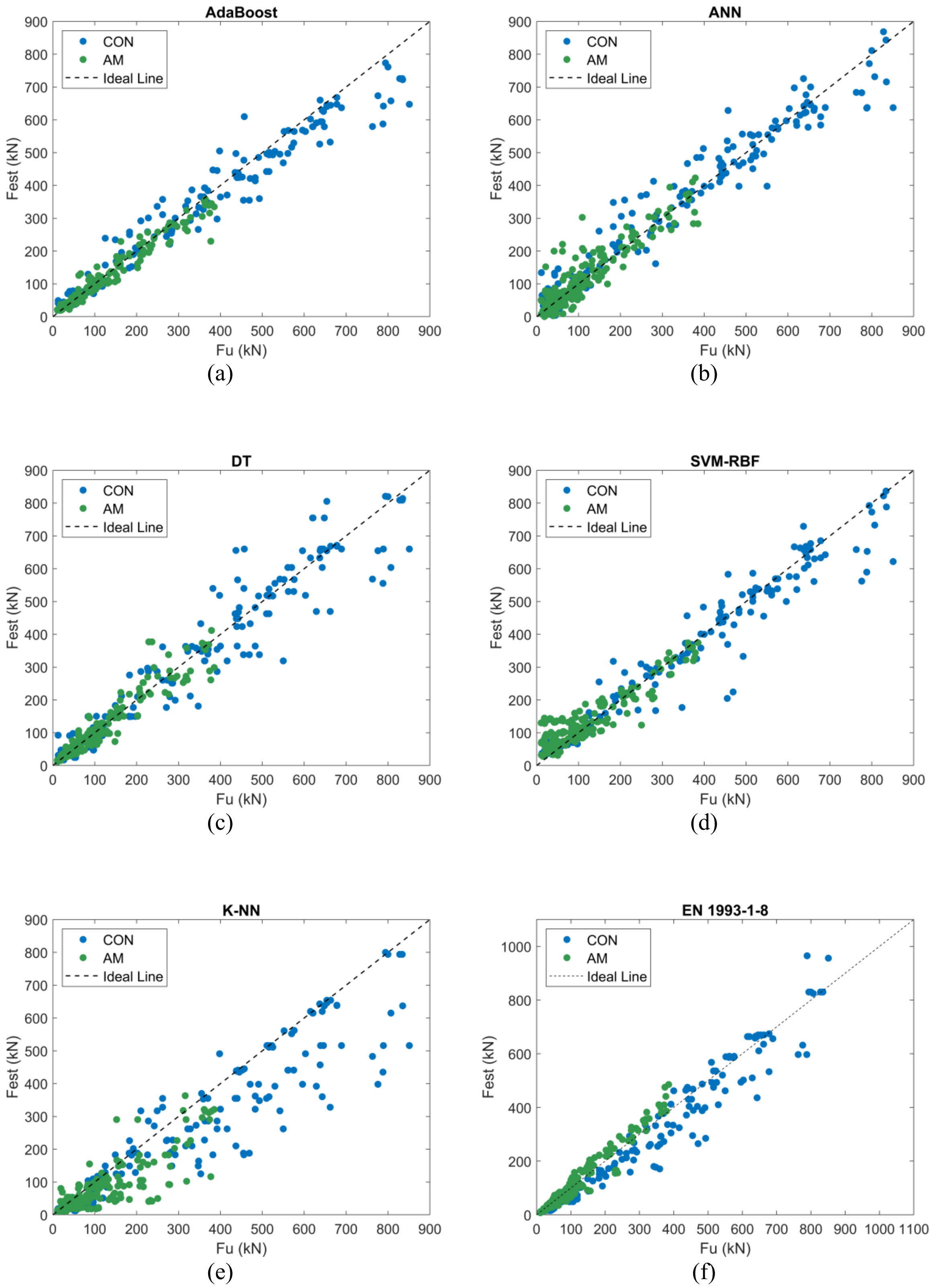

Figure 6.17: Comparison between actual failure loads, F_u and predicted values, F_{est} by machine learning models and design standards after expanding the dataset with AM bolted connections; conventional and AM specimens are shown in blue and green, respectively.

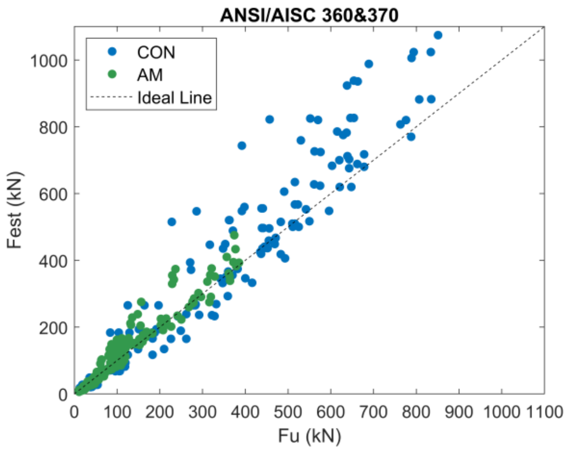

(g)

Figure 6.17: Comparison between actual failure loads, F_u and predicted values, F_{est} by machine learning models and design standards after expanding the dataset with AM bolted connections results; conventional and AM specimens are shown in blue and green, respectively (continued).

6.8.4.2 Classification models

Figure 6.18 shows the confusion matrices for the classification models after the dataset was expanded, and the ES failure mode associated with AM plates was included. With the exception of AdaBoost, the classification models showed a clear drop in overall accuracy, in contrast to the regression models, which improved with the same dataset expansion. AdaBoost improved to 75.4% accuracy, whereas DT decreased to 80.4%, SVM-RBF to 77.4%, ANN to 80.9%, and K-NN further to 71.3%. This decline is likely due to the greater class imbalance introduced by the expanded dataset, which reduced the precision and recall associated with the less represented BT and ES failure modes. Overall, ANN provided the best classification performance. These results also suggest that the relationship between the individual features and the corresponding failure modes is less distinct than that for failure load prediction.

AdaBoost Model

Predicted mode \ Actual mode	BT	EB	ES	NST	Recall
BT	19	2	2	1	79.2%
EB	8	217	26	27	78.1%
ES	0	2	22	0	91.7%
NST	6	24	15	89	66.4%
Precision	57.6%	88.6%	33.8%	76.1%	75.4% Accuracy

(a)

DT Model

Predicted mode \ Actual mode	BT	EB	ES	NST	Recall
BT	13	6	1	4	54.2%
EB	6	238	10	24	85.6%
ES	1	9	14	0	58.3%
NST	1	22	6	105	78.4%
Precision	61.9%	86.5%	45.2%	78.9%	80.4% Accuracy

(b)

SVM-RBF Model

Predicted mode \ Actual mode	BT	EB	ES	NST	Recall
BT	12	8	2	2	50.0%
EB	9	238	9	22	85.6%
ES	0	8	15	1	62.5%
NST	8	32	3	91	67.9%
Precision	41.4%	83.2%	51.7%	78.4%	77.4% Accuracy

(c)

K-NN Model

Predicted mode \ Actual mode	BT	EB	ES	NST	Recall
BT	9	10	2	3	37.5%
EB	9	238	5	26	85.6%
ES	0	9	14	1	58.3%
NST	11	49	7	67	50.0%
Precision	31.0%	77.0%	50.0%	69.1%	71.3% Accuracy

(d)

Figure 6.18: Classification models after expanding the dataset with AM bolted connections results.

ANN Model

		Actual mode				
Predicted mode		BT	EB	ES	NST	Recall
	BT	6	12	1	5	25.0%
	EB	3	258	3	14	92.8%
	ES	0	9	12	3	50.0%
	NST	3	31	4	96	71.6%
	Precision	50.0%	83.2%	60.0%	81.4%	80.9%
						Accuracy

(e)

Figure 6.18: Classification models after expanding the dataset with AM bolted connections results (continued).

6.8.5 Additional Conclusions after Expanding the dataset

After performing the reanalysis with expanding the dataset, it can be concluded that:

a) Expanding the dataset to include additional CON and AM specimens noticeably improved the MAE and RMSE of most of the regression models.

b) The AdaBoost model maintained the best performance among all machine learning models and design code predictions, with its validation R^2 increasing to 0.97 and its RMSE and MAE decreasing, confirming its robustness when trained on a larger dataset of double-lap bolted connections.

c) It is evident that the SVM-RBF model benefited most from the larger dataset, with its R^2 rising from 0.90 to 0.94, demonstrating that the added CON and AM dataset improved performance and helped the model capture the load capacity more reliably.

d) In contrast to the regression models, most classification models showed lower accuracy after the dataset was expanded and the ES failure mode was introduced. ANN provided the best classification performance with an accuracy of 80.9%, followed by DT at 80.4%. AdaBoost was the only model that improved, reaching 75.4%.

e) The reduction in classification performance is likely due to the greater class imbalance in the expanded dataset, together with the relatively low occurrence of BT and ES failure modes, which made the distinction between failure modes less clear.

f) These results show that adding more data is not necessarily beneficial in the same way for all prediction tasks. While the expanded dataset improved the regression models, it was less beneficial for failure mode classification.

Part III. Conclusions

Chapter 7. Overall Conclusions and Future Work

7.1 Synthesis of results and conclusions

This thesis investigated the static failure behaviour of hybrid double-lap shear bolted connections with 316L stainless steel inner plates made from conventional and additively manufactured materials. The thesis consists of articles presenting experimental testing, codified and literature-based strength estimations, TCD-based local stress assessment, and machine learning prediction. Based on the work presented in this thesis, the following overall conclusions, aligned with the research objectives, can be drawn:

Objective a): The results showed that the manufacturing methods varied in terms of mechanical properties of the test coupons. The conventional 316L stainless steel material showed the best overall tensile behaviour, while the wire arc additively manufactured (WAAM) material was more sensitive to extraction. The selective laser melting (SLM) material showed relatively high strength, but lower ductility. At the connection level, when the plate thickness was consistent between plates made through different manufacturing methods, the additive manufactured (AM) inner plates generally achieved load capacities close to those of the CON plates. This shows that the main difference was not in the global resistance itself, but more in the ductility and crack behaviour. The results also confirmed that the geometric design variables still play the main role in governing the static performance of the double-lap shear bolted connections, regardless of the manufacturing method. Variables such as end distance, edge distance, plate width, and horizontal pitch distance had a strong effect on the observed failure mode and response. This means that the behaviour of these joints is still mainly controlled by geometry, while the manufacturing method affects how cracking and deformation develop locally. The experimental observations showed that the AM plates, specifically the WAAM plates extracted diagonally with respect to the printing direction, can exhibit crack paths and deformation behaviour that differ from those of the CON plates. In contrast, the SLM plates showed more consistent behaviour and limited sensitivity to print orientation and surface condition within the tested configurations. In general, most AM plates still reached failure modes similar to those of the CON plates, which supports the use of AM inner plates in such connections when the design variables and manufacturing conditions are selected properly for structural engineering parts.

Objective b): The comparison with codified and literature-based design estimations showed that the current design standards do not yet represent AM double-lap shear bolted connections well. The stainless steel provisions were generally overly conservative, especially for the AM plates, while EC3-1-8 gave closer estimations even though it was developed for carbon steel connections. The literature-based equations gave the closest agreement with the experimental results. Overall, these findings show that the current codified methods are not yet fully suitable for WAAM and SLM inner plates and that there is a need for improved equations or modification factors based on AM-specific behaviour.

Objective c): The Theory of Critical Distances (TCD) can be applied to double-lap shear bolted connections and used as a local stress-based method for static failure assessment. The point method (TCD-PM), combined with linear elastic FE modelling, gave acceptable predictions for the CON inner plates and also for AM inner plates of matched thickness when the calibration was based on CON notched specimens. This shows that the bolt hole can be treated as a stress raiser and that a local stress-based framework can be used to assess static failure in these types of connections. However, the transferability of the TCD approach to the as-built WAAM (WAAM-AB) showed a reduction in accuracy. Recalibrating the PM method using WAAM-AB notched specimens improved the predictions and brought the overall error back within an acceptable range, although some non-conservative tendency remained and double-bolt configuration predictions tended to have higher errors.

Objective d): The machine learning results showed that data-driven models can provide a strong alternative to codified design methods for predicting the failure load of double-lap shear bolted connections. Adaptive boosting (AdaBoost) model gave the best failure load predictions and outperformed the codified design estimations. Artificial neural network (ANN) model gave the best overall balance when both regression and classification were considered. This shows that machine learning models can capture the combined influence of several interacting variables on the load capacity more effectively than simplified design equations. The expanded machine learning dataset showed that increasing the amount of data was more beneficial for failure load prediction than for failure mode classification. The larger dataset generally improved the regression performance of most models, with AdaBoost remaining the best model and Support vector machine with radial basis function kernel (SVM-RBF) model showing clear improvement. In contrast, the classification accuracy of most models dropped after the dataset expansion and the introduction of the end-splitting (ES) failure mode. This was mainly due to the increased class imbalance and the limited number of block tearing (BT) and ES cases.

Therefore, the results showed that expanding the dataset does not necessarily improve the performance of classification models.

Overall, this thesis addressed the main research gaps identified in the literature by providing an experimental and predictive assessment of CON, WAAM, and SLM 316L stainless steel hybrid double-lap shear bolted connections under comparable conditions. The results showed that, although the manufacturing method and extraction direction influence the plain material response and crack behaviour, the AM inner plates can achieve load capacities similar to those of the CON plates. The work also showed that a full assessment of such joints is better achieved by a comprehensive framework combining experimental observations with analytical estimations, local stress-based methods, and machine learning models rather than relying on only one approach.

7.2 Future work

By achieving the main objectives of the thesis, it is important to acknowledge that further work is still needed in a number of areas.

a) Further work at the microstructural level is needed to capture the full behaviour of WAAM and SLM 316L stainless steel materials. In particular, future work should relate the observed behaviour of the investigated plates to grain morphology, anisotropy, and residual stress.
b) Additional experimental work is also needed to expand the range of tested plates to three-bolt and other configurations, as well as other geometries, to broaden the current understanding of AM plates.
c) The predictive methods used in this thesis should also be extended beyond static loading. Since structural connections are also subjected to cyclic loading, future work should examine whether the same TCD-based analysis and machine learning methods can be applied under this loading condition.
d) Future work could explore using machine learning to support the design of AM hybrid bolted connections. Instead of only predicting the resistance of a proposed connection, the model could help identify suitable geometry, bolt configuration and manufacturing conditions to meet a required resistance before fabrication and testing.

References

[1] BS EN 1993-1-8. Eurocode 3. Design of steel structures. Part 1-8: joints 2024.

[2] BS EN 1993-1-4. Eurocode 3. Design of steel structures. Part 1-4: Stainless steel structures 2025.

[3] ANSI/AISC 360. Specification for Structural Steel Buildings 2022.

[4] ANSI/AISC 370. Specification for Structural Stainless Steel Buildings 2021.

[5] Liu XC, Cui FY, Jiang ZQ, Wang XQ, Xu L, Shang ZX, et al. Tension–bend–shear capacity of bolted-flange connection for square steel tube column. Eng Struct 2019;201. https://doi.org/10.1016/j.engstruct.2019.109798.

[6] Paolini A, Kollmannsberger S, Rank E. Additive manufacturing in construction: A review on processes, applications, and digital planning methods. Addit Manuf 2019;30. https://doi.org/10.1016/j.addma.2019.100894.

[7] Evans SI, Wang J, Qin J, He Y, Shepherd P, Ding J. A review of WAAM for steel construction – Manufacturing, material and geometric properties, design, and future directions. Structures 2022;44:1506–22. https://doi.org/10.1016/j.istruc.2022.08.084.

[8] Laghi V, Palermo M, Tonelli L, Gasparini G, Ceschini L, Trombetti T. Tensile properties and microstructural features of 304L austenitic stainless steel produced by wire-and-arc additive manufacturing. International Journal of Advanced Manufacturing Technology 2020;106:3693–705. https://doi.org/10.1007/s00170-019-04868-8.

[9] Gardner L. Metal additive manufacturing in structural engineering – review, advances, opportunities and outlook. Structures 2023;47:2178–93. https://doi.org/10.1016/j.istruc.2022.12.039.

[10] Wu P, Wang J, Wang X. A critical review of the use of 3-D printing in the construction industry. Autom Constr 2016;68:21–31. https://doi.org/10.1016/j.autcon.2016.04.005.

[11] Lange J, Feucht T, Erven M. 3D printing with steel: Additive Manufacturing for connections and structures. Steel Construction 2020;13:144–53. https://doi.org/10.1002/stco.202000031.

[12] BS EN ISO/ASTM 52900. Additive manufacturing — General principles — Fundamentals and vocabulary 2021.

[13] Kyvelou P, Slack H, Daskalaki Mountanou D, Wadee MA, Britton T Ben, Buchanan C, et al. Mechanical and microstructural testing of wire and arc additively manufactured sheet material. Mater Des 2020;192. https://doi.org/10.1016/j.matdes.2020.108675.

[14] Kühne R, Feldmann M, Citarelli S, Reisgen U, Sharma R, Oster L. 3D printing in steel construction with the automated Wire Arc Additive Manufacturing. Ce/Papers 2019;3:577–83. https://doi.org/10.1002/cepa.1103.

[15] Zhang C, Qiu Z, Zhu H, Wang Z, Muránsky O, Ionescu M, et al. On the effect of heat input and interpass temperature on the performance of inconel 625 alloy deposited using wire arc additive manufacturing–cold metal transfer process. Metals (Basel) 2022;12. https://doi.org/10.3390/met12010046.

[16] Tankova T, Andrade D, Branco R, Zhu C, Rodrigues D, Simões da Silva L. Characterization of robotized CMT-WAAM carbon steel. J Constr Steel Res 2022;199. https://doi.org/10.1016/j.jcsr.2022.107624.

[17] Sing SL, An J, Yeong WY, Wiria FE. Laser and electron-beam powder-bed additive manufacturing of metallic implants: A review on processes, materials and designs. Journal of Orthopaedic Research 2016;34:369–85. https://doi.org/10.1002/jor.23075.

[18] Ahmed A, Majeed A, Atta Z, Jia G. Dimensional quality and distortion analysis of thin-walled alloy parts of AlSi10Mg manufactured by selective laser melting. Journal of Manufacturing and Materials Processing 2019;3. https://doi.org/10.3390/jmmp3020051.

[19] Huang C, Kyvelou P, Gardner L. Stress-strain curves for wire arc additively manufactured steels. Eng Struct 2023;279. https://doi.org/10.1016/j.engstruct.2023.115628.

[20] AWS A5.18/A5.18M. Specification for Carbon Steel Electrodes and Rods for Gas Shielded Arc Welding 2005.

[21] AWS A5.28/A5.28M. Specification for low-alloy steel electrodes and rods for gas shielded arc welding 2022:50.

[22] Huang C, Kyvelou P, Zhang R, Ben Britton T, Gardner L. Mechanical testing and microstructural analysis of wire arc additively manufactured steels. Mater Des 2022;216. https://doi.org/10.1016/j.matdes.2022.110544.

[23] Gu J, Gao M, Yang S, Bai J, Zhai Y, Ding J. Microstructure, defects, and mechanical properties of wire + arc additively manufactured Al[sbnd]Cu4.3-Mg1.5 alloy. Mater Des 2020;186. https://doi.org/10.1016/j.matdes.2019.108357.

[24] Taha MA, Yousef AF, Gany KA, Sabour HA. On selective laser melting of ultra high carbon steel: Effect of scan speed and post heat treatment. Materwiss Werksttech 2012;43:913–23. https://doi.org/10.1002/mawe.201200030.

[25] Sanjari M, Mahmoudiniya M, Pirgazi H, Tamimi S, Ghoncheh MH, Shahriairi A, et al. Microstructure, texture, and anisotropic mechanical behavior of selective laser melted maraging stainless steels. Mater Charact 2022;192. https://doi.org/10.1016/j.matchar.2022.112185.

[26] Bartolomeu F, Buciumeanu M, Pinto E, Alves N, Carvalho O, Silva FS, et al. 316L stainless steel mechanical and tribological behavior—A comparison between selective laser melting, hot pressing and conventional casting. Addit Manuf 2017;16:81–9. https://doi.org/10.1016/j.addma.2017.05.007.

[27] Guo X, Kyvelou P, Ye J, Teh LH, Gardner L. Experimental investigation of wire arc additively manufactured steel single-lap shear bolted connections. Thin-Walled Structures 2022;181. https://doi.org/10.1016/j.tws.2022.110029.

[28] Guo X, Kyvelou P, Ye J, Teh LH, Gardner L. Experimental study of DED-arc additively manufactured steel double-lap shear bolted connections. Eng Struct 2023;281. https://doi.org/10.1016/j.engstruct.2023.115736.

[29] Liu Y, Ye J, Yang Y, Quan G, Wang Z, Zhao W, et al. Experimental study on wire and arc additively manufactured steel double-shear bolted connections. Journal of Building Engineering 2023;76. https://doi.org/10.1016/j.jobe.2023.107330.

[30] Liu Y, Ye J, He J, Lu H, Quan G, Wang Z, et al. Testing and design of wire and arc additively manufactured steel double-shear bolted connections with thick plates. J Constr Steel Res 2025;224. https://doi.org/10.1016/j.jcsr.2024.109069.

[31] Zuo W, Chen MT, Zhao O, Su A, Liu SW, Xu F, et al. Behavior of wire arc additively manufactured 316L austenitic stainless steel single shear bolted connections. Thin-Walled Structures 2024;202. https://doi.org/10.1016/j.tws.2024.112075.

[32] Zuo W, Chen MT, Liu SW, Yun X, Zhao O, Huang Y, et al. Experimental investigation on double-lap shear behavior of 3D printed austenitic stainless steel bolted connections. Eng Struct 2024;317. https://doi.org/10.1016/j.engstruct.2024.118501.

[33] Zuo W, Chen MT, Zhao O, Su A, Liu SW, Yun X, et al. Structural performance of wire arc additively manufactured duplex stainless steel single-lap shear bolted connections. Eng Struct 2024;319. https://doi.org/10.1016/j.engstruct.2024.118706.

[34] Kong Z, Li R, Wang X, Hu N, Jin Y, Tao Q, et al. Shear capacity of additively manufactured stainless steel bolted connections after fire. Eng Struct 2025;322. https://doi.org/10.1016/j.engstruct.2024.119102.

[35] Taylor D. The Theory of Critical Distances: A New Perspective in Fracture Mechanics. Elsevier Science; 2007.

[36] Susmel L. The theory of critical distances: a review of its applications in fatigue. Eng Fract Mech 2008;75:1706–24. https://doi.org/10.1016/j.engfracmech.2006.12.004.

[37] Li W, Susmel L, Askes H, Liao F, Zhou T. Assessing the integrity of steel structural components with stress raisers using the Theory of Critical Distances. Eng Fail Anal 2016;70:73–89. https://doi.org/10.1016/j.engfailanal.2016.07.007.

[38] Zakir Sarothi S, Sakil Ahmed K, Imtiaz Khan N, Ahmed A, Nehdi ML. Predicting bearing capacity of double shear bolted connections using machine learning. Eng Struct 2022;251:113497. https://doi.org/10.1016/j.engstruct.2021.113497.

[39] Jiang K, Liang Y, Zhao O. Machine-learning-based design of high strength steel bolted connections. Thin-Walled Structures 2022;179:109575. https://doi.org/10.1016/j.tws.2022.109575.

[40] Jiang K, Zhao O. Unified machine-learning-assisted design of stainless steel bolted connections. J Constr Steel Res 2023;211:108155. https://doi.org/10.1016/j.jcsr.2023.108155.

[41] Almuhanna H, Torelli G, Kindermann R, Susmel L. Failure investigation of hybrid double-lap shear bolted connections with additively manufactured 316L stainless steel inner plates. Eng Fail Anal 2025:109756. https://doi.org/10.1016/J.ENGFAILANAL.2025.109756.

[42] Caroline Brogan. World's first 3D-printed steel footbridge unveiled by Queen Máxima in Amsterdam. Imperial College London 2021.

[43] Feucht T, Waldschmitt B, Lange J, Erven M. 3D-Printing with Steel: Additive Manufacturing of a Bridge in situ 2021:1695–701. https://doi.org/10.1002/cepa.

[44] Buchanan C, Gardner L. Metal 3D printing in construction: A review of methods, research, applications, opportunities and challenges. Eng Struct 2019;180:332–48. https://doi.org/10.1016/j.engstruct.2018.11.045.

[45] ASTM F3187-16. Guide for Directed Energy Deposition of Metals 2023. https://doi.org/10.1520/F3187-16R23.

[46] Astarita A, Campatelli G, Corigliano P, Epasto G, Montevecchi F, Scherillo F, et al. Microstructure and mechanical properties of specimens produced using the wire-arc additive manufacturing process. Proc Inst Mech Eng C J Mech Eng Sci 2021;235:1788–98. https://doi.org/10.1177/0954406219883324.

[47] Ayan Y, Kahraman N. Wire Arc Additive Manufacturing of Low-Carbon Mild Steel Using Two Different 3D Printers. Physics of Metals and Metallography 2021;122:1521–9. https://doi.org/10.1134/S0031918X21140039.

[48] Bartolomeu F, Buciumeanu M, Pinto E, Alves N, Carvalho O, Silva FS, et al. 316L stainless steel mechanical and tribological behavior—A comparison between selective laser melting, hot pressing and conventional casting. Addit Manuf 2017;16:81–9. https://doi.org/10.1016/j.addma.2017.05.007.

[49] Dirisu P, Ganguly S, Mehmanparast A, Martina F, Williams S. Analysis of fracture toughness properties of wire + arc additive manufactured high strength low alloy structural steel components. Materials Science and Engineering: A 2019;765. https://doi.org/10.1016/j.msea.2019.138285.

[50] Goviazin GG, Shirizly A, Rittel D. Static and dynamic mechanical properties of wire and arc additively manufactured SS316L and ER70S6. Mechanics of Materials 2022;164. https://doi.org/10.1016/j.mechmat.2021.104108.

[51] Sanjari M, Mahmoudiniya M, Pirgazi H, Tamimi S, Ghoncheh MH, Shahriairi A, et al. Microstructure, texture, and anisotropic mechanical behavior of selective laser melted maraging stainless steels. Mater Charact 2022;192. https://doi.org/10.1016/j.matchar.2022.112185.

[52] Tripathi U, Saini N, Mulik RS, Mahapatra MM. Effect of build direction on the microstructure evolution and their mechanical properties using GTAW based wire arc

additive manufacturing. CIRP J Manuf Sci Technol 2022;37:103–9. https://doi.org/10.1016/j.cirpj.2022.01.010.

[53] Zhai W, Wu N, Zhou W. Effect of Interpass Temperature on Wire Arc Additive Manufacturing Using High-Strength Metal-Cored Wire. Metals (Basel) 2022;12. https://doi.org/10.3390/met12020212.

[54] Ron T, Levy GK, Dolev O, Leon A, Shirizly A, Aghion E. Environmental behavior of low carbon steel produced by a wire arc additive manufacturing process. Metals (Basel) 2019;9. https://doi.org/10.3390/met9080888.

[55] DebRoy T, Wei HL, Zuback JS, Mukherjee T, Elmer JW, Milewski JO, et al. Additive manufacturing of metallic components – Process, structure and properties. Prog Mater Sci 2018;92:112–224. https://doi.org/10.1016/j.pmatsci.2017.10.001.

[56] Voestalpine Boehler. 3Dprint AM 316L; product datasheet 2019.

[57] SLM Solutions Group AG. 316L powder material analysis certificate 2022.

[58] Outokumpu. Inspection Certificate 3.1 according to DIN EN 10204 for stainless steel grade 1.4404 / 316L plate 2023.

[59] SLM Solutions Group AG. STM A276 / DIN EN 10088 / 1.4404 material data sheet. 2022.

[60] Autodesk. Autodesk Fusion with Netfabb: Additive manufacturing, design, and simulation 2024.

[61] ASTM E8/E8M. Standard Test Methods for Tension Testing of Metallic Materials. International and American Society for Testing Materials 2024.

[62] Laghi V, Palermo M, Tonelli L, Gasparini G, Ceschini L, Trombetti T. Tensile properties and microstructural features of 304L austenitic stainless steel produced by wire-and-arc additive manufacturing. International Journal of Advanced Manufacturing Technology 2020;106:3693–705. https://doi.org/10.1007/s00170-019-04868-8.

[63] ISO 273. Fasteners - Clearance holes for bolts and screws . International Organization for Standardization 1979.

[64] Almuhanna H, Torelli G, Susmel L. Static Assessment of Hybrid Double-Lap Bolted Joints With Additively Manufactured 316L Plates. Fatigue Fract Eng Mater Struct 2026. https://doi.org/10.1111/ffe.70218.

[65] Liu G, Zhang X, Chen X, He Y, Cheng L, Huo M, et al. Additive manufacturing of structural materials. Materials Science and Engineering R: Reports 2021;145. https://doi.org/10.1016/j.mser.2020.100596.

[66] Gardner L, Kyvelou P, Herbert G, Buchanan C. Testing and initial verification of the world's first metal 3D printed bridge. J Constr Steel Res 2020;172. https://doi.org/10.1016/j.jcsr.2020.106233.

[67] BS EN 1993-1-8. Eurocode 3 Design of steel structures - Part 1-8 Design of joints 2021.

[68] Yang D, Kan X, Gao P, Zhao Y, Yin Y, Zhao Z, et al. Influence of porosity on mechanical and corrosion properties of SLM 316L stainless steel. Appl Phys A Mater Sci Process 2022;128. https://doi.org/10.1007/s00339-021-05191-4.

[69] Ni X qing, Kong D cheng, Wen Y, Zhang L, Wu W heng, He B bei, et al. Anisotropy in mechanical properties and corrosion resistance of 316L stainless steel fabricated by selective laser melting. International Journal of Minerals, Metallurgy and Materials 2019;26:319–28. https://doi.org/10.1007/s12613-019-1740-x.

[70] Teh LH, Uz ME. Ultimate Shear-Out Capacities of Structural-Steel Bolted Connections. Journal of Structural Engineering 2015;141. https://doi.org/10.1061/(asce)st.1943-541x.0001105.

[71] Teh LH, Uz ME. Combined Bearing and Shear-Out Capacity of Structural Steel Bolted Connections. Journal of Structural Engineering 2016;142. https://doi.org/10.1061/(asce)st.1943-541x.0001573.

[72] Xing H, Teh LH, Jiang Z, Ahmed A. Shear-Out Capacity of Bolted Connections in Cold-Reduced Steel Sheets. Journal of Structural Engineering 2020;146. https://doi.org/10.1061/(asce)st.1943-541x.0002565.

[73] Almuhanna H, Torelli G, Susmel L. The Theory of Critical Distances for Predicting the Static Failure of Double-Lap Bolted Joints With Conventional and Additively Manufactured 316L Stainless Steel Inner Plates. Fatigue Fract Eng Mater Struct 2026. https://doi.org/10.1111/ffe.70349.

[74] Liu Y, Ye J, Yang Y, Quan G, Wang Z, Zhao W, et al. Experimental study on wire and arc additively manufactured steel double-shear bolted connections. Journal of Building Engineering 2023;76. https://doi.org/10.1016/j.jobe.2023.107330.

[75] Gil B, Goñi R, Fábregas M, Bayo E. Design and testing of steel additive-manufactured moment-resistant beam-to-column connection. J Constr Steel Res 2024;219. https://doi.org/10.1016/j.jcsr.2024.108747.

[76] Erven M, Lange J, Feucht T. 3D-Printing with steel of a bolted connection 2021. https://doi.org/10.1002/cepa.

[77] Xie C, Bagheri Sabbagh A, Bakhshivand E, Iuorio O. Shape optimisation of metal additive manufacturing connections in lightweight steel structures. J Constr Steel Res 2026;241. https://doi.org/10.1016/j.jcsr.2026.110290.

[78] Zhang Z, He F, Chen Z, Yuan L, Guan H, Pan Z, et al. Comprehensive review of robotic wire arc additive manufacturing for steel structures: Process, material behaviour, structural applications and pathways to automated construction. Autom Constr 2026;182. https://doi.org/10.1016/j.autcon.2025.106758.

[79] Jiang K, Zhao O. Ferritic stainless steel thin sheet bolted connections failing by bearing–curling interaction: Testing, modelling and design. Eng Struct 2023;283:115919. https://doi.org/10.1016/j.engstruct.2023.115919.

[80] Wen H, Mahmoud H. Strength Determination and Fracture Characteristics of Bolted Connections. Journal of Structural Engineering 2021;147. https://doi.org/10.1061/(asce)st.1943-541x.0003076.

[81] Alena T, Kostina A, Oleg P, Luca S. Elasto-plastic TCD as a method of failure prediction. Procedia Structural Integrity, vol. 5, Elsevier B.V.; 2017, p. 569–76. https://doi.org/10.1016/j.prostr.2017.07.174.

[82] Susmel L, Taylor D. On the use of the Theory of Critical Distances to predict static failures in ductile metallic materials containing different geometrical features. Eng Fract Mech 2008;75:4410–21. https://doi.org/10.1016/j.engfracmech.2008.04.018.

[83] Susmel L, Taylor D. The Theory of Critical Distances to estimate the static strength of notched samples of Al6082 loaded in combined tension and torsion. Part I: Material cracking behaviour. Eng Fract Mech 2010;77:452–69. https://doi.org/10.1016/j.engfracmech.2009.11.015.

[84] Susmel L, Taylor D. The Theory of Critical Distances to estimate the static strength of notched samples of Al6082 loaded in combined tension and torsion. Part II: Multiaxial static assessment. Eng Fract Mech 2010;77:470–8. https://doi.org/10.1016/j.engfracmech.2009.10.004.

[85] Ameri AAH, Davison JB, Susmel L. On the use of linear-elastic local stresses to design load-carrying fillet-welded steel joints against static loading. Eng Fract Mech 2015;136:38–57. https://doi.org/10.1016/j.engfracmech.2015.02.004.

[86] Ahmed AA, Susmel L. Static assessment of plain/notched polylactide (PLA) 3D-printed with different infill levels: Equivalent homogenised material concept and Theory of Critical Distances. Fatigue Fract Eng Mater Struct 2019;42:883–904. https://doi.org/10.1111/ffe.12958.

[87] Susmel L, Taylor D. The theory of critical distances to predict static strength of notched brittle components subjected to mixed-mode loading. Eng Fract Mech 2008;75:534–50. https://doi.org/10.1016/j.engfracmech.2007.03.035.

[88] Lobanov D, Yankin A, Mullahmetov M, Chebotareva E, Melnikova V. The Analysis of Stress Raisers Affecting the GFRP Strength at Quasi-Static and Cyclic Loads by the Theory of Critical Distances, Digital Image Correlation, and Acoustic Emission. Polymers (Basel) 2023;15. https://doi.org/10.3390/polym15092087.

[89] Taylor D. Predicting the fracture strength of ceramic materials using the theory of critical distances. Eng Fract Mech 2004;71:2407–16. https://doi.org/10.1016/j.engfracmech.2004.01.002.

[90] ASTM E399. Standard Test Method for Linear-Elastic Plane-Strain Fracture Toughness of Metallic Materials 2023.

[91] Marsavina L, Sapora A, Susmel L, Taylor D. The application of the Theory of Critical Distances to nonhomogeneous materials. Fatigue Fract Eng Mater Struct 2023;46:1314–29. https://doi.org/10.1111/ffe.13922.

[92] ANSYS Inc. (2023). ANSYS® Academic Research Mechanical. n.d.

[93] Chung KF, Ip KH. Finite element modeling of bolted connections between cold-formed steel strips and hot rolled steel plates under static shear loading. vol. 22. 2000.

[94] Ju SH, Fan CY, Wu GH. Three-dimensional finite elements of steel bolted connections. Eng Struct 2004;26:403–13. https://doi.org/10.1016/j.engstruct.2003.11.001.

[95] Almuhanna H, Torelli G, Susmel L. Machine Learning Models to Predict the Static Failure of Double-Lap Shear Bolted Connections. Fatigue Fract Eng Mater Struct 2025;48:4041–55. https://doi.org/10.1111/ffe.70019.

[96] Može P, Beg D. A complete study of bearing stress in single bolt connections. J Constr Steel Res 2014;95:126–40. https://doi.org/10.1016/j.jcsr.2013.12.002.

[97] Teh LH, Uz ME. Block shear failure planes of bolted connections — Direct experimental verifications. J Constr Steel Res 2015;111:70–4. https://doi.org/10.1016/j.jcsr.2015.04.006.

[98] Hai L-T, Li G-Q, Wang Y-B, Sun F-F, Jin H-J. Experimental investigation on cyclic behavior of Q690D high strength steel H-section beam-columns about strong axis. Eng Struct 2019;189:157–73. https://doi.org/10.1016/j.engstruct.2019.03.060.

[99] Može P, Beg D. High strength steel tension splices with one or two bolts. J Constr Steel Res 2010;66:1000–10. https://doi.org/10.1016/j.jcsr.2010.03.009.

[100] Wang Y-B, Lyu Y-F, Li G-Q, Liew JYR. Behavior of single bolt bearing on high strength steel plate. J Constr Steel Res 2017;137:19–30. https://doi.org/10.1016/j.jcsr.2017.06.001.

[101] Cai Y, Young B. Carbon steel and stainless steel bolted connections undergoing unloading and re-loading processes. J Constr Steel Res 2019;157:337–46. https://doi.org/10.1016/j.jcsr.2019.03.007.

[102] Wang Y-B, Lyu Y-F, Li G-Q, Liew JYR. Bearing-strength of high strength steel plates in two-bolt connections. J Constr Steel Res 2019;155:205–18. https://doi.org/10.1016/j.jcsr.2018.12.011.

[103] Dobrić J, Cai Y, Young B, Rossi B. Behaviour of duplex stainless steel bolted connections. Thin-Walled Structures 2021;169:108380. https://doi.org/10.1016/j.tws.2021.108380.

[104] Ethem Alpaydin. Introduction to Machine Learning. MIT Press; 2014.

[105] MathWorks. MATLAB R2023a 2023.

[106] Feng D-C, Liu Z-T, Wang X-D, Chen Y, Chang J-Q, Wei D-F, et al. Machine learning-based compressive strength prediction for concrete: An adaptive boosting approach. Constr Build Mater 2020;230:117000. https://doi.org/10.1016/j.conbuildmat.2019.117000.

[107] Adnan M, Alarood AAS, Uddin MI, ur Rehman I. Utilizing grid search cross-validation with adaptive boosting for augmenting performance of machine learning models. PeerJ Comput Sci 2022;8:e803. https://doi.org/10.7717/peerj-cs.803.

[108] Kuo P-H, Huang M-J, Luan P-C, Yau H-T. Study on Bandwidth Analyzed Adaptive Boosting Machine Tool Chatter Diagnosis System. IEEE Sens J 2022;22:8449–59. https://doi.org/10.1109/JSEN.2022.3163914.

[109] Karsznia I, Sielicka K. When Traditional Selection Fails: How to Improve Settlement Selection for Small-Scale Maps Using Machine Learning. ISPRS Int J Geoinf 2020;9:230. https://doi.org/10.3390/ijgi9040230.

[110] Brandon H. Boyle. Support Vector Machines Data Analysis, Machine Learning and Applications. Nova Science Publishers; 2011.

[111] Yu D, Zhang A, Gao Z. Fault diagnosis using redundant data in analog circuits via slime module algorithm for support vector machine. J Ambient Intell Humaniz Comput 2023;14:14261–76. https://doi.org/10.1007/s12652-023-04664-z.

[112] Liu J, Danait R. Instance Selection in the Projected High Dimensional Feature Space for SVM. 2018 IEEE 3rd International Conference on Image, Vision and Computing (ICIVC), IEEE; 2018, p. 575–9. https://doi.org/10.1109/ICIVC.2018.8492723.

[113] Wang X-Y, Chen J-W, Yang H-Y. A new integrated SVM classifiers for relevance feedback content-based image retrieval using EM parameter estimation. Appl Soft Comput 2011;11:2787–804. https://doi.org/10.1016/j.asoc.2010.11.009.

[114] Nemes A, Roberts RT, Rawls WJ, Pachepsky YaA, van Genuchten MTh. Software to estimate −33 and −1500kPa soil water retention using the non-parametric k-Nearest Neighbor technique. Environmental Modelling & Software 2008;23:254–5. https://doi.org/10.1016/j.envsoft.2007.05.018.

[115] Musolf AM, Holzinger ER, Malley JD, Bailey-Wilson JE. What makes a good prediction? Feature importance and beginning to open the black box of machine learning in genetics. Hum Genet 2022;141:1515–28. https://doi.org/10.1007/s00439-021-02402-z.

[116] Kufel J, Bargieł-Łączek K, Kocot S, Koźlik M, Bartnikowska W, Janik M, et al. What Is Machine Learning, Artificial Neural Networks and Deep Learning?—Examples of Practical Applications in Medicine. Diagnostics 2023;13. https://doi.org/10.3390/diagnostics13152582.

[117] Aguilar V, Sandoval C, Adam JM, Garzón-Roca J, Valdebenito G. Prediction of the shear strength of reinforced masonry walls using a large experimental database and artificial neural networks. Structure and Infrastructure Engineering 2016;12:1661–74. https://doi.org/10.1080/15732479.2016.1157824.

[118] Das S, Choudhury S. Influence of effective stiffness on the performance of RC frame buildings designed using displacement-based method and evaluation of column effective stiffness using ANN. Eng Struct 2019;197. https://doi.org/10.1016/j.engstruct.2019.109354.

[119] Moradi MJ, Mehrpour G, Adelzadeh M, Hajiloo H. Structural damage levels of bridges in vehicular collision fires: Predictions using an artificial neural network (ANN) model. Eng Struct 2023;295. https://doi.org/10.1016/j.engstruct.2023.116840.

[120] Lyu Z, Yu Y, Samali B, Rashidi M, Mohammadi M, Nguyen TN, et al. Back-Propagation Neural Network Optimized by K-Fold Cross-Validation for Prediction of Torsional Strength of Reinforced Concrete Beam. Materials 2022;15:1477. https://doi.org/10.3390/ma15041477.

[121] Rokach L. Pattern classification using ensemble methods. 1st ed. Singapore ; Hackensack, NJ: World Scientific; 2010.

Appendices

Appendix A – Design Drawings

This appendix provides the design drawings of the tested inner plates. It should be noted that the as-built wire arc additive manufacturing plates (WAAM-AB) shared the same geometric design but differed in thickness.

IP1-1:

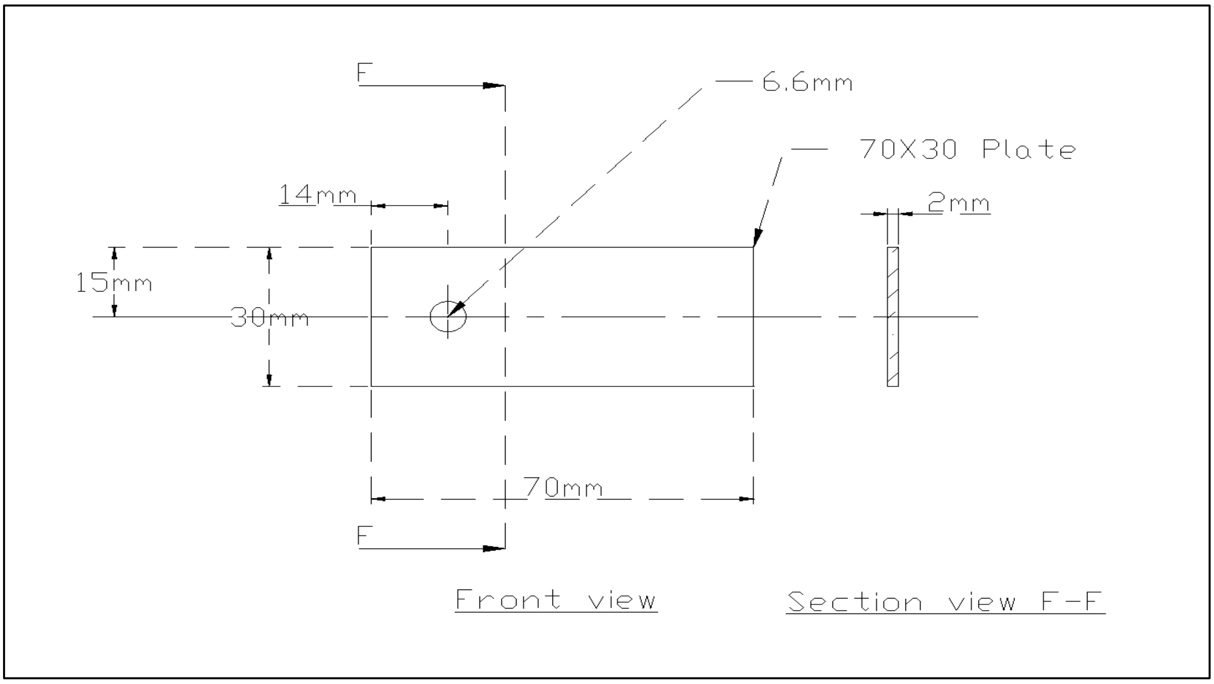

IP1-2:

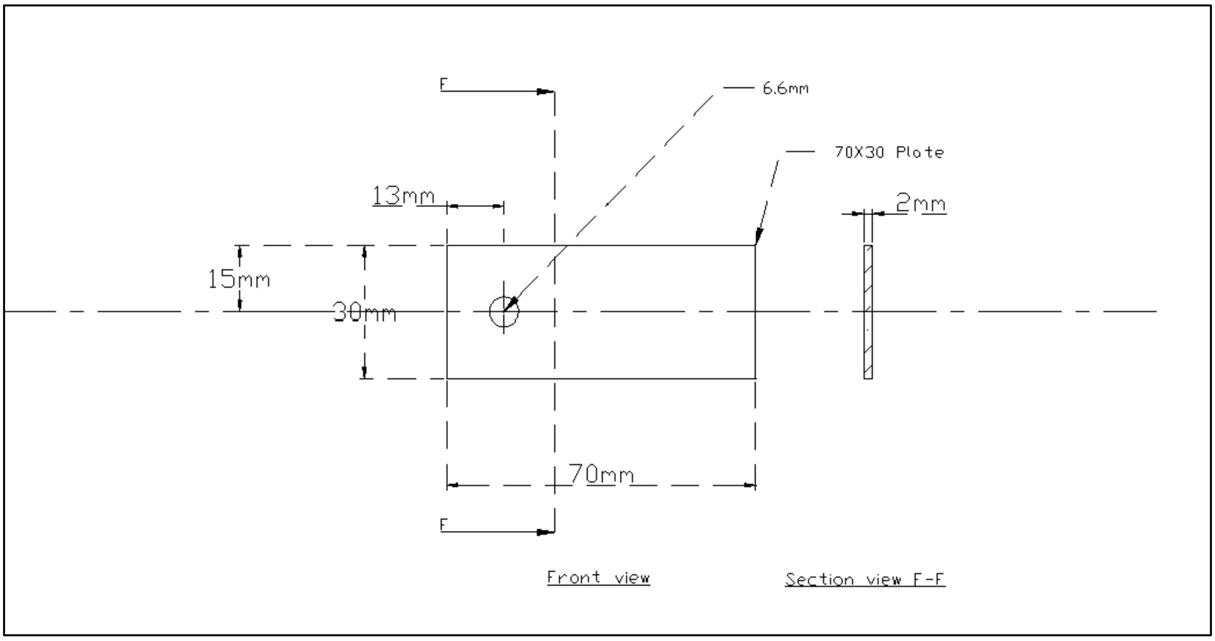

IP1-3:

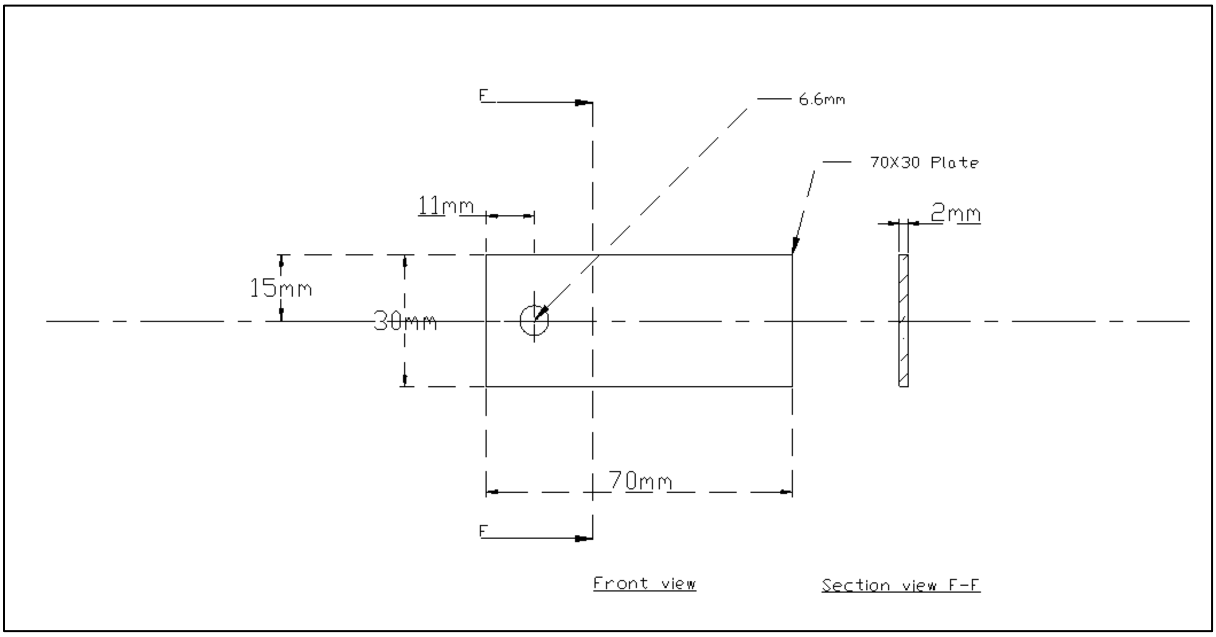
F
6.6mm
70X30 Plate
11mm
2mm
15mm
30mm
70mm
F
Front view
Section view F-F

IP1-4:

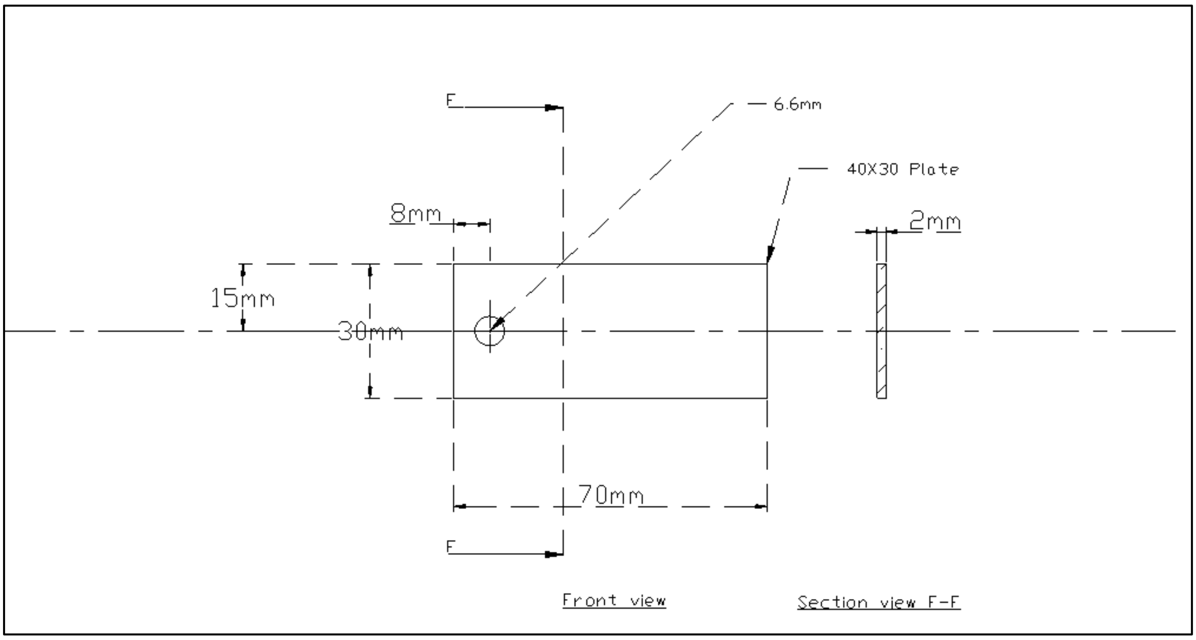
F
6.6mm
40X30 Plate
8mm
2mm
15mm
30mm
70mm
F
Front view
Section view F-F

IP1-5:

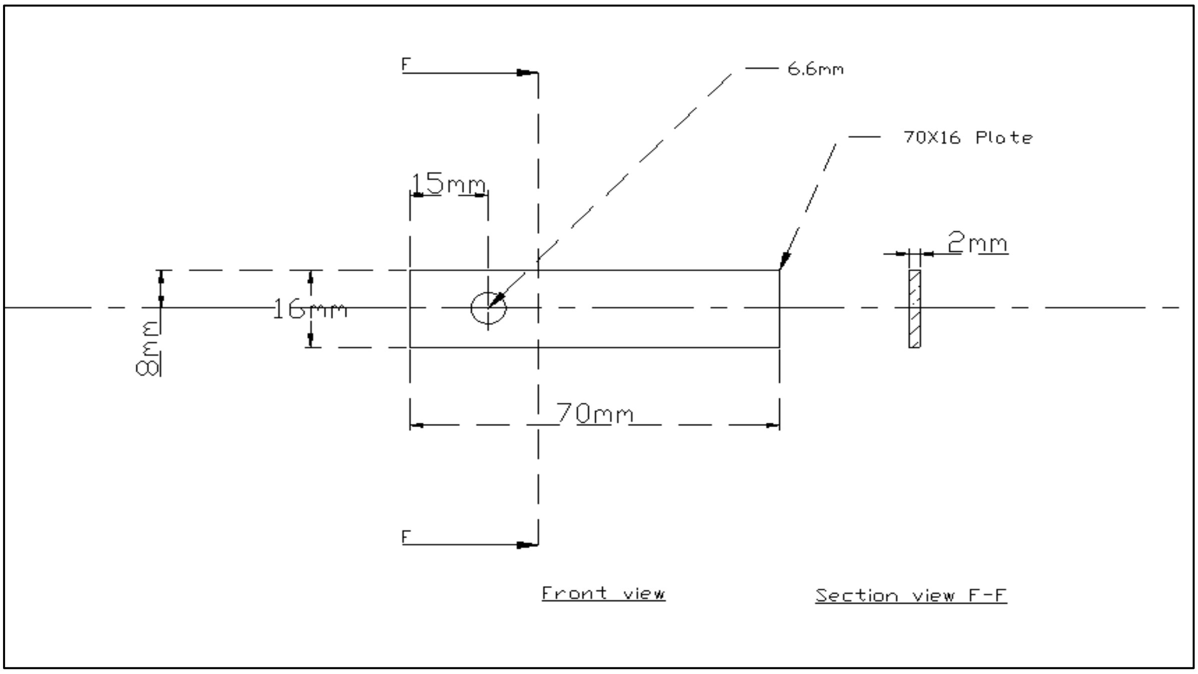
F
6.6mm
70X16 Plate
15mm
2mm
8mm
16mm
70mm
F
Front view
Section view F-F

IP2-1:

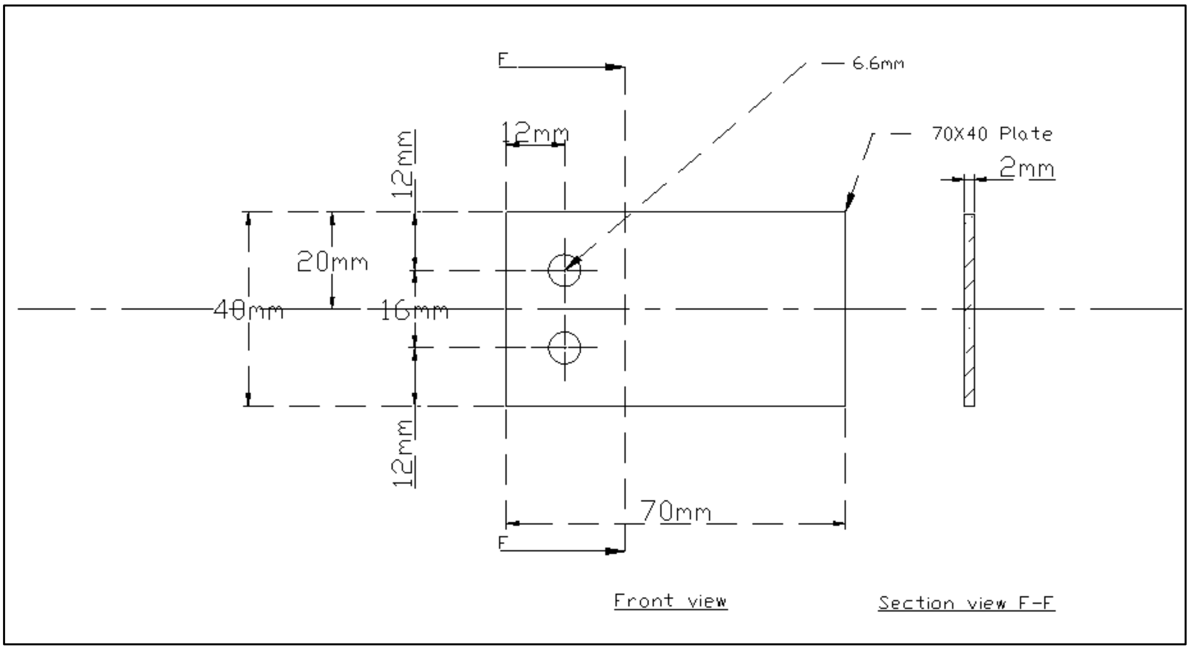
F
6.6mm
70X40 Plate
12mm
12mm
2mm
20mm
40mm
16mm
12mm
70mm
F
Front view
Section view F-F

IP2-2:

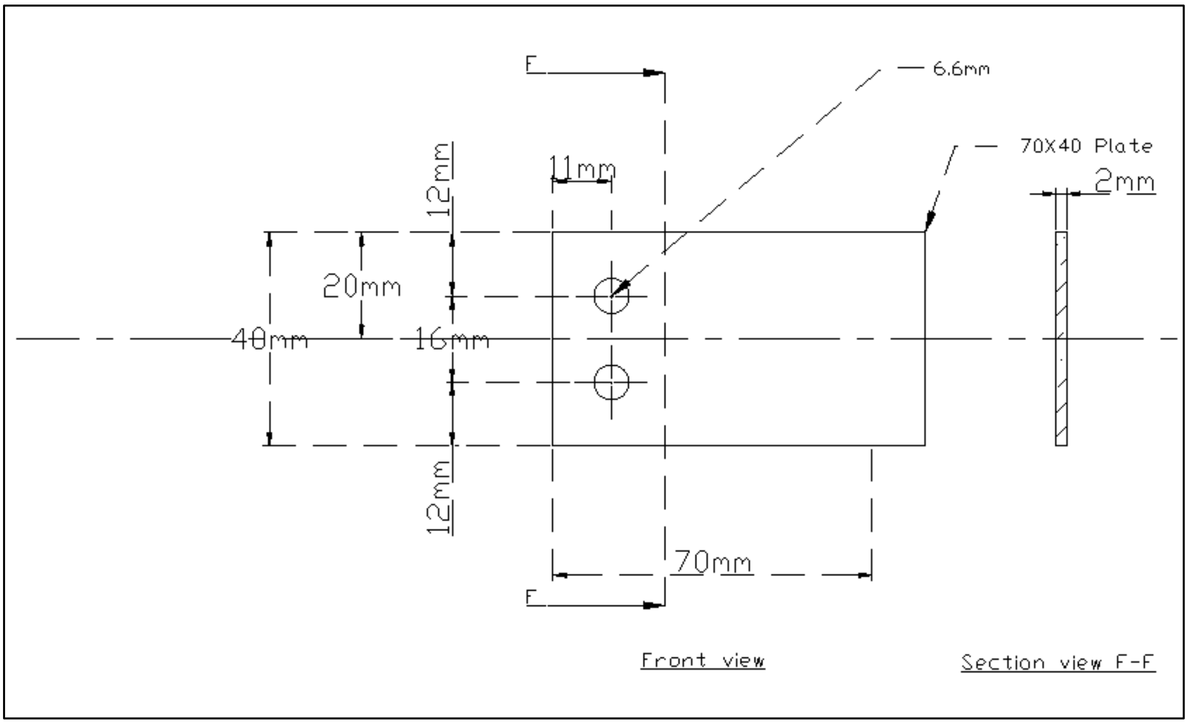
F
6.6mm
70X40 Plate
2mm
12mm
11mm
20mm
40mm
16mm
12mm
70mm
F
Front view
Section view F-F

IP2-3:

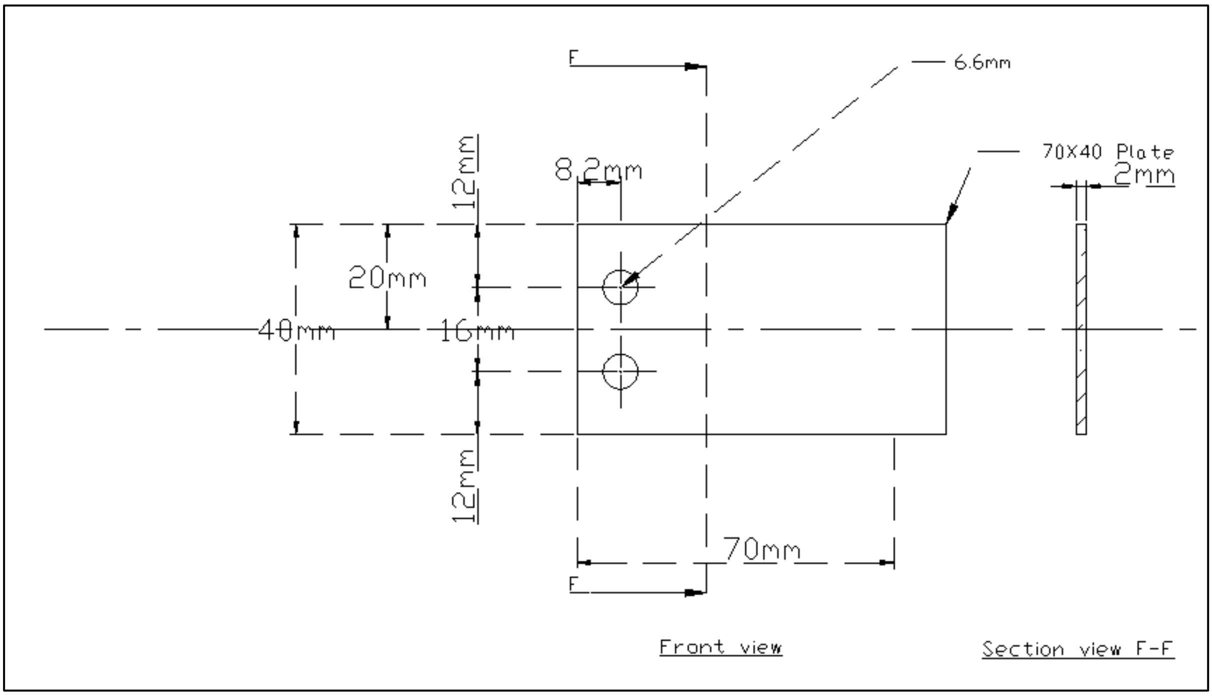
F
6.6mm
70X40 Plate
2mm
12mm
8.2mm
20mm
40mm
16mm
12mm
70mm
F
Front view
Section view F-F

IP2-4:

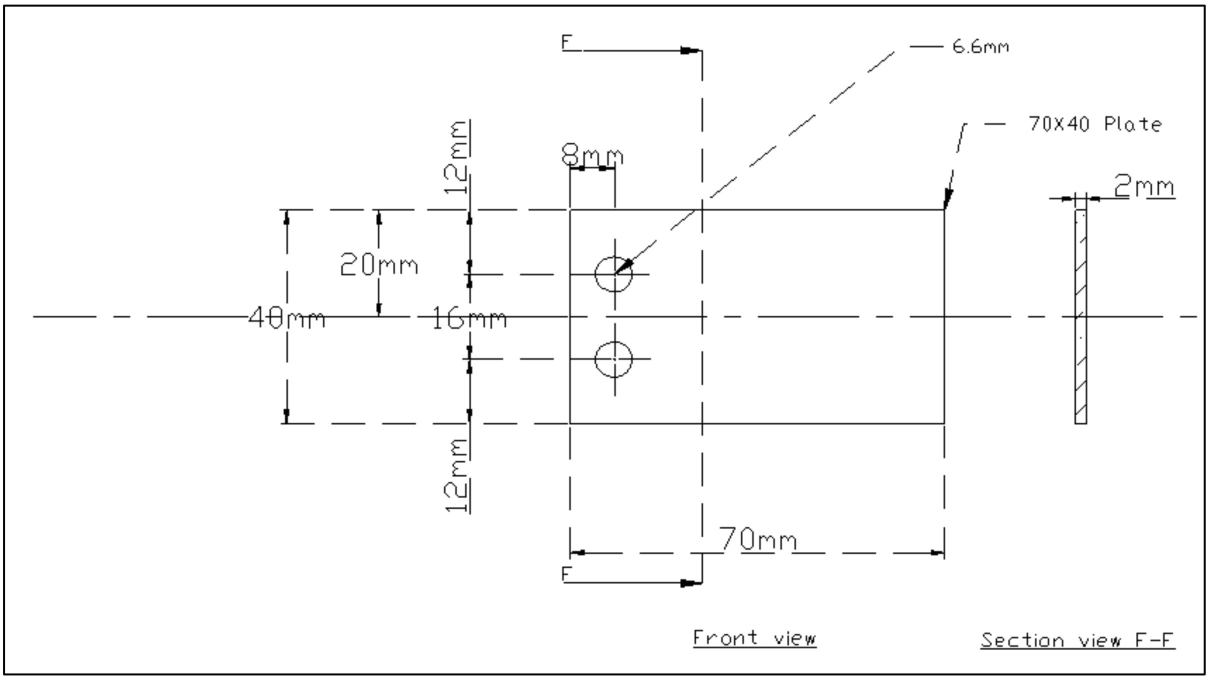
F
6.6mm
70X40 Plate
8mm
12mm
2mm
20mm
40mm
16mm
12mm
70mm
F
Front view
Section view F-F

IP2-5:

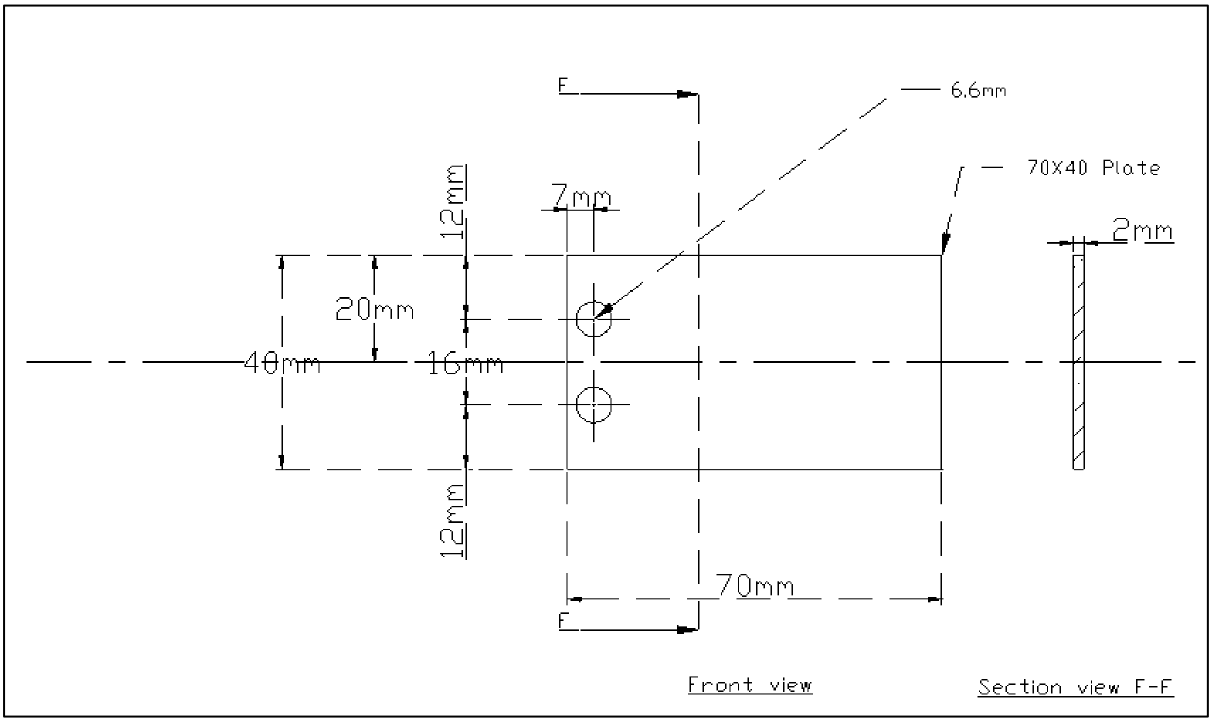
F
6.6mm
70X40 Plate
7mm
12mm
2mm
20mm
40mm
16mm
12mm
70mm
F
Front view
Section view F-F

IP2-6:

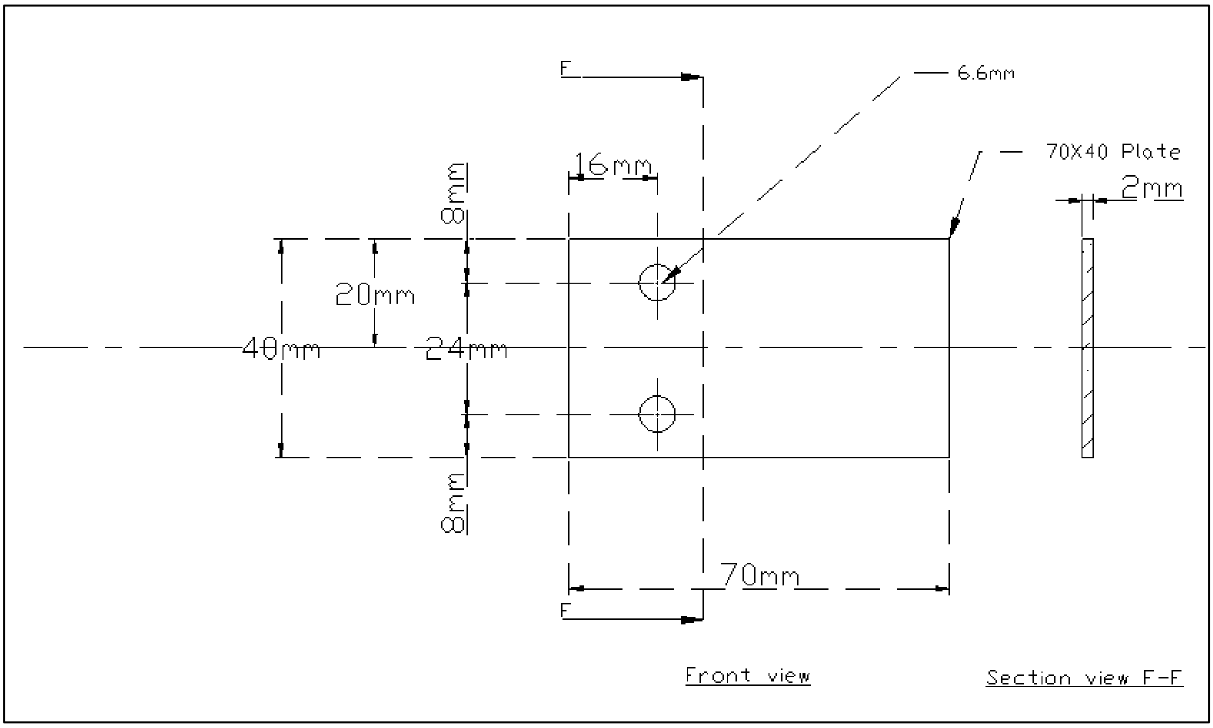
F
6.6mm
70X40 Plate
16mm
2mm
8mm
20mm
40mm
24mm
8mm
70mm
F
Front view
Section view F-F

IP2-7:

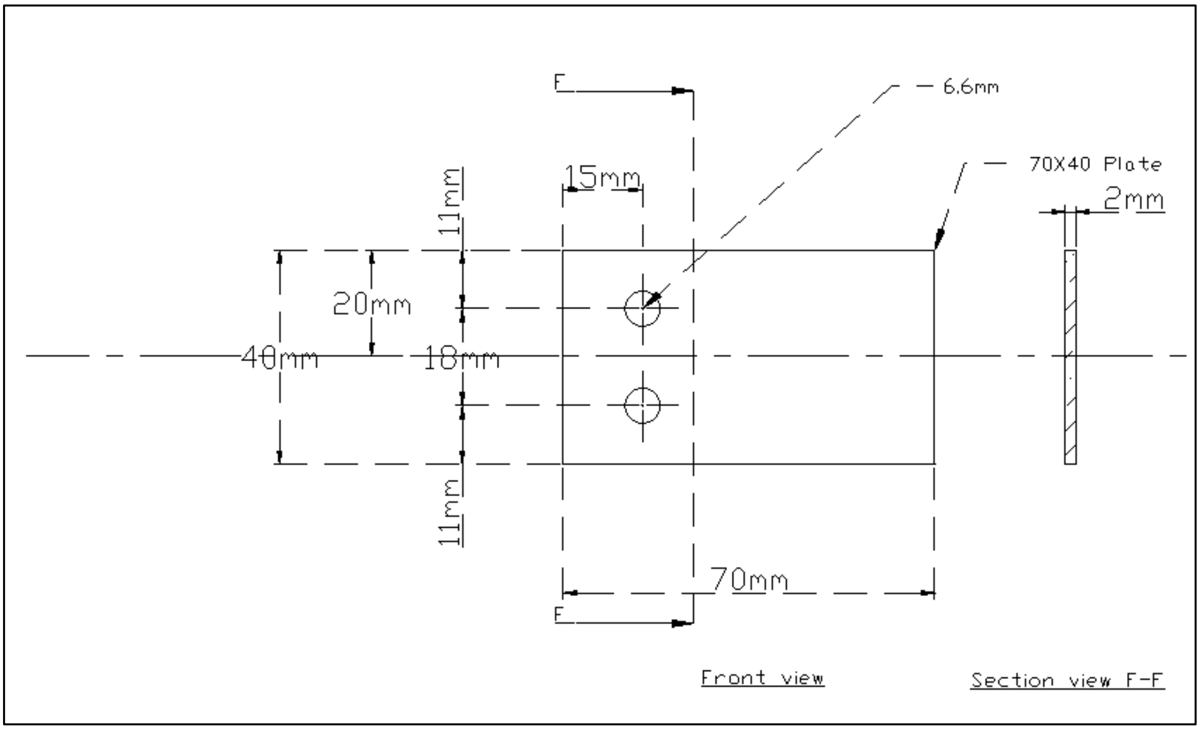
F
6.6mm
70X40 Plate
15mm
2mm
11mm
20mm
40mm
18mm
11mm
70mm
F
Front view
Section view F-F

Appendix B – FE Mesh Sensitivity and TCD Analysis Plots

This appendix presents the FE mesh sensitivity study for the notched specimens and the stress-distance plots used in the TCD analyses in Chapter 5. For the WAAM-AB plates, the plots were updated using the PM parameters calibrated from the WAAM-AB notched specimens.

Sensitivity study for the notched specimens:

The mesh sensitivity study was performed using the specimen with sharp notch, which had the smaller notch root radius of 0.5 mm and therefore the highest local stress gradient. A nominal element size of 1 mm was used for the general specimen geometry, while local refinement was introduced around the notch root using a sphere of influence. The local element size within the sphere of influence was reduced from 0.05 mm to 0.009 mm. The mesh response was assessed using the maximum equivalent stress at the notch root and the equivalent stress extracted at a representative distance of 0.2 mm from the notch root. This distance was selected to assess convergence within the local high stress-gradient region and was kept constant for all mesh densities.

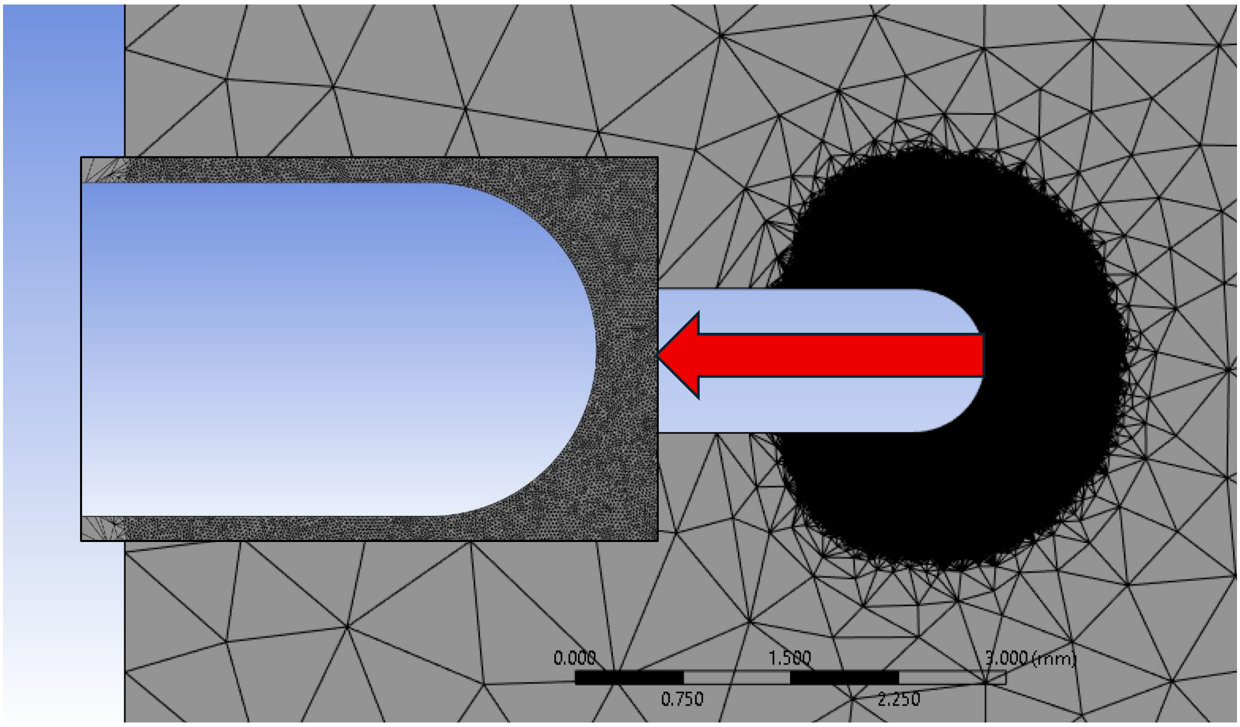

The peak equivalent stress showed very limited sensitivity to further refinement. Reducing the local element size from 0.01 mm to 0.009 mm changed the peak equivalent stress by only 0.04%. At the representative distance of 0.2 mm, the corresponding stress difference was 1.32%. The table below provides the mesh sensitivity results:

Local element mesh size around the notch (mm)	Peak equivalent stress (MPa)	Change in peak equivalent stress (%)	Equivalent stress at 0.2 mm from the root (MPa)	Change in equivalent stress at 0.2 mm from the root (%)
0.050	3023	-	1573	-
0.030	3039	0.52	1542	1.94
0.020	3043	0.15	1510	2.11
0.010	3052	0.27	1520	0.67
0.009	3050	0.04	1500	1.32

Therefore, a local element size of 0.009 mm within the sphere of influence was adopted for the subsequent analyses. The same refinement method was applied to the specimen with a blunt notch. Its larger notch root radius of 1.5 mm resulted in a lower stress gradient, and changes in the local mesh size had a smaller effect on the extracted stresses than for the specimen with a sharp notch.

2mm thick conventional single-bolted configuration inner plates' plots:

IP1-1-CON:

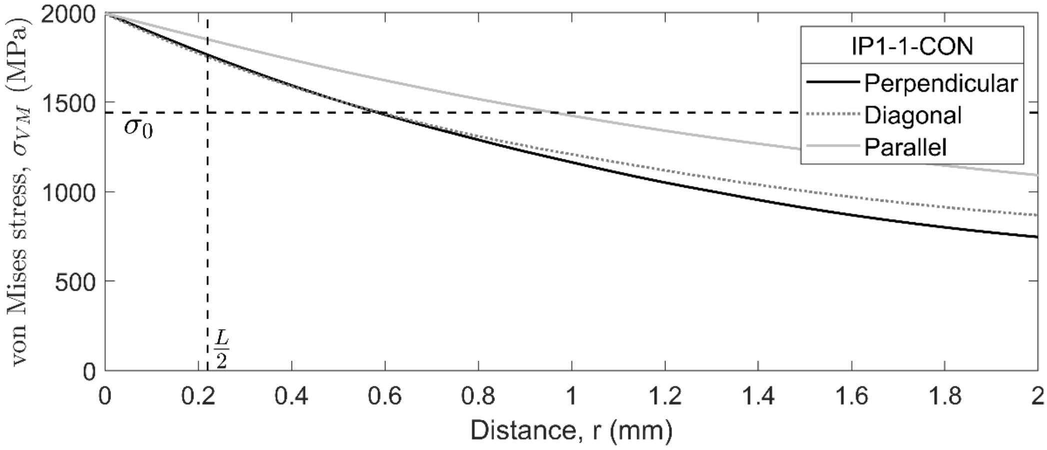

IP1-2-CON:

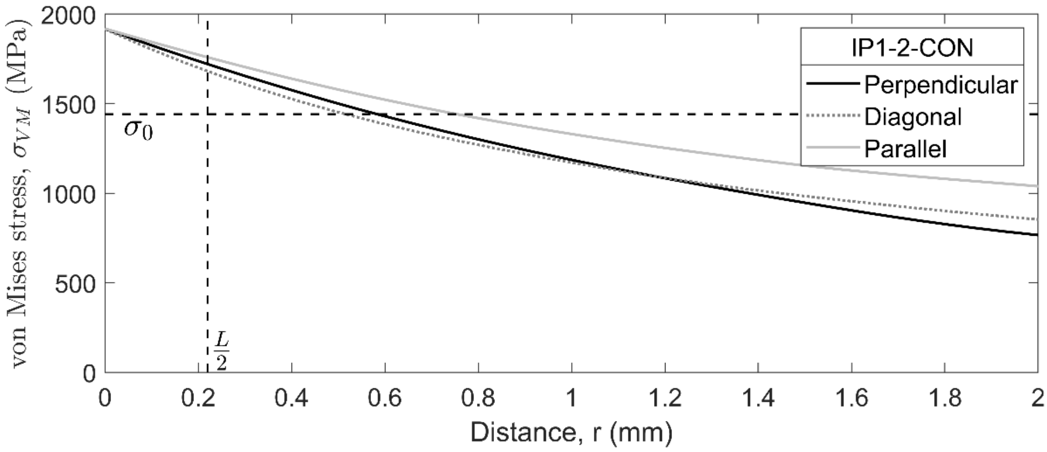

IP1-3-CON:

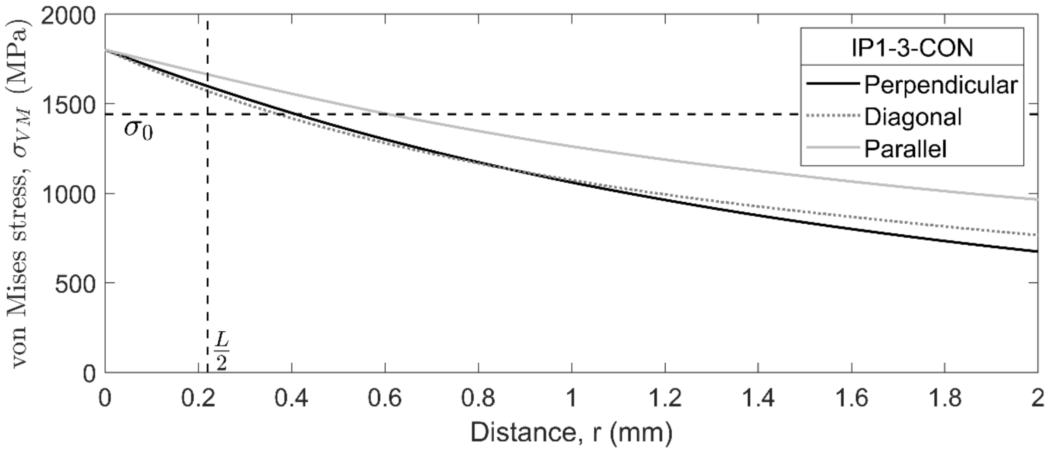

IP1-4-CON:

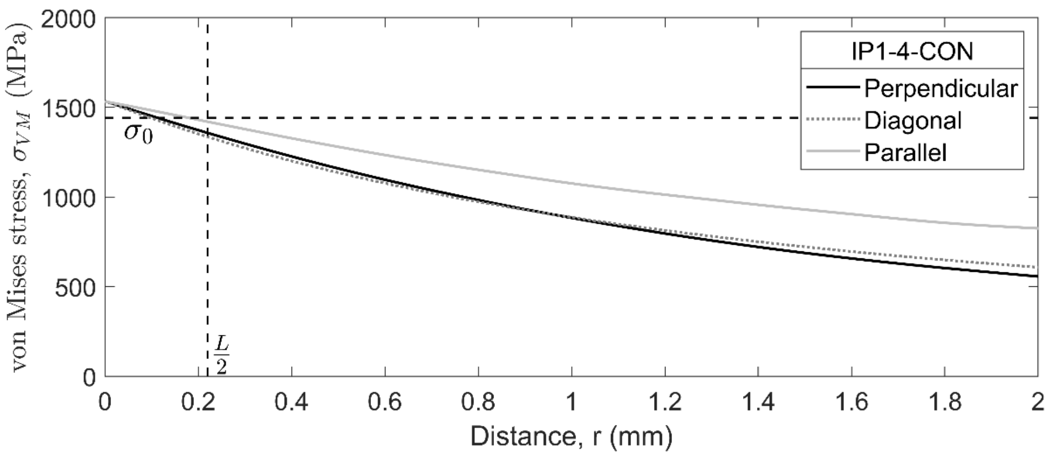

IP1-5-CON:

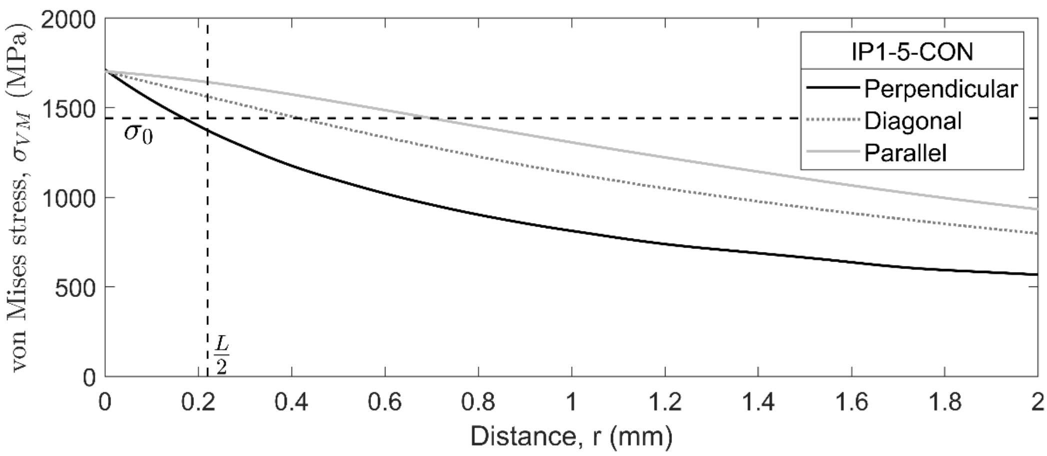

<u>2mm thick additively manufactured single-bolted configuration inner plates' plots:</u>

IP1-1-SLM-M-0°:

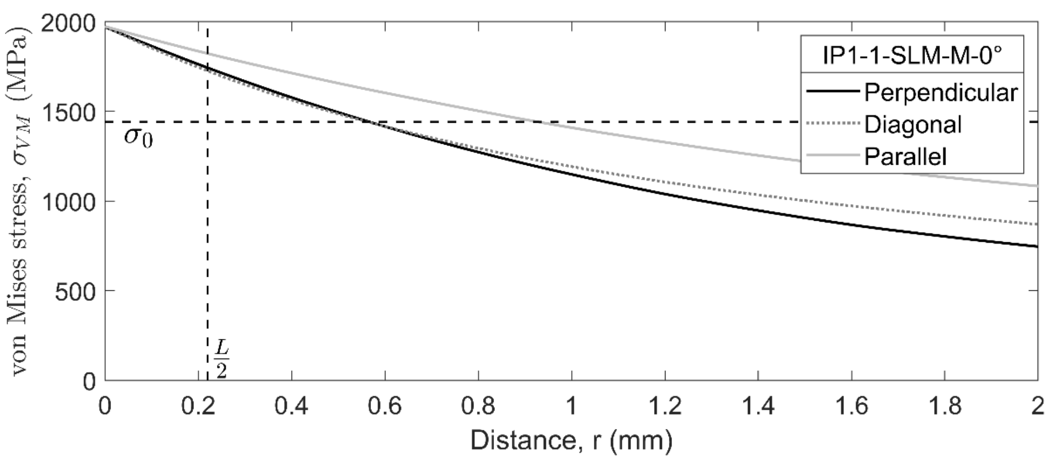

IP1-1-WAAM-M-0°:

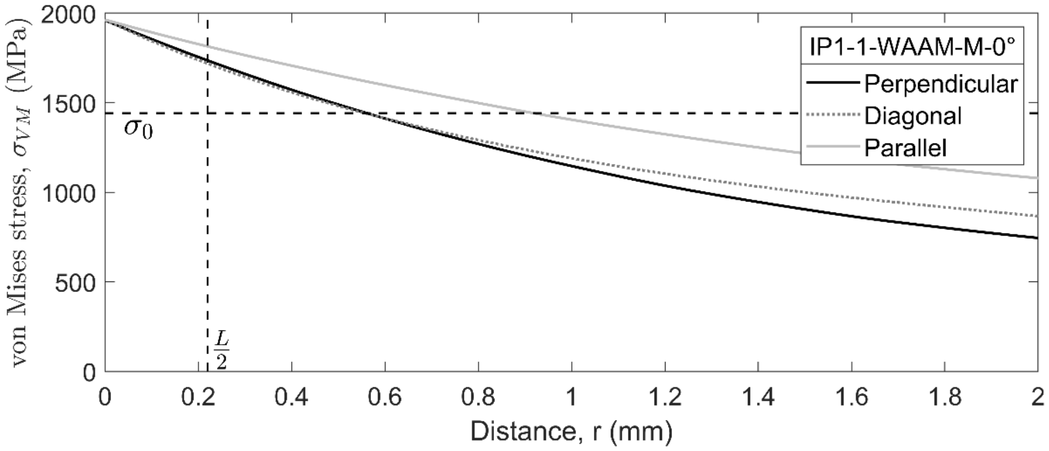

IP1-1-WAAM-M-45°:

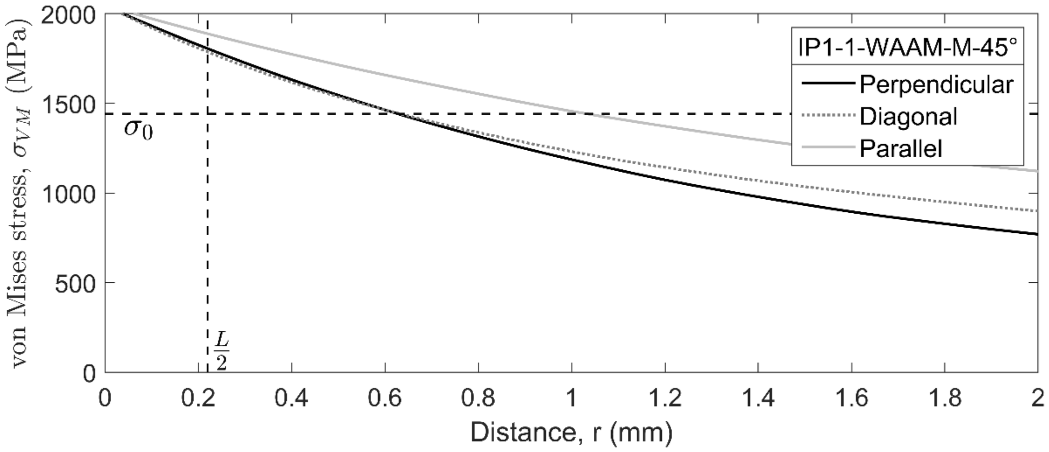

IP1-1-WAAM-M-60°:

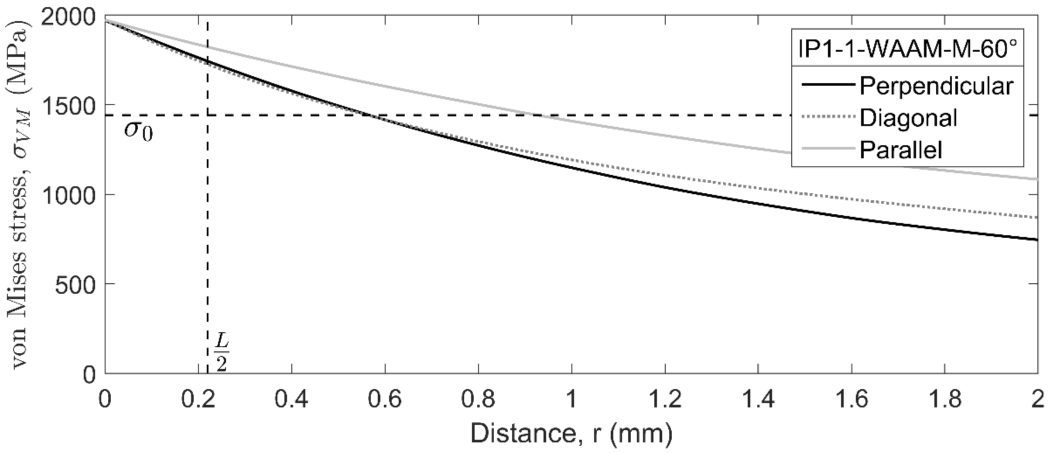

IP1-1-WAAM-M-90°:

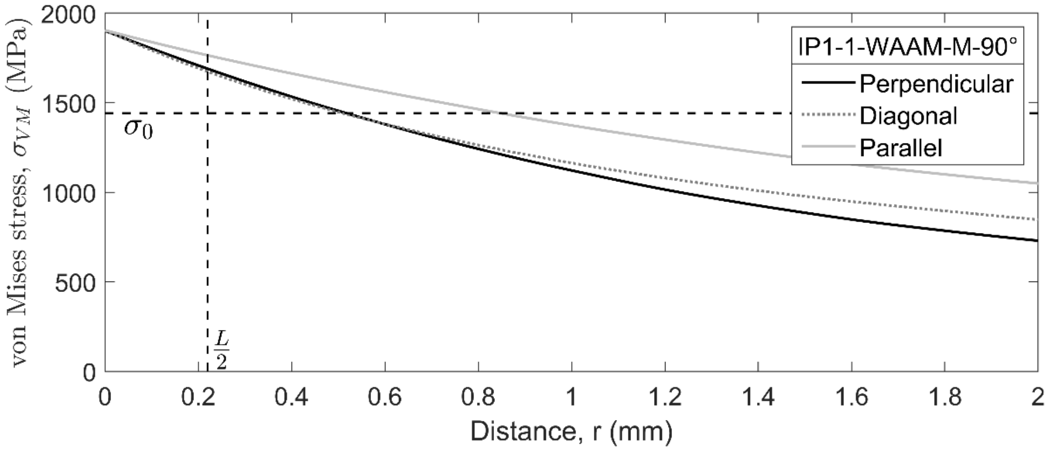

IP1-2-WAAM-M-0°:

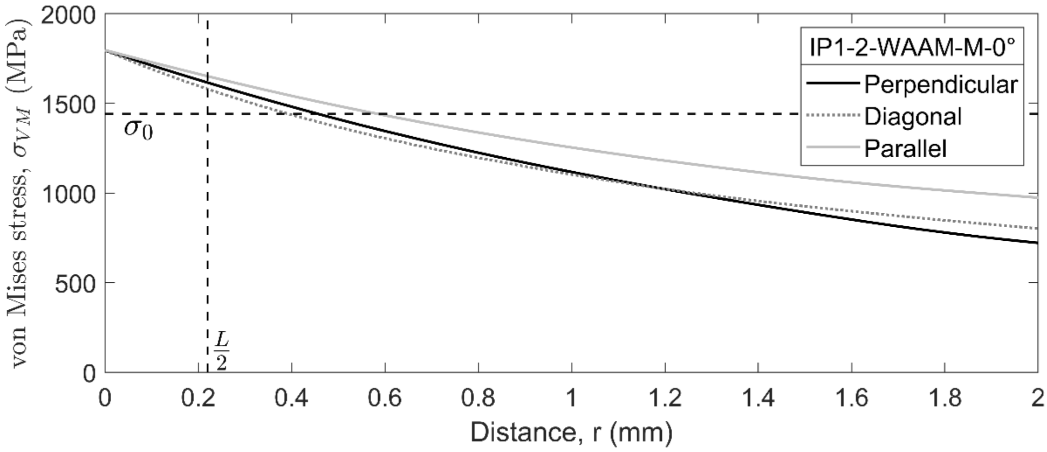

IP1-2-WAAM-M-45°:

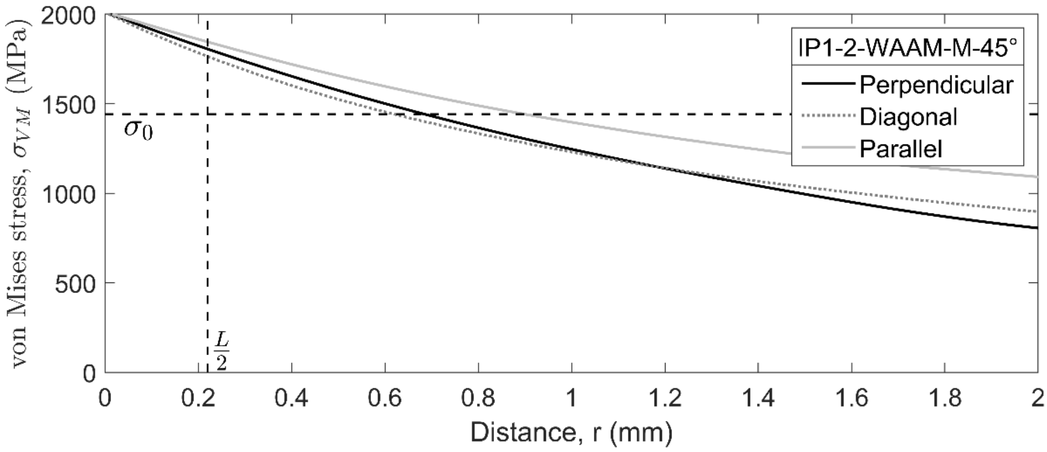

IP1-2-WAAM-M-60°:

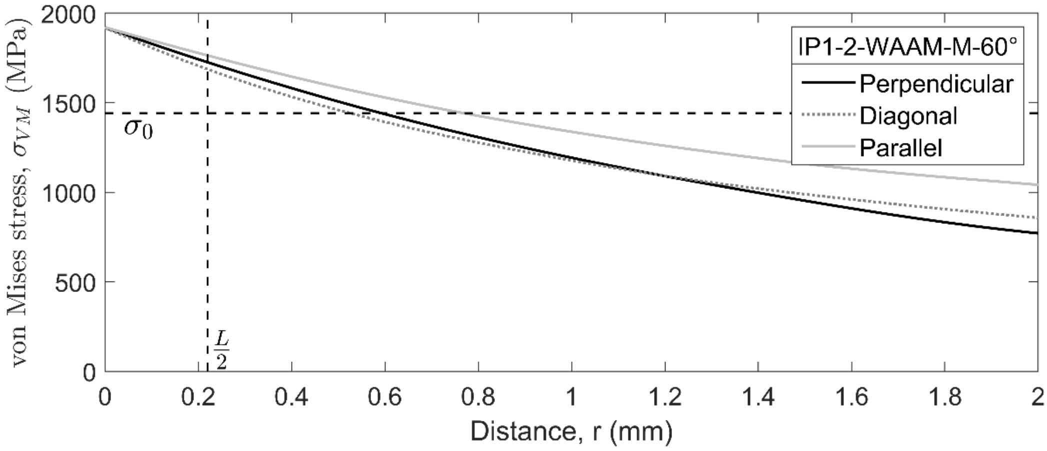

IP1-2-WAAM-M-90°:

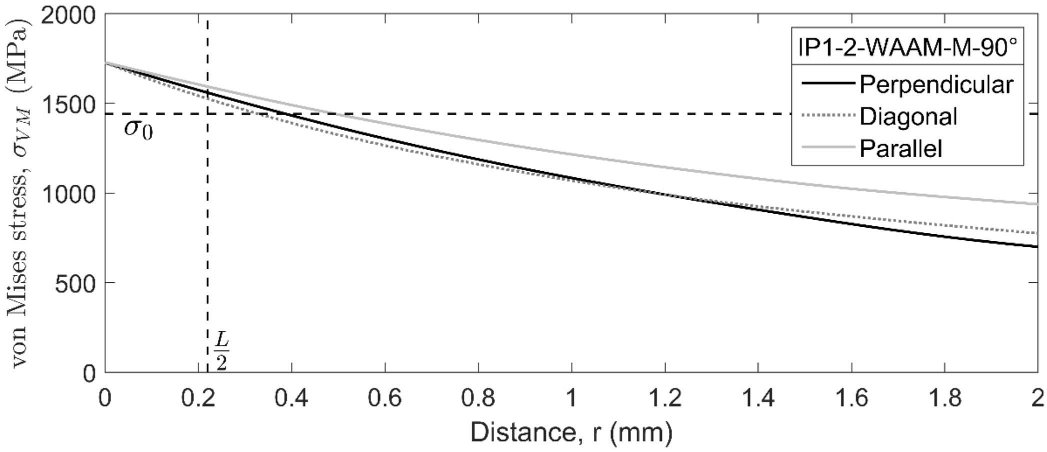

IP1-3-WAAM-M-0°:

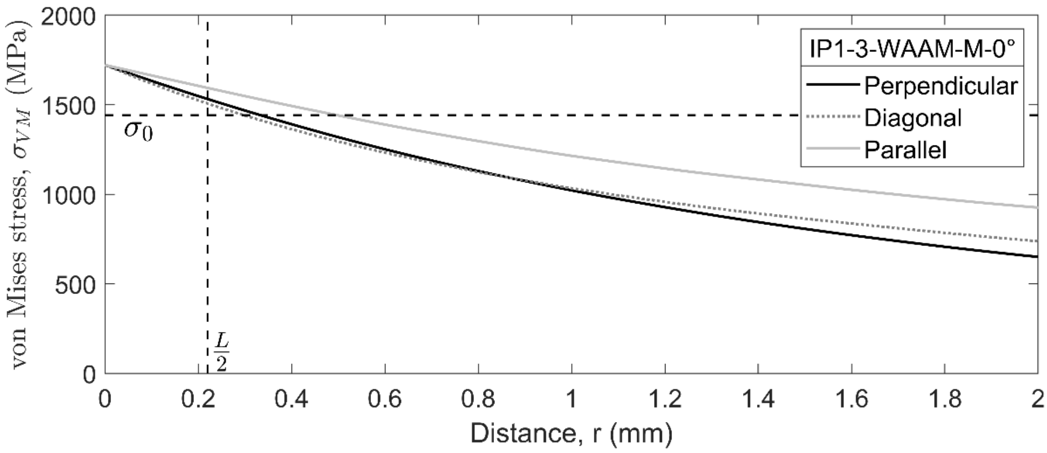

IP1-4-WAAM-M-0°:

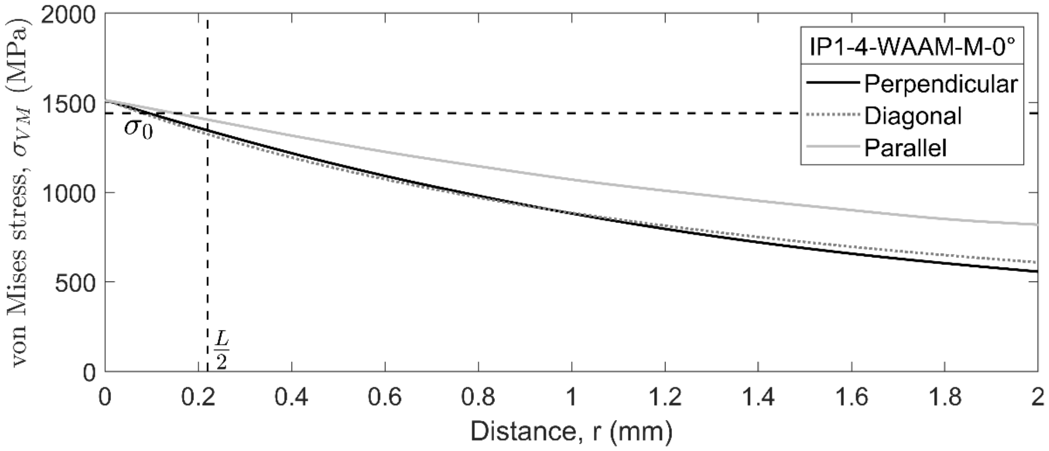

IP1-5-SLM-AB-0°:

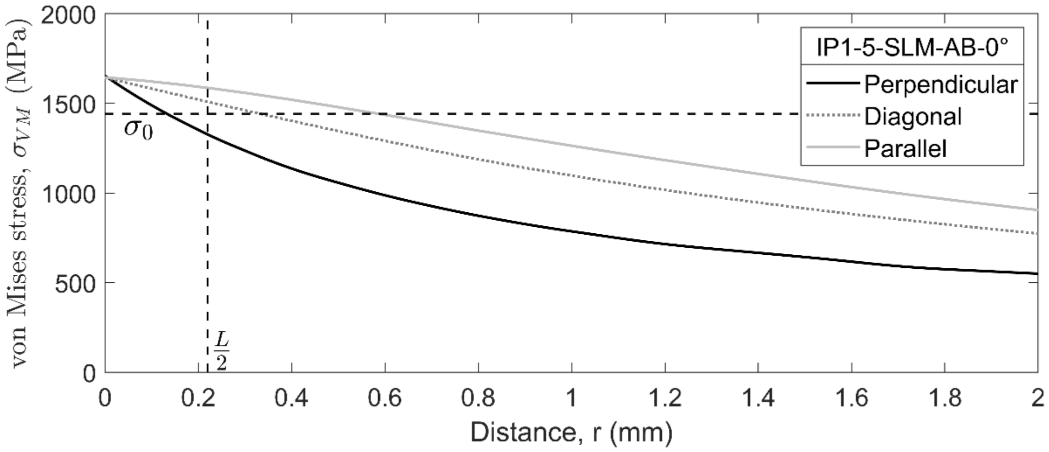

IP1-5-SLM-AB-45°:

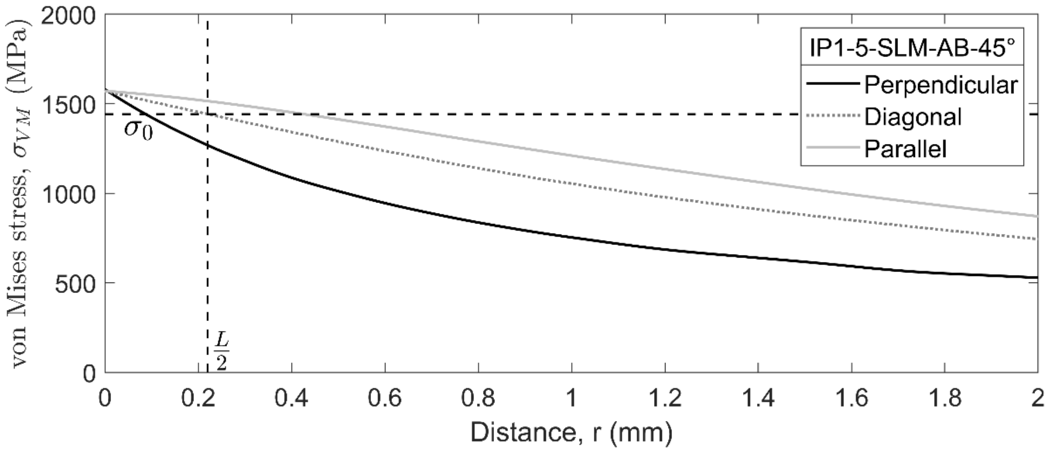

IP1-5-SLM-AB-90°:

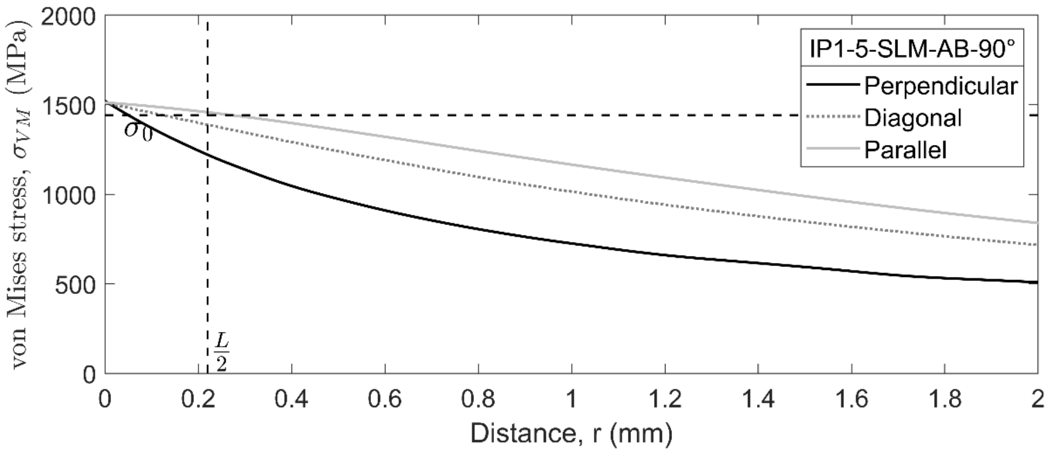

<u>2mm thick conventional double-bolted configuration inner plates' plots:</u>

IP2-1-CON:

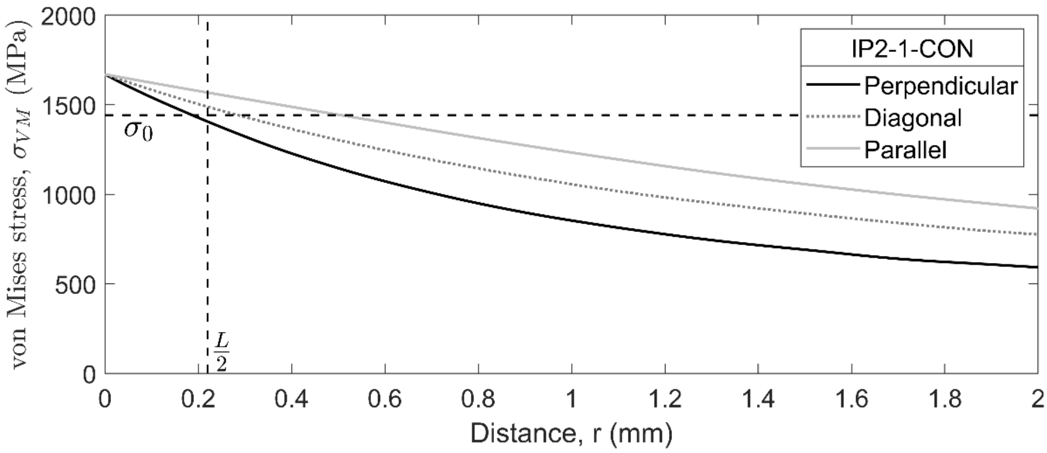

IP2-2-CON:

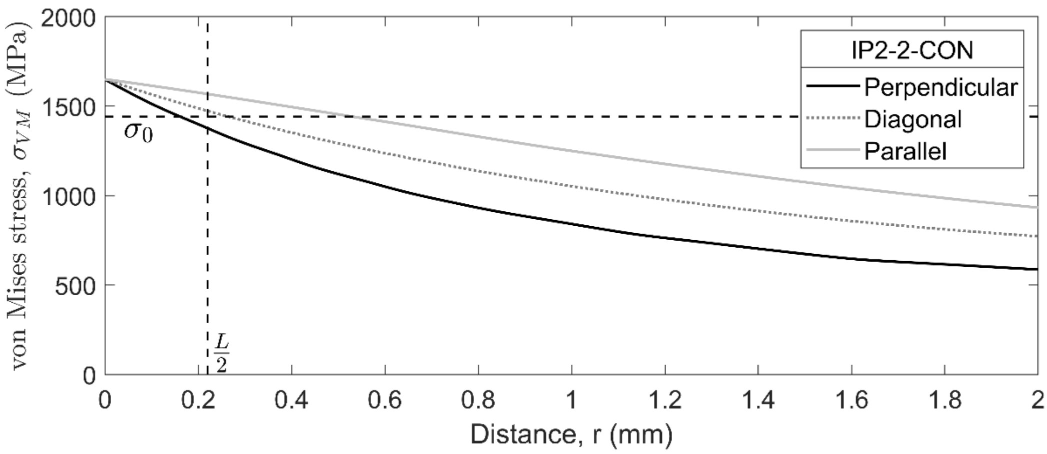

IP2-3-CON:

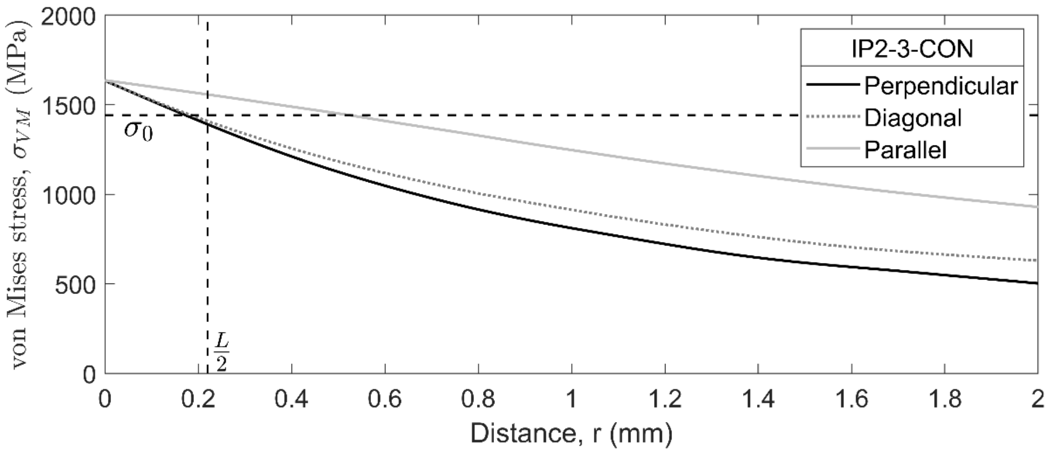

IP2-4-CON:

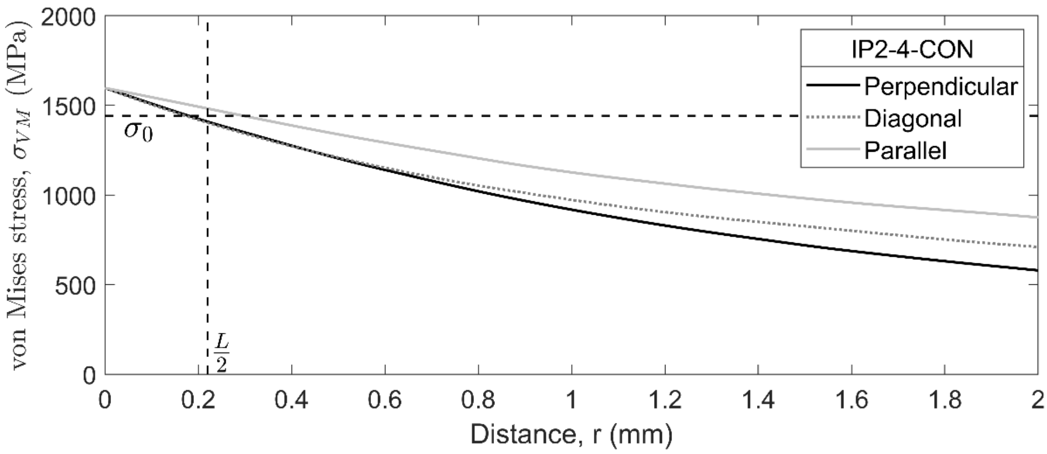

IP2-5-CON:

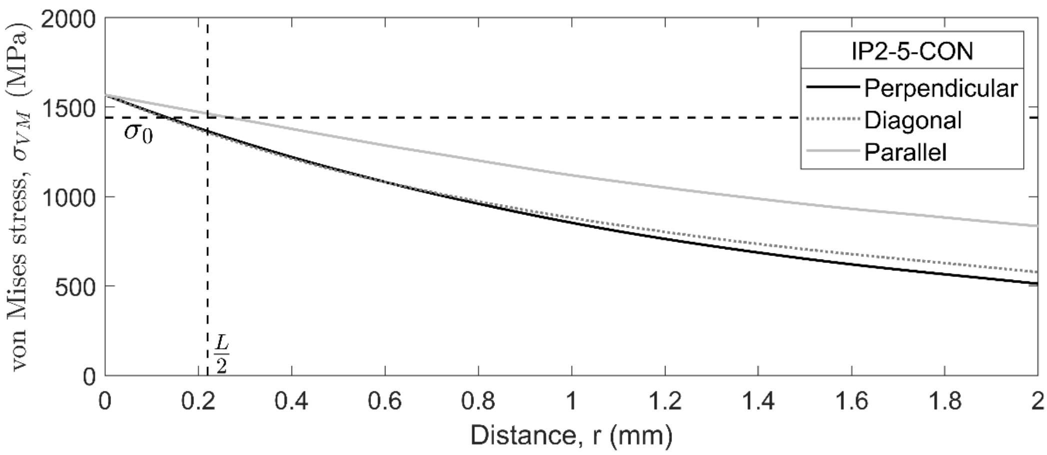

IP2-6-CON:

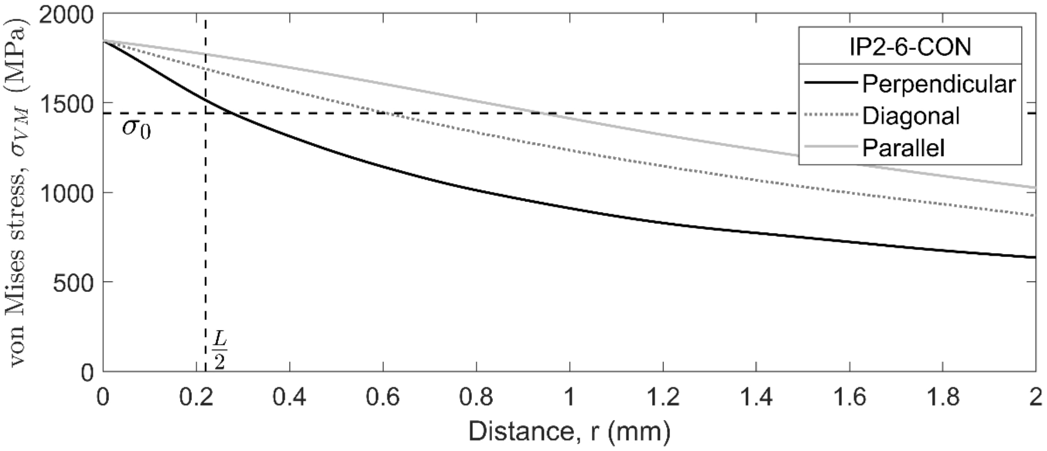

IP2-7-CON:

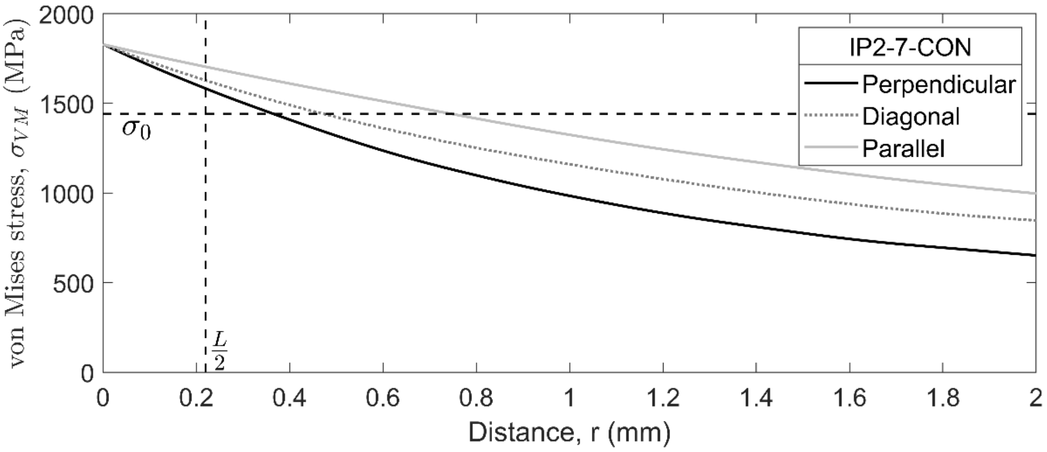

<u>2mm thick additively manufactured double-bolted configuration inner plates' plots:</u>

IP2-1-WAAM-M-0°:

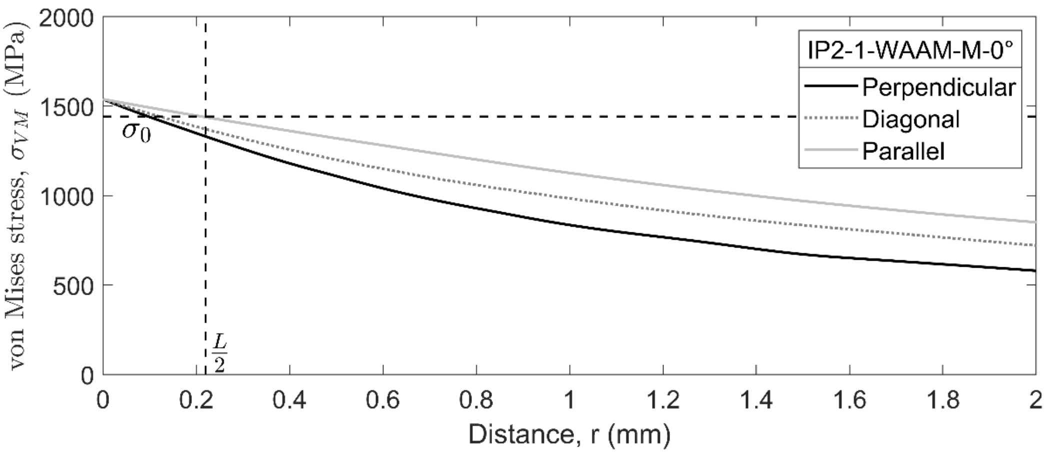

IP2-1-WAAM-M-45°:

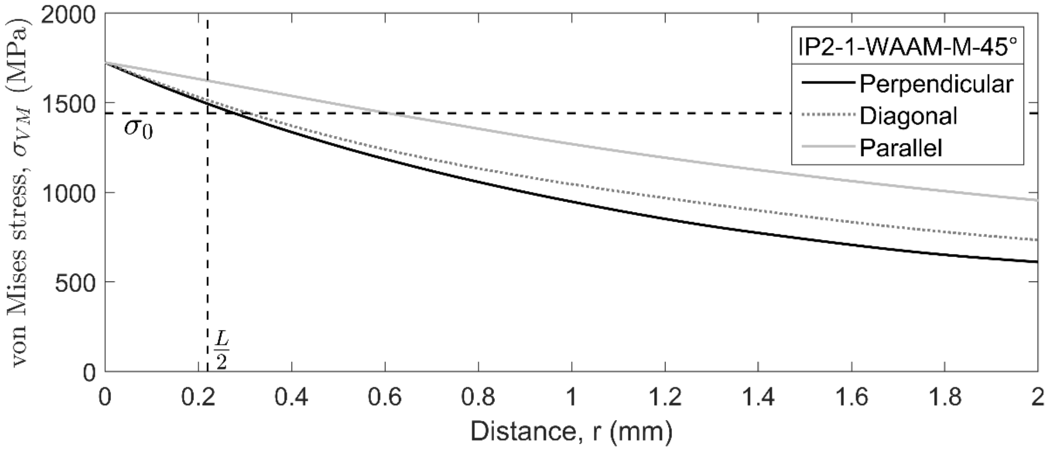

IP2-1-WAAM-M-60°:

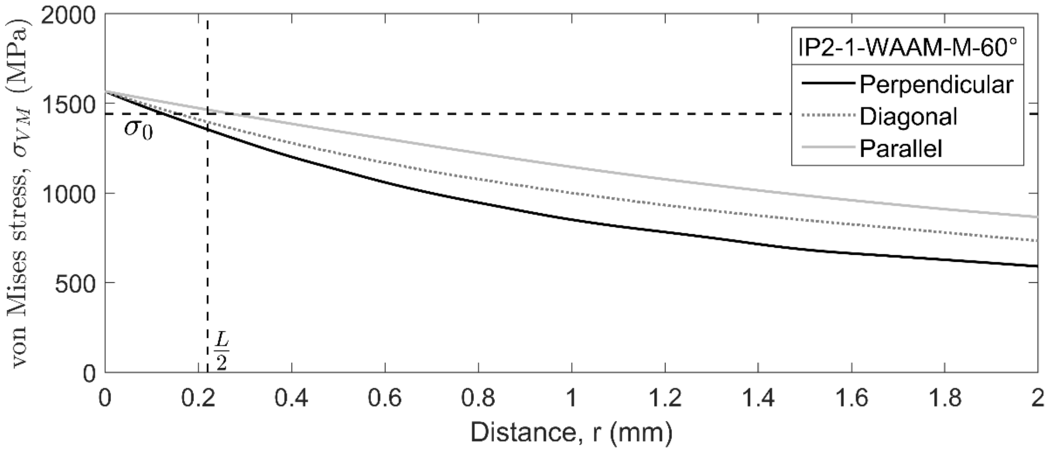

IP2-1-WAAM-M-90°:

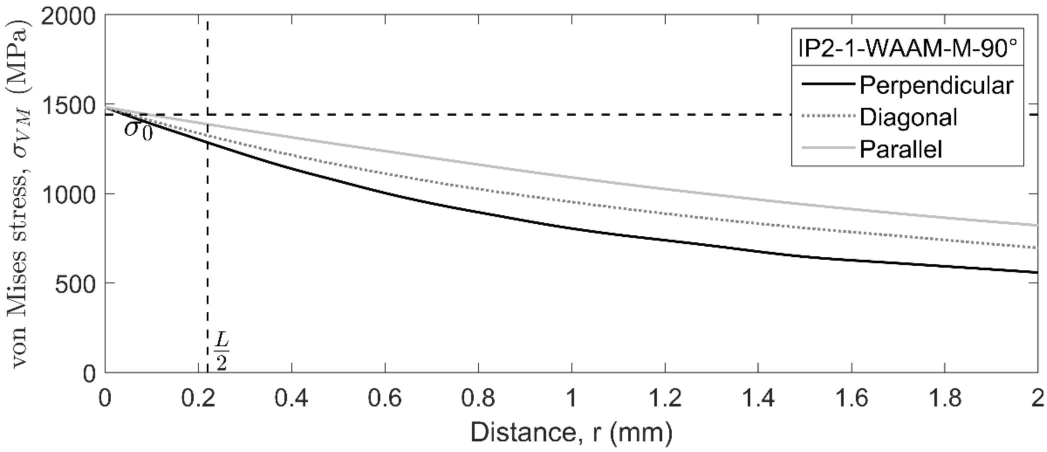

IP2-2-WAAM-M-0°:

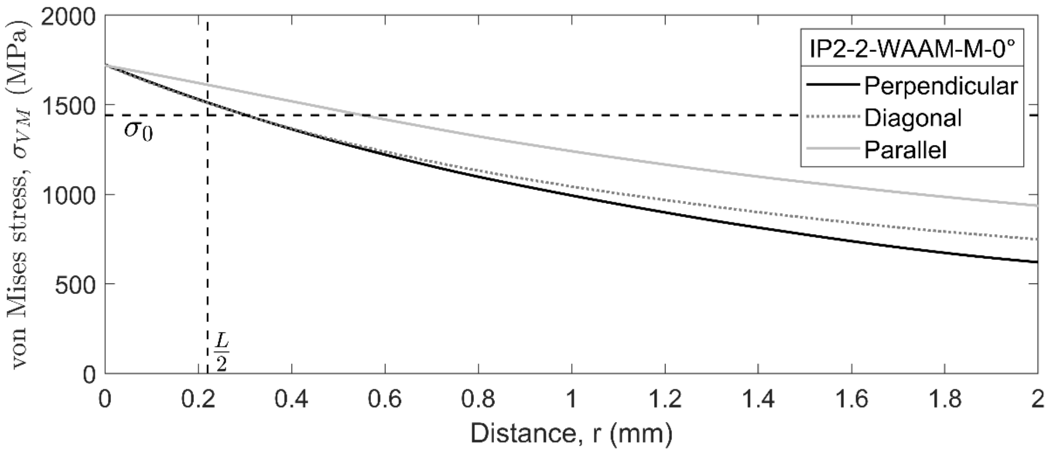

IP2-3-WAAM-M-0°:

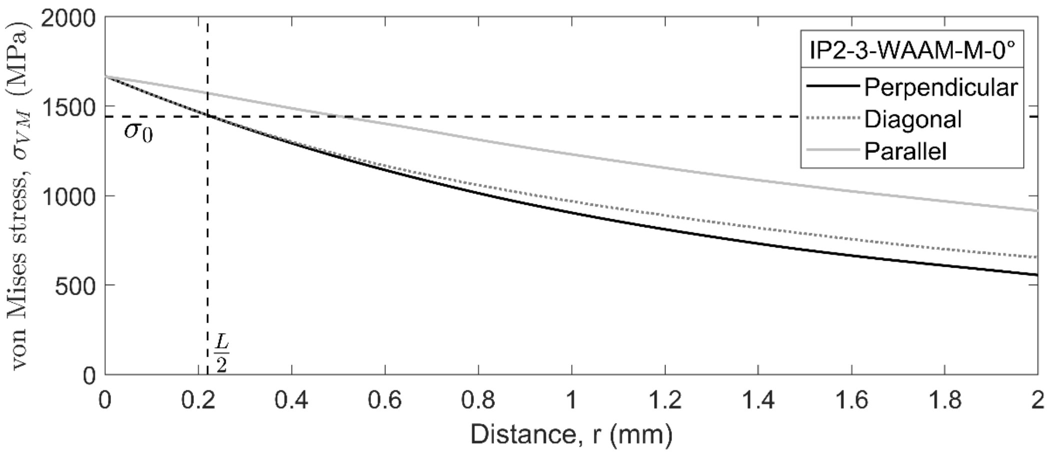

IP2-3-WAAM-M-45°:

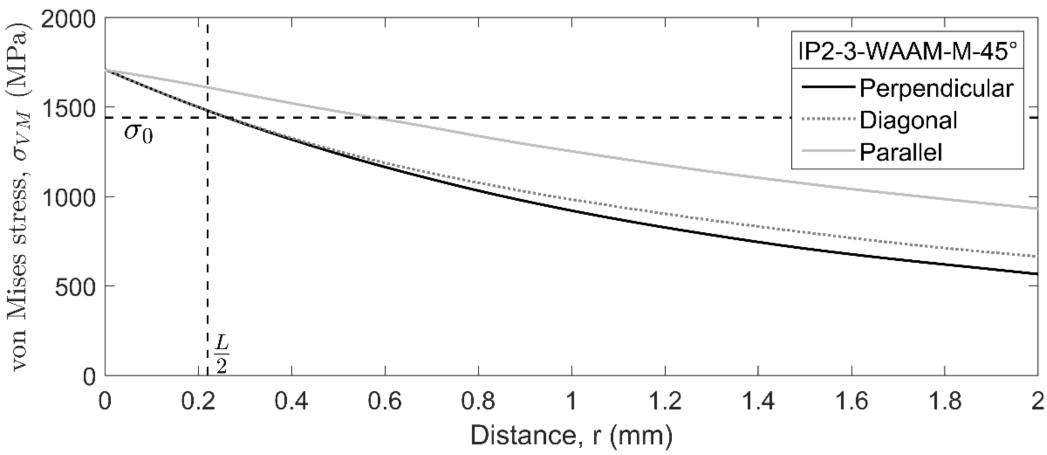

IP2-3-WAAM-M-60°:

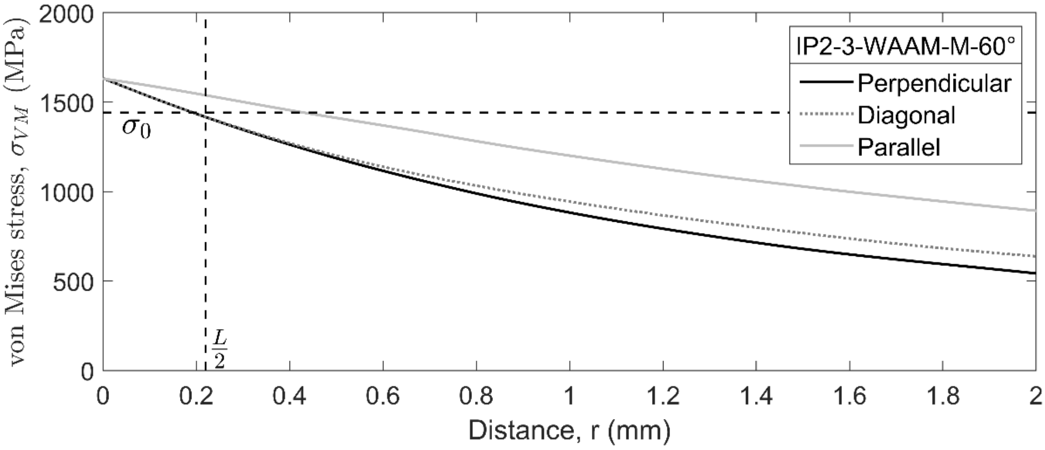

IP2-3-WAAM-M-90°:

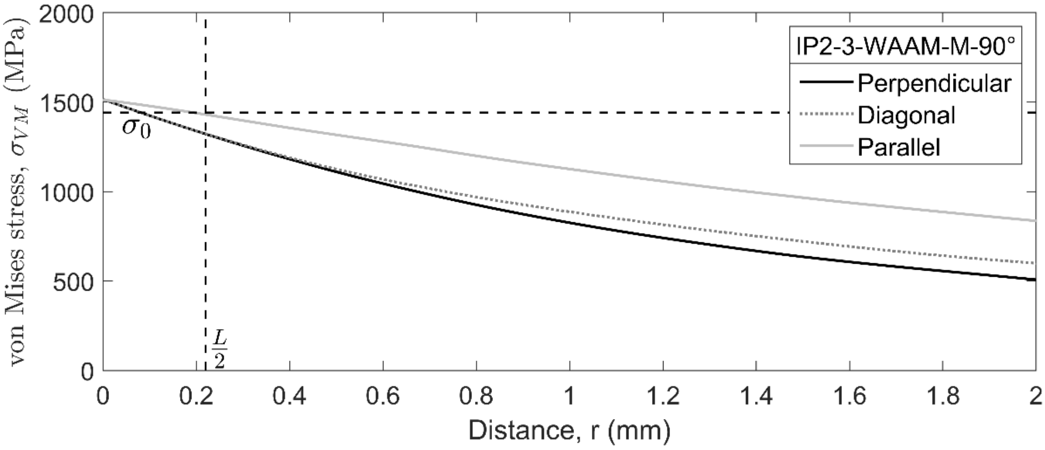

IP2-4-WAAM-M-0°:

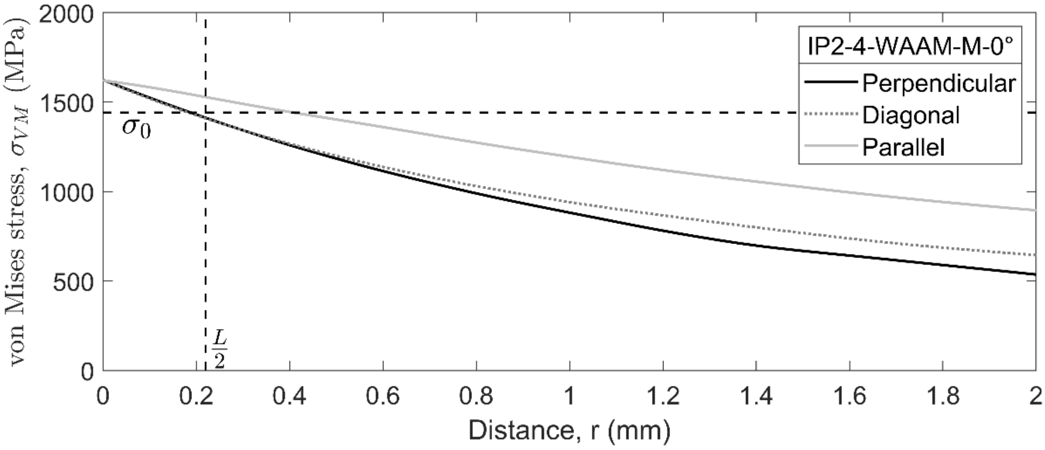

IP2-5-WAAM-M-0°:

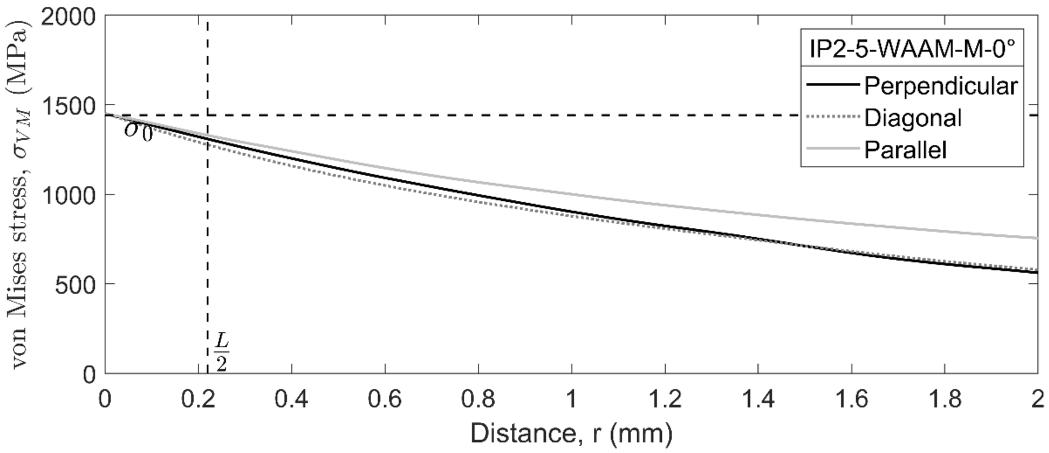

IP2-6-SLM-AB-0°:

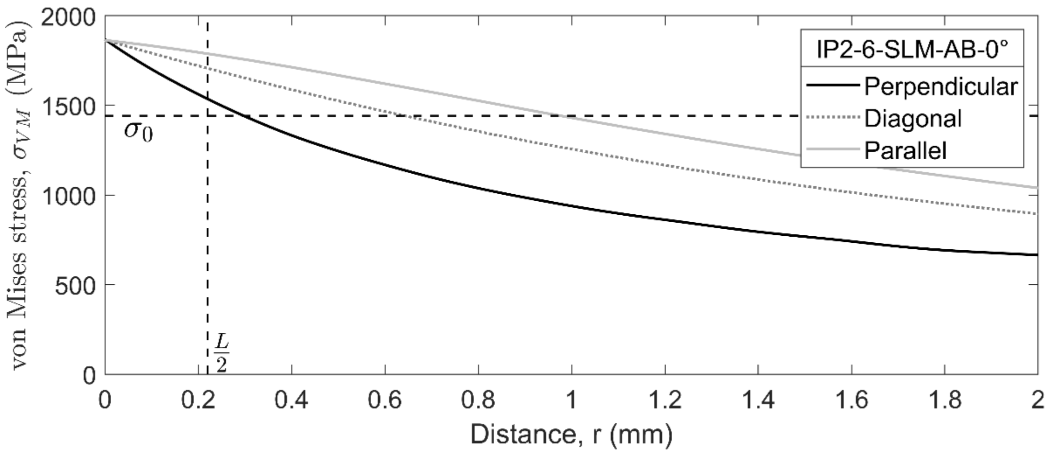

IP2-6-SLM-AB-45°:

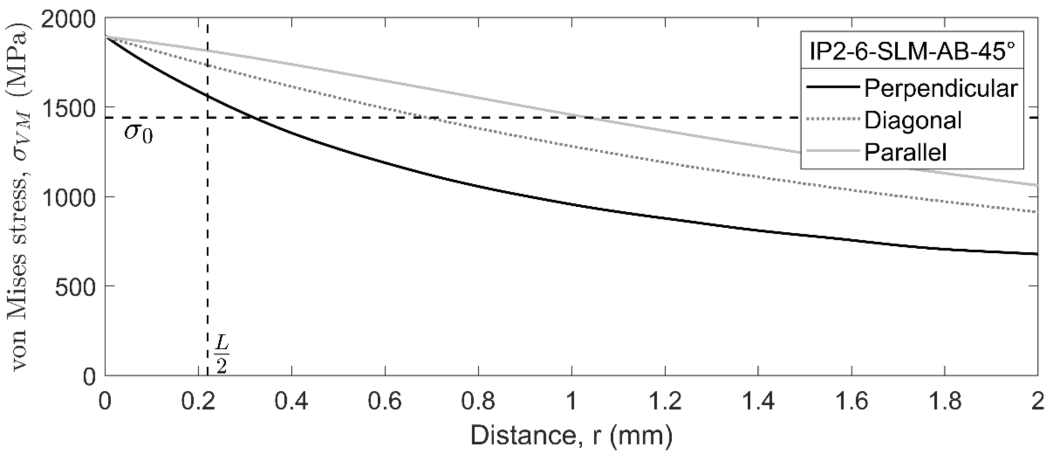

IP2-6-SLM-AB-90°:

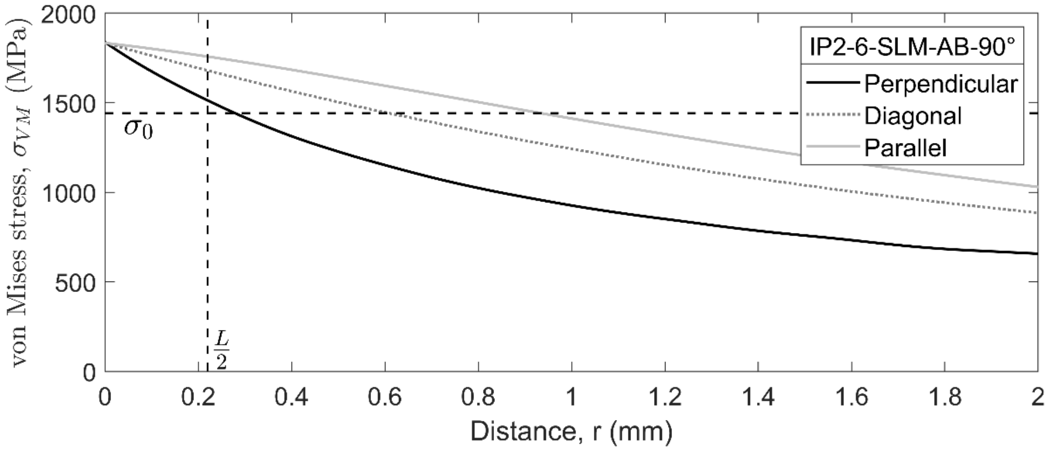

IP2-7-SLM-AB-0°:

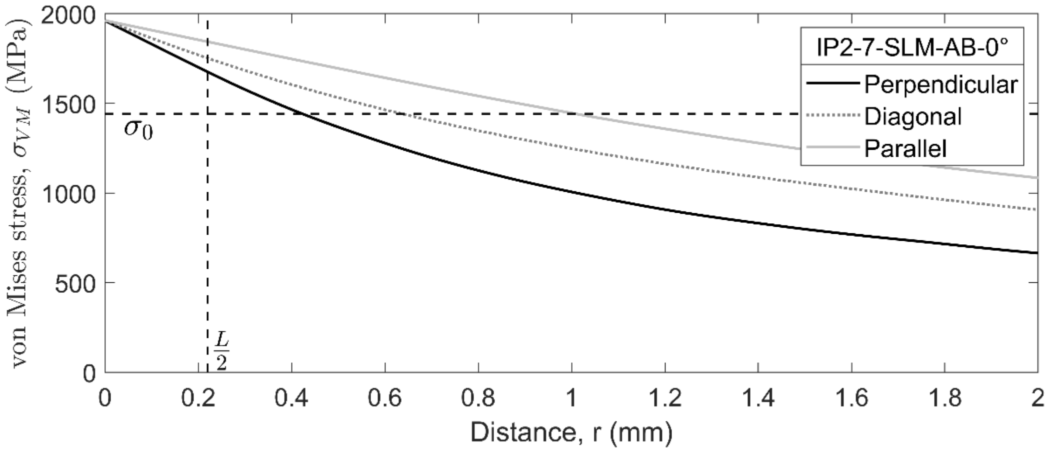

IP2-7-SLM-M-0°:

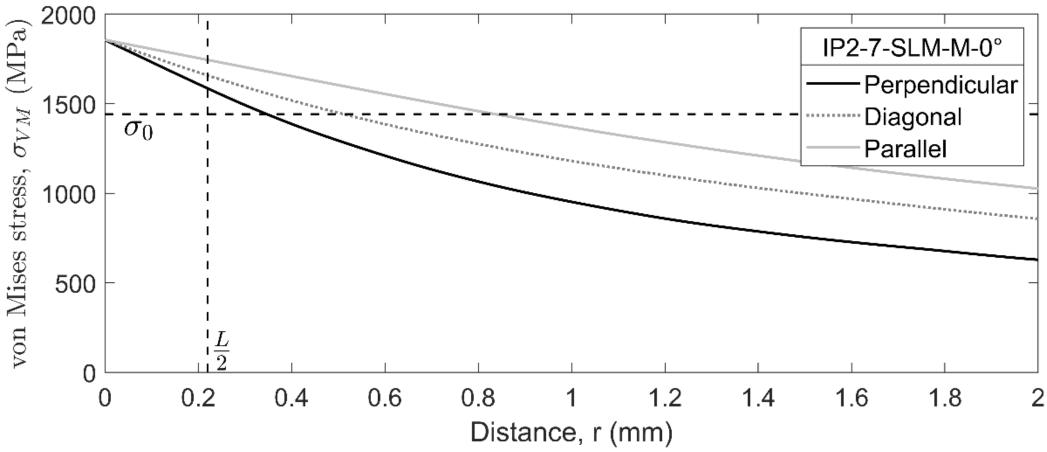

IP2-7-WAAM-M-0°:

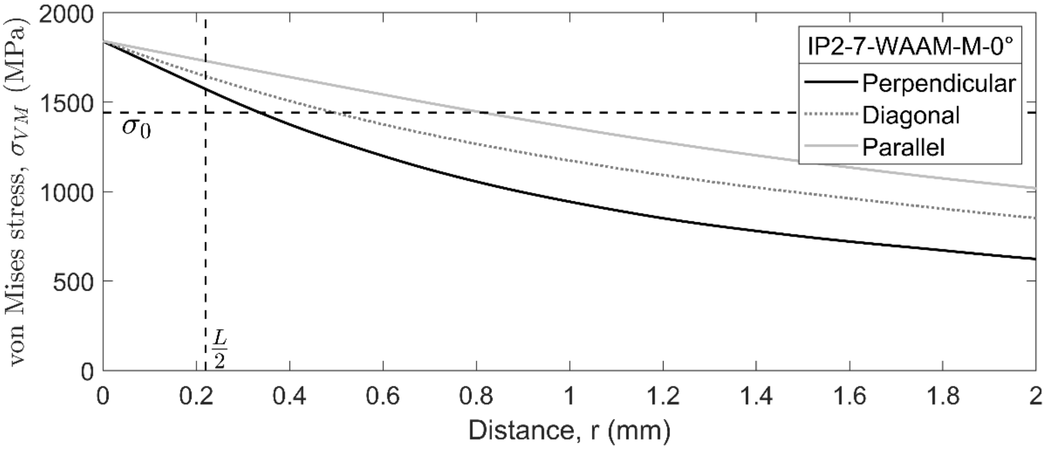

<u>As-built wire arc additively manufactured single-bolted configuration inner plates' plots:</u>

IP1-1-WAAM-AB-0°:

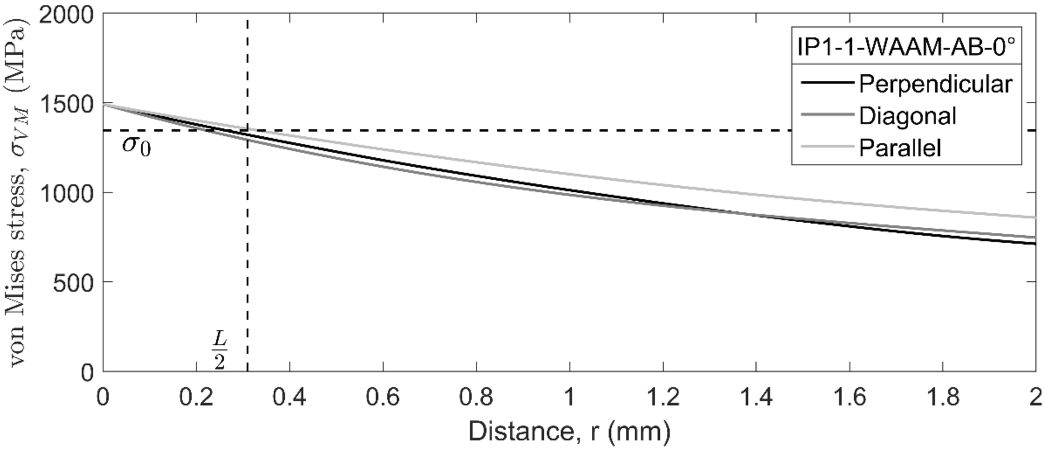

IP1-2-WAAM-AB-0°:

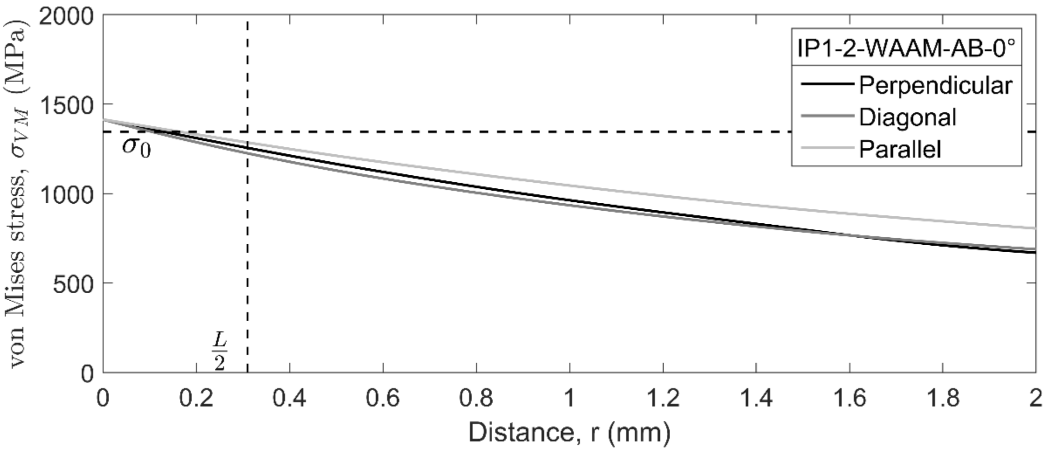

IP1-2-WAAM-AB-45°:

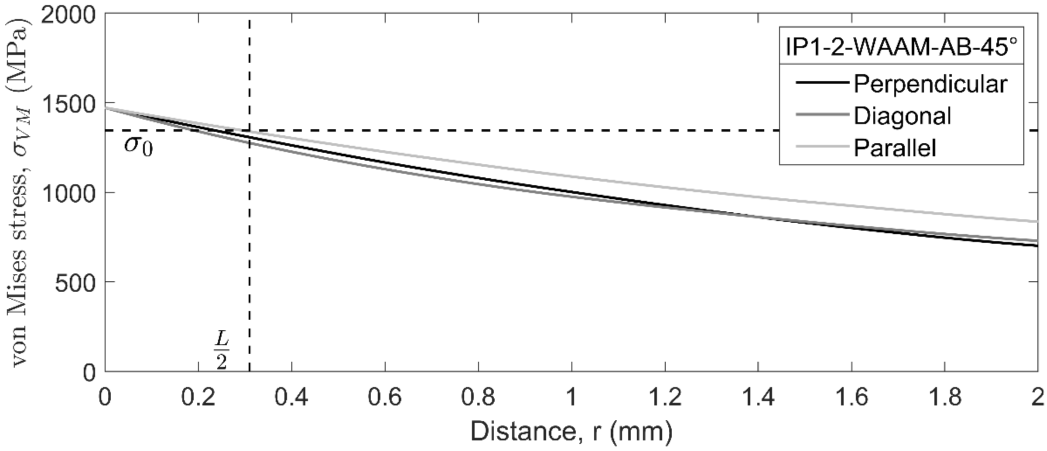

IP1-2-WAAM-AB-60°:

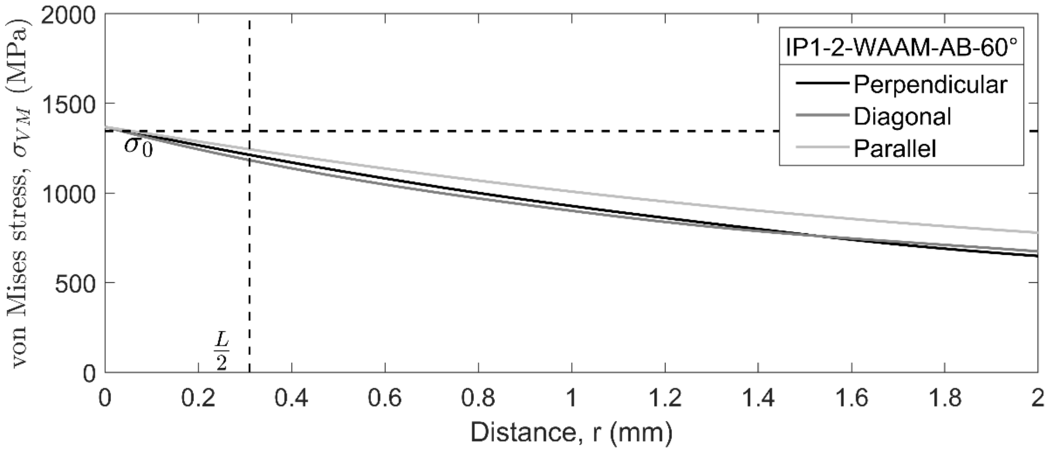

IP1-2-WAAM-AB-90°:

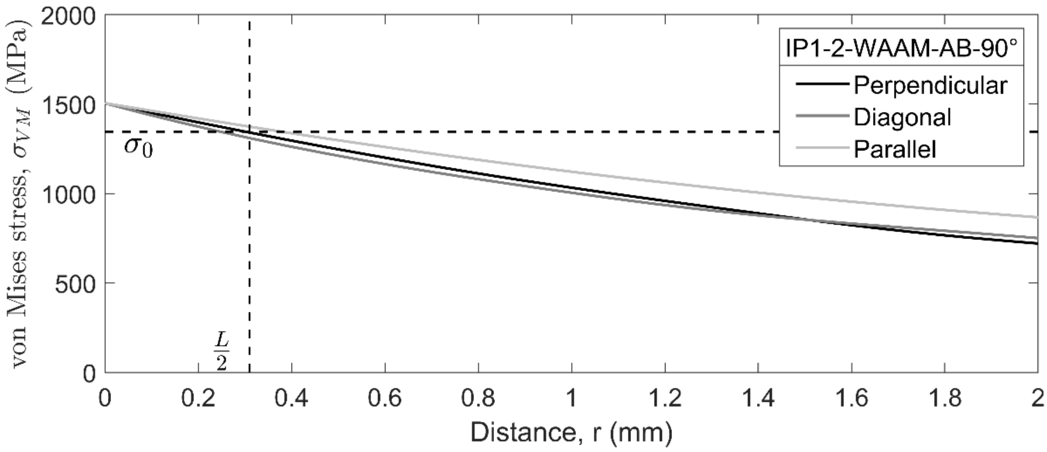

IP1-3-WAAM-AB-0°:

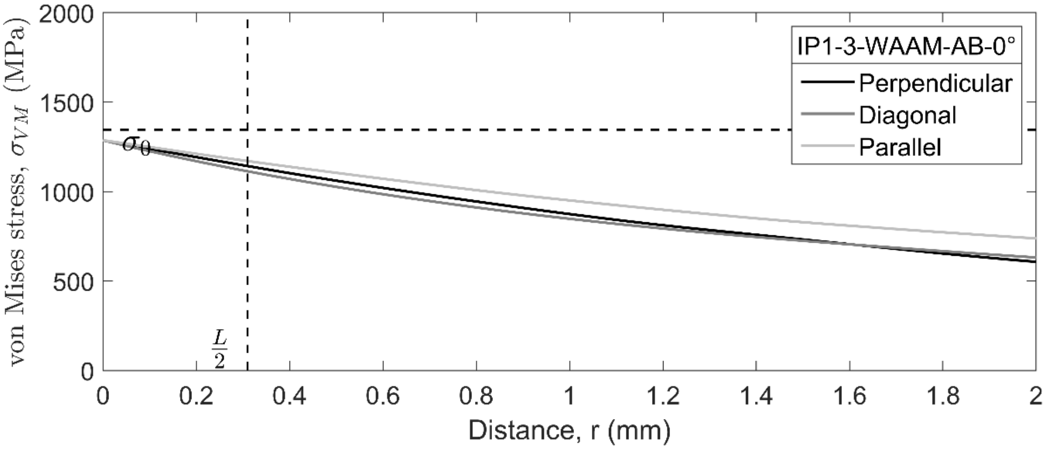

IP1-4-WAAM-AB-0°:

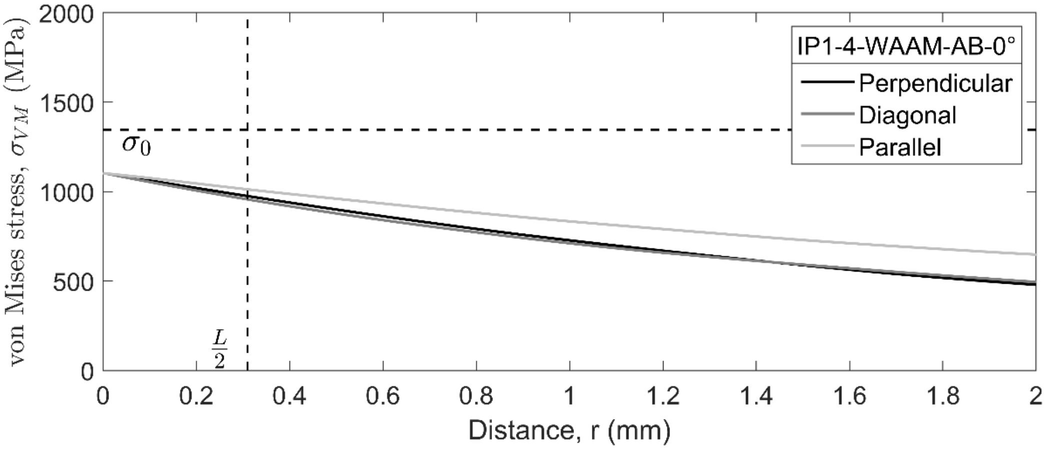

IP1-5-WAAM-AB-0°:

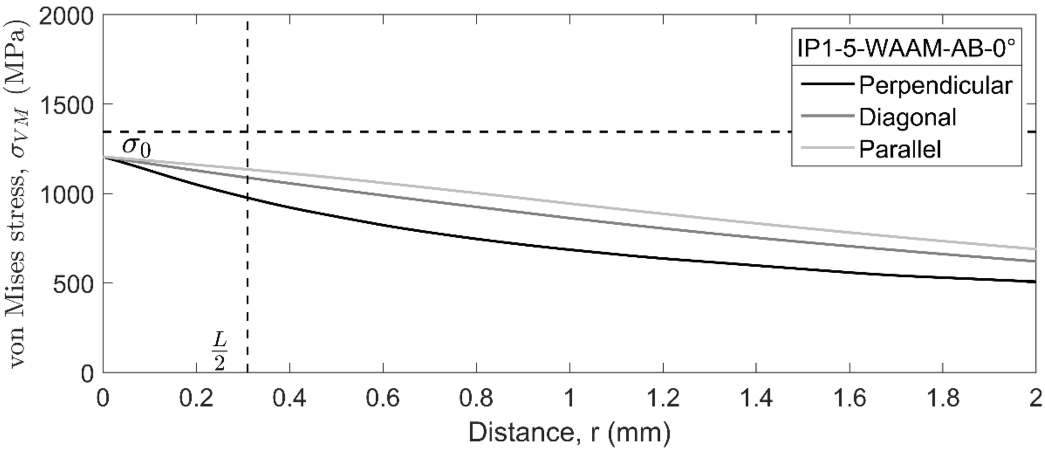

IP1-5-WAAM-AB-45°:

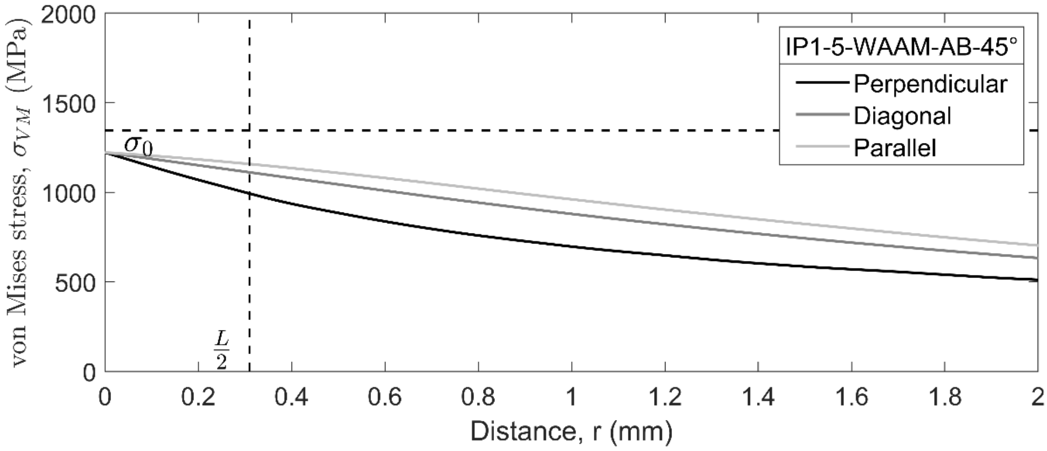

IP1-5-WAAM-AB-60°:

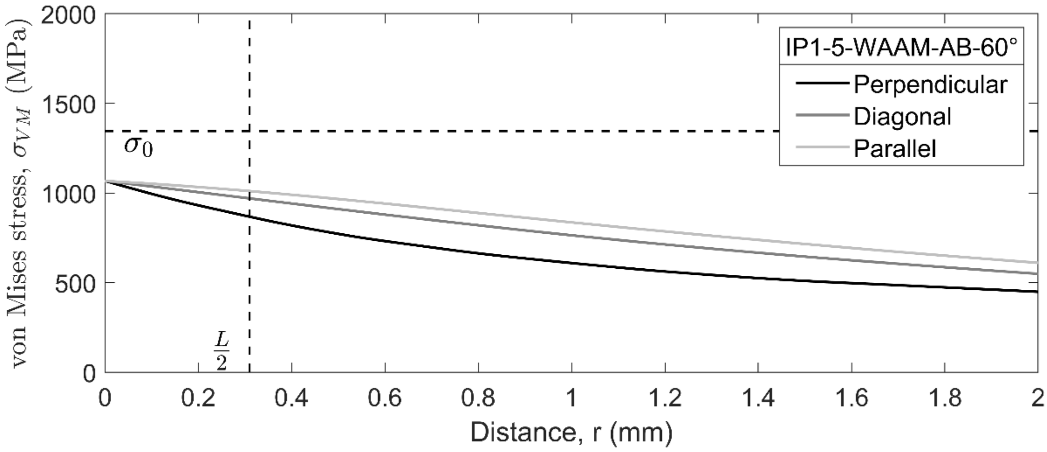

IP1-5-WAAM-AB-90°:

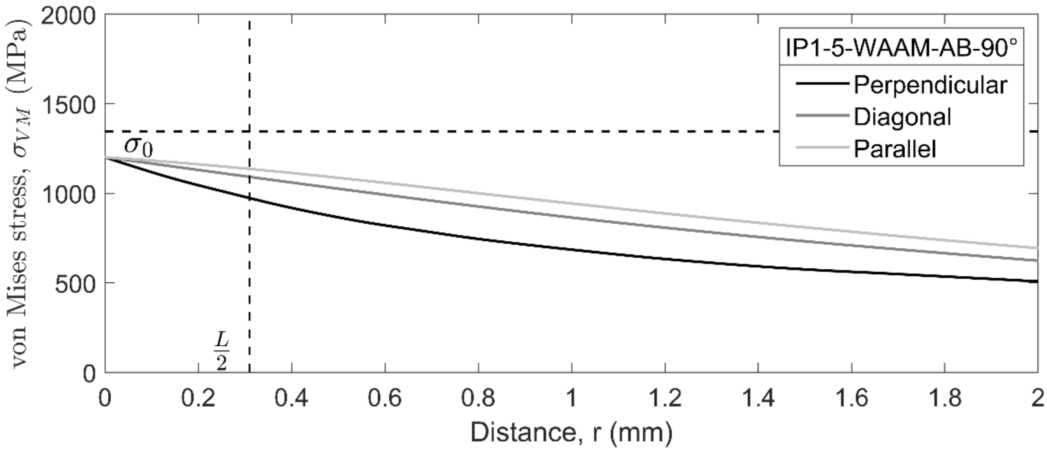

<u>As-built wire arc additively manufactured double-bolted configuration inner plates' plots:</u>

IP2-2-WAAM-AB-0°:

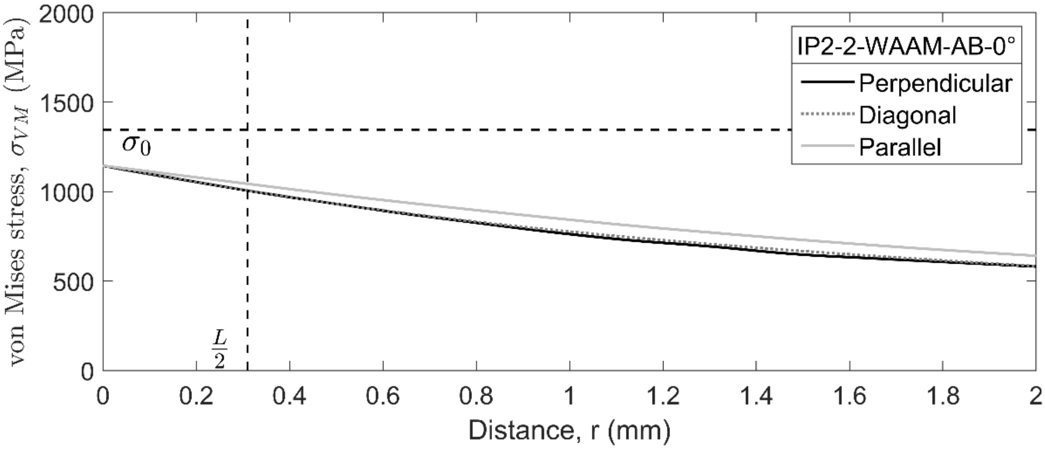

IP2-3-WAAM-AB-0°:

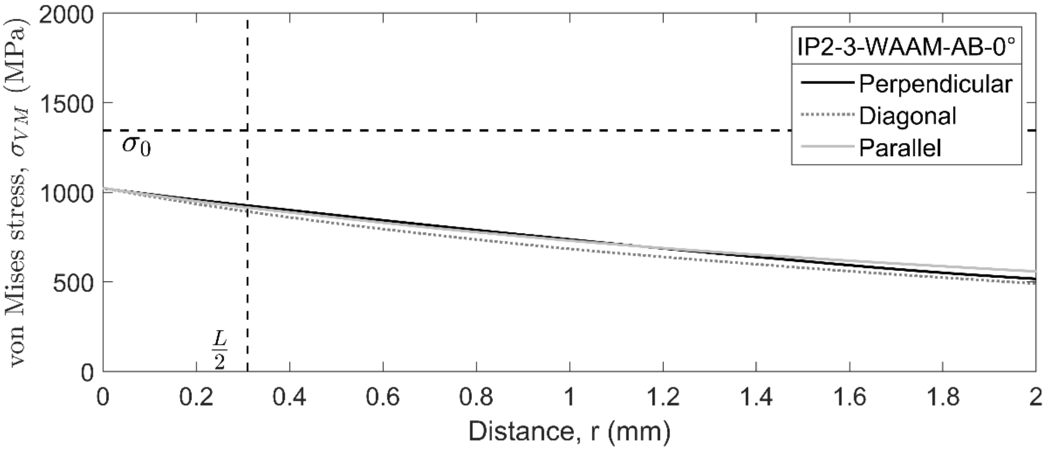

IP2-3-WAAM-AB-45°:

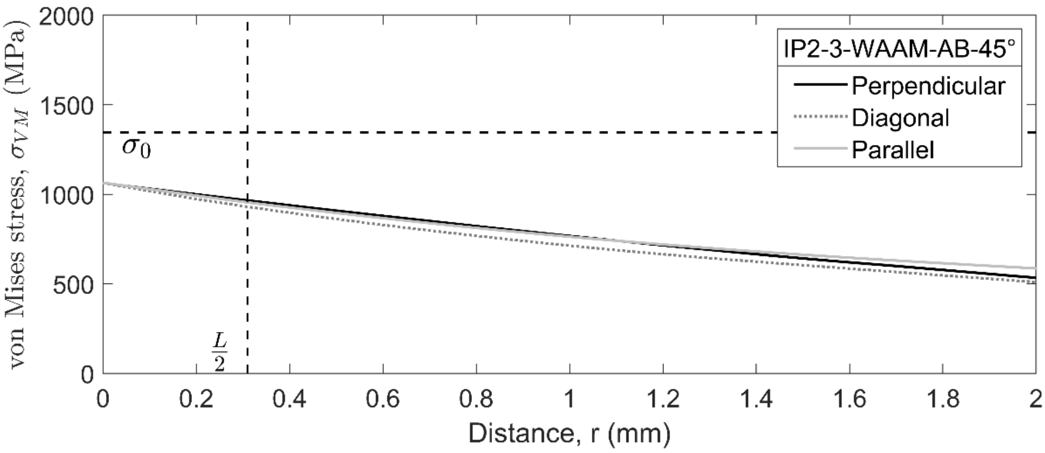

IP2-3-WAAM-AB-60°:

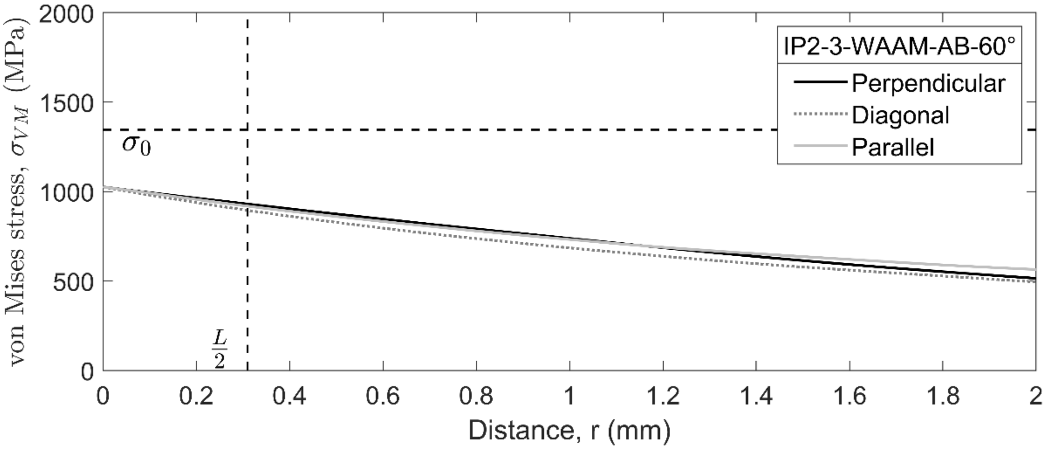

IP2-3-WAAM-AB-90°:

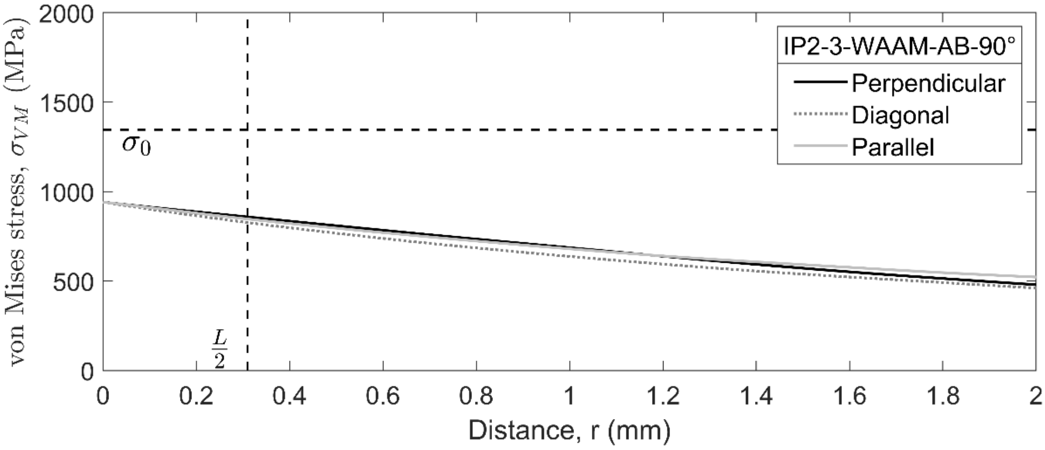

IP2-4-WAAM-AB-0°:

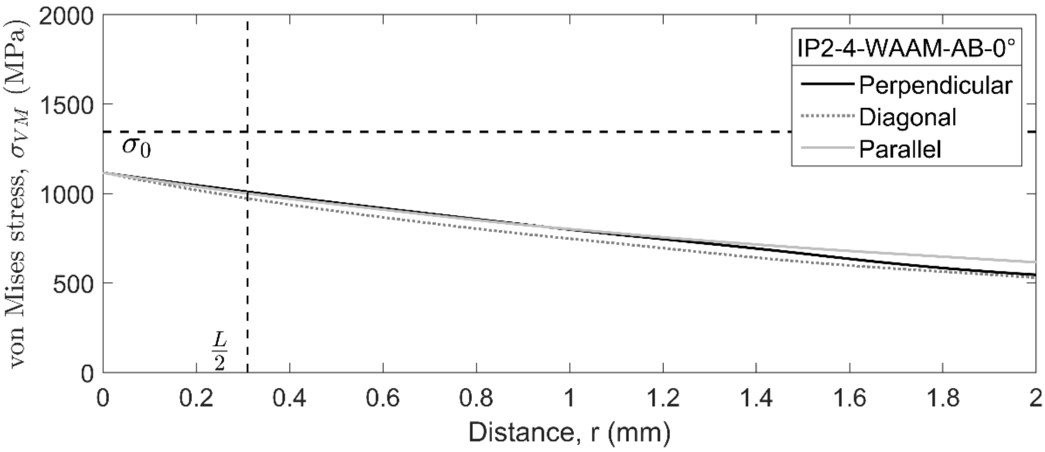

IP2-5-WAAM-AB-0°:

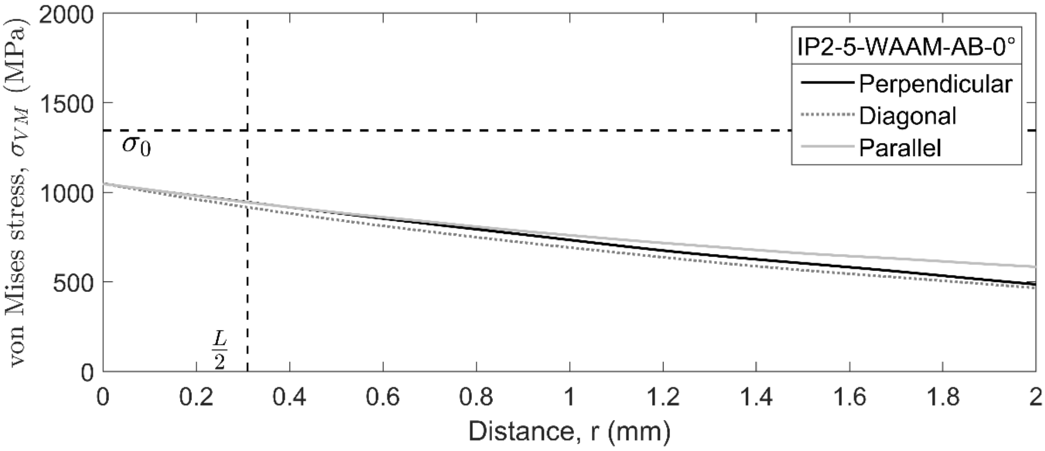

IP2-6-WAAM-AB-0°:

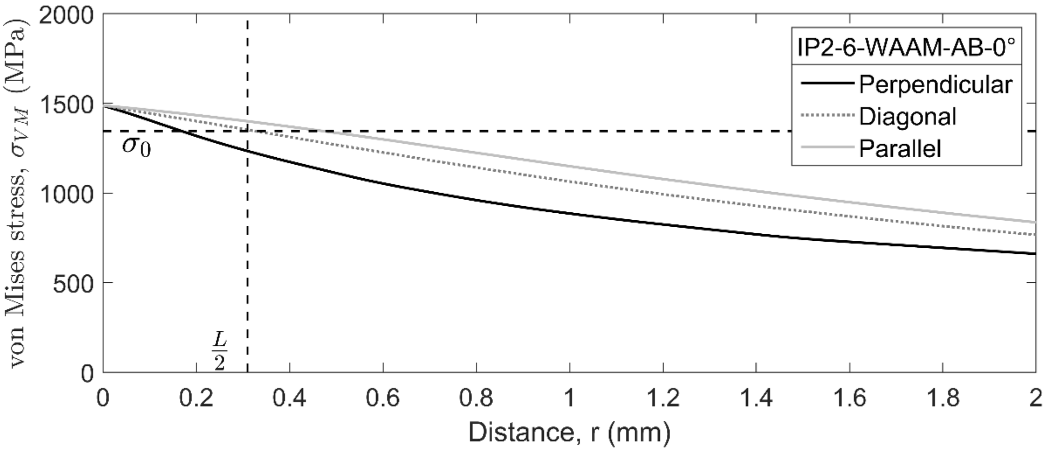

IP2-6-WAAM-AB-45°:

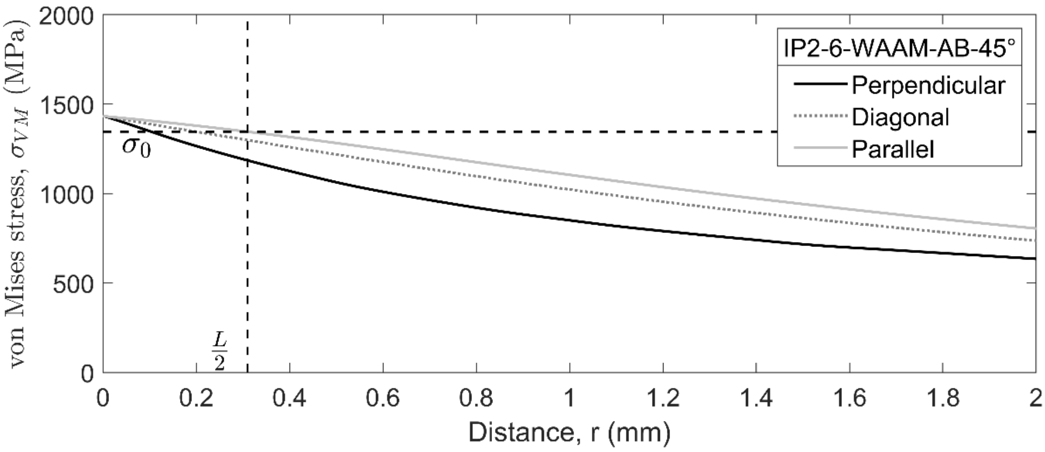

IP2-6-WAAM-AB-60°:

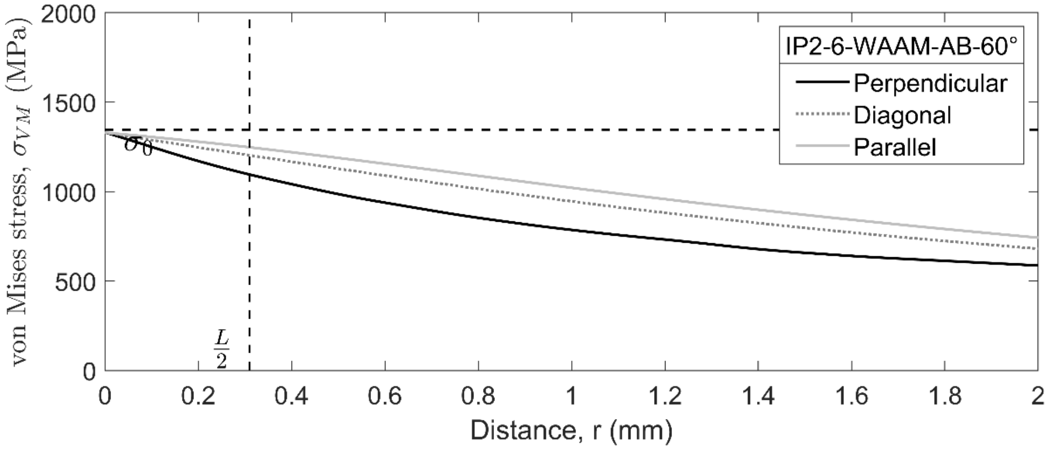

IP2-6-WAAM-AB-90°:

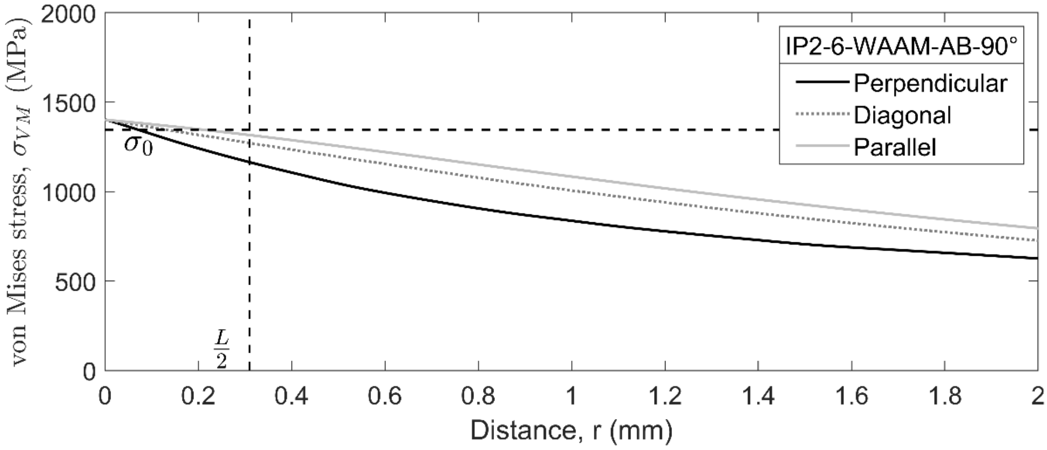

IP2-7-WAAM-AB-0°:

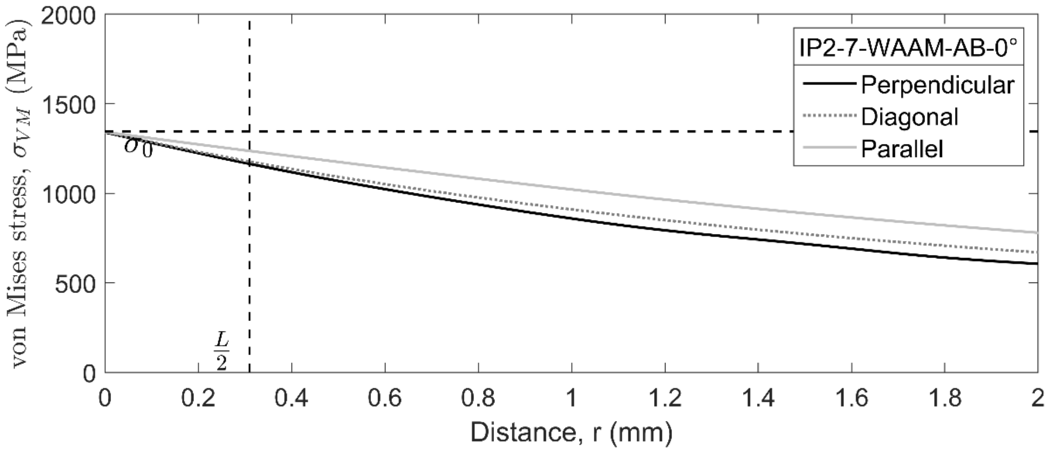

Appendix C – Machine Learning Study's Dataset and MATLAB Scripts

Dataset

Sources used to build the dataset, in addition to the data from the present study: [28], [29], [30], [32], [79], [96], [99], [100], [101], [102], and [103].

TypeofMaterial	Cut_Direction	Surface_finish	NumberofBolts_N_b	Thickness_m_m	DiameterOfHole_m_m	EndDistance_m_m	EdgeDistance_m_m	PitchDistanceHorizontal_m_m	PitchDistanceVertical_m_m	Length_m_m	Breadth_m_m	FailureLoad_k_N	FailureMode	YieldRatio
'austenitic stainless steel'	N/A	N/A	1	1.42	11	55	25	0	0	377	50	34.52	EB	0.63
'austenitic stainless steel'	N/A	N/A	1	1.41	14	70	25	0	0	377	50	37.86	EB	0.63
'ferritic stainless steel'	N/A	N/A	1	0.77	22.1	65.8	65.7	0	0	265.2	131.5	12.6	EB	0.68
'ferritic stainless steel'	N/A	N/A	1	0.77	22	87.9	65.9	0	0	266	131.8	12.8	EB	0.68
'ferritic stainless steel'	N/A	N/A	1	1.2	22	65.9	65.9	0	0	266.1	131.8	18.7	EB	0.6
'ferritic stainless steel'	N/A	N/A	1	1.2	21.9	82.2	66	0	0	330	131.9	19.3	EB	0.6
'ferritic stainless steel'	N/A	N/A	1	1.21	22	98.8	65.9	0	0	390.5	131.7	19.4	EB	0.6
'ferritic stainless steel'	N/A	N/A	1	1.99	22	87.7	65.7	0	0	390.1	131.4	35.7	EB	0.6
'ferritic stainless steel'	N/A	N/A	1	1.2	22	82.2	66	0	0	390.1	132	51.3	EB	0.6
'ferritic stainless steel'	N/A	N/A	1	1.21	21.9	98.8	65.9	0	0	390.2	131.8	54.4	EB	0.6
'duplex stainless steel'	N/A	N/A	1	1.47	14	14	25	0	0	381	50	19.5	EB	0.83
'duplex stainless steel'	N/A	N/A	1	1.47	14	16.8	25	0	0	381	50	23.5	EB	0.83
'duplex stainless steel'	N/A	N/A	1	1.47	14	21	25	0	0	381	50	29.5	EB	0.83
'duplex stainless steel'	N/A	N/A	1	1.47	14	28	25	0	0	381	50	37.5	EB	0.83
'duplex stainless steel'	N/A	N/A	1	1.47	14	35	25	0	0	381	50	45	EB	0.83
'duplex stainless steel'	N/A	N/A	1	1.47	14	42	25	0	0	381	50	45.2	NST	0.83
'duplex stainless steel'	N/A	N/A	1	1.47	14	45.8	25	0	0	381	50	45.5	NST	0.83
'duplex stainless steel'	N/A	N/A	1	3	14	14	30	0	0	381	60	40	EB	0.83
'duplex stainless steel'	N/A	N/A	1	3	14	16.8	30	0	0	381	60	48	EB	0.83
'duplex stainless steel'	N/A	N/A	1	3	14	21	30	0	0	381	60	61.5	EB	0.83
'duplex stainless steel'	N/A	N/A	1	3	14	28	30	0	0	381	60	74	EB	0.83
'duplex stainless steel'	N/A	N/A	1	3	14	35	30	0	0	381	60	86.5	EB	0.83

'duplex stainless steel'	N/A	N/A	1	3	14	42	30	0	0	381	60	91	EB	0.83
'duplex stainless steel'	N/A	N/A	1	3	14	52	30	0	0	381	60	93.2	EB	0.83
'duplex stainless steel'	N/A	N/A	1	1.46	14	70	25	0	0	377	50	44.38	EB	0.83
'S690QL ultra high strength steel'	N/A	N/A	1	10	30	90.3	28.5	0	0	200	57	262	NST	0.95
'S690QL ultra high strength steel'	N/A	N/A	1	10	30	36.3	36	0	0	200	72	273	EB	0.95
'S690QL ultra high strength steel'	N/A	N/A	1	10	30	45	34.5	0	0	200	69	342	EB	0.95
'S690QL ultra high strength steel'	N/A	N/A	1	10	30	60.3	35.7	0	0	200	71.4	360	NST	0.95
'S690QL ultra high strength steel'	N/A	N/A	1	10	30	89.4	34.8	0	0	200	69.6	355	NST	0.95
'S690QL ultra high strength steel'	N/A	N/A	1	10	30	75.6	39.9	0	0	200	79.8	445	NST	0.95
'S690QL ultra high strength steel'	N/A	N/A	1	10	30	90.6	39.6	0	0	200	79.2	440	NST	0.95
'S690QL ultra high strength steel'	N/A	N/A	1	10	30	100.2	35.1	0	0	200	70.2	370	NST	0.95
'S690QL ultra high strength steel'	N/A	N/A	1	10	30	30	44.1	0	0	200	88.2	228	EB	0.95
'S690QL ultra high strength steel'	N/A	N/A	1	10	30	36.3	45.9	0	0	200	91.8	286	EB	0.95
'S690QL ultra high strength steel'	N/A	N/A	1	10	30	45.3	44.4	0	0	200	88.8	363	EB	0.95
'S690QL ultra high strength steel'	N/A	N/A	1	10	30	60.3	44.1	0	0	200	88.2	483	EB	0.95
'S690QL ultra high strength steel'	N/A	N/A	1	10	30	74.7	43.8	0	0	200	87.6	516	NST	0.95
'S690QL ultra high strength steel'	N/A	N/A	1	10	30	90	43.8	0	0	200	87.6	510	NST	0.95
'S690QL ultra high strength steel'	N/A	N/A	1	10	30	90	39	0	0	200	78	435	NST	0.95
'S690QL ultra high strength steel'	N/A	N/A	1	10	30	45	42.6	0	0	200	85.2	371	EB	0.95
'S690QL ultra high strength steel'	N/A	N/A	1	10	30	45	44.4	0	0	200	88.8	362	EB	0.95
'S690QL ultra high strength steel'	N/A	N/A	1	10	30	45.9	57	0	0	200	114	392	EB	0.95
'S690QL ultra high strength steel'	N/A	N/A	1	10	30	61.8	57.9	0	0	200	115.8	530	EB	0.95

'S690QL ultra high strength steel'	N/A	N/A	1	10	30	76.8	58.8	0	0	200	117.6	629	EB	0.95
'S690QL ultra high strength steel'	N/A	N/A	1	10	30	91.8	60.6	0	0	200	121.2	763	EB	0.95
'S690QL ultra high strength steel'	N/A	N/A	1	10	30	106.2	58.5	0	0	200	117	788	NST	0.95
'S690QL ultra high strength steel'	N/A	N/A	1	10	24	101.28	38.64	0	0	200	77.28	483	NST	0.95
'S690QL ultra high strength steel'	N/A	N/A	1	10.2	24	101.04	34.56	0	0	200	69.12	400	NST	0.95
'S690QL ultra high strength steel'	N/A	N/A	1	10.15	24	101.04	28.32	0	0	200	56.64	322	NST	0.95
'S550Q high-strength steel'	N/A	N/A	1	9.8	26	25.74	77.74	0	0	200	155.48	183	EB	0.89
'S550Q high-strength steel'	N/A	N/A	1	9.8	26	30.94	77.74	0	0	200	155.48	226	EB	0.89
'S550Q high-strength steel'	N/A	N/A	1	9.9	26	38.74	77.74	0	0	200	155.48	292	EB	0.89
'S550Q high-strength steel'	N/A	N/A	1	9.9	26	51.74	78	0	0	200	156	382	EB	0.89
'S550Q high-strength steel'	N/A	N/A	1	9.9	26.1	64.989	78.039	0	0	200	156.078	456	EB	0.89
'S550Q high-strength steel'	N/A	N/A	1	9.9	26	38.74	39	0	0	200	78	271	EB	0.89
'S550Q high-strength steel'	N/A	N/A	1	9.9	26	38.74	28.34	0	0	200	56.68	242	NST	0.89
'S550Q high-strength steel'	N/A	N/A	1	10	25.9	38.591	20.72	0	0	200	41.44	125	NST	0.89
'S690Q high-strength steel'	N/A	N/A	1	10.1	26	26	78	0	0	200	156	210	EB	0.96
'S690Q high-strength steel'	N/A	N/A	1	10.1	26	31.2	78	0	0	200	156	249	EB	0.96
'S690Q high-strength steel'	N/A	N/A	1	10	26	39	78	0	0	200	156	332	EB	0.96
'S690Q high-strength steel'	N/A	N/A	1	10.2	26	52.26	78	0	0	200	156	437	EB	0.96
'S690Q high-strength steel'	N/A	N/A	1	10.2	26	65.26	78	0	0	200	156	542	EB	0.96
'S690Q high-strength steel'	N/A	N/A	1	10.2	26	39	39	0	0	200	78	317	EB	0.96
'S690Q high-strength steel'	N/A	N/A	1	10.2	26	38.74	28.6	0	0	200	57.2	284	NST	0.96

'S690Q high-strength steel'	N/A	N/A	1	10.2	26	39	20.8	0	0	200	41.6	149	NST	0.96
'S890Q high-strength steel'	N/A	N/A	1	10.3	26	26	78	0	0	200	156	262	EB	0.96
'S890Q high-strength steel'	N/A	N/A	1	10.3	26	30.94	78	0	0	200	156	328	EB	0.96
'S890Q high-strength steel'	N/A	N/A	1	10.3	26	39	78	0	0	200	156	416	EB	0.96
'S890Q high-strength steel'	N/A	N/A	1	10.4	26	52	78	0	0	200	156	550	EB	0.96
'S890Q high-strength steel'	N/A	N/A	1	10.3	26	64.74	78	0	0	200	156	662	EB	0.96
'S890Q high-strength steel'	N/A	N/A	1	10.4	26	38.74	38.74	0	0	200	77.48	392	EB	0.96
'S890Q high-strength steel'	N/A	N/A	1	10.3	26	39	28.6	0	0	200	57.2	347	NST	0.96
'S890Q high-strength steel'	N/A	N/A	1	10.3	26	39	20.8	0	0	200	41.6	183	NST	0.96
'Mild steel grade S235'	N/A	N/A	1	12	26	31.98	31.98	0	0	200	64	151	EB	0.73
'Mild steel grade S235'	N/A	N/A	1	12	26	39	31.98	0	0	200	64	192	NST	0.73
'Mild steel grade S235'	N/A	N/A	1	12	26	52	31.98	0	0	200	64	202	NST	0.73
'Mild steel grade S235'	N/A	N/A	1	12	26	26	39	0	0	200	78	125	EB	0.73
'Mild steel grade S235'	N/A	N/A	1	12	26	31.98	39	0	0	200	78	164	EB	0.73
'Mild steel grade S235'	N/A	N/A	1	12	26	39	39	0	0	200	78	197	EB	0.73
'Mild steel grade S235'	N/A	N/A	1	12	26	52	39	0	0	200	78	283	NST	0.73
'Mild steel grade S235'	N/A	N/A	1	12	26	65	39	0	0	200	78	279	NST	0.73
'Mild steel grade S235'	N/A	N/A	1	12	18	18	27	0	0	200	54	84	EB	0.73
'Mild steel grade S235'	N/A	N/A	1	12	18	21.96	27	0	0	200	54	104	EB	0.73
'Mild steel grade S235'	N/A	N/A	1	12	18	27	27	0	0	200	54	129	EB	0.73
'Mild steel grade S235'	N/A	N/A	1	12	18	36	27	0	0	200	54	182	NST	0.73
'Mild steel grade S235'	N/A	N/A	1	12	18	45	27	0	0	200	54	188	NST	0.73
'austenitic stainless steel'	N/A	N/A	2	1.43	9	45	25	0	27	377	50	42.08	EB	0.63
'ferritic stainless steel'	N/A	N/A	2	0.78	22	65.8	65.9	65.7	0	400.6	131.8	26	EB	0.68
'ferritic stainless steel'	N/A	N/A	2	0.78	22	65.7	65.9	87.7	0	439.4	131.8	26.2	EB	0.6
'ferritic stainless steel'	N/A	N/A	2	1.2	21.9	65.9	65.8	66	0	400.1	131.7	39.7	EB	0.6
'ferritic stainless steel'	N/A	N/A	2	2	21.9	66	65.7	65.5	0	400.2	131.5	83.4	EB	0.6
'ferritic stainless steel'	N/A	N/A	2	2	22	65.8	65.7	87.8	0	440.7	131.4	84.3	EB	0.6
'ferritic stainless steel'	N/A	N/A	2	2	22	65.7	65.9	65.7	0	390.3	131.8	97.3	EB	0.6

'ferritic stainless steel'	N/A	N/A	2	2	22.1	65.7	65.8	87.8	0	440	131.6	96.5	EB	0.6
'duplex stainless steel'	N/A	N/A	2	1.45	9	9	25	0	27	386	50	38	EB	0.83
'duplex stainless steel'	N/A	N/A	2	1.45	9	10.8	25	0	27	386	50	44	EB	0.83
'duplex stainless steel'	N/A	N/A	2	1.45	9	13.5	25	0	27	386	50	46	EB	0.83
'duplex stainless steel'	N/A	N/A	2	1.45	9	18	25	0	27	386	50	50.8	EB	0.83
'duplex stainless steel'	N/A	N/A	2	1.45	9	22.5	25	0	27	386	50	51.2	EB	0.83
'duplex stainless steel'	N/A	N/A	2	1.45	9	27	25	0	27	386	50	51.1	NST	0.83
'duplex stainless steel'	N/A	N/A	2	1.45	9	45.8	25	0	27	386	50	51.2	NST	0.83
'duplex stainless steel'	N/A	N/A	2	1.45	9	9	25	0	19.8	386	50	35.2	EB	0.83
'duplex stainless steel'	N/A	N/A	2	1.45	9	10.8	25	0	19.8	386	50	38.3	EB	0.83
'duplex stainless steel'	N/A	N/A	2	1.45	9	13.5	25	0	19.8	386	50	43	EB	0.83
'duplex stainless steel'	N/A	N/A	2	1.45	9	18	25	0	19.8	386	50	48	EB	0.83
'duplex stainless steel'	N/A	N/A	2	1.45	9	22.5	25	0	19.8	386	50	50.8	EB	0.83
'duplex stainless steel'	N/A	N/A	2	1.45	9	27	25	0	19.8	386	50	51.2	NST	0.83
'duplex stainless steel'	N/A	N/A	2	1.45	9	45.8	25	0	19.8	386	50	51.2	NST	0.83
'duplex stainless steel'	N/A	N/A	2	1.45	9	9	25	0	45	386	50	41.4	EB	0.83
'duplex stainless steel'	N/A	N/A	2	1.45	9	10.8	25	0	45	386	50	45.6	EB	0.83
'duplex stainless steel'	N/A	N/A	2	1.45	9	13.5	25	0	45	386	50	50.8	EB	0.83
'duplex stainless steel'	N/A	N/A	2	1.45	9	18	25	0	45	386	50	51	EB	0.83
'duplex stainless steel'	N/A	N/A	2	1.45	9	22.5	25	0	45	386	50	51.1	EB	0.83
'duplex stainless steel'	N/A	N/A	2	1.45	9	27	25	0	45	386	50	51.3	NST	0.83
'duplex stainless steel'	N/A	N/A	2	1.45	9	45.8	25	0	45	386	50	51.2	NST	0.83
'duplex stainless steel'	N/A	N/A	2	3	14	14	30	0	42	386	60	105	EB	0.83
'duplex stainless steel'	N/A	N/A	2	3	14	16.8	30	0	42	386	60	117.5	EB	0.83
'duplex stainless steel'	N/A	N/A	2	3	14	21	30	0	42	386	60	118.5	EB	0.83
'duplex stainless steel'	N/A	N/A	2	3	14	28	30	0	42	386	60	118.5	EB	0.83
'duplex stainless steel'	N/A	N/A	2	3	14	35	30	0	42	386	60	119.5	NST	0.83
'duplex stainless steel'	N/A	N/A	2	3	14	42	30	0	42	386	60	119.4	NST	0.83

'duplex stainless steel'	N/A	N/A	2	3	14	52	30	0	42	386	60	119.4	NST	0.83
'duplex stainless steel'	N/A	N/A	2	3	14	14	30	0	30.8	386	60	96	EB	0.83
'duplex stainless steel'	N/A	N/A	2	3	14	16.8	30	0	30.8	386	60	109.5	EB	0.83
'duplex stainless steel'	N/A	N/A	2	3	14	21	30	0	30.8	386	60	118	EB	0.83
'duplex stainless steel'	N/A	N/A	2	3	14	28	30	0	30.8	386	60	118.4	EB	0.83
'duplex stainless steel'	N/A	N/A	2	3	14	35	30	0	30.8	386	60	118.6	EB	0.83
'duplex stainless steel'	N/A	N/A	2	3	14	42	30	0	30.8	386	60	118.6	EB	0.83
'duplex stainless steel'	N/A	N/A	2	3	14	52	30	0	30.8	386	60	118.6	EB	0.83
'duplex stainless steel'	N/A	N/A	2	3	14	14	30	0	70	386	60	106.5	EB	0.83
'duplex stainless steel'	N/A	N/A	2	3	14	16.8	30	0	70	386	60	118.6	EB	0.83
'duplex stainless steel'	N/A	N/A	2	3	14	21	30	0	70	386	60	118.2	EB	0.83
'duplex stainless steel'	N/A	N/A	2	3	14	28	30	0	70	386	60	119.5	EB	0.83
'duplex stainless steel'	N/A	N/A	2	3	14	35	30	0	70	386	60	119.2	NST	0.83
'duplex stainless steel'	N/A	N/A	2	3	14	42	30	0	70	386	60	119.1	NST	0.83
'duplex stainless steel'	N/A	N/A	2	3	14	52	30	0	70	386	60	119.1	NST	0.83
'duplex stainless steel'	N/A	N/A	2	1.47	9	9	14	22	0	375	50	27	EB	0.83
'duplex stainless steel'	N/A	N/A	2	1.47	9	10.8	14	22	0	375	50	32.6	EB	0.83
'duplex stainless steel'	N/A	N/A	2	1.47	9	13.5	14	22	0	375	50	37.5	EB	0.83
'duplex stainless steel'	N/A	N/A	2	1.47	9	18	14	22	0	375	50	41.3	EB	0.83
'duplex stainless steel'	N/A	N/A	2	1.47	9	22.5	14	22	0	375	50	42.8	NST	0.83
'duplex stainless steel'	N/A	N/A	2	1.47	9	27	14	22	0	375	50	42.9	NST	0.83
'duplex stainless steel'	N/A	N/A	2	1.47	9	45.8	14	22	0	375	50	43.2	NST	0.83
'duplex stainless steel'	N/A	N/A	2	1.45	9	45	25	0	27	377	50	52.96	NST	0.83
'S690QL ultra high strength steel'	N/A	N/A	2	10.15	24	71.28	23.04	48.72	0	200	140.88	457	NST	0.95
'S690QL ultra high strength steel'	N/A	N/A	2	10.15	24	28.8	28.8	56.64	0	200	171.84	471	EB	0.95
'S690QL ultra high strength steel'	N/A	N/A	2	10.15	24	48.24	28.8	56.88	0	200	172.08	643	NST	0.95
'S690QL ultra high	N/A	N/A	2	10.15	24	71.76	28.8	56.64	0	200	171.84	638	NST	0.95

strength steel'														
'S690QL ultra high strength steel'	N/A	N/A	2	10.15	24	71.04	29.04	64.8	0	200	180.96	689	NST	0.95
'S690QL ultra high strength steel'	N/A	N/A	2	10.15	24	36	36	57.12	0	200	201.12	596	EB	0.95
'S690QL ultra high strength steel'	N/A	N/A	2	10.15	24	72.72	35.52	64.8	0	200	206.88	789	NST	0.95
'S690QL ultra high strength steel'	N/A	N/A	2	10.15	24	24.72	35.76	72	0	200	215.04	398	EB	0.95
'S690QL ultra high strength steel'	N/A	N/A	2	10.15	24	29.04	36	72	0	200	216	491	EB	0.95
'S690QL ultra high strength steel'	N/A	N/A	2	10.15	24	36.72	36	71.52	0	200	215.52	603	EB	0.95
'S690QL ultra high strength steel'	N/A	N/A	2	10.15	24	49.2	34.56	72	0	200	210.24	776	EB	0.95
'S690QL ultra high strength steel'	N/A	N/A	2	10.15	24	72.96	35.28	72.24	0	200	213.36	851	NST	0.95
'S690QL ultra high strength steel'	N/A	N/A	2	10.15	24	48.24	31.92	57.36	0	200	185.04	678	NST	0.95
'S550Q high-strength steel'	N/A	N/A	2	10	25.9	31.08	31.08	61.901	0	200	124.061	443	EB	0.89
'S550Q high-strength steel'	N/A	N/A	2	10	25.9	31.08	30.821	69.93	0	200	131.572	439	EB	0.89
'S550Q high-strength steel'	N/A	N/A	2	10	25.9	31.08	31.08	77.7	0	200	139.86	438	EB	0.89
'S550Q high-strength steel'	N/A	N/A	2	10	26	30.94	38.74	62.14	0	200	139.62	452	EB	0.89
'S550Q high-strength steel'	N/A	N/A	2	10	26.1	31.059	38.889	69.948	0	200	147.726	442	EB	0.89
'S550Q high-strength steel'	N/A	N/A	2	10	25.9	31.08	38.85	77.7	0	200	155.4	441	EB	0.89
'S550Q high-strength steel'	N/A	N/A	2	10	26	38.74	39	78	0	200	156	561	EB	0.89
'S550Q high-strength steel'	N/A	N/A	2	10	26	39	38.74	90.74	0	200	168.22	562	EB	0.89
'S550Q high-strength steel'	N/A	N/A	2	10	26.1	38.889	38.889	103.878	0	200	181.656	552	EB	0.89
'S550Q high-strength steel'	N/A	N/A	2	10	26	38.74	51.74	77.48	0	200	180.96	575	EB	0.89
'S550Q high-strength steel'	N/A	N/A	2	10	26	39	51.74	90.48	0	200	193.96	576	EB	0.89
'S550Q high-	N/A	N/A	2	10	26	38.74	51.74	103.48	0	200	206.96	570	EB	0.89

strength steel'														
'S690Q high-strength steel'	N/A	N/A	2	10.2	26	31.2	31.2	62.4	0	200	124.8	511	EB	0.96
'S690Q high-strength steel'	N/A	N/A	2	10.2	26	31.2	31.2	70.2	0	200	132.6	516	EB	0.96
'S690Q high-strength steel'	N/A	N/A	2	10.2	26	31.2	31.2	78	0	200	140.4	516	EB	0.96
'S690Q high-strength steel'	N/A	N/A	2	10.2	26	31.2	39	62.4	0	200	140.4	525	EB	0.96
'S690Q high-strength steel'	N/A	N/A	2	10.2	26	31.2	39	70.2	0	200	148.2	523	EB	0.96
'S690Q high-strength steel'	N/A	N/A	2	10.2	26	31.2	39	78	0	200	156	516	EB	0.96
'S690Q high-strength steel'	N/A	N/A	2	10.2	26	38.74	39	78	0	200	156	639	EB	0.96
'S690Q high-strength steel'	N/A	N/A	2	10.2	26	39	39	91	0	200	169	646	EB	0.96
'S690Q high-strength steel'	N/A	N/A	2	10.2	26	39	39	103.74	0	200	181.74	663	EB	0.96
'S690Q high-strength steel'	N/A	N/A	2	10.2	26	39.26	52	78	0	200	182	678	EB	0.96
'S690Q high-strength steel'	N/A	N/A	2	10.2	26	39	52	91	0	200	195	654	EB	0.96
'S690Q high-strength steel'	N/A	N/A	2	10.2	26	39	52	104	0	200	208	654	EB	0.96
'S890Q high-strength steel'	N/A	N/A	2	10.3	26	31.2	31.2	62.4	0	200	124.8	621	EB	0.96
'S890Q high-strength steel'	N/A	N/A	2	10.3	26	31.2	31.2	69.94	0	200	132.34	620	EB	0.96
'S890Q high-strength steel'	N/A	N/A	2	10.3	26	31.2	31.2	78	0	200	140.4	615	EB	0.96
'S890Q high-strength steel'	N/A	N/A	2	10.3	26	31.2	38.74	62.4	0	200	139.88	648	EB	0.96
'S890Q high-strength steel'	N/A	N/A	2	10.3	26	31.2	39.26	70.2	0	200	148.72	643	EB	0.96
'S890Q high-strength steel'	N/A	N/A	2	10.3	26	30.94	39	78	0	200	156	637	EB	0.96
'S890Q high-strength steel'	N/A	N/A	2	10.3	26	38.74	39	78	0	200	156	807	EB	0.96
'S890Q high-strength steel'	N/A	N/A	2	10.3	26	39	39	91	0	200	169	794	EB	0.96
'S890Q high-	N/A	N/A	2	10.3	26	39	39	104	0	200	182	800	EB	0.96

strength steel'														
'S890Q high-strength steel'	N/A	N/A	2	10.3	26	39	52	77.74	0	200	181.74	835	EB	0.96
'S890Q high-strength steel'	N/A	N/A	2	10.3	26	39	52	91	0	200	195	834	EB	0.96
'S890Q high-strength steel'	N/A	N/A	2	10.3	26	39	51.74	104	0	200	207.48	828	EB	0.96
'Mild steel grade S235'	N/A	N/A	2	12	22	33	53.02	53.02	0	200	159	359	BT	0.73
'Mild steel grade S235'	N/A	N/A	2	12	22	55	53.02	53.02	0	200	159	493	BT	0.73
'Mild steel grade S235'	N/A	N/A	2	12	22	33	27.06	80.96	0	200	134	348	EB	0.73
'Mild steel grade S235'	N/A	N/A	2	12	22	55	27.06	80.96	0	200	134	455	NST	0.73
'Mild steel grade S235'	N/A	N/A	2	12	22	33	33	66	0	200	132	353	EB	0.73
'Mild steel grade S235'	N/A	N/A	2	12	22	55	33	66	0	200	132	469	NST	0.73
'duplex stainless steel'	N/A	N/A	4	1.45	9	9	14	22	27	386	50	43	EB	0.83
'duplex stainless steel'	N/A	N/A	4	1.45	9	10.8	14	22	27	386	50	43.1	NST	0.83
'duplex stainless steel'	N/A	N/A	4	1.45	9	13.5	14	22	27	386	50	42.9	NST	0.83
'duplex stainless steel'	N/A	N/A	4	1.45	9	18	14	22	27	386	50	42.8	NST	0.83
'duplex stainless steel'	N/A	N/A	4	1.45	9	22.5	14	22	27	386	50	42.8	NST	0.83
'duplex stainless steel'	N/A	N/A	4	1.45	9	27	14	22	27	386	50	42.8	NST	0.83
'duplex stainless steel'	N/A	N/A	4	1.45	9	45.8	14	22	27	386	50	42.7	NST	0.83
'duplex stainless steel'	N/A	N/A	4	1.45	9	9	14	22	19.8	386	50	43	EB	0.83
'duplex stainless steel'	N/A	N/A	4	1.45	9	10.8	14	22	19.8	386	50	42.8	NST	0.83
'duplex stainless steel'	N/A	N/A	4	1.45	9	13.5	14	22	19.8	386	50	42.8	NST	0.83
'duplex stainless steel'	N/A	N/A	4	1.45	9	18	14	22	19.8	386	50	42.8	NST	0.83
'duplex stainless steel'	N/A	N/A	4	1.45	9	22.5	14	22	19.8	386	50	42.9	NST	0.83
'duplex stainless steel'	N/A	N/A	4	1.45	9	27	14	22	19.8	386	50	42.9	NST	0.83
'duplex stainless steel'	N/A	N/A	4	1.45	9	45.8	14	22	19.8	386	50	42.9	NST	0.83
'duplex stainless steel'	N/A	N/A	4	1.45	9	9	14	22	45	386	50	42.7	EB	0.83
'duplex stainless steel'	N/A	N/A	4	1.45	9	10.8	14	22	45	386	50	43	NST	0.83
'duplex stainless steel'	N/A	N/A	4	1.45	9	13.5	14	22	45	386	50	43	NST	0.83
'duplex stainless steel'	N/A	N/A	4	1.45	9	18	14	22	45	386	50	43	NST	0.83
'duplex stainless steel'	N/A	N/A	4	1.45	9	22.5	14	22	45	386	50	42.8	NST	0.83

'duplex stainless steel'	N/A	N/A	4	1.45	9	27	14	22	45	386	50	42.5	NST	0.83
'duplex stainless steel'	N/A	N/A	4	1.45	9	45.8	14	22	45	386	50	42.5	NST	0.83
ER70S_6	0	M	1	2.7	16	26.6	17.4	0	0	104.1	34.7	20.8	NST	0.79
ER70S_6	0	M	1	2.9	16	27.2	22.7	0	0	135.9	45.3	39.2	NST	0.79
ER70S_6	0	M	1	2.9	16	36.2	22.8	0	0	136.5	45.5	39.3	NST	0.79
ER70S_6	0	M	1	2.6	16	27.1	27.6	0	0	165.6	55.2	34.3	ES	0.79
ER70S_6	0	M	1	2.8	16	21.7	32.7	0	0	196.2	65.4	30.2	ES	0.79
ER70S_6	0	M	1	2.9	16	27.2	32.7	0	0	196.2	65.4	38.3	ES	0.79
ER70S_6	0	M	1	2.9	16	32.5	32.7	0	0	196.2	65.4	46.3	ES	0.79
ER70S_6	0	M	1	2.8	16	36.0	32.7	0	0	196.2	65.4	47.4	ES	0.79
ER70S_6	0	M	1	2.8	16	43.5	32.7	0	0	196.2	65.4	61.0	BT	0.79
ER70S_6	0	M	1	2.8	20	33.2	42.7	0	0	256.2	85.4	46.9	ES	0.79
ER70S_6	0	M	1	2.8	20	57.5	42.8	0	0	256.5	85.5	74.4	ES	0.79
ER70S_6	0	M	1	2.6	20	38.7	52.4	0	0	314.4	104.8	52.3	ES	0.79
ER70S_6	0	M	1	2.7	20	37.3	52.3	0	0	313.5	104.5	52.0	ES	0.79
ER70S_6	0	M	1	2.7	20	47.9	52.2	0	0	313.2	104.4	65.7	ES	0.79
ER70S_6	0	M	1	2.7	24	90.5	72.1	0	0	432.6	144.2	83.6	EB	0.79
ER70S_6	0	M	1	2.7	24	103.3	71.3	0	0	427.8	142.6	92.9	EB	0.79
ER70S_6	0	M	1	2.7	24	115.7	62.0	0	0	372.0	124.0	92.8	EB	0.79
ER70S_6	0	M	1	7.8	24	43.9	22.5	0	0	134.7	44.9	66.3	NST	0.72
ER70S_6	0	M	1	7.9	24	44.1	27.5	0	0	164.7	54.9	105.3	NST	0.72
ER70S_6	0	M	1	7.2	24	44.5	37.5	0	0	224.7	74.9	147.7	NST	0.72
ER70S_6	0	M	1	7.9	24	44.1	40.0	0	0	239.7	79.9	169.1	EB	0.72
ER70S_6	0	M	1	7.7	24	25.9	45.1	0	0	270.6	90.2	87.6	EB	0.72
ER70S_6	0	M	1	7.7	24	39.0	45.1	0	0	270.6	90.2	138.2	ES	0.72
ER70S_6	0	M	1	7.5	24	52.0	45.1	0	0	270.6	90.2	182.7	ES	0.72
ER70S_6	0	M	1	7.5	24	65.2	45.1	0	0	270.3	90.1	208.8	NST	0.72
ER70S_6	0	M	1	7.6	24	91.3	45.2	0	0	270.9	90.3	214.9	NST	0.72
ER70S_6	0	M	1	7.4	30	48.0	60.1	0	0	360.3	120.1	155.1	EB	0.72
ER70S_6	0	M	1	7.5	30	64.1	60.1	0	0	360.3	120.1	207.6	EB	0.72
ER70S_6	0	M	1	7.5	30	80.0	60.0	0	0	360.0	120.0	276.7	EB	0.72
ER70S_6	0	M	1	7.5	30	111.7	60.0	0	0	360.0	120.0	280.3	NST	0.72
ER70S_6	90	M	1	2.7	16	27.0	17.6	0	0	105.6	35.2	23.1	NST	0.75
ER70S_6	90	M	1	2.9	16	27.3	22.6	0	0	135.6	45.2	39.1	NST	0.75
ER70S_6	90	M	1	3	16	36.2	22.7	0	0	136.2	45.4	39.0	NST	0.75
ER70S_6	90	M	1	2.7	16	27.1	27.7	0	0	165.9	55.3	34.3	ES	0.75
ER70S_6	90	M	1	2.9	16	21.7	32.7	0	0	195.9	65.3	31.0	EB	0.75
ER70S_6	90	M	1	2.9	16	27.2	32.6	0	0	195.6	65.2	38.5	ES	0.75
ER70S_6	90	M	1	2.9	16	32.6	32.7	0	0	195.9	65.3	46.1	ES	0.75
ER70S_6	90	M	1	2.8	16	36.5	32.8	0	0	196.8	65.6	48.4	EB	0.75
ER70S_6	90	M	1	2.7	16	43.7	32.7	0	0	195.9	65.3	57.1	BT	0.75
ER70S_6	90	M	1	2.7	20	33.1	42.7	0	0	255.9	85.3	44.7	EB	0.75
ER70S_6	90	M	1	2.8	20	57.3	42.8	0	0	256.5	85.5	75.7	NST	0.75
ER70S_6	90	M	1	2.8	20	37.4	52.5	0	0	315.0	105.0	51.9	EB	0.75
ER70S_6	90	M	1	2.8	20	39.5	52.7	0	0	315.9	105.3	53.9	ES	0.75
ER70S_6	90	M	1	2.8	20	48.2	52.5	0	0	314.7	104.9	66.9	ES	0.75
ER70S_6	90	M	1	2.7	24	91.0	71.9	0	0	431.4	143.8	102.4	EB	0.75
ER70S_6	90	M	1	2.6	24	104.1	72.2	0	0	432.9	144.3	85.8	EB	0.75
ER70S_6	90	M	1	2.7	24	118.4	71.9	0	0	431.1	143.7	84.6	EB	0.75
ER70S_6	90	M	1	7.4	24	43.9	22.4	0	0	134.1	44.7	61.9	NST	0.69
ER70S_6	90	M	1	7.4	24	43.9	27.4	0	0	164.1	54.7	91.8	NST	0.69
ER70S_6	90	M	1	7.4	24	44.1	37.4	0	0	224.4	74.8	144.9	NST	0.69
ER70S_6	90	M	1	7.4	24	44.3	40.0	0	0	239.7	79.9	152.1	EB	0.69
ER70S_6	90	M	1	7.7	24	26.0	45.1	0	0	270.6	90.2	85.5	EB	0.69
ER70S_6	90	M	1	7.6	24	39.1	45.2	0	0	270.9	90.3	134.0	ES	0.69
ER70S_6	90	M	1	7.6	24	52.3	45.1	0	0	270.3	90.1	182.5	NST	0.69
ER70S_6	90	M	1	7.7	24	65.0	45.1	0	0	270.6	90.2	208.8	NST	0.69
ER70S_6	90	M	1	7.6	24	91.1	45.1	0	0	270.6	90.2	206.4	NST	0.69
ER70S_6	90	M	1	7.6	30	48.0	60.2	0	0	360.9	120.3	162.3	EB	0.69

ER70S_6	90	M	1	7.6	30	64.0	60.1	0	0	360.6	120.2	216.1	EB	0.69
ER70S_6	90	M	1	7.8	30	80.1	60.1	0	0	360.3	120.1	276.2	NST	0.69
ER70S_6	90	M	1	7.7	30	112.0	60.1	0	0	360.3	120.1	267.9	NST	0.69
ER50_6	0	AB	1	3.4	18.4	26.3	15.1	0	0	90.3	30.1	18.3	NST	0.85
ER50_6	0	AB	1	3.3	18.4	25.5	19.8	0	0	118.8	39.6	41.2	NST	0.85
ER50_6	0	AB	1	3.5	17.9	26.5	30.3	0	0	181.8	60.6	50.4	ES	0.85
ER50_6	0	AB	1	3.3	18	26.6	34.9	0	0	209.1	69.7	49.8	ES	0.85
ER50_6	0	AB	1	3.4	18.2	35.1	34.8	0	0	208.8	69.6	67.0	ES	0.85
ER50_6	0	AB	1	3.4	17.9	54.2	34.8	0	0	208.8	69.6	92.2	NST	0.85
ER50_6	0	AB	1	3.3	17.8	62.6	49.9	0	0	299.1	99.7	96.4	EB	0.85
ER50_6	0	AB	1	3.2	17.4	64.0	49.8	0	0	298.8	99.6	103.7	EB	0.85
ER50_6	0	AB	1	3.2	17.4	72.8	55.0	0	0	330.0	110.0	110.5	EB	0.85
ER50_6	0	AB	1	3.4	21.6	32.4	25.0	0	0	150.0	50.0	56.3	NST	0.85
ER50_6	0	AB	1	3.3	21.6	33.0	34.7	0	0	208.2	69.4	62.6	ES	0.85
ER50_6	0	AB	1	3.5	21.9	53.0	44.1	0	0	264.3	88.1	97.6	EB	0.85
ER50_6	0	AB	1	3.4	21.8	74.8	49.8	0	0	298.8	99.6	117.0	EB	0.85
ER50_6	0	AB	1	3.2	21.4	76.2	65.1	0	0	390.6	130.2	105.0	EB	0.85
ER50_6	0	AB	1	3.5	26	67.8	39.8	0	0	238.5	79.5	102.4	NST	0.85
ER50_6	0	AB	1	3.4	26	64.8	55.0	0	0	329.7	109.9	112.4	ES	0.85
ER50_6	0	AB	1	3.2	26	95.8	70.1	0	0	420.3	140.1	119.3	EB	0.85
ER50_6	0	AB	1	3.4	26	102.7	73.6	0	0	441.3	147.1	108.9	EB	0.85
ER50_6	90	AB	1	3.3	17.8	24.1	15.1	0	0	90.6	30.2	19.8	NST	0.79
ER50_6	90	AB	1	3.3	18	26.2	19.8	0	0	118.5	39.5	37.7	NST	0.79
ER50_6	90	AB	1	3.1	17.8	26.3	30.3	0	0	181.5	60.5	52.7	EB	0.79
ER50_6	90	AB	1	3.2	17.8	25.7	34.8	0	0	208.8	69.6	46.4	EB	0.79
ER50_6	90	AB	1	3.3	17.8	36.5	35.1	0	0	210.6	70.2	67.6	NST	0.79
ER50_6	90	AB	1	3.1	17.8	53.3	34.7	0	0	208.2	69.4	84.2	NST	0.79
ER50_6	90	AB	1	3.4	17.8	62.3	49.7	0	0	298.2	99.4	106.0	EB	0.79
ER50_6	90	AB	1	3.1	17.8	64.5	49.7	0	0	298.2	99.4	100.5	EB	0.79
ER50_6	90	AB	1	3.2	17.8	70.5	55.0	0	0	330.0	110.0	110.8	EB	0.79
ER50_6	90	AB	1	3.1	21.6	32.8	25.4	0	0	152.1	50.7	50.6	NST	0.79
ER50_6	90	AB	1	3.1	21.4	33.3	34.8	0	0	208.5	69.5	63.2	EB	0.79
ER50_6	90	AB	1	3.4	21.4	51.9	44.3	0	0	265.5	88.5	88.2	EB	0.79
ER50_6	90	AB	1	3.4	21.6	76.2	49.8	0	0	298.5	99.5	120.2	EB	0.79
ER50_6	90	AB	1	3.2	21.6	77.6	65.0	0	0	389.7	129.9	127.4	EB	0.79
ER50_6	90	AB	1	3.2	26.2	64.9	39.9	0	0	239.4	79.8	90.6	NST	0.79
ER50_6	90	AB	1	3.4	26	65.6	54.9	0	0	329.4	109.8	118.7	EB	0.79
ER50_6	90	AB	1	3.6	25.8	97.9	70.1	0	0	420.3	140.1	116.4	EB	0.79
ER50_6	90	AB	1	3.2	26	103.8	74.0	0	0	444.0	148.0	154.9	EB	0.79
ER316L	0	M	1	3.43	19.68	19.8	60.49	0	0	422.0	140.7	64.0	EB	0.58
ER316L	0	M	1	3.38	19.69	29.7	60.3	0	0	420.9	140.3	88.0	EB	0.58
ER316L	0	M	1	3.29	19.67	29.8	60.54	0	0	422.3	140.8	82.6	EB	0.58
ER316L	0	M	1	3.46	19.64	39.9	60.24	0	0	420.4	140.1	99.4	EB	0.58
ER316L	0	M	1	3.71	19.77	50.0	60.17	0	0	420.3	140.1	116.2	EB	0.58
ER316L	0	M	1	3.43	19.59	59.9	60.38	0	0	421.0	140.3	114.0	EB	0.58
ER316L	0	M	1	3.47	19.84	79.9	60.16	0	0	420.5	140.2	135.4	EB	0.58
ER316L	45	M	1	3.33	19.6	19.6	60.12	0	0	419.5	139.8	60.9	EB	0.64
ER316L	45	M	1	3.37	19.74	29.9	60.22	0	0	420.5	140.2	80.4	EB	0.64
ER316L	45	M	1	3.35	19.71	29.8	60.15	0	0	420.0	140.0	87.3	EB	0.64
ER316L	45	M	1	3.58	19.7	39.8	59.6	0	0	416.7	138.9	111.0	EB	0.64
ER316L	45	M	1	3.47	19.69	49.9	60.16	0	0	420.0	140.0	108.4	EB	0.64
ER316L	45	M	1	3.5	19.92	60.1	60.57	0	0	420.2	140.1	114.0	EB	0.64
ER316L	45	M	1	3.44	19.53	79.8	60.28	0	0	420.3	140.1	132.5	EB	0.64
ER316L	90	M	1	3.36	19.78	20.0	60.09	0	0	419.9	140.0	63.1	EB	0.61
ER316L	90	M	1	3.43	19.7	29.9	60.24	0	0	420.5	140.2	85.6	EB	0.61
ER316L	90	M	1	3.28	19.71	29.8	60.41	0	0	421.6	140.5	87.0	EB	0.61
ER316L	90	M	1	3.52	19.63	39.8	60.25	0	0	420.4	140.1	88.8	EB	0.61
ER316L	90	M	1	3.43	19.79	50.0	60.18	0	0	420.4	140.1	106.9	EB	0.61
ER316L	90	M	1	3.59	19.63	59.3	60.24	0	0	420.3	140.1	110.4	EB	0.61
ER316L	90	M	1	3.51	19.73	79.0	59.95	0	0	418.9	139.6	131.3	EB	0.61
ER316L	30	M	1	3.42	19.77	30.4	60.06	0	0	419.6	139.9	82.2	EB	0.65
ER316L	30	M	1	3.58	19.9	29.4	59.76	0	0	418.2	139.4	81.3	EB	0.65
ER316L	60	M	1	3.49	19.64	29.6	60.15	0	0	419.8	139.9	83.5	EB	0.65
ER316L	30	M	1	3.36	19.61	59.9	60.33	0	0	420.8	140.3	103.6	EB	0.65
ER316L	60	M	1	3.37	19.62	60.0	60.16	0	0	419.8	139.9	108.0	EB	0.65
ER316L	0	M	1	3.41	19.58	39.8	16.41	0	0	157.2	52.4	62.8	NST	0.58
ER316L	0	M	1	3.38	19.85	39.9	30.02	0	0	239.7	79.9	91.7	EB	0.58
ER316L	0	M	1	3.44	19.67	39.7	40.32	0	0	300.9	100.3	102.5	EB	0.58

ER316L	45	M	1	3.34	19.75	40.0	15.61	0	0	152.9	51.0	61.6	NST	0.64
ER316L	90	M	1	3.35	19.93	39.7	16.09	0	0	156.3	52.1	63.2	NST	0.61
ER316L	90	M	1	3.23	19.76	39.7	30.5	0	0	242.3	80.8	98.6	EB	0.61
ER316L	90	M	1	3.14	19.83	40.0	39.81	0	0	298.3	99.4	99.6	EB	0.61
ER316L	30	M	1	3.47	19.62	39.8	30.08	0	0	239.3	79.8	87.6	EB	0.65
ER316L	60	M	1	3.4	19.83	40.0	30.14	0	0	240.3	80.1	103.3	EB	0.65
ER316L	0	AB	1	6.12	19.95	29.9	59.99	0	0	419.8	139.9	148.3	EB	0.59
ER316L	0	AB	1	6.33	26.1	52.1	52.15	0	0	391.2	130.4	228.9	EB	0.59
ER316L	0	AB	1	6.32	26.07	52.2	38.93	0	0	311.8	103.9	232.9	EB	0.59
ER316L	0	AB	1	6.26	20.02	39.9	15.95	0	0	155.8	51.9	108.8	NST	0.59
ER316L	90	AB	1	6.4	19.99	30.0	59.92	0	0	419.5	139.8	156.5	EB	0.56
ER316L	90	AB	1	6.43	25.98	52.4	51.94	0	0	389.6	129.9	236.6	EB	0.56
ER316L	90	AB	1	6.41	26.1	52.1	38.99	0	0	312.2	104.1	229.1	EB	0.56
ER316L	90	AB	1	6.23	20.08	40.1	15.94	0	0	155.9	52.0	109.3	NST	0.56
ER50–6	0	AB	1	8.4	24	39.0	35.0	0	0	209.7	69.9	166.7	EB	0.79
ER50–6	90	AB	1	8.2	24	38.7	34.9	0	0	209.1	69.7	160.9	EB	0.79
ER50–6	0	AB	1	8.1	24	39.2	45.2	0	0	270.9	90.3	152.7	EB	0.79
ER50–6	90	AB	1	8.5	24	38.5	44.9	0	0	269.4	89.8	160.8	EB	0.79
ER50–6	0	AB	1	8.8	24	51.5	50.0	0	0	300.0	100.0	226.5	EB	0.79
ER50–6	90	AB	1	8	24	51.5	50.2	0	0	301.2	100.4	215.2	EB	0.79
ER50–6	0	AB	1	8.5	24	56.8	49.8	0	0	298.8	99.6	250.3	ES	0.79
ER50–6	90	AB	1	8.2	24	57.1	50.1	0	0	300.6	100.2	241.4	EB	0.79
ER50–6	0	AB	1	8.4	24	72.4	50.2	0	0	301.2	100.4	296.4	EB	0.79
ER50–6	90	AB	1	8.4	24	72.7	50.1	0	0	300.3	100.1	290.4	NST	0.79
ER50–6	0	AB	1	8.5	24	77.0	55.4	0	0	332.1	110.7	328.5	EB	0.79
ER50–6	90	AB	1	8.2	24	77.7	55.1	0	0	330.3	110.1	321.2	EB	0.79
ER50–6	0	AB	1	8.6	24	82.5	55.1	0	0	330.6	110.2	356.6	EB	0.79
ER50–6	90	AB	1	8.9	24	83.3	55.0	0	0	330.0	110.0	374.2	NST	0.79
ER50–6	0	AB	1	8.7	30	47.4	35.2	0	0	210.9	70.3	159.7	NST	0.79
ER50–6	90	AB	1	8.8	30	47.6	35.1	0	0	210.6	70.2	152.1	NST	0.79
ER50–6	0	AB	1	8.4	30	47.7	45.0	0	0	270.0	90.0	202.3	EB	0.79
ER50–6	90	AB	1	8.1	30	48.6	44.8	0	0	268.5	89.5	202.5	NS	0.79
ER50–6	0	AB	1	8.4	30	89.0	60.5	0	0	362.7	120.9	363.2	EB	0.79
ER50–6	90	AB	1	8.7	30	90.9	60.0	0	0	360.0	120.0	372.2	NST	0.79
ER50–6	0	AB	1	8.3	30	95.8	65.2	0	0	390.9	130.3	378.7	EB	0.79
ER50–6	90	AB	1	7.9	30	93.9	65.3	0	0	391.5	130.5	377.0	EB	0.79
ER50–6	0	AB	1	8.4	30	77.3	49.9	0	0	299.1	99.7	278.9	NST	0.79
ER50–6	90	AB	1	9.2	30	79.8	49.6	0	0	297.6	99.2	318.0	NST	0.79
ER50–6	0	AB	1	8.8	30	79.3	55.7	0	0	333.9	111.3	319.3	NST	0.79
ER50–6	90	AB	1	8	30	79.0	55.0	0	0	330.0	110.0	311.3	NST	0.79
ER50–6	0	AB	1	8.2	30	76.6	60.3	0	0	361.5	120.5	315.9	EB	0.79
ER50–6	90	AB	1	9.3	30	76.6	60.2	0	0	361.2	120.4	385.2	EB	0.79
ER50–6	0	AB	1	8.7	30	86.4	65.6	0	0	393.3	131.1	364.3	EB	0.79
ER50–6	90	AB	1	8.7	30	86.0	65.1	0	0	390.6	130.2	361.3	EB	0.79
austenitic stainless steel	N/A	N/A	1	2	6.6	14	15	0	0	70.0	30.0	18.8	EB	0.73
austenitic stainless steel	N/A	N/A	1	2	6.6	13	15	0	0	70.0	30.0	18.1	EB	0.73
austenitic stainless steel	N/A	N/A	1	2	6.6	11	15	0	0	70.0	30.0	15.7	EB	0.73
austenitic stainless steel	N/A	N/A	1	2	6.6	8	15	0	0	70.0	30.0	11.3	EB	0.73
austenitic stainless steel	N/A	N/A	1	2	6.6	15	8	0	0	70.0	16.0	12	NST	0.73
austenitic stainless steel	N/A	N/A	2	2	6.6	12	12	16	0	70.0	40.0	27.3	BT	0.73
austenitic stainless steel	N/A	N/A	2	2	6.6	11	12	16	0	70.0	40.0	26.6	BT	0.73
austenitic stainless steel	N/A	N/A	2	2	6.6	8.2	12	16	0	70.0	40.0	23.1	EB	0.73

austenitic stainless steel	N/A	N/A	2	2	6.6	8	12	16	0	70.0	40.0	23	BT	0.73
austenitic stainless steel	N/A	N/A	2	2	6.6	7	12	16	0	70.0	40.0	21.1	EB	0.73
austenitic stainless steel	N/A	N/A	2	2	6.6	16	8	24	0	70.0	40.0	30.4	NST	0.73
austenitic stainless steel	N/A	N/A	2	2	6.6	15	11	18	0	70.0	40.0	32.1	BT	0.73
ER316L	0	M	1	2	6.6	14	15	0	0	70	30	18.4	EB	0.55
ER316L	45	M	1	2	6.6	14	15	0	0	70	30	19.2	EB	0.59
ER316L	60	M	1	2	6.6	14	15	0	0	70	30	18.5	EB	0.56
ER316L	90	M	1	2	6.6	14	15	0	0	70	30	17.8	EB	0.5
ER316L	0	M	1	2	6.6	14	15	0	0	70	30	16.9	EB	0.55
ER316L	45	M	1	2	6.6	14	15	0	0	70	30	19	EB	0.59
ER316L	60	M	1	2	6.6	14	15	0	0	70	30	18.1	EB	0.56
ER316L	90	M	1	2	6.6	14	15	0	0	70	30	16.2	EB	0.5
ER316L	0	M	1	2	6.6	11	15	0	0	70	30	15	EB	0.55
ER316L	0	M	1	2	6.6	8	15	0	0	70	30	11.2	EB	0.55
ER316L	0	AB	1	5.4	8.4	14	15	0	0	70	30	44.3	EB	0.56
ER316L	0	AB	1	5.4	8.4	13	15	0	0	70	30	40.8	EB	0.56
ER316L	45	AB	1	5.3	8.4	13	15	0	0	70	30	41.6	EB	0.52
ER316L	60	AB	1	5.2	8.4	13	15	0	0	70	30	38	EB	0.57
ER316L	90	AB	1	5.2	8.4	13	15	0	0	70	30	41.6	EB	0.55
ER316L	0	AB	1	5.3	8.4	11	15	0	0	70	30	33.6	EB	0.56
ER316L	0	AB	1	5.4	8.4	8	15	0	0	70	30	23.8	EB	0.56
ER316L	0	AB	1	5.2	8.4	15	8	0	0	70	16	22.6	NST	0.56
ER316L	45	AB	1	5.4	8.4	15	8	0	0	70	16	23.9	NST	0.52
ER316L	60	AB	1	5.3	8.4	15	8	0	0	70	16	20.5	NST	0.57
ER316L	90	AB	1	5.3	8.4	15	8	0	0	70	16	23	NST	0.55
SLM316LP	0	M	1	2	6.6	14	15	0	0	70	30	18.5	EB	0.83
SLM316LP	0	AB	1	2	6.6	14	15	0	0	70	30	18.7	EB	0.83
SLM316LP	0	AB	1	2	6.6	13	15	0	0	70	30	18.3	EB	0.56
SLM316LP	45	AB	1	2	6.6	13	15	0	0	70	30	18.7	EB	0.75
SLM316LP	90	AB	1	2	6.6	13	15	0	0	70	30	17.5	EB	0.76
SLM316LP	0	AB	1	2	6.6	15	8	0	0	70	16	11.6	NST	0.83
SLM316LP	45	AB	1	2	6.6	15	8	0	0	70	16	11.1	NST	0.75
SLM316LP	90	AB	1	2	6.6	15	8	0	0	70	16	10.7	NST	0.76
ER316L	0	M	2	2	6.6	12	12	16	0	70.0	40.0	26.3	BT	0.55
ER316L	45	M	2	2	6.6	12	12	16	0	70.0	40.0	27.4	BT	0.59
ER316L	60	M	2	2	6.6	12	12	16	0	70.0	40.0	26.8	BT	0.56
ER316L	90	M	2	2	6.6	12	12	16	0	70.0	40.0	25.3	BT	0.5
ER316L	0	M	2	2	6.6	11	12	16	0	70.0	40.0	27.3	BT	0.55
ER316L	0	M	2	2	6.6	8.2	12	16	0	70.0	40.0	23.8	EB	0.55
ER316L	45	M	2	2	6.6	8.2	12	16	0	70.0	40.0	24.4	BT	0.59
ER316L	60	M	2	2	6.6	8.2	12	16	0	70.0	40.0	23.3	BT	0.56
ER316L	90	M	2	2	6.6	8.2	12	16	0	70.0	40.0	21.6	BT	0.5
ER316L	0	M	2	2	6.6	8	12	16	0	70.0	40.0	23.1	EB	0.55
ER316L	0	M	2	2	6.6	7	12	16	0	70.0	40.0	20.7	EB	0.55
ER316L	0	M	2	2	6.6	15	11	18	0	70.0	40.0	31.4	BT	0.55
ER316L	0	AB	2	5.5	8.4	11	12	16	0	70.0	40.0	57	BT	0.56
ER316L	0	AB	2	5.6	8.4	8.2	12	16	0	70.0	40.0	49.5	BT	0.56
ER316L	45	AB	2	5.2	8.4	8.2	12	16	0	70.0	40.0	47.7	BT	0.52
ER316L	60	AB	2	5.5	8.4	8.2	12	16	0	70.0	40.0	48.9	EB	0.57
ER316L	90	AB	2	5.3	8.4	8.2	12	16	0	70.0	40.0	44.9	BT	0.55
ER316L	0	AB	2	5	8.4	8	12	16	0	70.0	40.0	47.6	BT	0.56
ER316L	0	AB	2	5.3	8.4	7	12	16	0	70.0	40.0	43.7	EB	0.56
ER316L	0	AB	2	5.4	8.4	16	8	24	0	70.0	40.0	70.8	NST	0.56
ER316L	45	AB	2	5	8.4	16	8	24	0	70.0	40.0	62.8	NST	0.52
ER316L	60	AB	2	5.3	8.4	16	8	24	0	70.0	40.0	61.8	NST	0.57
ER316L	90	AB	2	5	8.4	16	8	24	0	70.0	40.0	61.7	NST	0.55
ER316L	0	AB	2	5.4	8.4	15	11	18	0	70.0	40.0	69.1	NST	0.56
SLM316LP	0	M	2	2	2	15	11	18	0	70.0	40.0	31.1	NST	0.83
SLM316LP	0	AB	2	2	2	16	8	24	0	70.0	40.0	31.6	NST	0.83

SLM316LP	45	AB	2	2	2	16	8	24	0	70.0	40.0	30.6	NS T	0.75
SLM316LP	90	AB	2	2	2	16	8	24	0	70.0	40.0	31.7	BT	0.76
SLM316LP	0	AB	2	2	2	15	11	18	0	70.0	40.0	33.5	BT	0.83

Regression models script:

```
clc;
clearvars -except MyVariables5;
rng(1);


% Loading the dataset
data = MyVariables5;

% Converting categorical variables to categorical type
categorical_vars = {'Cut_Direction','Surface_finish','TypeofMaterial','FailureMode'};
for var = categorical_vars
    data.(var{1}) = categorical(data.(var{1}));
end

% Defining the target variable
targetVariable = 'FailureLoad_k_N';

% Extracting features
predictorVars = setdiff(data.Properties.VariableNames, {targetVariable});
Xtable = data(:, predictorVars);

% Numeric part
Xnum = table2array(Xtable(:, vartype('numeric')));

% Categorical part (encoding)
Xdummies = [];
catNames = Xtable.Properties.VariableNames(vartype('categorical'));
for i = 1:numel(catNames)
    Xdummies = [Xdummies dummyvar(Xtable.(catNames{i}))];
end

% scaling numeric variables only with leaving dummies as 0/1
Xnum_min = min(Xnum, [], 1);
Xnum_max = max(Xnum, [], 1);
num_range = Xnum_max - Xnum_min;
num_range(num_range == 0) = 1; %  to avoid dividing by zero
Xnum_scaled = (Xnum - Xnum_min) ./ num_range;

X = [Xnum_scaled Xdummies];

% Target
y = data.(targetVariable);


% Cross-validation setup
NumSplits = 5;
cv = cvpartition(size(X, 1), 'KFold', NumSplits);

% Structures for storing aggregated validation predictions
allValPreds = struct('DT', [], 'KNN', [], 'AdaBoost', [], 'SVM_RBF', [], 'ANN', []);
allValTrue = [];

% Accumulating training metrics per fold
```

```
trainMetricsAccum = struct('DT', [], 'KNN', [], 'AdaBoost', [], 'SVM_RBF', [], 'ANN', []);

for split = 1:NumSplits
    % Partition data
    X_train_cv = X(training(cv, split), :);
    y_train_cv = data{training(cv, split), targetVariable};
    X_val_cv = X(test(cv, split), :);
    y_val_cv = data{test(cv, split), targetVariable};

    % DT
    dtModel = fitrtree(X_train_cv, y_train_cv, 'MaxNumSplits', 35);
    y_pred_dt_val = predict(dtModel, X_val_cv);
    y_pred_dt_train = predict(dtModel, X_train_cv);
    rmse_dt_train = sqrt(mean((y_train_cv - y_pred_dt_train).^2));
    trainMetricsAccum.DT = [trainMetricsAccum.DT; struct('RMSE', rmse_dt_train, 'MAE',
mean(abs(y_train_cv - y_pred_dt_train)), 'R2', 1 - sum((y_train_cv - y_pred_dt_train).^2) / sum((y_train_cv -
mean(y_train_cv)).^2))];
    allValPreds.DT = [allValPreds.DT; y_pred_dt_val];

    % KNN
    knnModel = fitcknn(X_train_cv, y_train_cv, 'NumNeighbors', 3);
    y_pred_knn_val = predict(knnModel, X_val_cv);
    y_pred_knn_train = predict(knnModel, X_train_cv);
    rmse_knn_train = sqrt(mean((y_train_cv - y_pred_knn_train).^2));
    trainMetricsAccum.KNN = [trainMetricsAccum.KNN; struct('RMSE', rmse_knn_train, 'MAE',
mean(abs(y_train_cv - y_pred_knn_train)), 'R2', 1 - sum((y_train_cv - y_pred_knn_train).^2) / sum((y_train_cv
- mean(y_train_cv)).^2))];
    allValPreds.KNN = [allValPreds.KNN; y_pred_knn_val];

    % AdaBoost
    AdaboostModel = fitrensemble(X_train_cv, y_train_cv, 'Method', 'LSBoost', 'NumLearningCycles', 30,
'LearnRate', 0.1);
    y_pred_Adaboost_val = (predict(AdaboostModel, X_val_cv));
    y_pred_Adaboost_train = (predict(AdaboostModel, X_train_cv));
    rmse_Adaboost_train = sqrt(mean((y_train_cv - y_pred_Adaboost_train).^2));
    trainMetricsAccum.AdaBoost = [trainMetricsAccum.AdaBoost; struct('RMSE', rmse_Adaboost_train, 'MAE',
mean(abs(y_train_cv - y_pred_Adaboost_train)), 'R2', 1 - sum((y_train_cv - y_pred_Adaboost_train).^2) /
sum((y_train_cv - mean(y_train_cv)).^2))];
    allValPreds.AdaBoost = [allValPreds.AdaBoost; y_pred_Adaboost_val];

    % SVM RBF
    svmModel = fitrsvm(X_train_cv, y_train_cv, 'KernelFunction', 'rbf', 'KernelScale', 0.8, 'BoxConstraint',
1000);
    y_pred_svm_val = predict(svmModel, X_val_cv);
    y_pred_svm_train = predict(svmModel, X_train_cv);
    rmse_svm_train = sqrt(mean((y_train_cv - y_pred_svm_train).^2));
    trainMetricsAccum.SVM_RBF = [trainMetricsAccum.SVM_RBF; struct('RMSE', rmse_svm_train, 'MAE',
mean(abs(y_train_cv - y_pred_svm_train)), 'R2', 1 - sum((y_train_cv - y_pred_svm_train).^2) / sum((y_train_cv
- mean(y_train_cv)).^2))];
    allValPreds.SVM_RBF = [allValPreds.SVM_RBF; y_pred_svm_val];

    % ANN
    hiddenLayerSize = 20;
    annModel = fitnet(hiddenLayerSize);
    annModel.trainParam.epochs = 50;
    annModel = train(annModel, X_train_cv', y_train_cv');
    y_pred_ann_val = annModel(X_val_cv')';
    y_pred_ann_train = annModel(X_train_cv')';
    rmse_ann_train = sqrt(mean((y_train_cv - y_pred_ann_train).^2));
```

```
    trainMetricsAccum.ANN = [trainMetricsAccum.ANN; struct('RMSE', rmse_ann_train, 'MAE',
mean(abs(y_train_cv - y_pred_ann_train)), 'R2', 1 - sum((y_train_cv - y_pred_ann_train).^2) / sum((y_train_cv
- mean(y_train_cv)).^2))];
    allValPreds.ANN = [allValPreds.ANN; y_pred_ann_val];

    % Storing the true values
    allValTrue = [allValTrue; y_val_cv];
end

% Computing average training metrics
averageTrainMetrics = struct();
modelFields = fieldnames(trainMetricsAccum);
for i = 1:numel(modelFields)
    modelName = modelFields{i};
    allMetrics = trainMetricsAccum.(modelName);
    avgRMSE = mean([allMetrics.RMSE]);
    avgMAE = mean([allMetrics.MAE]);
    avgR2 = mean([allMetrics.R2]);
    averageTrainMetrics.(modelName) = struct('RMSE', avgRMSE, 'MAE', avgMAE, 'R2', avgR2);
end

% Computing metrics and plotting validation scatter plots
metrics_DT = cvMetricsAndPlot(allValTrue, allValPreds.DT, 'DT', averageTrainMetrics.DT);
metrics_KNN = cvMetricsAndPlot(allValTrue, allValPreds.KNN, 'K-NN', averageTrainMetrics.KNN);
metrics_AdaBoost = cvMetricsAndPlot(allValTrue, allValPreds.AdaBoost, 'AdaBoost',
averageTrainMetrics.AdaBoost);
metrics_SVM_RBF = cvMetricsAndPlot(allValTrue, allValPreds.SVM_RBF, 'SVM-RBF',
averageTrainMetrics.SVM_RBF);
metrics_ANN = cvMetricsAndPlot(allValTrue, allValPreds.ANN, 'ANN', averageTrainMetrics.ANN);


function metricsTable = cvMetricsAndPlot(y_true, y_pred, modelName, trainMetrics)

    % Validation metrics
    RMSE_val = sqrt(mean((y_true - y_pred).^2));
    MAE_val = mean(abs(y_true - y_pred));
    R2_val = 1 - sum((y_true - y_pred).^2) / sum((y_true - mean(y_true)).^2);
    Mean_val = mean(y_true);
    COV_val = std(y_true) / Mean_val;

    % Training metrics
    RMSE_train = trainMetrics.RMSE;
    MAE_train = trainMetrics.MAE;
    R2_train = trainMetrics.R2;

    %  Metrics tables
    metricsTable = table(RMSE_train, MAE_train, R2_train, RMSE_val, MAE_val, R2_val, COV_val, ...
        'VariableNames', {'RMSE_Train', 'MAE_Train', 'R2_Train', ...
                        'RMSE_Val', 'MAE_Val', 'R2_Val', 'COV_Val'});
    disp([modelName]);
    disp(metricsTable);

    % Plotting
    figure;
    scatter(y_true, y_pred, 'filled'); hold on;
    plot([0, max(y_true)], [0, max(y_true)], '--k');

    xlabel('Fu (kN)', 'FontSize', 12);
    ylabel('Fest (kN)', 'FontSize', 12);
    legend('Data Points', 'Ideal Line', 'Location', 'NorthWest', 'FontSize', 12);
```

```
    title([modelName], 'FontSize', 12);
    xlim([0, 900]);
    ylim([0, 900]);

    print(gcf, [modelName '_CrossValPlot.tiff'], '-dtiff', '-r660');
end
```

Separate colour for CON and AM plots:

```
% Plotting conventional in blue and AM in green

% This should be run after the original regression script noting that it will not alter folds, predictions, or metrics.

assert(exist('allValTrue', 'var') == 1, ...
    'Run the original ML script first.');

assert(exist('allValPreds', 'var') == 1, ...
    'Run the original ML script first.');

assert(exist('data', 'var') == 1 && exist('cv', 'var') == 1, ...
    'Run the original ML script first without clearing the workspace.');

allValCutDirection = categorical([]);

for split = 1:cv.NumTestSets
    allValCutDirection = [allValCutDirection; ...
        data.Cut_Direction(test(cv, split))];
end

isCON = strcmpi(string(allValCutDirection), 'N/A');
isAM = ~isCON;

% Using existing validation predictions from the original script
modelNames = {'DT', 'K-NN', 'AdaBoost', 'SVM-RBF', 'ANN'};

predictionSets = { ...
    allValPreds.DT, ...
    allValPreds.KNN, ...
    allValPreds.AdaBoost, ...
    allValPreds.SVM_RBF, ...
    allValPreds.ANN};

% Creating coloured validation plots only
for i = 1:numel(modelNames)

    y_pred = predictionSets{i};

    figure;
    hold on;
    box on;

scatter(allValTrue(isCON), y_pred(isCON), 36, [0 0.4470 0.7410], 'filled');

scatter(allValTrue(isAM), y_pred(isAM), 36, [0.20 0.60 0.30], 'filled');

    plot([0 900], [0 900], '--k', 'LineWidth', 1);

    xlabel('Fu (kN)', 'FontSize', 12);
    ylabel('Fest (kN)', 'FontSize', 12);
```

```
    legend('CON', 'AM', 'Ideal Line', ...
        'Location', 'NorthWest', 'FontSize', 12);

    title(modelNames{i}, 'FontSize', 12);

    xlim([0 900]);
    ylim([0 900]);
    set(gca, 'FontSize', 12);

    print(gcf, [modelNames{i} '_CrossValPlot_Coloured.tiff'], ...
        '-dtiff', '-r660');

    hold off;
end
```

Classification models script:

for ANN

```
clc;

clearvars -except MyVariables5;
rng(1);


% Loading dataset
data = MyVariables5;

% Converting categorical variables to categorical type
categorical_vars = {'Cut_Direction','Surface_finish','TypeofMaterial','FailureMode'};
for var = categorical_vars
    data.(var{1}) = categorical(data.(var{1}));
end

% Defining the target variable
targetVariable = 'FailureMode';

% Extracting features
predictorVars = setdiff(data.Properties.VariableNames, {targetVariable});
Xtable = data(:, predictorVars);

% Numeric part
Xnum = table2array(Xtable(:, vartype('numeric')));

% Categorical part (encoding)
Xdummies = [];
catNames = Xtable.Properties.VariableNames(vartype('categorical'));
for i = 1:numel(catNames)
    Xdummies = [Xdummies dummyvar(Xtable.(catNames{i}))];
end

% Scaling numeric variables only with leaving dummies as 0/1
Xnum_min = min(Xnum, [], 1);
Xnum_max = max(Xnum, [], 1);
num_range = Xnum_max - Xnum_min;
num_range(num_range == 0) = 1; % To avoid dividing by zero
Xnum_scaled = (Xnum - Xnum_min) ./ num_range;

X = [Xnum_scaled Xdummies];
```

```
% Target
y = data.(targetVariable);

% Fixing category names (to remove unused old naming for NST (NS))
y = categorical(y);
y = removecats(y);

% Cross-validation setup
NumSplits = 5;
cv = cvpartition(size(X, 1), 'KFold', NumSplits);

% Storing validation predictions and actual labels across all splits
all_y_val = [];
all_y_pred_ann = [];

bestMetrics = struct('ANN', struct('Accuracy', 0));
bestModels = struct('ANN', []);

numClasses = numel(categories(y));
confMat = zeros(numClasses);

for split = 1:NumSplits
    % Partitioning data
    X_train_cv = X(training(cv, split), :);
    y_train_cv = y(training(cv, split));
    X_val_cv = X(test(cv, split), :);
    y_val_cv = y(test(cv, split));

    % ANN setup
    hiddenLayerSize = 20;
    annModel = patternnet(hiddenLayerSize);
    annModel.trainParam.epochs = 50;

    % One-hot encoding training labels
    y_train_dummy = dummyvar(y_train_cv);

    % Training ANN
    annModel = train(annModel, X_train_cv', y_train_dummy');

    % Predicting validation set
    y_pred_ann = annModel(X_val_cv');
    [~, y_pred_indices] = max(y_pred_ann);

    % Actual validation labels (numeric indices)
    [~, y_val_indices] = max(dummyvar(y_val_cv), [], 2);

    % Aggregate validation results
    all_y_val = [all_y_val; y_val_indices];
    all_y_pred_ann = [all_y_pred_ann; y_pred_indices'];

    % Confusion matrix for current fold (for reference)
    confMatFold = confusionmat(y_val_indices, y_pred_indices, 'Order', 1:numClasses);
    confMat = confMat + confMatFold;

    % Evaluating fold accuracy
    accuracyANN = sum(y_pred_indices' == y_val_indices) / numel(y_val_indices);

    if accuracyANN > bestMetrics.ANN.Accuracy
```

```
        bestMetrics.ANN.Accuracy = accuracyANN;
        bestModels.ANN = annModel;
    end
end

% Final aggregate confusion matrix (validation results only)
disp('Aggregate Validation Confusion Matrix:');
disp(confMat);

% Final validation accuracy
finalValidationAccuracy = sum(all_y_pred_ann == all_y_val) / numel(all_y_val);
fprintf('Final ANN Validation Accuracy: %.2f%%\n', finalValidationAccuracy * 100);
```

For other models

```
clc;
clearvars -except MyVariables5;
rng(1);

% Loading dataset
data = MyVariables5;

% Converting categorical variables to categorical type
categorical_vars = {'Cut_Direction','Surface_finish','TypeofMaterial','FailureMode'};
for var = categorical_vars
    data.(var{1}) = categorical(data.(var{1}));
end

% Defining the target variable
targetVariable = 'FailureMode';

% Extracting features
predictorVars = setdiff(data.Properties.VariableNames, {targetVariable});
Xtable = data(:, predictorVars);

% Numeric part
Xnum = table2array(Xtable(:, vartype('numeric')));

% Categorical part (encoding)
Xdummies = [];
catNames = Xtable.Properties.VariableNames(vartype('categorical'));
for i = 1:numel(catNames)
    Xdummies = [Xdummies dummyvar(Xtable.(catNames{i}))];
end

% scaling numeric variables only with leaving dummies as 0/1
Xnum_min = min(Xnum, [], 1);
Xnum_max = max(Xnum, [], 1);
num_range = Xnum_max - Xnum_min;
num_range(num_range == 0) = 1; %  to avoid dividing by zero
Xnum_scaled = (Xnum - Xnum_min) ./ num_range;

X = [Xnum_scaled Xdummies];


% Target
y = data.(targetVariable);

% Fixing category names (to remove old naming for NST (NS))
y = categorical(y);
```

```
y = removecats(y);

% Cross-validation setup
NumSplits = 5;
cv = cvpartition(size(X, 1), 'KFold', NumSplits);

% Storing predictions
all_y_true = [];
all_predictions = struct('DT', [], 'KNN', [], 'AdaBoost', [], 'SVM_RBF', []);

for split = 1:NumSplits
   X_train = X(training(cv, split), :);
   y_train = y(training(cv, split));
   X_val = X(test(cv, split), :);
   y_val = y(test(cv, split));

   % DT
   dtModel = fitctree(X_train, y_train, 'MaxNumSplits', 35);
   y_pred_dt = predict(dtModel, X_val);

   % KNN
   knnModel = fitcknn(X_train, y_train, 'NumNeighbors', 3);
   y_pred_knn = predict(knnModel, X_val);

   % AdaBoost
   adaboostModel = fitcensemble(X_train, y_train, 'Method', 'RUSBoost', 'NumLearningCycles', 35,
'LearnRate', 0.1);
   y_pred_adaboost = predict(adaboostModel, X_val);

   % SVM RBF
   template = templateSVM('KernelFunction', 'RBF', 'KernelScale', 0.8, 'BoxConstraint', 1000);
   svmModel = fitcecoc(X_train, y_train, 'Learners', template, 'Coding', 'onevsall');
   y_pred_svm = predict(svmModel, X_val);

   % Storing predictions
   all_y_true = [all_y_true; y_val];
   all_predictions.DT = [all_predictions.DT; y_pred_dt];
   all_predictions.KNN = [all_predictions.KNN; y_pred_knn];
   all_predictions.AdaBoost = [all_predictions.AdaBoost; y_pred_adaboost];
   all_predictions.SVM_RBF = [all_predictions.SVM_RBF; y_pred_svm];
end

% Displaying aggregate validation results for each model
displayValidationResults(all_y_true, all_predictions.DT, 'DT');
displayValidationResults(all_y_true, all_predictions.KNN, 'KNN');
displayValidationResults(all_y_true, all_predictions.AdaBoost, 'AdaBoost');
displayValidationResults(all_y_true, all_predictions.SVM_RBF, 'SVM-RBF');

% Function to build confusion matrix and accuracy
function displayValidationResults(y_true, y_pred, modelName)
   [confMat] = confusionmat(y_true, y_pred);

% Final aggregate confusion matrix (validation results ONLY)
fprintf('\n%s Aggregate Validation Confusion Matrix:\n', modelName);
disp(confMat);

% Final validation accuracy
finalValidationAccuracy = sum(y_true == y_pred) / numel(y_true);
fprintf('Final %s Validation Accuracy: %.2f%%\n', modelName, finalValidationAccuracy * 100);
end
```